Stability and Collapse Dynamics of Dipolar Bose-Einstein Condensates in One-Dimensional Optical Lattices

Von der Fakultät Mathematik und Physik der Universität Stuttgart
zur Erlangung des akademischen Grades eines Doktors der
Naturwissenschaften (Dr. rer. nat.) genehmigte Abhandlung

vorgelegt von

Stefan Müller

aus Heidenheim an der Brenz

Hauptberichter:	Prof. Dr. Tilman Pfau
Mitberichter:	Prof. Dr. Harald Giessen
Prüfungsvorsitzender:	Prof. Dr. Günter Wunner
Tag der mündlichen Prüfung:	23.11.2012

5. Physikalisches Institut
Universität Stuttgart
2013

Abstract

The subject of this thesis is the investigation of the stability and the collapse dynamics of a dipolar ^{52}Cr Bose-Einstein condensate (BEC) in a one-dimensional (1D) optical lattice potential. In this work, it is experimentally shown that the stability of the dipolar BEC is strongly modified when increasing the modulation depth of the sinusoidal potential landscape: a cross-over from dipolar destabilization to dipolar stabilization is observed. For deep lattices, the dipolar BEC is split into a linear array of highly oblate, spatially separated "sub-condensates", located on the different sites of the optical lattice. While stabilized by repulsive dipolar *on-site* interactions, numerical mean-field calculations reveal a significant destabilization of the system by dipolar *inter-site* interactions in this deep lattice regime. In a second set of measurements, the collapse of a coherent array of dipolar BECs, formed by the 1D lattice, is studied. The system is driven from the stable to the unstable region by lowering the lattice depth, while keeping the strength of the inter-atomic interactions fixed. Operating in the unstable regime, the time evolution of the collapsing system is found to be slowed down for larger lattice depths. Unexpectedly, when the system is released from a *stable* in-trap configuration, still a collapsed atomic cloud is observed after time-of-flight (TOF). Such novel collapse scenario, with the collapse being triggered by the TOF itself, is confirmed by real-time simulations and is identified to be a combined effect of the coherence between the sub-condensates and the anisotropy of the dipole-dipole interaction.

Contents

Zusammenfassung

Gegenstand dieser Arbeit ist die experimentelle Untersuchung eines dipolaren Bose-Einstein-Kondensates (BEK) mit Chromatomen in einem eindimensionalen optischen Gitterpotential. Zunächst wird der Einfluss der periodischen Potentiallandschaft auf die wechselwirkungsabhängige Stabilität des dipolaren Quantengases untersucht. Aufbauend auf diesen Messung wird die Kollapsdynamik des Systems, also dessen Zeitentwicklung wenn die Grenze vom stabilen zum instabilen Bereich plötzlich überschritten wird, beobachtet und analysiert. Mit den beiden Untersuchungen wird ein Beitrag zum allgemeinen Verständnis von dipolaren Quantengasen angestrebt. Die Studien bilden zudem eine Grundlage für zukünftige Experimente mit dipolaren BEKs in optischen Gittern, wobei die Beobachtung von selbstorganisierten Dichtestrukturen ein großes Ziel dieses Forschungsbereiches darstellt.

Seit 1995 die ersten BEKs in ultrakalten atomaren Gasen erzeugt wurden [1–4], haben sich entartete Quantengase zu einem idealen Testobjekt für Untersuchungen von Vielteilchen-Quantensystemen entwickelt. In einem BEK besetzen viele Teilchen (typischerweise 10.000 - 1 Million) den Grundzustand eines Systems und können mit einer einzigen Wellenfunktion beschrieben werden. Dies erlaubt eine relativ einfache mathematische Beschreibung des Systems im Rahmen einer Molekularfeldtheorie, die jedoch komplex genug ist um interessante Quantenphänomene zu beschreiben. Auf der experimentellen Seite können die internen und externen Freiheitsgrade eines BEK sehr gut kontrolliert werden. Insbesondere das externe Fallenpotential, durch welches das BEK räumlich eingeschlossen wird, ist beinahe beliebig formbar: sogar periodische Potentiale, wie das oben beschriebene optische Gitterpotential, können erzeugt und dynamisch verändert werden. Schließlich lässt sich ein BEK direkt, z.B. per Schattenwurf, auf eine CCD Kamera abbilden. Meist verwendet man dabei zur Vergrößerung des nur wenige Mikrometer großen BEK die sog. Flugzeitmethode, bei der das Bild erst eine gewisse Zeit nach Abschalten des Fallenpotentials aufgenommen wird. Inzwischen sind aber auch *in-situ* Aufnahmen, teilweise von einzelnen Atomen, mit Hilfe speziell angefertigter Mikroskope gelungen [5, 6].

Trotz der geringen Dichte der Quantengase bestimmen die inter-atomaren *Wechselwirkungen* die grundlegenden Eigenschaften eines BEK. Ohne ihren Einfluss gäbe es keine kollektiven Phänomene in dem Vielteilchensystem, wie z.B. die charakteristische Suprafluidität [7, 8]. Für gewöhnlich sind die Wechselwirkungen zwischen den Atomen *kurzreichweitig* und können durch ein *isotropes* Kontakt-Wechselwirkungspotential beschrieben werden. Dieses Potential wird durch einen einzigen skalaren Parameter, der s-Wellenstreulänge a charakterisiert. Für positive Werte der Streulänge ist die (repulsive) Wechselwirkung vergleichbar mit dem Stoß harter Billiardkugeln. Negative Streulängen hingegen weisen auf eine attraktive Wechselwirkung zwischen den Atomen hin und das Modell der harten Kugeln versagt. Typischerweise ist das BEK im Fall $a < 0$ instabil und es kollabiert [9, 10]. Wie beim externen Fallenpotential, gibt es auch bei den Wechselwirkungen die Möglichkeit

zur experimentellen Kontrolle: viele atomare Spezies verfügen über *Feshbach-Resonanzen*, in deren Nähe die s-Wellenstreulänge über ein externes Magnetfeld eingestellt werden kann [11, 12].

Aufgrund des großen magnetischen Dipolmoments der Chromatome spielt in den hier gezeigten Experimenten außerdem die *Dipol-Dipol-Wechselwirkung* (DDW) eine zentrale Rolle. Im Unterschied zur Kontaktwechselwirkung ist die DDW *langreichweitig* und *anisotrop*, d.h. sie ist anziehend und abstoßend zugleich, je nach relativer Ausrichtung zweier Dipole. Diese beiden Eigenschaften der DDW beeinflussen entscheidend das Verhalten der Vielteilchen-Quantensysteme, wie in zahlreichen experimentellen und theoretischen Studien gezeigt wird [13, 14]. Ein besonderes Merkmal welches für dipolare BEKs vorhergesagt ist, ist das sogenannte Roton-Maxon-Anregungsspektrum [15, 16]: die Energie der Anregungen im Quantengas kann ein lokales Minimum für einen bestimmten Wert des Impulses aufweisen, ähnlich wie es in flüssigem Helium beobachtet wurde [17–19]. Verschiedene selbstorganisierte Strukturen in der Dichteverteilung von gefangenen dipolaren BEKs [20, 21], sowie suprasolide Phasen in optischen Gittern [22, 23] sind nur zwei der interessanten Phänomene die mit dem Roton-Maxon-Spektrum in Verbindung gebracht werden.

Die Vorraussetzung zur Beobachtung der selbstorganisierten dichtemodulierten Zustände ist ein starker Einschluss des dipolaren BEK in der Polarisationsrichtung der Dipole[1] und ein schwacher Einschluss in den beiden senkrechten Raumrichtungen. Solch extrem oblate (pfannkuchenförmige) Fallengeometrien können zum Beispiel mit eindimensionalen (1D) optischen Gittern realisiert werden [24, 25]. Das dipolare BEK wird dabei durch das periodische Potential in eine Reihe von räumlich getrennten Unter-Kondensaten mit der gewünschten oblaten Form aufgeteilt, wobei für genügend hohe Potentialbarrieren das Tunneln von Atomen zwischen den Gitterplätzen stark unterdrückt ist. Eine Besonderheit des dipolaren Systems ist, dass sich die Unter-Kondensate selbst in diesem Fall nicht als isolierte Ensembles beschreiben lassen: sie sind alle untereinander durch die langreichweitige DDW gekoppelt. Diese Kopplung führt zum Beispiel zu kollektiven Anregungen im Gesamtsystem, die ein band-ähnliches Roton-Maxon-Anregungsspektrum mit vielen Eigenmoden aufweisen [26, 27]. Außerdem kann die Wechselwirkung zwischen den Gitterplätzen zu einer Verstärkung der selbstorganisierten Dichtestrukturen führen, wie in numerischen Simulationen gezeigt wurde [28, 29]. Die Vorhersagen dieser interessanten Phänomene sind die Motivation für die experimentellen Untersuchungen die in dieser Arbeit präsentiert werden.

Die Grundlage der Untersuchungen bildet ein ^{52}Cr BEK, welches im harmonischen Potential einer optischen Dipolfalle[2] gefangen ist [30]. Trotz des großen magnetischen Dipolmomentes von 6 Bohrschen Magneton (μ_B) der Chromatome, ist zunächst die Kontaktwechselwirkung im BEK dominierend [31]. In der Nähe einer Feshbach-Resonanz kann

[1] Es wird angenommen, dass alle Dipole entlang eines äußeren Magnetfeldes ausgerichtet sind.

[2] Eine optische Dipolfalle schließt (nach dem Prinzip einer optischen Pinzette) das BEK mit Hilfe fokussierter Laserstrahlen ein.

die s-Wellenstreulänge jedoch reduziert und somit ein Quantengas mit starker dipolarer Wechselwirkung erzeugt werden [32]. Die Kalibration der Streulänge, d.h. die experimentelle Bestimmung ihrer Abhängigkeit von der angelegten Magnetfeldstärke, spielt in den Experimenten eine wichtige Rolle und wird in dieser Arbeit neu betrachtet. Das zentrale neue Element der Messungen ist das eindimensionale optische Gitter, welches einen Abstand der Gitterplätze von 534 nm aufweist. Es wird durch zwei gekreuzte (beinahe gegenläufige) Laserstrahlen erzeugt, wobei die Modulationstiefe ("Gittertiefe") des sinusförmigen Gitterpotentials durch die Intensität der Laserstrahlen kontinuierlich eingestellt werden kann. Die Eigenschaften eines BEK im optischen Gitter werden in der Arbeit ausführlich besprochen, zunächst unter Vernachlässigung der dipolaren Wechselwirkung. Die Kalibration der Gittertiefe wird dabei behandelt, genauso wie der Grundzustand eines BEK in einem kombinierten Potential aus Dipolfalle und optischem Gitter. Auch die Expansion eines BEK nach Abschalten des Gitterpotentials wird theoretisch und experimentell untersucht. Für geringe und mittlere Gittertiefen werden nach einer Flugzeit mehrere diskrete Dichtemaxima aufgezeichnet, ähnlich dem Interferenzmuster von kohärentem Laserlicht nach Passieren eines Mehrfachspaltes. Sehr tiefe Gitter führen hingegen zu komplexeren Dichteverteilungen in den Flugzeitaufnahmen. Dies lässt auf eine Interferenz mehrerer Unter-Kondensate mit unterschiedlichen Phasen rückschließen. Die Charakterisierung des BEK im optischen Gitter ist die Grundvoraussetzung für die anschließend präsentierten Untersuchungen des Systems in einem Regime mit dominanter DDW.

Die ersten Messungen konzentrieren sich auf die *Stabilität* des ^{52}Cr BEK im 1D optischen Gitter. Betrachtet man ein nicht-dipolares BEK, so hängt dessen Stabilität praktisch nur vom Vorzeichen der s-Wellenstreulänge a ab. Oberhalb der kritischen Streulänge $a_{\mathrm{crit}} = 0$ ist das Quantengas stabil, während für kleinere Streulängen kein stabiler Grundzustand existiert[3]. Im Gegensatz dazu wird die Stabilität eines einzelnen dipolaren BEK stark von der Fallengeometrie beeinflusst [35]. In einer prolaten (zigarrenförmigen) Falle, mit den Dipolen entlang der Symmetrieachse ausgerichtet, dominiert der anziehende Charakter der DDW. Die dipolare Wechselwirkung destabilisiert daher das BEK, was zu einer positiven kritischen Streulänge führt. Wählt man hingegen eine oblate Fallengeometrie, so überwiegt die repulsive Wechselwirkung der hauptsächlich nebeneinander angeordneten Dipole. Ein dipolares BEK kann somit selbst für negative Streulängen stabil sein, wobei solch eine dipolare Stabilisierung bisher noch nicht experimentell demonstriert wurde.
Die Stabilität eines dipolaren BEK in einem 1D optischen Gitter ist aus den obigen Betrachtungen eines einzelnen Kondensates nicht vorherzusehen. Während die extrem oblate Form der Unter-Kondensate auf den Gitterplätzen eine dipolare Stabilisierung vermuten lässt, führt die attraktive dipolare Wechselwirkung zwischen den räumlich getrennten Ensembles zu einer Destabilisierung. Daher wird in dieser Arbeit die Stabilität des ^{52}Cr BEK im Bereich von sehr flachen bis sehr tiefen 1D optischen Gittern experimentell untersucht. In den Messungen wird ausgehend von einer stabilen Konfiguration die

[3]Für kleine Atomzahlen und einen schwachen Einschluss können nicht-dipolare BEKs auch für $a < 0$ stabil sein [33, 34]. Die hier erfolgende Stabilisierung durch den Quantendruck kann in unseren Experimenten aber vernachlässigt werden.

Streulänge reduziert, bis der kritische Wert a_{crit} erreicht ist, bei der ein plötzlicher Verlust der Atome im Kondensat eintritt. Für genügend kleine Gittertiefen werden positive kritische Streulängen bis zu $a_{\mathrm{crit}} = (12 \pm 2)\, a_0$ gemessen, mit $a_0 \simeq 0.053\,\mathrm{nm}$ dem Bohrschen Radius. Aufgrund der hohen Tunnelrate zwischen den Gitterplätzen ist hier die prolate Form des harmonischen Fallenpotentials (erzeugt durch die Dipolfalle) ausschlaggebend für die dipolare Destabilisierung des BEK. Im Bereich sehr tiefer optischer Gitter hingegen wird ein negativer Wert von bis zu $a_{\mathrm{crit}} = (-17 \pm 3)\, a_0$ gemessen. Dies zeigt, dass die repulsive dipolare Wechselwirkung auf den Gitterplätzen ein BEK mit attraktiver Kontaktwechselwirkung stabilisiert. Im gesamten Messbereich stimmt die gemessene Stabilitätsgrenze sehr gut mit dem Ergebnis numerischer Rechnungen überein. Diese Rechnungen wurden im Rahmen einer Kollaboration von der Theoriegruppe um Luis Santos in Hannover durchgeführt. Im Bereich sehr tiefer Gitterpotentiale wird die kritische Streulänge außerdem durch Variationsrechnungen bestimmt, bei denen eine Gaußförmige Dichteverteilung der Unter-Kondensate auf den Gitterplätzen angenommen wird. Beide Arten von Rechnungen bestätigen die Stabilisierung des Systems durch die repulsive dipolare Wechselwirkung auf den Gitterplätzen, zeigen aber auch, dass die attraktive Wechselwirkung *zwischen* den räumlich getrennten Unter-Kondensaten die Stabilität deutlich beeinflusst.

Das experimentell ermittelte Stabilitätsdiagramm, welches die kritische Streulänge a_{crit} als eine Funktion der Gittertiefe U_{lat} darstellt, bildet die Grundlage für Untersuchungen der *dynamischen* Eigenschaften des ^{52}Cr BEK im optischen Gitter. Dafür wird ein stabiles dipolares System bei mittlerer Gittertiefe präpariert, welches als eine Reihe kohärenter BEKs beschrieben werden kann. Die gemeinsame globale Phase der BEKs wird dabei durch das Tunneln von Atomen zwischen den Gitterplätzen sichergestellt. Bei konstanter Streulänge wird dann die Gittertiefe reduziert und damit sehr schnell die Grenze zum instabilen Parameterbereich überschritten. Während das BEK in sich zusammenstürzt kommt es aufgrund von inelastischen Dreikörperstößen zu Atomverlusten, durch deren Messung auf die Zeitskala der Kollapsdynamik rückgeschlossen wird. Die Messungen zeigen, dass sich für zunehmende Gittertiefen (aber immernoch im instabilen Bereich) die Kollapsdynamik verlangsamt. Oberhalb der Stabilitätsgrenze werden, wie erwartet, kaum Atomverluste des gefangenen BEK registriert. Wird das dipolare BEK jedoch aus der stabilen Gitterkonfiguration losgelassen, kann es während der Flugzeit zu einem Kollaps kommen. Dieses, vor Durchführung der Experimente unerwartete, Phänomen basiert sowohl auf der Kohärenz der Unter-Kondensate als auch auf der Anisotropie der DDW. Kurz nach dem Öffnen des Fallenpotentials interferieren die bis dahin räumlich getrennten, extrem oblaten Ensembles und bilden atomare Wellenpakete. Die Form dieser Wellenpakete ist nun nicht mehr oblat, sondern entspricht der Einhüllenden des ursprünglich gefangenen BEK. Daher kann sich der dominante Charakter der DDW während der Flugzeit von abstoßend zu anziehend verändern und die Wellenpakete zum Einsturz bringen. Tatsächlich zeigt der Schattenwurf eines der Wellenpakete eine Kleeblattstruktur, wie sie nach dem Kollaps eines einzelnen dipolaren BEK beobachtet

wurde [36]. Dieses neuartige Kollapsszenario wird durch Echtzeit-Simulationen der Gruppe aus Hannover bestätigt.

Die im Rahmen dieser Arbeit durchgeführten Untersuchungen zeigen neue, teils unerwartete dipolare Effekte und sind außerdem für zukünftige Experimente mit dipolaren BEKs in optischen Gittern relevant. Insbesondere die Realisierung einer stabilen Reihe von extrem oblaten dipolaren BEKs mit attraktiver Kontaktwechselwirkung lässt auf eine Beobachtung von Phänomenen hoffen, die im Zusammenhang mit dem Roton-Maxon-Anregungsspektrum stehen. Zum Beispiel werden nahe der Stabilitätsgrenze in sehr tiefen optischen Gittern dichtemodulierte Grundzustände erwartet, die in einem "Roton-Kollaps" in mehrere lokale Dichtemaxima zerfallen [37, 38]. Für experimentelle Untersuchungen in diesem Parameterbereich sind jedoch einige Herausforderungen zu meistern: das Dephasieren der Unter-Kondensate oder ein Kollaps in der Flugzeit kann die erzeugten Strukturen "verwischen". Am Ende dieser Arbeit werden anhand von Testmessungen Möglichkeiten aufgezeigt, wie diese Experimente dennoch erfolgreich durchgeführt werden könnten.

Obwohl eine präzise Kontrolle über die Wechselwirkungen im ^{52}Cr BEK und über das externe Fallenpotential erreicht ist, sind die technischen Möglichkeiten des gegenwärtigen experimentellen Systems weitestgehend ausgeschöpft. Daher wurde, parallel zur Durchführung der hier gezeigten Messungen, ein neuer Aufbau geplant und bereits teilweise installiert. Zur Zeit werden diese Arbeiten abgeschlossen, eine Dokumentation des Aufbaus wird in den folgenden Dissertationen erfolgen. Es werden technische Neuerungen implementiert, wie z.B. ein hochauflösendes Mikroskopobjektiv, das Strukturen im Bereich von 1 µm auflösen soll - etwa ein Faktor 6 besser als das bisherige Abbildungssystem. Außerdem wird dieses Objektiv dafür verwendet werden, den Laserstrahl einer optischen Dipolfalle auf einen Strahlradius von ebenfalls ca. 1 µm zu fokussieren. Durch schnelles Bewegen dieses Laserstrahls können dann fast beliebige, zeitlich-gemittelte Fallenpotentiale realisiert werden [39]. Somit können die Studien von selbstorganisierten Grundzuständen mit einer noch höheren Präzision und Kontrolle durchgeführt werden. Die bedeutendste Neuerung ist jedoch der Wechsel der atomaren Spezies von Chrom auf Dysprosium. Letzteres wurde im Jahr 2011 von der Gruppe um B. Lev erfolgreich kondensiert [40] (^{164}Dy BEK) und weist das größtmögliche magnetische Dipolmoment eines Atoms von $10\,\mu_{\mathrm{B}}$ auf. Da inzwischen auch das fermionische Isotop ^{161}Dy unter die Fermi-Temperatur gekühlt wurde [41], sind zukünfig auch erstmals Untersuchungen von entarteten dipolaren Fermigasen und dipolaren Bose-Fermi-Mischungen möglich.

1 Introduction

Since the realization of Bose-Einstein condensates (BECs) in ultracold dilute atomic vapours in 1995 [1–4], degenerate quantum gases have become an ideal environment to study many-body systems in the quantum regime. Essentially, BECs represent macrosopic quantum objects, with around $10,000 - 1$ million atoms described by one single wave function. In a standard experimental setup, they may be directly observed by optical means, e.g. through the technique of absorption imaging [42]. Furthermore, their internal and external degrees of freedom can be controlled with a very high precision, in particular, their external trapping potential can be almost arbitrarily designed. Even periodic potentials may be realized, trapping the atoms in the high intensity regions of a standing light wave [43]. Among the various studies in such *optical lattices*, bosonic as well as fermionic quantum gases have successfully modelled solid state systems [44, 45]. One of the greatest successes was the demonstration of the quantum phase transition from a superfluid to a Mott insulator [46], recently confirmed by in-situ imaging techniques at the single atom level [5, 6].

Besides the external confinement, it is the inter-atomic interactions which govern most properties of a BEC. Only in their presence, the atoms in a condensate show a collective behaviour, e.g. leading to the characteristic superfluid flow [7, 8]. Usually these interactions are modelled by a *short-range* and *isotropic* contact interaction potential, characterized by a single scalar parameter: the s-wave scattering length a. In the case of positive values for a, such model is equivalent to the (repulsive) scattering of hard spheres. Negative scattering lengths, in contrast, correspond to an attractive contact interaction between the atoms, where no simple model exists. Experimentally, one can control the s-wave scattering length by means of an external magnetic field in the vicinity of a *Feshbach resonance* [11, 12]. The tunability of the local interactions enabled e.g. the study of new quantum phases such as the one-dimensional Tonks-Girardeau gas [47]. On a more fundamental level it has been shown that a BEC is typically unstable for negative s-wave scattering lengths [9]. When suddenly driven into this unstable regime, the "violent" collapse dynamics of the condensate shows bursts and jets of atoms that are expelled from the sample [10].

As the properties of BECs are crucially depending on the interactions, there is a quest for realizing quantum gases with new types of interactions. In particular, *dipolar* quantum gases have attracted a major attention in the recent years. Here, the interaction potential between two (electric or magnetic) dipoles is *anisotropic* and has a *long-range* character − two features that significantly enrich the physics of ultracold many-body systems. When starting the work on this thesis, the only condensed atomic species with a relevant magnetic dipole-dipole interaction (DDI) was chromium (Cr). The first ^{52}Cr BEC was created in Stuttgart in 2004 [30], followed by the group of O. Gorceix in Paris in 2007 [48]. Even though chromium has a large magnetic dipole moment ($\mu_{\mathrm{m}} = 6\,\mu_{\mathrm{B}}$, with μ_{B} the Bohr magneton), the dipolar interactions are typically much weaker than

the contact interactions in the system. Nevertheless, dipolar effects have been observed e.g. by measuring the expansion velocity of the chromium BEC [31] or the frequency of a collective excitation mode [49]. An anisotropic sound velocity in the dipolar BEC (dBEC), depending on the orientation of the dipoles, was furthermore observed by measuring the excitation spectrum of the condensate [50]. With the possibility to reduce the *s*-wave scattering length via the Feshbach resonance technique, weak dipolar effects were also observed in alkali BECs of ^{39}K [51] and ^{7}Li [52].
In the vicinity of such Feshbach resonance in chromium, a *strongly* dipolar ^{52}Cr BEC could be realized [32]. It was found that for dominant dipolar interactions the stability of the dBEC depends on the geometry of the confining trap [35]: in a prolate trap (cigar-shaped) with the polarized dipoles sitting mainly in the attractive head-to-tail configuration, the dipolar interactions destabilize the atomic sample. In contrast, the dBEC is more stable when confined in an oblate trapping geometry (pancake-shaped) where the dipoles repell each other in a side-by-side configuration. By suddenly driving the system from the stable into the unstable regime, the dBEC undergoes a collapse and explosion. Images of a *d*-wave symmetric density distribution after such collapse have directly visualized the anisotropy the DDI [36]. Even though the collapse is a violent process it does not completely destroy the coherence in the system, as shown by the interference between multiple collapsed dipolar condensates [53].

The family of dipolar bosonic quantum gases has recently been extended by condensates of ^{168}Er (erbium) [54] and ^{164}Dy (dysprosium) [40], with the large magnetic moments $\mu_\mathrm{m} = 7\,\mu_\mathrm{B}$ and $\mu_\mathrm{m} = 10\,\mu_\mathrm{B}$, respectively. Erbium provides several Feshbach resonances at low magnetic fields that allow to reach the strongly dipolar regime. The dysprosium BEC shows features of dominant dipolar interactions even without reducing the contact interaction strength. Long observation times of a strongly dipolar BEC may thus be possible in the dysprosium system, while the lifetime of the samples is usually limited by the enhanced atom losses in the vicinity of Feshbach resonances [55]. Both atomic species are furthermore expected to show a more complex scattering behaviour than chromium or the alkali elements, due to the strong DDI and the nonzero angular momentum in their ground-states [56]. The elastic collisions observed in an ultracold gas of fermionic ^{161}Dy could be already a first signature of universal dipolar scattering [57, 58]. These collisions allowed to cool the pure sample below the Fermi temperature and thus to create the first quantum degenerate dipolar Fermi gas [41].
While dysprosium is the most magnetic atom available, heteronuclear molecules provide an even stronger (and tunable) DDI via their electric dipole moment. Well-studied systems are samples of fermionic ^{40}K^{87}Rb ground-state molecules [59], which were unfortuntely found to be unstable due to exothermic bimolecular reactions [60, 61]. However, the reaction rate could be substantially lowered by applying a tight confinement along the polarization direction of the dipoles, creating meta-stable systems on experimental time scales [62]. A promising candidate to form a chemically stable gas are fermionic ^{23}Na^{40}K molecules, where weakly bound Feshbach molecules have recently been created [63]. The

last dipolar system being presented here are homonuclear Rb_2 molecules, with one of the atoms excited to a high-lying Rydberg state [64]. Contrary to the general case of homonuclear molecules, such system exhibits a large permanent electric dipole moment through the asymmetric excitation between the atoms [65].

The active experimental branch in the field of dipolar quantum gases evolves in a symbiosis with the theoretical progress. Especially dipolar gases in reduced dimensions have been subject to many theoretical studies in the recent years. One major property of a dipolar BEC, strongly confined along the polarization direction, is the *roton-maxon excitation spectrum* [15, 16]: similar to the spectrum observed in liquid helium [17–19], the energy of the excitations of a dipolar gas can show a local minimum at a finite momentum value. Various structures in the atomic ground-state density of trapped dBECs [20, 21], as well as supersolid phases in optical lattices [22, 23] are some of the most interesting phenomena related to the rotonic excitation spectrum. These density modulations have their beautiful analogon in the multi-peak structures of a classical ferrofluid that undergoes a Rosensweig instability in an external magnetic field [66]. For very large dipole strengths, as can be provided by polar molecules, a quantum phase transition from a superfluid to a strongly correlated crystalline phase is expected to occur in a two-dimensional (2D) bosonic system [67, 68]. Two-dimensional dipolar condensates furthermore support the formation of anisotropic bright solitons [69–71] and vortex lattices of different symmetries are predicted to form in rotating 2D dipolar BECs [72]. Dipolar many-body systems in reduced dimensions thus hold many fascinating phenomena, with a detailed overview given in two recent reviews [13, 14].

Regarding the experimental realization, low dimensional ultracold gases can be created for example by using the optical lattice potentials discussed before [24, 25, 47]. An ultracold cloud can thus be split into a linear array of spatially separated two-dimensional samples when trapped in a one-dimensional (1D) lattice potential. In such lattice geometry, the non-local character of the DDI has an interesting effect: even if the tunneling of atoms between the lattice sites is suppressed, the spatially separated samples interact with each other through the long-range DDI. The physics of 2D dipolar condensates therefore becomes even richer in such multi-layer geometry. In particular, the roton-maxon excitation spectrum is expected to develop a band-like structure through the inter-site coupling of the excitations [26, 27]. Furthermore, modulated ground-state structures of the 2D on-site condensates are predicted to be enhanced [28, 29]. Experimentally, weak effects of the dipolar inter-site interactions were already observed in the damping of Bloch oscillations of a ^{39}K BEC in a 1D lattice [51]. The properties of strongly dipolar BECs in optical lattices, however, have not been studied so far, motivating the experimental investigations presented in this thesis.

This thesis

In this thesis I report on the investigation of a ^{52}Cr BEC in a one-dimensional optical lattice, operating in a regime with dominant dipolar interactions. The experimental work presented here, relies greatly on the previous achievement of a ^{52}Cr BEC with the *s*-wave scattering length tunable by the Feshbach resonance technique [73, 74]. To this existing setup, we added a 1D lattice potential aligned in the polarization direction of the dipoles. Our first studies address the most fundamental property of the system, its stability, in the range from shallow to deep lattices. Slicing a prolate dBEC into a stack of highly oblate sub-condensates, one encounters both an on-site repulsion and an inter-site attraction between the dipoles. Therefore, the stability of the system is *a priori* unknown and may not be deduced from the measurements performed on a single trapped dBEC. Experimentally, we observe a cross-over from a dipolar destabilization to a dipolar stabilization of the system when increasing the lattice depth. The dipolar repulsion inside the quasi-two-dimensional[4] on-site condensates thus dominates over the dipolar inter-site attraction. Nevertheless, our investigations show that the attractive inter-site interactions must be taken into account to correctly calculate the stability threshold of the system. The experimental work has been performed in a close collaboration with the theory group of Luis Santos in Hannover, with the results published in Ref. [75].
Moreover, measurements on the dynamic properties of the dBEC in the 1D lattice configuration are presented in this thesis. Taking advantage of the stability measurements, we induce the collapse of an initially stable system by reducing only the depth of the optical lattice potential while keeping the two-body interaction strength fixed. With this new technique to induce the collapse by a change of the confinement, we study the time-scale of the collapse dynamics of the dBEC in the lattice. In addition, we investigate a dynamic phenomenon that was unexpected: the dBEC can become unstable after the release from a *stable* lattice configuration to perform a so-called time-of-flight (TOF). Such behaviour contradicts the standard assumption made on TOF measurements that a BEC remains stable if it was stable in-trap. Again, the measurements are supported by the theory group in Hannover performing numerical real-time simulations of the collapse dynamics, with the results being published in Ref. [76].

Outline

The thesis is structured as follows. Chapter 2 gives a theoretical introduction to the physics of dipolar BECs. The mean-field model is introduced, which allows for an efficient computation of the properties of the system, taking into account the contact and the dipolar interactions. In addition to a single dBEC, also a configuration with multiple,

[4] In a *quasi*-two-dimensional gas the excitations are frozen along one direction, while the scattering is still three-dimensional. The phenomena described above, as e.g. the roton-maxon excitation spectrum, are expected to occur in such a system.

spatially separated dipolar condensates is considered in the discussion. Chapter 3 describes the production process of a ^{52}Cr BEC with tunable contact interactions. Special emphasis is put on the principle and the application of the Feshbach resonance technique as it is a key ingredient in our experiments. The setup of the 1D optical lattice and the basic physics of a (non-dipolar) BEC in such periodic potential is presented in chapter 4. The procedure to calibrate the lattice depth is explained and the ground-state properties of a contact interacting BEC in the lattice are considered. Furthermore, the expansion of a BEC from the optical lattice is discussed, including expansion measurements in both shallow and deep lattice regimes. The stability of the dBEC in the 1D optical lattice is the central topic of chapter 5. Before presenting our measurements, I introduce the basic instability mechanisms (phonon and roton instability) and briefly review the stability of a single trapped dBEC. It is discussed in details how the stability of a dBEC in the lattice depends on the interplay between the on-site and inter-site interactions and the tunneling in the system. Chapter 6 is dedicated to the dynamic properties of a strongly dipolar lattice gas. Measurements and numerical simulations of the collapse dynamics are presented, with a focus on the new scenario of a post-release collapse. Finally, a summary of our findings and an outlook to the future prospects of the experiment is given in chapter 7.

2 Dipolar Quantum Gases

This chapter gives a brief introduction to the physics of bosonic dipolar quantum gases. It provides the basic formalisms to understand the experimental results presented in this thesis. For more details, two recent reviews on dipolar quantum gases give an excellent overview of the field [13, 14].

The chapter starts with an introduction to the phenomenon of Bose-Einstein condensation. Including contact and dipolar interactions, we then derive the non-local Gross-Pitaevskii equation (GPE), a mean-field description of the dipolar Bose-Einstein condensate (dBEC). In the limit of dominant interactions, we may apply the so-called Thomas-Fermi approximation and solve the GPE exactly. This approach reveals some basic properties of a dBEC, such as its elongation along an external magnetic field. In the last part of the chapter, we focus on the interaction of spatially separated dipolar BECs. We first consider two interacting samples before showing that the dipolar inter-site interaction may be enhanced in a linear array of multiple dipolar clouds.

2.1 Bose-Einstein Condensation

At any time in everyday life, we are surrounded by gases. In a microscopic view, even when taking only one single atomic species, all the atoms in gas are different and can be indentified one by one: they may differ in their position in space, their speed and the direction they move, or any other property like internal excitation, magnetization, etc.. Generally speaking, they differ by the state that they occupy in the system.

Over the past three decades, experimental physicists made tremendous effort to cool and trap neutral atoms [77]. They were motivated by Einstein's prediction in 1925 that at ultra-low temperatures, dilute gases of bosonic atoms exhibit a novel type of phase transition: below a critical temperature the atoms may become indistinguishable by occupying the very same single-particle state and form a so-called *Bose-Einstein condensate* (BEC) [78]. Finally in 1995, Bose-Einstein condensates were realized in dilute gases of the alkali elements rubidium, sodium, and lithium [1–4]. Since then, condensation has been achieved in many other atomic species[5], the latest being dysprosium [40] and erbium [54].

Early contributions to the theory of BECs were made in the late 1920s. Eventually, the observation of superfluidity of liquid helium in 1938 [83, 84] triggered further theoretical progress: London was the first to connect superfluidity and Bose-Einstein condensation in 1938 [85]. Landau and Lifschitz, and Penrose and Onsager developed this idea further and formulated the concept of *non-diagonal long-range order* [86–88]. In essence, their definition of a Bose-Einstein condensate does not only require superfluidity, but also

[5]Bose-Einstein condensation has also been achieved in other bosonic systems. For example BECs of photons [79], excitions [80], and polaritons [81, 82] are reported.

a *macroscopic phase coherence* throughout the sample. A detailed treatment on the fundamental properties of BECs is given in Refs. [8, 89].

For an intuitive picture, let us consider the realistic case of a thermal sample of bosonic atoms confined in a harmonic trapping potential, with ω_0 the characteristic angular oscillation frequency of a single particle. The thermal de-Broglie wavelength is defined as [89]

$$\lambda_T(T) \stackrel{\text{def}}{=} \sqrt{\frac{2\pi\hbar^2}{mk_BT}}, \tag{2.1}$$

where $\hbar = \frac{h}{2\pi}$ is the reduced Planck constant, m the atomic mass, k_B the Boltzmann constant, and T the temperature of the sample. Typically in a gas, λ_T is much smaller than the mean distance between the particles, and therefore the gas shows only classical behaviour without any wave-like character. However, if the temperature is decreased below a critical value, λ_T becomes on the order of the mean inter-particle separation. The atoms thus form overlapping wave packets and loose their individual identities. To obtain the critical temperature T_c for this phase transition to the Bose-Einstein condensate, we approximate the density in the gas by $n = \frac{N}{R^3}$, with N the atom number and $R \sim \sqrt{\frac{k_BT}{m\omega_0^2}}$ the size of the sample. Replacing the thermal de-Broglie wavelength by the mean inter-particle distance $n^{-1/3}$, Eq. (2.1) results in

$$k_BT_c = C \cdot \hbar\omega_0 N^{1/3}, \tag{2.2}$$

where C is a numerical constant which is determined by more advanced calculations to be $C \approx 0.94$ [90]. The equation (2.2) provides a good estimate of the critical temperature in experiments with ultracold atoms. Typical experimental parameters are $\omega_0 \approx 2\pi \cdot 100\,\text{Hz}$ and $N = 10^4$ - 10^7 resulting in a range of T_c from about 100 nK to a few µK. When the critical temperature is reached, not all the particles in the sample occupy the ground state of the system. According to the Bose-Einstein distribution, N_{ex} particles still populate excited states, while the number of particles in the condensate is given by[6] [91]

$$N_0(T) = N - N_{\text{ex}}(T) = N\left[1 - \left(\frac{T}{T_c}\right)^3\right]. \tag{2.3}$$

The physics of the ideal Bose gas extends far beyond the brief description given above. Early works on quantum statistics, thermodynamical and local properties of ideal Bose gases are summarized e.g. in Ref. [92]. Our goal, however, is the study of interactions in such degenerate quantum gas. Therefore, we next turn our attention to the theoretical description of the binary interactions present in BECs.

[6] In general the number of atoms in the excited states depends on the dimensionality of the system and the shape of the trapping potential [89, 90]. Equation (2.3) is valid only in the case of a three-dimensional harmonic trapping potential.

2.2 Two-Body Interactions

The atomic density in a BEC is typically around $n_{\mathrm{BEC}} = 10^{14} - 10^{15}\,\mathrm{cm}^{-3}$, which is very low compared to solids ($n_{\mathrm{carbon}} \sim 10^{23}\,\mathrm{cm}^{-3}$) or even air ($n_{\mathrm{air}} \sim 10^{19}\,\mathrm{cm}^{-3}$). From such low density we might deduce that interactions between the particles do not play any role regarding the physics of BECs. Yet, despite the diluteness of a condensate, the interactions determine the fundamental properties of a BEC, as for example its shape, stability, dynamics, and even its decay [8, 89, 91, 93, 94].

In this section we examine the relevant two-body interactions in a dipolar BEC. We will first show that, in the ultracold limit, the combined potential of all the short-range interactions can be replaced by a zero-range pseudo-potential. The only remaining contribution, that is not incorporated in the pseudo-potential, is the long-range dipolar interaction which we will treat separately.

2.2.1 Short-range Interactions

At small separations $\boldsymbol{r}$ between two atoms, several interactions contribute to the so-called *molecular potential* $V(\boldsymbol{r})$. This potential is usually unknown, except from some general properties:

(i) at very small distances the electron clouds of the atoms overlap, leading to a strong *Coulomb repulsion*,

(ii) at slightly larger distance *exchange interaction* takes over, causing strong attraction and a minimum of the potential at $r = r_{\mathrm{min}}$,

(iii) further out induced dipole-dipole interaction leads to a weak attraction between the particles, known as the *van-der-Waals interaction*, with a scaling $V_{\mathrm{vdW}} \propto -1/r^6$.

The molecular potential has typically a depth of $|V(r_{\mathrm{min}})|\,/k_{\mathrm{B}} \sim 10^3\,\mathrm{K}$. Therefore, a large amount of energy can be released, if two atoms in the BEC bind together to form a molecular state. This indicates that even though the temperature of an ultracold atomic samples is as low as $T \sim 1\,\mu\mathrm{K}$, the BEC is not the true ground state of the system which corresponds to a solid phase [8, Ch.9.1]. Fortunately, the rate at which molecules are created in a BEC is usually sufficiently low to enable (meta-)stable condensates on the time scale of around one second.
To estimate the spatial range of the molecular potential, we consider Heisenberg's uncertainty principle: any confinement of a particle to a region Δx demands a momentum uncertainty $\Delta p \approx \hbar/\Delta x$. Then, by equating the corresponding kinetic energy $(\Delta p)^2/(2m)$

with the van-der-Waals term of the molecular potential[7], we obtain an interaction radius $r_0 \sim 100\, a_0$ of the molecular potential. This defines the maximal distance between two atoms at which the weakest bound-state can be formed.
The interaction range r_0 is typically much smaller than the mean inter-particle distance d_{mean} in a BEC, with $d_{\mathrm{mean}} = (n_{\mathrm{BEC}})^{-1/3} \sim 4000\, a_0$. Therefore, in most regions of the condensate, the atoms propagate freely without any perturbation by the interactions. Only if two atoms are separated by less than r_0, they undergo an elastic scattering process and then move again freely. This means that, to compute the effect of the interactions in the condensate, it is not crucial to know the exact shape of the interaction potential. We only have to know the resulting wave function of the two-particle system after the scattering process. Following this idea, we can replace the (unknown) molecular potential by any suited *two-body pseudo-potential* of a simpler form which yields the same scattering properties of the two-particle system.
To discuss the elastic scattering properties of an ultracold atomic gas[8], let us consider the simple picture of two colliding atoms of radius r_0, illustrated in Fig. 2.1 *(a)*. At first, we address the question which states of relative angular momenta are involved in such elastic scattering process, as this will define the symmetry of the scattered wave function. With the pair of colliding atoms moving at a relative velocity v, we obtain a relative angular momentum of $\hbar l \simeq m_{\mathrm{red}} v\, r_{\mathrm{impact}}$, with r_{impact} the impact parameter defined in Fig. 2.1 *(a)* and l the quantum number of the relative orbital angular momentum. At ultra-low temperatures, we may express the maximum relative velocity in terms of the de-Broglie wavelength [97]: $\lambda_{\mathrm{dB}} \stackrel{\mathrm{def}}{=} h/p \simeq h/(m_{\mathrm{red}} v)$. By identifying the impact parameter with the range of the interaction potential r_0, we obtain the condition for the angular momentum $l \leq 2\pi r_0/\lambda_{\mathrm{dB}}$. As we know that, in a condensate, the de-Broglie wavelength is much larger than r_0 and since l is an integer value, the only possible solution is $l = 0$. Therefore, the scattered wave function takes a spherically symmetric shape, representing a so-called *s-wave*. As a consequence, we can replace the true molecular potential (that might even by anisotropic), by a spherically symmetric pseudo potential, which is convenient for any further calculations. From several existing pseudo potentials [93], we consider two particularly useful cases:

(i) the *hard sphere potential* V_{hs}, with $V_{\mathrm{hs}}(r \leq a) \stackrel{\mathrm{def}}{=} \infty$ and $V_{\mathrm{hs}}(r > a) \stackrel{\mathrm{def}}{=} 0$, and

(ii) the zero-range *contact interaction potential*,

$$V_{\mathrm{contact}} \stackrel{\mathrm{def}}{=} g\, \delta(\boldsymbol{r}) \tag{2.4a}$$

[7]Equating the kinetic energy with the van-der-Waals potential results in $\hbar^2/(2m_{\mathrm{red}} r_0^2) = C_6/r_0^6$, where we have inserted $\Delta x = r_0$. With the van-der-Waals coefficient in chromium [95] $C_6 = 733$ atomic units, and the reduced mass $m_{\mathrm{red}} = m/2$ of the two-particle system, we obtain the range $r_0 \sim 100\, a_0$ given in the text.
[8]The following argumentation is valid for finite range potentials and potentials with a power-law scaling $V \propto r^{-n}$, if $n > 3$ [93]. A detailed theoretical treatment on the scattering of ultracold atoms can be found e.g. in Ref. [96, Ch.8].

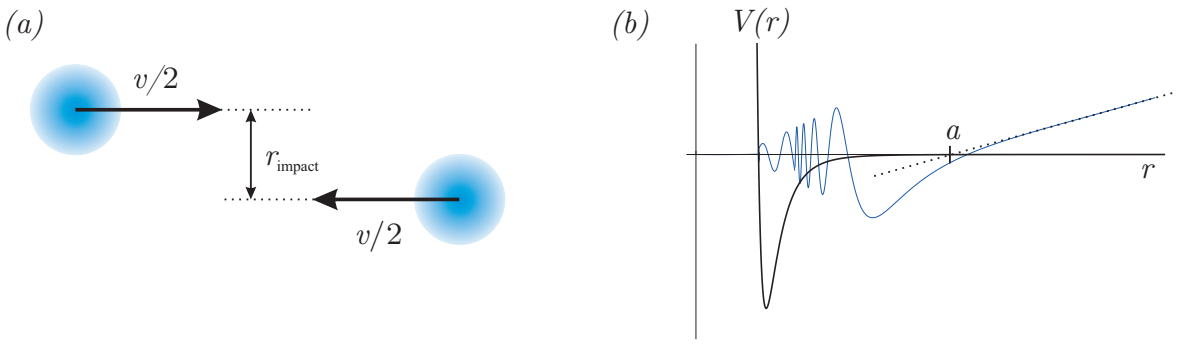

Fig. 2.1, Elastic two-body scattering: *(a)* Classical picture of two colliding atoms moving at the relative velocity v. The impact parameter r_{impact} defines the minimum distance of the particles in the scattering process. *(b)* The two-body wave function $\psi(r)$ (blue), scattered from the molecular potential $V(r)$. The scattering length a is determined by extrapolating the wave function back from the asymptotic regime (dashed line).

with g the so-called *contact coupling strength*,

$$g \stackrel{\text{def}}{=} \frac{4\pi\hbar^2}{m}\, a. \tag{2.4b}$$

In both cases, we have used the same parameter a which plays the role of the hard sphere radius in the potential V_{hs}.

Concerning the scattering properties, a matter mave scattered by the hard sphere potential $V_{\text{hs}}(r)$ must fulfill the boundary condition $\psi(a) = 0$. In contrast, the scattering of a matter wave from the true molecular potential is much more complicated, with the phase of the wave function undergoing many periods of oscillations in the regime $r < r_0$. At large distances $r \gg r_0$, however, the scattered wave function resembles the one reflected by a hard sphere of radius a (see Fig. 2.1*(b)*). The scattering properties of an ultracold bosonic gas are therefore fully described by a single scalar parameter, the so-called *s-wave scattering length* a, which may even become zero or negative. In the latter case, of course, the picture of the hard sphere scattering does not hold anymore.

The hard sphere potential V_{hs} is typically used, when performing quantum Monte-Carlo simulations of an interacting condensate [98]. It is, however, not suited for the computationally less demanding mean-field calculations, presented in section 2.3 and used throughout this thesis. We therefore consider now the case of the zero-range contact interaction potential, defined in Eq. (2.4). In the ultra-cold limit, the two-body wave function may then be written in the simple form [96]

$$\psi(r) \propto 1 - \frac{m_{\text{red}}\, g}{2\pi\hbar^2 r} = 1 - \frac{a}{r}, \tag{2.5}$$

using the reduced mass $m_{\mathrm{red}} = m/2$. We immediately see that the prefactors in the contact coupling strength g, defined in Eq. (2.4b), are chosen such that $r = a$ is the intersection point of the wave function with the r-axis. Thus, the parameter a may be identified with the s-wave scattering length introduced above and the scattering from the δ-shape potential V_{contact} can be related to the intuitive picture of the hard sphere scattering. The fact that we can replace the full molecular potential by the contact interaction potential, determined only by the scalar value of the s-wave scattering length, will be of great benefit when later, we will turn our attention to the mean-field description of a many-body system.

2.2.2 Dipolar Interactions

We now introduce the interactions between two dipoles which, in contrast to the interactions considered in section 2.2.1, cannot be described by the pseudo contact interaction potential. This arises from the *long-range* nature of the dipole-dipole interaction potential that we also discuss here.

Throughout this thesis we consider magnetic dipoles polarized by a sufficiently strong external magnetic field. The *dipole-dipole interaction potential* then reads [14]

$$V'_{\mathrm{dd}}(r, \vartheta) = \frac{\mu_0 \mu_{\mathrm{m}}^2}{4\pi} \frac{1 - 3\cos^2\vartheta}{r^3}, \tag{2.6}$$

where $\mu_0 \stackrel{\mathrm{def}}{=} 4\pi \cdot 10^{-7}\,\mathrm{T\,m/A}$ is the permeability in free space, μ_{m} is the permanent magnetic dipole moment and ϑ is the angle between the polarization direction and the relative position of the dipoles $\boldsymbol{r}$, as illustrated in Fig. 2.2*(a)*. The prime denotes the fact that we only consider the case $r > 0$ which is important, because V'_{dd} diverges when r tends to zero.

The dipole-dipole interaction (DDI) potential has two characteristic features:

(i) its *anisotropy*, illustrated in Fig. 2.2: depending on the relative position of two dipoles, they attract each other ($\vartheta = 0$, head-to-tail configuration), repel each other ($\vartheta = \pi/2$, side-by-side configuration) or do not interact at all ($\vartheta = \vartheta_{\mathrm{m}} \approx 54.7°$, magic angle configuration), and

(ii) its *long-range character*, which we now discuss in more detail.

We will use two methods to address the question whether a potential has a short-range or long-range character [99]. Let us first consider an homogeneous system from a thermodynamical point of view. If the particles in the system interact only via short-range interactions, the energy per particle is intensive, i.e. it depends only on the local properties, such as the density. In contrast, in systems with long-range interactions, the energy per particle also depends on global parameters, as for example the total number of atoms. The classification of a potential $V_{\mathrm{int}}(r)$ can be immediately checked by testing the convergence

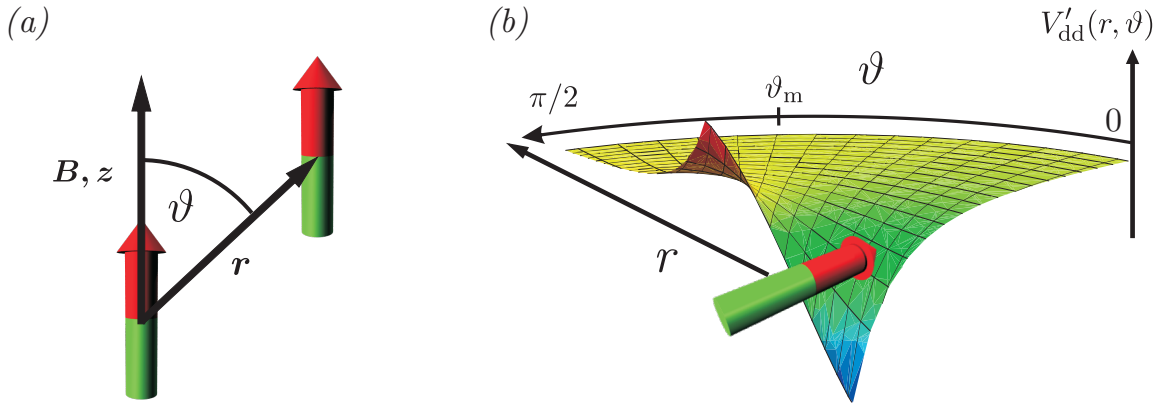

Fig. 2.2, Dipole-dipole interaction (DDI): *(a)* Two dipoles polarized by an external magnetic field $\boldsymbol{B}$ along the z-direction. The separation $r = |\boldsymbol{r}|$ and the angle $\vartheta = \angle(\boldsymbol{z}, \boldsymbol{r})$ enter the DDI potential given by Eq. (2.6). *(b)* The interaction between two dipoles is attractive in a head-to-tail configuration ($\vartheta = 0$), repulsive in a side-by-side configuration ($\vartheta = \pi/2$) and vanishes at the *magic angle* $\vartheta = \vartheta_{\mathrm{m}}$.

of the potential energy at large distances. We therefore evaluate the following integral

$$I = \int_{r_{\mathrm{cutoff}}}^{\infty} V_{\mathrm{int}}\, r^{D-1} \mathrm{d}r, \tag{2.7}$$

where r_{cutoff} is some small but finite cut-off radius, and D is the dimensionality of the system. Following this definition, the potential V_{int} is short-range if it decays faster than r^{-D} in D dimensions, as the integral I converges in this case. Hence, the DDI potential $V_{\mathrm{dd}} \propto r^{-3}$ is long-range in three dimensions (3D) and short-range in one and two dimensions (1D and 2D).

The second method to determine the characteristic behaviour of a potential is more closely connected to the physics of ultracold atomic samples. Referring to the considerations in section 2.2.1, short-range potentials may be replaced by a hard sphere potential[9] characterized by one single parameter, the s-wave scattering length a. By solving the two-body scattering problem for a potential $V_{\mathrm{int}} \propto r^{-3}$, the authors of Ref. [99] show explicitly that, in one and three dimensions, the resulting wave function (at large distances r) is not compatible with the freely propagating waves obtained in the hard sphere scattering. This means that the DDI potential shows a long-range character in 1D and 3D. In two dimensions, it is however possible to define a 2D scattering length a_{2D}, reproducing correctly the wave function for $r \to \infty$.

Interestingly, the two methods deliver different answers on the question of the interaction range of the DDI in one dimension. For all the calculations in this thesis we will use the exact form of the DDI potential given by Eq. (2.6). In this way, we obtain a correct description of the interactions, independent of the dimensionality of the system.

[9]This approach is not limited to the three-dimensional case. In one and two dimensions we would call it a hard-wall potential.

After investigating the long-range behaviour of the DDI potential, we now consider its behaviour at small distances r. If the DDI potential acts on a two-body wave function that does not vanish at the origin, i.e. $\psi(r=0) \neq 0$, the divergence of V_{dd} at this point must be cured. In an according mathematical treatment in Ref. [100], a term proportional to $\mu_{\mathrm{m}}^2 \delta(\boldsymbol{r})$ is added to the DDI potential, resembling the pseudo contact interaction potential given by Eq. (2.4). We therefore seem to have a direct contribution of the dipoles to the long-range *and* the short-range interactions, each depending on the magnetic moment. However, we have to be careful: taking into account the real short-range interactions, we know that at small distances r, strongly repulsive Coulomb forces ensure that the wave function has zero amplitude at the origin. Thus, the DDI potential does not probe the critical point $r = 0$, and a regularization of the dipolar potential is not required in the context of an interacting atomic sample[10].

In conclusion, the full pseudo-potential describing binary contact and dipolar interactions reads

$$V_{\mathrm{int}}^{(2)}(\boldsymbol{r}, \vartheta) = \frac{4\pi\hbar^2}{m}\, a\, \delta(\boldsymbol{r}) + \frac{\mu_0 \mu_{\mathrm{m}}^2}{4\pi}\, \frac{1 - 3\cos^2\vartheta}{r^3}. \tag{2.8}$$

Its validity has been approved by distributed Monte-Carlo simulations performed in Refs. [101, 102], under the condition that the scattering length a is replaced by a dipole dependent scattering length $a(d)$, where d is the dipole strength of either electric or magnetic dipoles. This seems to contradict our statement from above, saying that the dipoles do *not* influence the s-wave scattering properties of the system. However, the modification of the scattering length mentioned here does not result from the regularization of the DDI potential. It stems either from dipolar induced shape resonances of s-wave bound states [101–103] or from an effective s-wave scattering via dipolar coupling to the $l = 2$ partial wave [57]. Both of these effects are expected to be small in the case of magnetic chromium atoms, as we discuss in more detail in section A.1. In any case, the s-wave scattering length a is usually determined experimentally (see section 3.2.3), and therefore automatically includes all kinds of contributions.

To describe the physics of dipolar BECs, we now define some useful parameters. In analogy to the scattering length a, we define a characteristic *dipolar length*

$$a_{\mathrm{dd}} \stackrel{\mathrm{def}}{=} \frac{\mu_0 \mu_{\mathrm{m}}^2 m}{12\pi\hbar^2}, \tag{2.9a}$$

and the *dipolar coupling strength*

$$g_{\mathrm{dd}} \stackrel{\mathrm{def}}{=} \frac{4\pi\hbar^2}{m}\, a_{\mathrm{dd}} = \frac{\mu_0 \mu_{\mathrm{m}}^2}{3}. \tag{2.9b}$$

[10] Even though the regularization is not required from a physical point of view, in calculations the divergence of the DDI potential at the origin may cause difficulties. In practice they are resolved by either truncating the interaction potential at sufficiently large momenta in Fourier space, or by adding a hard sphere potential in real space [101, 102] to account for the short-range contact interactions.

We stress here that the dipolar length a_{dd} does not correspond to a finite interaction radius of the dipolar interactions. Such radius cannot be defined for long-range interactions. With the prefactors given in Eq. (2.9a), the value of a_{dd} seems chosen arbitrarily at the moment. But we will see in section 5 that it was chosen such that an homogeneous dipolar condensate becomes unstable, when $a = a_{\mathrm{dd}}$. Finally, we define the ratio of the dipolar and the contact coupling strength,

$$\epsilon_{\mathrm{dd}} \overset{\mathrm{def}}{=} \frac{g_{\mathrm{dd}}}{g} = \frac{a_{\mathrm{dd}}}{a} = \frac{\mu_0 \mu_{\mathrm{m}}^2 m}{12\pi\hbar^2 a}, \tag{2.9c}$$

which needs to be non-negligible to observe dipolar effects in a BEC.

2.3 Mean-Field Description of Dipolar Bose-Einstein Condensates

While considering the interactions between *two* atoms only in the previous section, the description of an interacting Bose-Einstein condensate (containing around 10^4 atoms) requires a *many-body* theory. We therefore start from the many-body Hamiltonian, which contains the two-body correlations between all the atom pairs. Then, we derive the Gross-Pitaevskii equation (GPE), representing an effective single-particle description of the full system in the so-called *mean-field model*. Such reduction in complexity greatly simplifies the theoretical description of dipolar BECs, but relies on certain validity criteria which we also discuss.

2.3.1 Gross-Pitaevskii Equation

The fundamental starting point for describing a system of interacting bosonic particles confined in a external potential $V_{\mathrm{ext}}(\boldsymbol{r})$ is the general many-body Hamiltonian [8, 89, 91]

$$\begin{aligned}\hat{\mathrm{H}} = &\int \mathrm{d}^3 r\, \hat{\Psi}^\dagger(\boldsymbol{r}) \left[-\frac{\hbar^2}{2m}\boldsymbol{\nabla}^2 + V_{\mathrm{ext}}(\boldsymbol{r}) \right] \hat{\Psi}(\boldsymbol{r}) \\ &+ \frac{1}{2}\int \mathrm{d}^3 r \int \mathrm{d}^3 r'\, \hat{\Psi}^\dagger(\boldsymbol{r})\hat{\Psi}^\dagger(\boldsymbol{r}')\, V_{\mathrm{int}}^{(2)}(\boldsymbol{r},\boldsymbol{r}')\, \hat{\Psi}(\boldsymbol{r})\hat{\Psi}(\boldsymbol{r}'),\end{aligned} \tag{2.10}$$

where $V_{\mathrm{int}}^{(2)}(\boldsymbol{r},\boldsymbol{r}')$ is the full two-body interaction potential, given by Eq. (2.8), and $\hat{\Psi}^\dagger(\boldsymbol{r})$ and $\hat{\Psi}(\boldsymbol{r})$ are the bosonic field operators creating and annihilating a particle at the position $\boldsymbol{r}$, respectively. These operators can be expanded in terms of the creation and annihilation

operators[11] $\hat{\mathrm{a}}_k^\dagger$ and $\hat{\mathrm{a}}_k$, such that

$$\hat{\Psi}^\dagger(\boldsymbol{r}) = \sum_k \phi_k(\boldsymbol{r})\,\hat{\mathrm{a}}_k^\dagger \quad \text{and} \quad \hat{\Psi}(\boldsymbol{r}) = \sum_k \phi_k(\boldsymbol{r})\,\hat{\mathrm{a}}_k, \tag{2.11}$$

with $\phi_k(\boldsymbol{r})$ a set of single-particle states. Assuming a macroscopic population N of the lowest lying single-particle state ϕ_0 (such that $N+1 \simeq N \gg 1$) we can replace the according operators by numbers [91], with $\hat{\mathrm{a}}_0^\dagger = \hat{\mathrm{a}}_0 = \sqrt{N}$. We may then rewrite the field operator in the form

$$\hat{\Psi}(\boldsymbol{r}) = \sqrt{N}\,\phi_0(\boldsymbol{r}) \,+\, \sum_{k>0} \phi_k(\boldsymbol{r})\,\hat{\mathrm{a}}_k \;\stackrel{\text{def}}{=}\; \sqrt{N}\,\psi(\boldsymbol{r}) \,+\, \delta\hat{\Psi}(\boldsymbol{r}), \tag{2.12}$$

where we have introduced the complex function $\psi(\boldsymbol{r})$, defined by the expectation value of the field operator[12] $\left\langle \hat{\Psi}(\boldsymbol{r}) \right\rangle = \sqrt{N}\psi(\boldsymbol{r})$. The function $\psi(\boldsymbol{r})$ has the meaning of an order parameter and exhibits a well defined phase, which is spontaneously chosen at the phase transition from the normal gas to a Bose-Einstein condensate [91]. Hence, the phase transition to a BEC manifests itself by a broken gauge symmetry in the many-body system. In the following, we will call $\psi(\boldsymbol{r})$ *the wave function of the condensate*.
In general, the field operator is time-dependent with a time evolution described by the Heisenberg equation,

$$\begin{aligned} i\hbar\frac{\partial}{\partial t}\hat{\Psi}(\boldsymbol{r},t) &= \left[\hat{\Psi}, \hat{\mathrm{H}}\right] \\ &= \left[-\frac{\hbar^2}{2m}\boldsymbol{\nabla}^2 + V_{\mathrm{ext}}(\boldsymbol{r}) + \int \mathrm{d}^3r'\,\hat{\Psi}^\dagger(\boldsymbol{r}',t)\,V_{\mathrm{int}}^{(2)}(\boldsymbol{r}-\boldsymbol{r}')\,\hat{\Psi}(\boldsymbol{r}',t)\right]\,\hat{\Psi}(\boldsymbol{r},t). \end{aligned} \tag{2.13}$$

With the field operator given by Eq. (2.12), and neglecting the fluctuations $\delta\hat{\Psi}(\boldsymbol{r})$, we obtain the *time-dependent Gross-Pitaevskii equation (GPE)* of a dipolar condensate

$$\begin{aligned} i\hbar\frac{\partial}{\partial t}\psi(\boldsymbol{r},t) = \Big[&-\frac{\hbar^2}{2m}\boldsymbol{\nabla}^2 + V_{\mathrm{ext}}(\boldsymbol{r}) \\ &+ gN\,|\psi(\boldsymbol{r},t)|^2 + N\int \mathrm{d}^3r'\,V'_{\mathrm{dd}}(\boldsymbol{r}-\boldsymbol{r}')\,|\psi(\boldsymbol{r}',t)|^2\Big]\psi(\boldsymbol{r},t), \end{aligned} \tag{2.14}$$

where we have inserted the two-body interaction potential $V_{\mathrm{int}}^{(2)}(\boldsymbol{r}-\boldsymbol{r}')$, given by Eq. (2.8). Note that the DDI potential $V'_{\mathrm{dd}}(\boldsymbol{r}-\boldsymbol{r}')$ adds a *non-local character* to the Gross-Pitaevskii equation. In contrast, the "standard" GPE of a purely contact interacting BEC depends only on the local density $n(\boldsymbol{r},t) = N\,|\psi(\boldsymbol{r},t)|^2$ of the condensate.

[11] The operators $\hat{\mathrm{a}}_k^\dagger$ and $\hat{\mathrm{a}}_k$ obey the usual bosonic commutation relations
$\left[\hat{\mathrm{a}}_\alpha, \hat{\mathrm{a}}_\beta^\dagger\right] = \delta_{\alpha,\beta}, \quad [\hat{\mathrm{a}}_\alpha, \hat{\mathrm{a}}_\beta] = 0, \quad \text{and} \quad \left[\hat{\mathrm{a}}_\alpha^\dagger, \hat{\mathrm{a}}_\beta^\dagger\right] = 0.$

[12] We choose the function $\psi(\boldsymbol{r})$ to be normalized to unity.

Inserting the ansatz $\psi(\boldsymbol{r},t) = \psi(\boldsymbol{r})\,\exp(-i\mu t/\hbar)$ into Eq. (2.14), where μ is the chemical potential of the condensate, we obtain the *stationary Gross-Pitaevskii equation*

$$\mu\,\psi(\boldsymbol{r}) = \left[-\frac{\hbar^2}{2m}\boldsymbol{\nabla}^2 + V_{\text{ext}}(\boldsymbol{r}) + \Phi_{\text{contact}}(\boldsymbol{r}) + \Phi_{\text{dip}}(\boldsymbol{r})\right]\psi(\boldsymbol{r}), \tag{2.15a}$$

with $\Phi_{\text{contact}}(\boldsymbol{r})$ and $\Phi_{\text{dip}}(\boldsymbol{r})$ the mean-field potentials of the contact and dipolar interactions, respectively. They are explicitly given by

$$\Phi_{\text{contact}}(\boldsymbol{r}) \overset{\text{def}}{=} g\,n(\boldsymbol{r}) \qquad \text{and} \tag{2.16a}$$

$$\Phi_{\text{dip}}(\boldsymbol{r}) \overset{\text{def}}{=} \int \mathrm{d}^3r'\, V'_{\text{dd}}(\boldsymbol{r}-\boldsymbol{r}')n(\boldsymbol{r}'). \tag{2.16b}$$

Total energy of a dipolar BEC

An important quantity in a dipolar Bose-Einstein condensate is the total energy per particle E/N for a given wave function. It is given by[13] [14, Ch.4.3]

$$\begin{aligned} E[\psi]/N &\overset{\text{def}}{=} \langle\psi|\,\hat{\mathrm{H}}\,|\psi\rangle\,/N \\ &\overset{(2.10)}{=} \int \mathrm{d}^3r \left[+\frac{\hbar}{2m}\,|\boldsymbol{\nabla}\psi(\boldsymbol{r})|^2 + V_{\text{ext}}(\boldsymbol{r})\;|\psi(\boldsymbol{r})|^2 + \frac{\Phi_{\text{contact}}(\boldsymbol{r}) + \Phi_{\text{dip}}(\boldsymbol{r})}{2}\;|\psi(\boldsymbol{r})|^2\right], \end{aligned} \tag{2.17}$$

and is obtained by inserting $\hat{\Psi}(\boldsymbol{r}) = \sqrt{N}\,\psi(\boldsymbol{r})$ into the many-body Hamiltonian given by Eq. (2.10). The three terms in Eq. (2.17) correspond respectively to the kinetic, the potential, and the interaction energy. The last contains the contributions from both contact and dipolar interactions. With an educated guess for the shape of the wave function $\psi(\boldsymbol{r})$, e.g. using a Gaussian shape, all the terms in the Gross-Pitaevskii energy functional can be directly evaluated. Such procedure will be useful when we investigate a system of spatially separated dipolar samples in section 2.5. Furthermore, variational calculations based on Eq. (2.17) provide an efficient tool to test the stability a trapped dipolar BEC [35], as we will show in section 5.

2.3.2 Validity of the Mean-Field Model

The efficient description of Bose-Einstein condensates by the mean-field model may explain partly the success of such systems as quantum mechanical model systems [104]. However, we have to be aware that the validity of the non-local GPE is limited. We summarize the basic validity criteria as follows:

[13] We use the notation in Heisenberg representation $\psi(\boldsymbol{r}) \overset{\text{def}}{=} \langle\boldsymbol{r}|\psi\rangle$.

(i) $N \gg 1$: The macroscopic population of a single particle state allows for the replacement of the creation and annihilation operators by classical numbers [91], $\hat{a} \approx \hat{a}^\dagger \approx \sqrt{N}$. With typical BEC atom numbers $N \sim 10^4$ the condition $N \approx N+1 \gg 1$ is well satisfied.

(ii) $r_0 \ll \lambda_{\mathrm{dB}}$: The de-Broglie wavelength λ_{dB} must be much larger than the range r_0 of the short-range interactions. Then, as shown in section 2.2, the scattering properties in the atomic sample are fully determined by the s-wave scattering length a, which enters the non-local GPE. In a chromium BEC, the range of the interactions is $r_0 \sim 100\, a_0$ and the de-Broglie wavelength is on the order of the mean inter-particle distance, i.e. $\lambda_{\mathrm{dB}} \sim 4000\, a_0$. Therefore, the required condition $r_0 \ll \lambda_{\mathrm{dB}}$ is fulfilled.

(iii) $\bar{n}\, a^3 \ll 1$: The product $\bar{n}\, a^3$, with $\bar{n}$ the mean density, is a measure of the diluteness[14] of a sample consisting of hard spheres with radius a. In the context of an ultracold atomic sample, the density and the scattering length a must be low enough, such that correlations between the atoms are negligible and the use of pseudo-potentials (see section 2.2) is justified[15]. With a maximum peak density $n_0 \sim 10^{15}\,\mathrm{cm}^{-3}$ in our BEC and $a \sim 100\, a_0$, we obtain $n_0 a^3 \sim 1.5 \cdot 10^{-4}$, which is well within the validity region.

(iv) $E \ll E_D$: The energy in the system must be much smaller than the characteristic *dipole energy* [58] $E_D = \hbar^6 / m_{\mathrm{red}}^3 \cdot \left(\mu_0 \mu_{\mathrm{m}}^2 / (4\pi)\right)^{-4}$, with $m_{\mathrm{red}} = m/2$ the reduced mass. Then, as shown in appendix A.1, the scattering in a dipolar gas occurs mainly in the s-wave channel, even though the long-range DDI in principle leads to scattering in all partial wave channels [106]. At condensation temperatures $T_c \lesssim 1\,\mu\mathrm{K}$ this criterion is well satisfied for chromium, since the dipole energy evaluates to $E_D / k_{\mathrm{B}} \sim 13\,\mathrm{mK}$.

(v) $a_{\mathrm{dd}} \ll r_0$: The dipole length a_{dd} must be much smaller than the short-range interaction radius r_0. This requirement, stated in Ref. [107], ensures the absence of bound-states in the dipolar potential[16]. At larger dipole lengths, the so-called *dipolar s-wave shape resonances* can occur, strongly changing the scattering properties of the particles. In chromium, with $a_{\mathrm{dd}} \simeq 15\, a_0$ and $r_0 \sim 100\, a_0$ the condition is fulfilled. In the recently realized dipolar BEC of dysprosium [40], this condition is probably violated[17]. Nevertheless, we expect the GPE (2.15a) to be valid even for dysprosium, as any dipolar effects on the s-wave scattering length may be absorbed by the contact interaction term [101, 102, 108, 109].

[14] In a box of volume V, N hard spheres of radius a will occupy the volume $V_N = N \cdot (4\pi/3)\, a^3$. Therefore, the fraction $V_N / V \propto \bar{n}\, a^3$, with $\bar{n} = N/V$, describes the filling of the box.

[15] A rigorous mathematical derivation of this condition is given in Ref. [105].

[16] In the calculations in Ref. [107], the occurence of bound-states was examined in a dipolar potential with a hard-sphere boundary at $r = r_0$.

[17] The interaction range r_0 for ^{164}Dy is so far unknown, but for an estimation we may use the chromium value $r_0 \sim 100\, a_0$. With a dipole length $a_{\mathrm{dd}} \sim 134\, a_0$ for ^{164}Dy, the condition $a_{\mathrm{dd}} \ll r_0$ is violated.

Since in our experiments with a chromium BEC, all the validity criteria are fulfilled, we will make use of the mean-field description in the remaining part of this thesis.

2.4 Solutions of the Non-Local Gross-Pitaevskii Equation

In this section, we discuss different solutions of the stationary Gross-Pitaevskii equation, assuming the realistic case of an harmonic external trapping potential of the form

$$V_{\text{ext}}(\boldsymbol{r}) = \frac{m}{2}\left(\omega_x^2 x^2 + \omega_y^2 y^2 + \omega_z^2 z^2\right), \tag{2.18}$$

with the ω_i ($i = x, y, z$) denoting the *trap frequencies*. At first, we consider a BEC with negligible interactions, where we encounter the well-known problem of the quantum-mechanical harmonic oscillator. We then examine the case with dominant contact interactions, which also leads to a simple solution of the GPE due to the local character of the interactions. Including the dipolar interactions, the problem becomes non-trivial, however, an exact solution of the GPE can still be found. With the results obtained here, we finally discuss some basic properties of dipolar BECs.

2.4.1 GPE with Negligible Interactions

For sufficiently weak interactions, we can neglect their contribution in the stationary GPE (2.15a). The remaining differential equation,

$$\mu\,\psi(\boldsymbol{r}) = \left[-\frac{\hbar^2}{2m}\boldsymbol{\nabla}^2 + \frac{m}{2}\sum_{i=x,y,z}\omega_i^2 r_i^2\right]\psi(\boldsymbol{r}), \tag{2.19}$$

corresponds to the well-known problem of the three-dimensional quantum-mechanical harmonic oscillator [96]. Its discrete solutions in each direction are given by the Hermite functions $h_n(r_i)$ with eigenenergies $E_{n,i} = (n+1/2)\,\hbar\omega_i$, where n only takes integer values. In a spherically symmetric trapping potential $V_{\text{int}}(r) = m\omega_0^2 r^2/2$, the ground-state wave function $\psi(r) \propto h_0(r)$ has a Gaussian shape[18]:

$$\psi(r) = \left(\sqrt{\pi}a_{\text{ho}}\right)^{-3/2} \mathrm{e}^{-\frac{r^2}{2a_{\text{ho}}^2}}, \tag{2.20a}$$

$$\text{where} \quad a_{\text{ho}} \stackrel{\text{def}}{=} \sqrt{\frac{\hbar}{m\omega_0}} \tag{2.20b}$$

is the so-called *harmonic oscillator length*. The characteristic size a_{ho} of a non-interacting condensate may also be deduced from a simple variational calculation [89]: When the radius R of the condensate is large, the energy of the system is given by the potential

[18] As stated in section 2.3.1, we choose the normalization condition $\int \mathrm{d}r^3 |\psi(r)|^2 = 1$.

energy $V_{\text{ext}}(R) = m\omega_0^2 R^2/2$. In the other limit of small and decreasing radii, Heisenberg's uncertainty relation $p = \hbar/R$ leads to a divergence in the kinetic energy, given by $E_{\text{kin}} = p^2/(2m) = \hbar^2/(2mR^2)$. This energy divergence results in the so-called *quantum pressure*, which stabilizes the non-interacting condensate. The energy in the system is minimal when the contributions from the potential energy and the kinetic energy are the same, resulting in the condensate radius $R = \sqrt{\hbar/(m\omega_0)} = a_{\text{ho}}$. Finally, the chemical potential μ in a non-interacting condensate is given by the *zero point energy* of the three-dimensional quantum-mechanical harmonic oscillator, $\mu = 3\hbar\omega_0/2$, and is therefore independent of the atom number.

2.4.2 GPE with Dominant Contact Interactions

The contact interactions contribute with the mean-field potential $\Phi_{\text{contact}}(\boldsymbol{r}) = g\, n(\boldsymbol{r})$ (see Eq. (2.16a)) to the stationary GPE. While in a non-interacting BEC the quantum pressure stabilizes the system at small radii, it is now the interactions that take over this role, if they are sufficiently strong. In this case, the kinetic term in the GPE may be neglected, and we obtain the GPE in *Thomas-Fermi (TF) approximation*

$$\mu\psi(\boldsymbol{r}) \overset{\text{TF}}{=} [V_{\text{ext}}(\boldsymbol{r}) + g\, n(\boldsymbol{r})]\, \psi(\boldsymbol{r}). \tag{2.21}$$

Inserting the harmonic trapping potential $V_{\text{ext}}(\boldsymbol{r})$, given by Eq. (2.18), into Eq. (2.21) yields the parabolic density of the BEC:

$$\begin{aligned} n(\boldsymbol{r}) = N\,|\psi(\boldsymbol{r})|^2 &= \frac{\mu - V_{\text{ext}}(\boldsymbol{r})}{g} \\ &= n_0 \cdot \max\left\{\left(1 - \frac{x^2}{R_x^2} - \frac{y^2}{R_y^2} - \frac{z^2}{R_z^2}\right), 0\right\}, \end{aligned} \tag{2.22}$$

with $n_0 = 15N/(8\pi R_x R_y R_z)$ the density at the center of the condensate, and with $R_{x,y,z}$ the TF-radii in the respective directions. The central density may also be expressed in terms of the mean radius $\bar{R} \overset{\text{def}}{=} (R_x R_y R_z)^{1/3}$, which in the case of a spherically symmetric trap is given by[19] $\bar{R} = 15^{1/5} a_{\text{ho}}\, (Na/a_{\text{ho}})^{1/5}$. We see that the calculated mean radius of a contact interacting BEC is only significantly larger than the harmonic oscillator length a_{ho}, if the condition $Na/a_{\text{ho}} \gg 1$ is fulfilled. Therefore, this condition defines the regime in which the TF-approximation is valid. For a typical set of parameters in a chromium BEC, $\{N = 20,000,\ a = 100\, a_0,\ \omega_0 = 2\pi \cdot 500\,\text{Hz}\}$, we obtain $Na/a_{\text{ho}} \simeq 170$ and thus the system is typically well inside the Thomas-Fermi regime.

[19] In the case of a non-spherically symmetric trap, the harmonic oscillator length a_{ho} has to be replaced by the mean harmonic oscillator length $\bar{a}_{\text{ho}} = \sqrt{\hbar/(m\bar{\omega})}$, with the mean trap frequency $\bar{\omega} = (\omega_x\omega_y\omega_z)^{1/3}$, as we show in appendix A.2. Note, that these formulae hold only for moderate trap frequencies with $\hbar\omega_{x,y,z} \ll \mu$. We discuss the case of an highly oblate trap with $\hbar\omega_z \gg \mu \gg \hbar\omega_{x,y}$ in section 4.3.2.

2.4.3 TF-Approximation with Contact and Dipolar Interactions

The long-range character of the dipole-dipole interaction significantly complicates the description of a BEC in the TF-approximation. It has been found [110, 111] that in this regime, the dipolar mean-field potential Φ_{dip} only contains terms that are either constant or quadratic in the spatial coordinates. This leads to the remarkable fact that dipolar BECs in the TF regime also have an *inverted parabola shape*, just like purely contact interacting condensates.

To obtain an intuitive understanding how the dipolar interactions modify the properties of a BEC, we choose a trapping potential with a cylindrical symmetry along the polarization direction z of the dipoles. The radial and axial coordinates are then defined by $\boldsymbol{r} = (\rho, z)$ with the according trap frequencies ω_ρ and ω_z, and the *trap ratio* $\lambda \stackrel{\mathrm{def}}{=} \omega_\rho/\omega_z$. In a first step, we assume weak dipolar interactions, such that the shape of the BEC still resembles an inverted parabola, with the *cloud aspect ratio* $\kappa \stackrel{\mathrm{def}}{=} R_z/R_\rho$ defined by the TF-radii R_ρ and R_z in the radial and axial directions. The dipoles then generate a mean-field potential $\Phi_{\mathrm{dip}}^{\mathrm{TF},\kappa}(\boldsymbol{r})$ that enters the GPE and which in the cylindrical coordinates reads [110]

$$\Phi_{\mathrm{dip}}^{\mathrm{TF},\kappa}(\boldsymbol{r}) = n_0 g_{\mathrm{dd}} \left[\frac{\rho^2}{R_\rho^2} - \frac{2z^2}{R_z^2} - f_{\mathrm{dip}}(\kappa) \left(1 - \frac{3}{2} \frac{\rho^2 - 2z^2}{R_\rho^2 - R_z^2} \right) \right], \tag{2.23a}$$

with the *dipolar anisotropic function* $f_{\mathrm{dip}}(\kappa)$ given by

$$f_{\mathrm{dip}}(\kappa) = \frac{1 + 2\kappa^2}{1 - \kappa^2} - \frac{3\kappa^2 \operatorname{artanh}\left(\sqrt{1 - \kappa^2}\right)}{(1 - \kappa^2)^{3/2}}. \tag{2.23b}$$

We illustrate the function $f_{\mathrm{dip}}(\kappa)$, taking numerical values in the interval $[-2, 1]$, in Fig. 2.3*(a)*. As stated before, the terms in Eq. (2.23a) are either constant or quadratic in ρ and z, i.e. the general form of the GPE is the same as in the purely contact interacting case[20]. Therefore, in the TF-approximation, we obtain the same parabolic density distribution of the dipolar BEC, as given by Eq. (2.22). However, now the radii of the condensate depend on both the contact interaction strength g and the relative dipole strength ϵ_{dd} and are given by the following expressions [110, 111]:

$$R_\rho = \left[\frac{15 g N \kappa}{4\pi m \omega_\rho^2} \left\{ 1 + \epsilon_{\mathrm{dd}} \left(\frac{3}{2} \frac{\kappa^2 f_{\mathrm{dip}}(\kappa)}{1 - \kappa^2} - 1 \right) \right\} \right]^{1/5}, \tag{2.24}$$

and $R_z = R_\rho/\kappa$. At given trap ratio λ, the cloud aspect ratio κ may be evaluated via the implicit equation

$$3\kappa\epsilon_{\mathrm{dd}} \left[\left(\frac{\lambda^2}{2} + 1 \right) \frac{f_{\mathrm{dip}}(\kappa)}{1 - \kappa^2} - 1 \right] + (\epsilon_{\mathrm{dd}} - 1) \left(\kappa^2 - \lambda^2 \right) = 0. \tag{2.25}$$

[20] In Eq. (2.23a), the constant term proportional to $f_{\mathrm{dip}}(\kappa)$ only adds an offset to the chemical potential and the quadratic terms are of the same form as the trapping potential.

Hence, for a given external trapping potential, we obtain an exact solution for the stationary GPE, with the chemical potential given by $\mu = gn_0\,[1 - \epsilon_{\mathrm{dd}} f_{\mathrm{dip}}(\kappa)]$.

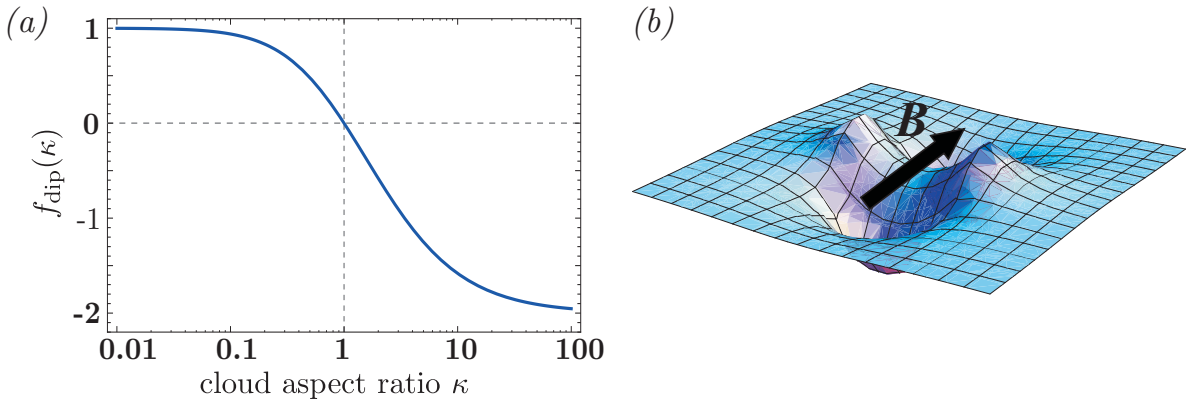

Fig. 2.3, Dipolar anisotropic function and dipolar mean-field potential: *(a)* The dipolar anisotropic function f_{dip} versus the cloud aspect ratio $\kappa \overset{\mathrm{def}}{=} R_z/R_\rho$. The asymptotic values are $f_{\mathrm{dip}}(0) = 1$ and $f_{\mathrm{dip}}(\infty) = -2$, while f_{dip} vanishes for $\kappa = 1$. *(b)* The dipolar mean-field potential in the case $\kappa = 1$. It exhibits a saddle-like shape with minima on the axis parallel to the external magnetic field $\boldsymbol{B}$.

Using the analytical expressions derived in this section, we can already learn some characteristic properties of a dipolar BEC. Let us consider a spherically symmetric contact interacting BEC with radius R, i.e. $\kappa = 1$, and add some weak dipolar interactions. Then, the dipolar mean-field dipolar potential is given by [112]

$$\Phi_{\mathrm{dip}}^{\mathrm{TF},1}(\boldsymbol{r}) = \epsilon_{\mathrm{dd}} \frac{m\omega^2}{5} \left(1 - 3\cos^2\vartheta\right) \begin{cases} r^2 & \text{if } r \leq R \\ R^5/r^3 & \text{if } r > R \end{cases}, \tag{2.26}$$

which has a saddle-like shape, with the minima on the axis parallel to the polarizing external magnetic field $\boldsymbol{B}$, as shown in Fig. 2.3*(b)*. With increasing relative dipole strength ϵ_{dd}, the cloud will elongate more and more along the polarization direction of the dipoles, as the minima of the saddle-like potential become more prominent. This effect persists even in the case of anisotropic trapping potentials [109, 110], where the dipolar mean-field potential does not necessarily take a saddle-like shape [113, Ch. A.5.6]. We furthermore note that the dipolar contribution to the chemical potential vanishes in the case of a spherically symmetric cloud since $f_{\mathrm{dip}}(\kappa = 1) = 0$. At a given dipole strength ϵ_{dd}, the required trap ratio λ to design such sample without dipolar mean-field contribution is given by[21] $\lambda = [3/(1 - 2\epsilon_{\mathrm{dd}}/5) - 2]^{1/2}$.

Finally, we mention that not only the properties of a BEC, but also the validity of the Thomas-Fermi approximation is affected by the presence of the dipolar interactions. Due to the anisotropic character of the DDI, the validity criterion depends on the trap

[21] We have to restrict the range of possible trap ratios to $0.5 \leq \lambda \leq 2.4$. Else, the solution of the GPE does not represent a stable configuration of the condensate [114].

ratio [114]. It is given by $N(a - a_{\mathrm{dd}})/a_{\mathrm{ho}} \gg 1$ for trap ratios $\lambda \lesssim 1$, used e.g. in the measurements for the calibration of the scattering length, presented in section 3.2.3.

Concluding this section, we have seen that the dipolar interactions influence the ground-state properties of a BEC. While in the TF approximation the *shape* of the condensate remains the same as in the purely contact interacting case, the radii are different: a dipolar BEC elongates along an external magnetic field. Furthermore, the chemical potential μ of the condensate depends on the relative dipole strength ϵ_{dd}, with $\mu = gn_0\,[1 - \epsilon_{\mathrm{dd}} f_{\mathrm{dip}}(\kappa)]$. Depending on the aspect ratio κ of the atomic cloud, the chemical potential can be lower or higher than in the case without dipolar interactions.

2.5 Dipolar Interactions between Spatially Separated Condensates

After describing *single* dipolar BECs in the previous section, we now turn our attention to systems with *multiple* spatially separated atomic samples. The distant dBECs can interact with each other by the long-range dipolar interactions, whereas purely short-range interacting condensates do not show any inter-site coupling, if particle exchange is suppressed.
In this section, we give a basic introduction to dipolar multi-site systems, while more detailed descriptions of their ground-state properties are given in Refs. [28, 29, 115–120]. We first investigate the inter-site mean-field potential in the minimal system of two dipolar layers. We then calculate the inter-site energy between two Gaussian-shaped dipolar BECs. This allows us to examine the relevance of the *inter-site* interactions with respect to the *on-site* interactions in such system. At the end of this chapter we show that, under realistic experimental conditions, the inter-site energy can be enhanced when adding more layers to the system.

2.5.1 Mean-Field Potential in a Dipolar Double-Layer System

We consider a system composed of two identical discs of radius R, with the dipoles aligned perpendicular to the disc plane, as illustrated in Fig. 2.4*(a)*. The separation $\Delta z = d_{\mathrm{lat}}$ of the two samples is assumed to be much larger than their "thickness" in the z-direction. Then, the distance r between two dipoles (belonging to different layers) only depends on d_{lat} and their *in-plane separation*[22] r_{in}, and is given by $r = \sqrt{d_{\mathrm{lat}}^2 + r_{\mathrm{in}}^2}$. The angle ϑ, defining the relative alignment of the dipoles (see Fig. 2.2), is given by $\cos\vartheta = d_{\mathrm{lat}}/r$. Therefore, using Eq. (2.6), the dipole-dipole interaction potential of two dipoles belonging

[22] The in-plane separation is the distance between the two dipoles, when the discs are projected onto each other.

to different layers reads

$$\begin{aligned} V_{\mathrm{dd}}^{\mathrm{disc}}(r_{\mathrm{in}}, d_{\mathrm{lat}}) &= \frac{\mu_0 \mu_{\mathrm{m}}^2}{4\pi} \, \frac{1 - 3\, d_{\mathrm{lat}}^2/(r_{\mathrm{in}}^2 + d_{\mathrm{lat}}^2)}{(r_{\mathrm{in}}^2 + d_{\mathrm{lat}}^2)^{3/2}} \\ &= \frac{\mu_0 \mu_{\mathrm{m}}^2}{4\pi} \, \frac{r_{\mathrm{in}}^2 - 2\, d_{\mathrm{lat}}^2}{(r_{\mathrm{in}}^2 + d_{\mathrm{lat}}^2)^{5/2}}. \end{aligned} \tag{2.27}$$

Since we have chosen the extension of the discs in z-direction to be infinitely small, it is useful to define the 2D atomic density n_{2D}:

$$n_{\mathrm{2D}}(\rho) = \begin{cases} \frac{N}{\pi R^2} & \text{if } \rho \leq R \\ 0 & \text{if } \rho > R, \end{cases} \tag{2.28}$$

where $N = \int n_{\mathrm{2D}} \, \mathrm{d}^2\rho$ is the number of atoms in each disc and R the disc radius. In the given geometry, we may introduce the cylindrical coordinates $(\rho, \varphi, 0)$ and $(\rho', \varphi', d_{\mathrm{lat}})$ for the first and the second disc, respectively. We can then evaluate the mean-field potential $\Phi_{\mathrm{inter}}^{\mathrm{disc}}(\rho = 0)$ at the center of the first disc that is created by the presence of the second disc, with

$$\begin{aligned} \Phi_{\mathrm{inter}}^{\mathrm{disc}}(\rho = 0) &= \int_0^{2\pi} \int_0^{R} V_{\mathrm{dd}}^{\mathrm{disc}}(\rho', d_{\mathrm{lat}}) \, n_{\mathrm{2D}}(\rho') \, \rho' \, \mathrm{d}\rho' \, \mathrm{d}\varphi' \\ &= \frac{\mu_0 \mu_{\mathrm{m}}^2}{4\pi} \, \frac{-2N}{(R^2 + d_{\mathrm{lat}}^2)^{3/2}}, \end{aligned} \tag{2.29}$$

which is valid in the cases $d_{\mathrm{lat}} \neq 0$ and $R > 0$. Considering the central mean-field potential, given by Eq. (2.29), in different limits for the separation d_{lat} and the disc radius R, we can learn some basic properties of the dipolar inter-site interactions (we use the abbreviation $\Phi_{\mathrm{inter}}^{\mathrm{disc}} \overset{\mathrm{def}}{=} \Phi_{\mathrm{inter}}^{\mathrm{disc}}(\rho = 0)$):

(i) $\lim\limits_{d_{\mathrm{lat}} \gg R} \Phi_{\mathrm{inter}}^{\mathrm{disc}} \propto (-2N)/d_{\mathrm{lat}}^3$

When the distance between the two discs is much larger than their radial extension, we recover the r^{-3} scaling law of the two-body DDI potential (Eq. (2.6)). We further recognize that the interaction of the two samples is enhanced by the population N of the discs, when compared to the case of only two dipoles in head-to-tail configuration.

(ii) $\lim\limits_{R \gg d_{\mathrm{lat}}} \Phi_{\mathrm{inter}}^{\mathrm{disc}} \propto (-2N)/R^3$

At large disc radii or at small separations, the mean-field potential does not depend on d_{lat} anymore. This means, that the central part of two large and thin magnetic discs does not contribute to a relative attraction, as there is no potential gradient in the z-direction. However, we should be aware of edge effects which we discuss below.

(iii) $\lim\limits_{R \to \infty} \Phi_{\mathrm{inter}}^{\mathrm{disc}} = 0$

This expression means that two infinite planes of dipoles do not interact [121]. In this limit, the system is translationally invariant in the xy-plane, and therefore the mean-field potential is zero everywhere.

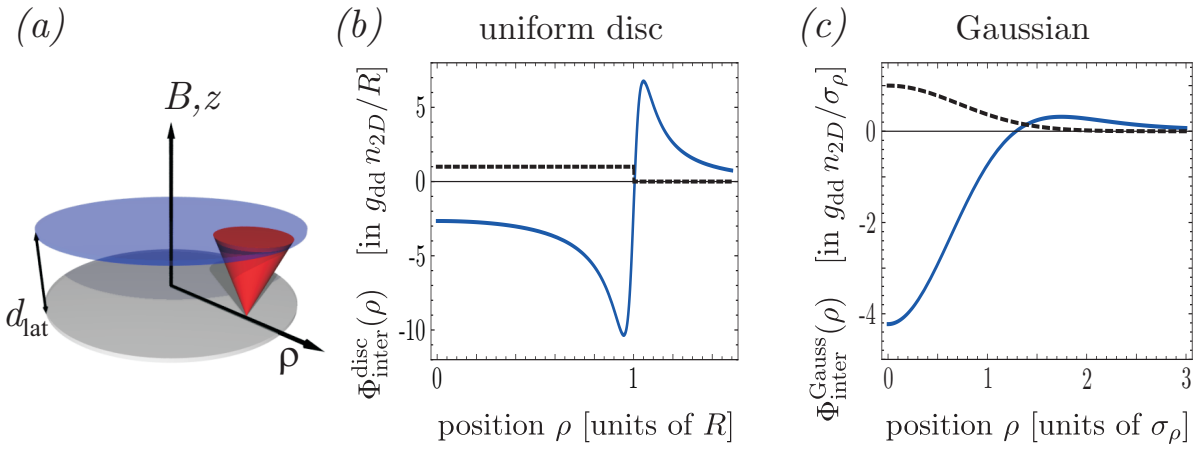

Fig. 2.4, Mean-field potential of two distant dipolar samples: *(a)* Schematic drawing of the system. The two flat samples with the dipoles oriented along z are separated by the distance d_{lat}. Dipoles with angle $\vartheta < \vartheta_{\mathrm{m}}$ (red cone) give negative contributions to the inter-site mean-field potential at the position ρ of the probe dipole (tip of the cone). In contrast, for $\vartheta > \vartheta_{\mathrm{m}}$ the contribution is positive. *(b),(c)* Inter-site mean-field potential (solid blue line) and density distribution (dashed black line, normalized to the central density) in homogeneous disc-shaped samples and in samples with Gaussian density distribution, respectively.

Let us now discuss the *position dependent* inter-site mean-field potential $\Phi_{\mathrm{inter}}^{\mathrm{disc}}(\rho)$. For the geometry of two discs at a given ratio $R/d_{\mathrm{lat}} = 20$, we numerically obtain the result for $\Phi_{\mathrm{inter}}^{\mathrm{disc}}(\rho)$ shown in Fig. 2.4*(b)*. As expected for homogeneous discs, the mean-field potential close to the center (at $\rho = 0$) is almost constant and negative (see case *(ii)* above). Towards the edges, however, the potential develops first a deep minimum and then a maximum at $\rho \gtrsim R$, before it eventually approaches the zero value. The behaviour of $\Phi_{\mathrm{inter}}^{\mathrm{disc}}(\rho)$ close to the edge may be understood with the following geometrical argument: only dipoles within the magic angle ϑ_{m}, indicated by the red cone in Fig. 2.4*(a)*, give a negative contribution to the mean-field potential since they attract each other. In contrast, the dipoles just outside the cone give the strongest positive contribution, as the dipolar potential falls off with r^{-3}. Therefore, once the edge of the cone comes closer to the edge of the neighbouring disc, there are less and less atoms with positive contributions to the mean-field potential which therefore develops a minimum. For the chosen ratio $R/d_{\mathrm{lat}} = 20$, the minimum sits at the position $\rho \simeq R - d_{\mathrm{lat}} \tan\vartheta_{\mathrm{m}} \sim 0.9\, R$. Further out, the number of dipoles *inside* the cone reduces and eventually vanishes, which leads to the maximum in the mean-field potential. Far outside the disc, the potential finally approaches the zero value due to the increasing distance to the neighbouring sample.

Considering a real trapped dipolar gas with weak interactions, the density of the sample will rather be described by a Gaussian than a disc shape, as we have shown in section 2.4.1. We therefore write the 2D density distribution of the samples in the Gaussian form

$$n_{\mathrm{2D}}^{\mathrm{Gauss}}(\rho) = \frac{N}{\pi\sigma_\rho^2}\,\mathrm{e}^{-\frac{\rho^2}{\sigma_\rho^2}}, \tag{2.30}$$

with σ_ρ the width of the cloud in the radial directions. For the ratio $\sigma_\rho/d_{\mathrm{lat}} = 20$, we obtain the mean-field potential $\Phi_{\mathrm{inter}}^{\mathrm{Gauss}}(\rho)$, shown in Fig. 2.4*(c)*. Contrary to the case of the discs, here the potential has its minimum at the center and becomes only slightly positive at $\rho \gtrsim \sigma_\rho$. As the atoms are attracted to the potential minimum, we deduce that the dipolar inter-site interactions lead to a radial contraction of the samples. The equilibrium size of the sample is eventually defined by the competition between the inter-site interactions, the on-site (contact and dipolar) interactions and the quantum pressure.

2.5.2 Interaction Energy of Two Dipolar Samples with a Gaussian Shape

The inter-site mean-field potential yields a good qualitative description of a system with distant dipolar clouds. We now evaluate the energy related to the inter-site interaction to investigate its relevance compared to the other energy scales in the system. A thorough theoretical treatment of such system has been the subject of a recent diploma thesis in our group [118]. Here, we aim for a basic understanding of the system, while more mathematical details are given in appendix A.5.

We choose a similar system as before, but we now consider two spatially separated dBECs with identical Gaussian wave functions $\Psi_1(\boldsymbol{r})$ and $\Psi_2(\boldsymbol{r})$. The wave functions are extended in all three spatial dimensions with σ_ρ (σ_z) their radial (axial) size, and they are explicitly given by

$$\Psi_1(\boldsymbol{r}) = \frac{1}{\pi^{3/4}\sigma_\rho\sqrt{\sigma_z}}\exp\left(-\frac{\rho^2}{2\sigma_\rho^2} - \frac{z^2}{2\sigma_z^2}\right), \quad \text{and} \tag{2.31a}$$

$$\Psi_2(\boldsymbol{r}) = \frac{1}{\pi^{3/4}\sigma_\rho\sqrt{\sigma_z}}\exp\left(-\frac{\rho^2}{2\sigma_\rho^2} - \frac{(z-d_{\mathrm{lat}})^2}{2\sigma_z^2}\right). \tag{2.31b}$$

Note that the two samples with aspect ratio $\kappa \stackrel{\mathrm{def}}{=} \sigma_\rho/\sigma_z$ are separated in the polarization direction z by the distance d_{lat}. Based on the expression for the energy of a single dipolar BEC, given by Eq. (2.17), we define the inter-site interaction energy in a system of two dipolar clouds by

$$E_{\mathrm{inter}}^{(2)} \stackrel{\mathrm{def}}{=} \int \mathrm{d}^3r \int \mathrm{d}^3r'\, n_1(\boldsymbol{r}) V_{\mathrm{dd}}'(\boldsymbol{r},\boldsymbol{r}') n_2(\boldsymbol{r}'), \tag{2.32}$$

where $n_i(\boldsymbol{r}) = N\,|\Psi_i(\boldsymbol{r})|^2$ (with $i = 1, 2$) is the Gaussian density distribution on the separated sites, with N the atom number in each sample. The six-fold integral in Eq. (2.32) may be reduced to a single integral, as we show in appendix A.5 (compare also

Refs. [51, 118]),

$$E^{(2)}_{\text{inter}}(d_{\text{lat}}) = -\frac{g_{\text{dd}}N^2}{(2\pi)^{3/2}\sigma_\rho^3}\int_0^1 \mathrm{d}u\,\frac{(1-3u^2)(1-u^2(\eta+L^2))}{(1-\eta u^2)^{5/2}}\exp\left(-\frac{L^2u^2}{2(1-\eta u^2)}\right), \quad (2.33)$$

where $L \overset{\text{def}}{=} d_{\text{lat}}/\sigma_\rho$ is the normalized distance between the samples, and $\eta \overset{\text{def}}{=} 1-\kappa^{-2}$. The remaining integral in Eq. (2.33) must be computed numerically.

We show the value of the inter-site energy per particle, $E^{(2)}_{\text{inter}}/N$, versus the normalized distance L for the cases of spherical clouds ($\kappa = 1$) and pancake-shaped clouds ($\kappa = 10$) in Fig. 2.5. Furthermore, we show the overlap of the wave functions $N_{12}/(2N) \overset{\text{def}}{=} \int \Psi_1(\boldsymbol{r})\Psi_2(\boldsymbol{r})\mathrm{d}^3r$. This value corresponds to the number of atoms in the region where the clouds overlap, normalized by the total atom number $2N$ in the system. For the calculations, we use typical chromium parameters: $N = 3000$, $\mu_{\text{m}} = 6\,\mu_{\text{B}}$, and $\sigma_\rho = 3\,\mu\text{m}$.

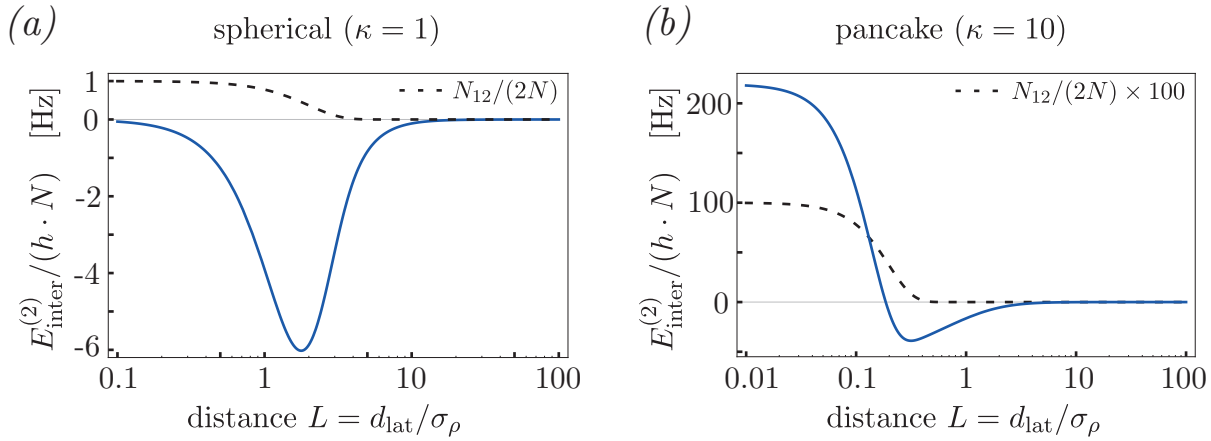

Fig. 2.5, Inter-site energy of two Gaussian shaped dipolar clouds: The figures show the inter-site energy per particle (solid blue lines) and the overlap of the wave functions $N_{12}/(2N)$ (dashed black lines) versus the normalized distance $L = d_{\text{lat}}/\sigma_\rho$. *(a)* Case of two spherical clouds ($\kappa = 1$) and *(b)* case of two pancake-shaped clouds with $\kappa = 10$. We use typical chromium parameters specified in the text.

We first consider the case of two spherical dipolar clouds, displayed in Fig. 2.5*(a)*. At large distances $L \gg 1$ the inter-site interaction energy is practically zero. When the clouds approach each other, the energy becomes more and more negative until the clouds show a significant overlap of $N_{12}/(2N) \sim 0.5$. The minimum value $\left|\text{Min}\left\{E^{(2)}_{\text{inter}}/N\right\}\right| \sim h \cdot 6\,\text{Hz}$ close to $L = 2$ is small compared to the total energy per particle in the system for our parameters[23], $E/N \sim h \cdot 1\,\text{kHz}$. In the limit $L \to 0$ the clouds entirely overlap and the

[23] For weak interactions, i.e. $N\,a/a_{\text{ho}} \lesssim 10$, the typical energy per particle is $E/N \simeq 2\hbar\bar{\omega}$ [89, Ch.6.2]. Inserting a typical mean trapping frequency $\bar{\omega} = 2\pi \cdot 500\,\text{Hz}$, we obtain the value $E/N \simeq h \cdot 1\,\text{kHz}$ given in the text.

inter-site energy vanishes. Thus, we recover the result obtained in the Thomas-Fermi approximation, where we found a vanishing dipolar contribution to the chemical potential of a spherically symmetric cloud (see section 2.4.3).
The pancake-shaped density distribution leads to an even more complex behaviour for the inter-site energy, as displayed in Fig. 2.5*(b)*. The minimum value of the inter-site energy is now $\left|\mathrm{Min}\left\{E^{(2)}_{\mathrm{inter}}/N\right\}\right| \sim h \cdot 40\,\mathrm{Hz}$. This means that the inter-site interactions are stronger than in the spherical case, but still remain small when compared to the total energy per particle. The reason for the increased interaction strength is the following: at a large cloud aspect ratio κ (but constant radial size) the two samples can get much closer to each other without overlapping, strongly increasing the DDI between the neighbouring dipoles. For $L \to 0$, i.e. when the clouds fully overlap, we find a finite *positive* value for $E^{(2)}_{\mathrm{inter}}/N$. This value corresponds to twice the dipolar energy of a single cloud containing N atoms, and we can therefore define the on-site dipolar energy $E_{\mathrm{on,dip}}$ as

$$E_{\mathrm{on,dip}} \stackrel{\mathrm{def}}{=} \frac{1}{2}\lim_{L\to 0} E^{(2)}_{\mathrm{inter}} = -\frac{g_{\mathrm{dd}}N^2}{2(2\pi)^{3/2}\sigma_\rho^3}\int_0^1 \mathrm{d}u \frac{1-3u^2}{(1-\eta u^2)^{3/2}} \tag{2.34a}$$

$$= -\frac{g_{\mathrm{dd}}N^2}{2(2\pi)^{3/2}\sigma_\rho^3}\,\kappa f_{\mathrm{dip}}(\kappa), \tag{2.34b}$$

with the dipolar anisotropic function $f_{\mathrm{dip}}(\kappa)$ introduced in section 2.4.3.

We have seen, that the inter-site interaction between two dipolar clouds is rather small compared to the total energy in the system when using typical parameters for chromium condensates. However, if we consider more than two clouds in a linear array, we may enhance the dipolar inter-site interaction energy, as we discuss next.

2.5.3 Interaction Energy in a Linear Chain of Dipolar BECs

Let us consider a stack of N_{lat} regularly spaced pancake-shaped dipolar clouds, aligned in the polarization direction z, as illustrated in Fig. 2.6*(a)*. The *total inter-site energy* $E_{\mathrm{inter,tot}}$ in such system may be calculated by summing over the inter-site energy contributions $E^{(2)}_{\mathrm{inter}}(\Delta z)$ of all the possible pairs of condensates,

$$E_{\mathrm{inter,tot}} = \sum_{j=1}^{N_{\mathrm{lat}}-1} (N_{\mathrm{lat}} - j) \cdot E^{(2)}_{\mathrm{inter}}(\Delta z = j \cdot d_{\mathrm{lat}}), \tag{2.35}$$

where we make use of the equal spacing d_{lat} between the next-neighbours. We also take care in Eq. (2.35) that each pair of samples is only counted once.

In Fig. 2.6*(b)*, we plot the total inter-site interaction energy divided by the total number of particles $N_{\mathrm{tot}} = N_{\mathrm{lat}} \cdot N$ as a function of the number of samples in the linear array. We choose parameters close to the experimental ones (see section 5) $\{\sigma_\rho = 3\,\mu\mathrm{m},\ \kappa = 50,\ d_{\mathrm{lat}} = 534\,\mathrm{nm},\ \mu_{\mathrm{m}} = 6\,\mu_{\mathrm{B}}\}$, and a constant on-site population $N = 3000$. Comparing

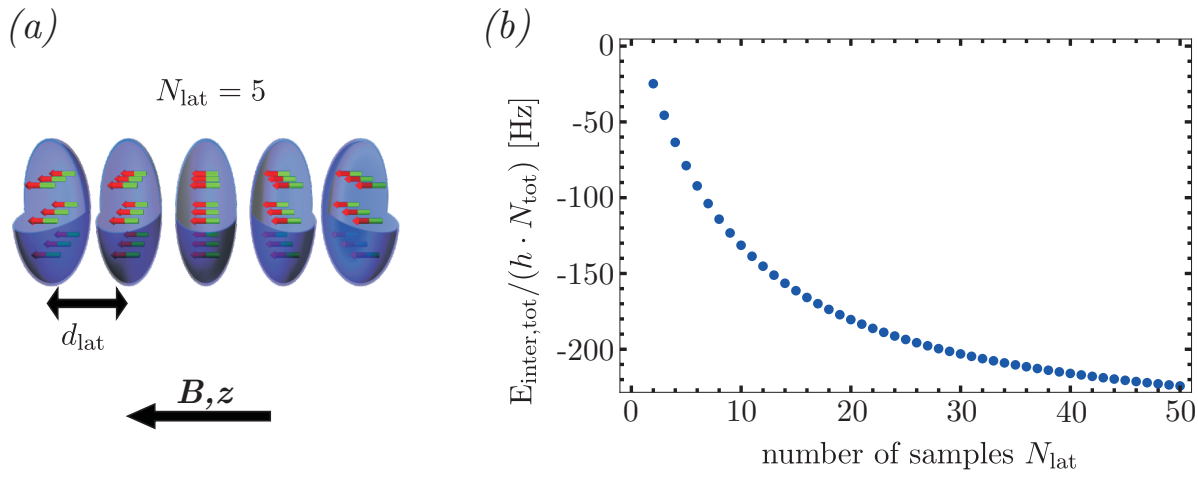

Fig. 2.6, Inter-site energy in a dipolar multi-site system with constant filling of the sites: *(a)* Sketch of the system. The N_{lat} samples, containing N atoms each, with the dipoles oriented along the symmetry axis $\boldsymbol{z}$, are equally separated by the distance d_{lat}. *(b)* Total inter-site energy, $E_{\mathrm{inter,tot}}$, divided by the total atom number, $N_{\mathrm{tot}} = N_{\mathrm{lat}} \cdot N$, using the parameters $\{N = 3000,\ \sigma_\rho = 3\,\mu\mathrm{m},\ \kappa = 50,\ d_{\mathrm{lat}} = 534\,\mathrm{nm},\ \mu_{\mathrm{m}} = 6\,\mu_{\mathrm{B}}\}$. From $N_{\mathrm{lat}} = 2$ to $N_{\mathrm{lat}} = 50$ the total inter-site energy per particle is multiplied by a factor of about 10.

the absolute value of the total inter-site energy per particle for the cases $N_{\mathrm{lat}} = 2$ and $N_{\mathrm{lat}} = 50$, we observe a value about 10 times higher in the latter case. Note that, if we consider only next-neighbour coupling, we obtain only a factor around 2 between the two cases[24]. Therefore, the coupling between distant atomic samples by the long-range dipolar interactions must be taken into account for a correct description of the system.

We have above considered a constant on-site population N of the spatially separated samples. In a real experimental system, however, there is usually a limited *total* number of atoms N_{tot} which can be distributed over the N_{lat} condensates. Performing variational calculations, using a fixed total atom number $N_{\mathrm{tot}} = 20,000$ and an on-site trap ratio $\lambda = 50$, we find a maximum absolute value of the inter-site interaction energy per particle in a system of about $N_{\mathrm{lat}} = 10$ atomic samples [122, Ch.5.5.4]. We will see in chapter 5 that we are close to this optimum value in our experiment.

Conclusion

In this chapter, we have reviewed the basic ground-state properties of a dipolar BEC. Using mean-field calculations, we have shown that the shape of the condensate depends crucially on the strength of the short-range contact interactions and the long-range dipolar interactions between the particles. We have then investigated systems of multiple spatially

[24] This is easily seen by the fact that all the samples have two next-neighbours, except from the first and the last one.

separated dipolar BECs. The calculations have shown that the inter-site interaction energy is strongly enhanced when considering more than two layers of the dipolar gas. Based on the theoretical results presented here, we will address the role of the inter-site interactions in a real experimental system in chapter 5.

3 Producing a ^{52}Cr BEC with Tunable Interactions

To investigate dipolar effects in an ultra-cold bosonic gas, we routinely create a ^{52}Cr condensate with tunable contact interactions. The complex production process of the condensate has been developed in our group over several years, with detailed descriptions of the trapping and cooling techniques given in Refs. [73, 123–127]. In the first part of this chapter, we show the experimental setup and explain the way to produce a tunable ^{52}Cr condensate. We also briefly comment on the different laser systems used for creating the BEC. In the second part, we focus on the Feshbach resonance (FR) technique [12] which plays a central role in our experiments, as it provides the mechanism to tune the s-wave scattering length. After the discussion of the underlying principle of Feshbach resonances, we describe the experimental implementation of the FR technique in our system [74]. In particular, we have revisited the calibration of the scattering length, which is the final topic of this chapter.

3.1 Creating a ^{52}Cr - BEC

3.1.1 Experimental Setup

In our experiment, we create the ultracold ^{52}Cr samples in a stainless steel chamber, shown in Fig. 3.1. The full apparatus is divided into two parts: the *oven chamber*, containing the chromium effusion cell, is kept under high vacuum at a pressure $p \sim 10^{-9}$ mbar, and the *trapping chamber* which is operated under ultra-high vacuum of $p < 10^{-11}$ mbar. Such low pressure is required to reduce the collisions of the trapped chromium atoms with the background gas during the cooling process. In between the two chambers, an 80 cm long *Zeeman slower* acts as a differential pumping stage.

The magnetic field, required for the initial trapping stages, is provided by a set of water-cooled coils in a "cloverleaf" configuration [128]. Such setup allows for sufficiently high optical access for the various laser beams used for the cooling, trapping, and imaging of the atoms as detailed in the following section. Additional pairs of coils in Helmholtz configuration (not shown in Fig. 3.1) can provide homogeneous magnetic fields along all spatial directions to compensate for external magnetic fields. The additional coils are also used to control the position of the cloud in the magnetic trap, and to provide a quantization axis of the system. We define the z-axis of the system to be aligned with the symmetry axis of the magnetic trapping field. Along this direction, we can apply a strong homogeneous magnetic offset field ($B \sim 600$ G) to reach a Feshbach resonance, with the details discussed in section 3.2.

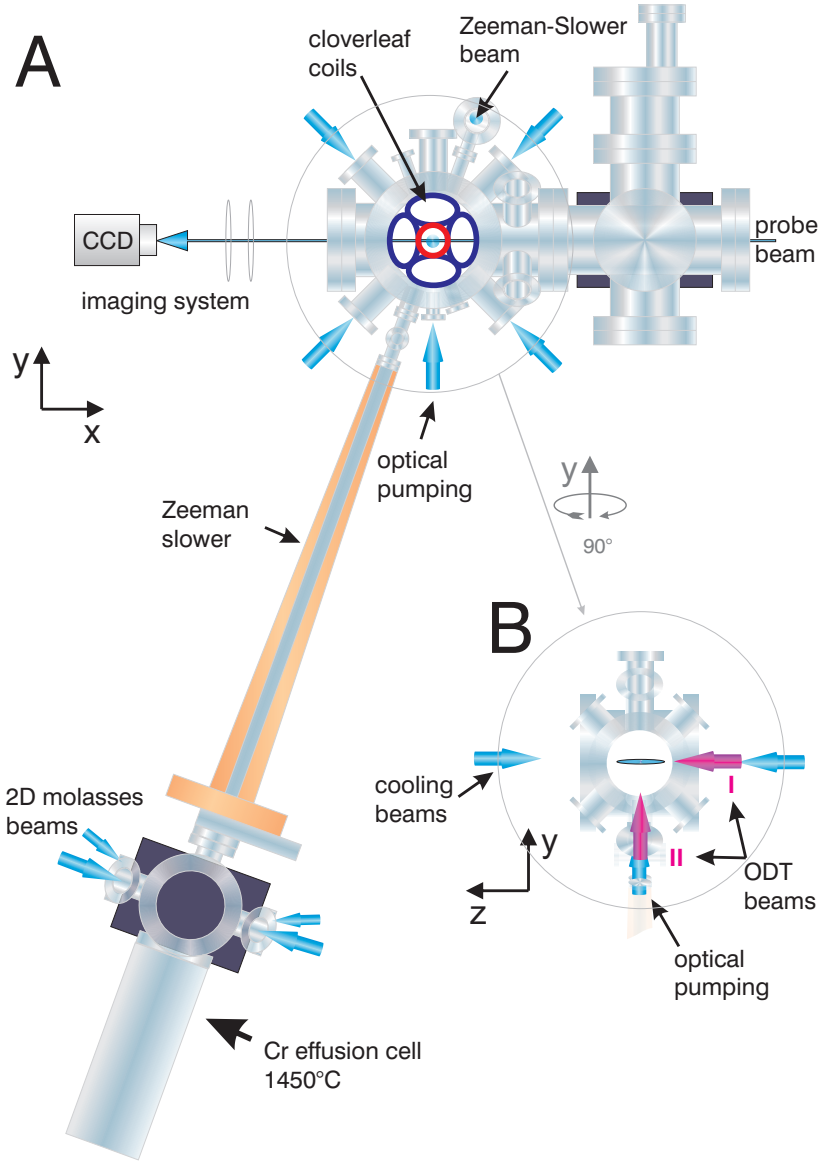

Fig. 3.1, Experimental Setup: The full chamber (A) is divided into the oven chamber (containing the chromium effusion cell) and the trapping chamber (rotated by 90° along y in B). The two chambers are separated by the 80 cm long Zeeman slower. Blue arrows indicate the laser beams for cooling and optical pumping and the red arrows (in B) illustrate the optical dipole trap beams. The symmetry axis of the cloverleaf coils define the z-direction. The imaging laser beam (probe beam) propagates along the x-direction and the optical pumping beam along the y-direction. Figure taken from Ref. [73].

3.1.2 Procedure

We create a beam of chromium atoms by sublimation in an effusion cell[25] at a temperature $T \sim 1450°\mathrm{C}$. The atomic beam is first collimated by a set of apertures, and then radially cooled by a two-dimensional optical molasses [129, Ch.9.3]. For the radial cooling, we use blue laser light at a power $P \sim 120\,\mathrm{mW}$ and at the wavelength $\lambda = 425.6\,\mathrm{nm}$, close to the $^7\mathrm{S}_3 \leftrightarrow {}^7\mathrm{P}_4$ transition (see Fig. 3.2(a)). We have chosen a single beam setup in a back-reflected geometry to maximally use the available laser power.

After the radial cooling stage, the atoms enter a spin-flip *Zeeman slower* (ZS) [124, Ch.3.4]. There, the atoms are decelerated by scattering the light from a counterpropagating resonant laser beam. The efficient deceleration from a maximum velocity $v_{\mathrm{max}} \sim 580\,\mathrm{m/s}$ to a final velocity $v_f \sim 30\,\mathrm{m/s}$ is obtained by designing a magnetic gradient field such that the Zeeman-shift exactly compensates the Doppler-shift at any position inside the ZS. This leads to persistent resonant absorption of the laser light [130, 131].

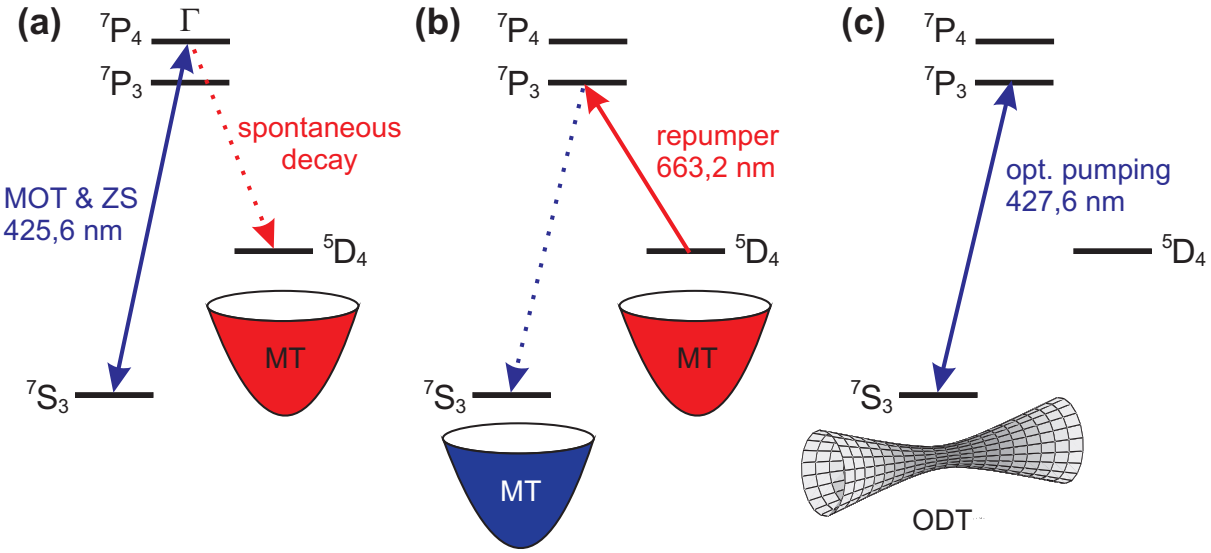

Fig. 3.2, Cooling and trapping of ^{52}Cr : *(a)* The magnetic quadrupole field created by the cloverleaf coils is used to operate the magneto-optical trap (MOT) on the $^7\mathrm{S}_3 \leftrightarrow {}^7\mathrm{P}_4$ transition. The field also provides a magnetic trap (MT) for the atoms in the meta-stable $^5\mathrm{D}_4$ state. *(b)* To transfer back the atoms from the $^5\mathrm{D}_4$ state to the $^7\mathrm{S}_3$ ground-state, a repump laser is used at a wavelength $\lambda = 663.2\,\mathrm{nm}$, resonant with the transition to the $^7\mathrm{P}_3$ excited state. *(c)* After loading the atoms from the MT to the optical dipole trap (ODT), the atoms are optically pumped from the $m_J = +3$ to the $m_J = -3$ magnetic sublevel of the $^7\mathrm{S}_3$ ground-state. Figure taken from [113].

[25] Supplier: CreaTec Fischer & Co. GmbH, part number: HTC-40-10-2000-284-SHM + WK-63-40-267. We additionally use crucibles made of ZrO_2 (stabilized by Y_2O_3) inside the tungsten crucible of the effusion cell, to avoid an chromium-tungsten alloy to form [123, Ch.4.2.1]. Supplier of crucibles: Cesima Ceramics. Internal link to technical drawings of oven and crucibles.

From the exit of the ZS, the atoms travel only a short distance until they reach the center of the trapping chamber, where they are captured in a *magneto-optical trap* (MOT). While standard three-dimensional MOTs [129, Ch.9.4] are widely used in experiments with alkali atoms [132, 133], a large inelastic two-body loss coefficient for excited state collisions severly limits the maximum number of chromium atoms that can be accumulated in such trap [123, 134]. Fortunately, the large magnetic dipole moment of chromium allows for an alternative loading mechanism: the **C**ontinuous **L**oading of a **I**offe-**P**ritchard (CLIP) magnetic trap [135, 136], illustrated in Fig. 3.2*(a)*. The magnetic quadrupole field, produced by the pair of cloverleaf coils, is used for operating a two-dimensional MOT in radial direction plus a molasses on the z-axis, using the ${}^7\mathrm{S}_3 \leftrightarrow {}^7\mathrm{P}_4$ cooling transition. With a branching ratio $1 : 250,000$ the atoms decay from the excited state ${}^7\mathrm{P}_4$ to the ${}^5\mathrm{D}_4$ meta-stable state. There they are decoupled from the MOT cycle, but remain magnetically trapped. Owing to the small branching ratio, the atoms are cooled approximately to Doppler temperature ($T_D = 124\,\mu\mathrm{K}$) in the MOT cycle, before they arrive in the meta-stable state. After around six seconds of loading time, the population in the ${}^5\mathrm{D}_4$ state saturates at $N \sim 2 \cdot 10^8$. We then switch off the MOT light and excite the atoms from the ${}^5\mathrm{D}_4$ to the ${}^7\mathrm{P}_3$ state by a 20 ms light pulse from the *repump-laser* at $\lambda = 663.2\,\mathrm{nm}$. From there the atoms decay back to the ${}^7\mathrm{S}_3$ ground-state, as shown in Fig. 3.2*(b)*.

As a next step, we compress the atomic cloud in the *magnetic trap* (MT) by maximally ramping up the current through the cloverleaf coils. The sample heats up to $T \sim 1\,\mathrm{mK}$, and we then perform *Doppler cooling* by flashing the axial MOT beams onto the dense sample [137]. Without loosing atoms, we gain two orders of magnitude in phase-space density (PSD) [138]. After this process, the PSD is $\rho \sim 10^{-7}$ which provides good starting conditions for the RF-induced *evaporation cooling*[26] [128, 139–141].

In most experiments using alkali elements, evaporative cooling in a magnetic trap is used to reach the ultra-low critical temperature for Bose-Einstein condensation [1–3, 128]. However, it turned out that this is not possible in chromium: due to the anisotropic dipole-dipole interaction, the magnetic quantum number m_J is not a conserved quantity in a two-body scattering process, which leads to a heating of the chromium sample by the so-called *dipolar relaxation* [126, 142–144]. As the atoms are initially trapped in the magnetic sublevel of highest Zeeman energy[27] ($m_J = +3$) spin-changing collisions are accompanied with a release of energy leading to the heating of the sample. By adjusting daily the magnetic offset field during the RF evaporation to the minimum possible positive

[26] The RF-induced evaporation technique is based on the selective removal of the hottest atoms from the sample which, after a rethermalization time, will possess a lower temperature than before.

[27] Only the so-called 'low-field seeking' states are magnetically trappable as local minima of magnetic fields can be produced, while the creation of local maxima is impossible as a consequence of Maxwell's equations [145].

value[28], we minimize the Zeeman energy that is released in a dipolar relaxation process. Still, the heating is too strong to reach the critical temperature for condensation.

To overcome the limitation in temperature, imposed by the dipolar relaxation, we stop the RF evaporation after reaching the following conditions: $N \sim 6 \cdot 10^6$, $T \sim 20\,\mu\text{K}$, and PSD $\rho \sim 10^{-5}$ [73]. We then transfer the atoms into a single-beam *optical dipole trap* (ODT) oriented along z. The ODT is produced by a strong laser beam at a wavelength $\lambda = 1076\,\text{nm}$, which is far red-detuned from the strongest transitions in ^{52}Cr (close to $\lambda = 425\,\text{nm}$). The basic principle of an optical dipole trap is explained in section 4.1.1, and a review on the topic is given in Ref. [43]. The resulting trapping potential, that is proportional to the position-dependent intensity of the tightly focussed Gaussian laser beam[29], is able to capture atoms in *all* magnetic sublevels of the $^7S_3$ ground-state [73, Ch.4]. Therefore, as shown in Fig. 3.2*(c)*, we can transfer the atoms by *optical pumping* to the magnetic sublevel of lowest Zeeman energy ($m_J = -3$) via the $^7P_3$ excited state, and thus prevent any further heating by dipolar relaxation[30].

The transfer efficiency from the MT to the ODT is around 40 %, leaving $N \sim 2.5 \cdot 10^6$ atoms for the final evaporation steps. While keeping the intensity of the first trapping laser beam ("ODT1", along z-direction) constant, we ramp up a second trapping beam ("ODT2", along y-direction) within 4 seconds. In this crossed ODT, the elastic collision rate is sufficiently high to reach Bose-Einstein condensation by *forced evaporation*, i.e. by successively lowering the power of the ODT laser beams [30, 73].

When performing experiments close to the center of the *Feshbach resonance* at $B_0 = 589.1\,\text{G}$ [12, 32], we pause the evaporation process well before reaching degeneracy. We then switch on the strong magnetic field oriented along the z-direction, before we continue the evaporation to produce the BEC. In this way, we avoid strong atom losses when crossing other Feshbach resonances [55] that are too narrow to be used for a well controlled tuning of the contact interaction strength [95, 127].

We thus produce a ^{52}Cr -BEC containing approximately $N = 30,000$ atoms, either in low magnetic field or close to a Feshbach resonance at $B_0 \sim 589\,\text{G}$. There, we can tune the contact interaction strength in the dBEC, as we will describe in section 3.2. During the time of this thesis, we could realize a cycle time to produce the chromium BEC of around 23 s. The reduction by a few seconds compared to previous cycle times was mainly achieved by reducing the MOT loading time, owing to the higher atomic flux after implementing the radial laser cooling in the oven chamber.

[28] The magnetic field strength should not reach the zero value, as Majorana losses [146] would destroy the sample [73, 135]. The minimum magnetic field strength that can be reached in our setup is defined by our resolution $\Delta B \sim 35\,\text{mG}$ [73].

[29] The strength of the potential created by the ODT can be calculated using the known energy level scheme of chromium [73, Ch.4]

[30] We could even exploit the spin-changing collisions in the ODT to cool the atomic cloud without atom losses by the so-called demagnetization technique [147]. Currently we are not using this scheme, as the required high-precision control of the external magnetic field is not implemented in the system.

3.1.3 Laser Systems

We now give a brief overview of the lasers that are involved in the production process of the BEC.

425 nm MOT laser system
The laser light at wavelength $\lambda = 425.6\,\text{nm}$, resonant with the $^7S_3 \leftrightarrow {}^7P_4$ transition, is used for several purposes on the experiment: radial cooling in oven chamber (120 mW), Zeeman slower (100 mW), magneto-optical trap (radial: $2 \times 60\,\text{mW}$, axial: 10 mW), and imaging (10 mW). We produce the blue light in a multi-step process: a diode-pumped solid state (DPSS) laser[31] delivers 18 W of green light at a wavelength $\lambda = 532\,\text{nm}$, which we use to optically pump a Ti:sapphire crystal inside a ring cavity[32]. At the output of the Ti:sapphire system we obtain around 3 W of infrared light at $\lambda = 851.2\,\text{nm}$, with a narrow linewidth of $\Delta\nu \sim 75\,\text{kHz}$. Finally, the infrared light is frequency-doubled by using a lithium triborate (LBO) crystal inside a home-made monolithic ring cavity[33] [149, Ch.5] from which we obtain typically around 800 mW of blue light[34].
The laser frequency is actively stabilized by performing *Doppler free polarization spectroscopy*[35] [151] with an electronic feedback to the external cavity of the Ti:sapphire system[36]. The resulting laser linewidth $\Delta\nu_{425} \sim 1\,\text{MHz}$ is well below the natural linewidth $\Gamma/(2\pi) \sim 5\,\text{MHz}$ of the $^7P_4$ excited state. It is therefore sufficiently small for the cooling and the imaging of the atomic cloud.

663 nm repump laser system
The repump laser system operating at $\lambda = 663.2\,\text{nm}$ is a home-built external-cavity diode laser. It is frequency stabilized by a passively stable reference cavity[37] using the Pound-Drever-Hall (PDH) stabilization scheme [152, 153]. The output power of the laser ($P = 10\,\text{mW}$) is split into two beams, one going to the experiment ($P = 7\,\text{mW}$) and one used for the stabilization. The long-term frequency stability of the repump laser depends on the thermal expansion properties of the reference cavity and exhibits a drift of around 2 MHz per hour. Therefore, the laser frequency has to be readjusted several times per day. Recently, a new cavity has been built [154] using the material SuperInvar® which shows a low coefficient of thermal expansion. In addition, the new device shows a much higher finesse than the one currently used, and can be actively stabilized in length via a piezoelectric actuator.

[31] Coherent, Inc.: Verdi V18.
[32] Coherent, Inc.: MBR 110
[33] The length of the doubling cavity is actively stabilized using the Hänsch-Couillaud locking technique [148], which does not require a frequency modulation of the incoming laser light.
[34] The total blue power specified here includes the main beam after the doubling cavity and two separately outcoupled beams used for imaging and spectroscopy.
[35] We use a hollow cathode lamp [150] to provide the atomic chromium vapour in the spectroscopy setup.
[36] See [113, Ch.3.2.1] for the latest improvements of the light detection electronics.
[37] Reference cavity: length $l = 1\,\text{m}$, free spectral range FSR = 75 MHz (TEM01 mode).

427 nm optical pumping laser system

The setup of the optical pumping laser system ($\lambda = 427.6\,\mathrm{nm}$) is similar to the MOT laser system, however, involving much lower laser powers. We produce around 60 mW of light at a wavelength $\lambda = 855.2\,\mathrm{nm}$ from an external-cavity diode laser[38], which is frequency stabilized to the same reference cavity as the repump laser, using as well the PDH technique. The infrared light is frequency doubled by a potassium niobate ($KNbO_3$) crystal[39] inside a home-made ring-cavity [155]. We obtain around 10 mW of blue light at the output of the cavity. The light level is then actively stabilized to around $P = 200\,\mu\mathrm{W}$, which is the optimum value for the optical pumping using the $^7S_3 \leftrightarrow {}^7P_3$ transition (see [73, Ch.4.8] for details of the optical pumping process).

1076 nm optical dipole trap laser system

The laser light at $\lambda = 1076\,\mathrm{nm}$ for trapping the atoms in the crossed ODT is provided by an ytterbium fiber laser[40], which we operate at an output power $P = 61\,\mathrm{W}$. Behind the exit of the fiber, the light is split into the horizontal ('ODT1') and the vertical ('ODT2') trapping beams, separately controlled in intensity by AOMs. During the BEC production sequence, we use the maximum powers $P_1 = 17\,\mathrm{W}$ and $P_2 = 9\,\mathrm{W}$ in ODT1 and ODT2, respectively. The two linearly polarized laser beams are crossing under an angle of 90°, with their polarization directions being perpendicular to each other to avoid interferences. The waists of the Gaussian laser beams are $w_1 = 30\,\mu\mathrm{m}$ and $w_2 = 50\,\mu\mathrm{m}$ for the ODT1 and the ODT2, respectively. We thus obtain a maximum trap depth of $|V_{\mathrm{ODT}}|/k_{\mathrm{B}} \sim 250\,\mu\mathrm{K}$ in the crossed configuration [74].

An issue that occurs when dealing with high laser powers are thermal expansion effects in the lenses that are placed in the optical path. To keep these effects as low as possible, we are using thin quartz lenses with a thermal expansion coefficient around 10 times lower than standard lenses made of the material BK7 [74].

In addition, to minimize the movement of the laser beams during the intensity ramps[41], we have developed a two-frequency driver for the AOMs [156]. Compared to the standard single frequency operation, we are able to decrease the beam displacement by a factor of around 20. Recently, we have exchanged the analogue power control by a digital one; this system shows the same performance while being more user-friendly [122, Ch.A.1].

[38] Laser diode: 'LD-0850-0100-1, SDL-5411-G1', supplier: Toptica Photonics AG.

[39] Here, we use $KNbO_3$ instead of LBO to enhance the conversion efficiency at such low input laser powers. The temperature of the crystal is actively stabilized ($T \sim 15^{\circ}\mathrm{C}$), also in contrast to the LBO crystal, where this is not needed.

[40] IPG Photonics, model: YLR-100-LP.

[41] The beam movement during the intensity ramps is induced by a heating of the AOM crystal when increasing the RF driving power.

3.2 Tuning of the Contact Interactions

In a chromium BEC, the dipolar interactions are much stronger than e.g. in condensates of alkali elements, due to the six times larger magnetic moment of the atoms. However, when compared to the contact interaction strength, the dipolar interactions are still weak and induce only perturbative effects in the system [157]. Since the magnetic moment of the atoms is fixed, the only way to enhance the dipolar effects is to reduce the strength of the contact interactions, e.g. by using the Feshbach resonance technique [12]. In this way, a system with strong dipolar effects can be created [32], and therefore the tuning of the contact interactions is an important part in our experiments.

3.2.1 Feshbach Resonances in Ultracold Gases

Dealing with the short-range interactions in section 2.2.1, we have introduced the molecular potential $V(r)$ of a two-body system. We have shown that, despite the complicated form of the interaction potential, the resulting wave function from a two-body scattering process is fully determined by a single scalar parameter, the s-wave scattering length a. Usually, the scattering length has a value close to the range of the potential r_0, with $r_0 \sim 100\,a_0$ in chromium (reminder: a_0 is the Bohr radius). However, if the potential $V(r)$ supports a *bound-state* with an energy close to the kinetic energy of the incident particles ($E \sim 0$), the scattering length diverges due to a resonant coupling mechanism [93].
In principle it is possible to shift the energy of the last bound-state of the molecular potential by applying strong DC-electric fields [103], which would thus enable the tuning of the scattering length. Unfortunately, the required electric field strength is too large for this technique to be applied in the typical high vacuum setups of BEC experiments[42] [159]. In our experiment, we therefore use the *Feshbach resonance technique* which involves *magnetic* fields with a strength within experimental reach.
So far, we have considered only a single molecular potential in the scattering problem, which represents a so-called *open channel* of the collision process. Here, the atoms can separate to infinite distance after the collision process. In a real atomic system, there furthermore exist other collision channels, where the molecular state differs in (at least) one quantum number with respect to the open channel. In Fig. 3.3*(a)*, we show a system of two channels: one is the open channel, and one is a *closed channel*, as the potential at large distances r is higher than the kinetic energy in the system. While in general, the coupling to the closed channel is weak [160], it becomes strong when the energy E of the incident particles becomes resonant with the energy E_c of a bound-state in the closed channel. This has first been theoretically demonstrated by Herman Feshbach in the context of nuclear physics [161]. Close to this so-called *Feshbach resonance* (FR), the

[42] The required electric field strength for tuning the s-wave scattering length is about 100 kV/cm [103]. This very large value is expected to be significantly reduced in systems of ultracold polar molecules [57, 58, 101, 102, 158].

scattering properties in the system can be tuned by changing the potential difference ΔE between the open and the closed channel, which is the basic idea of the Feshbach resonance technique.

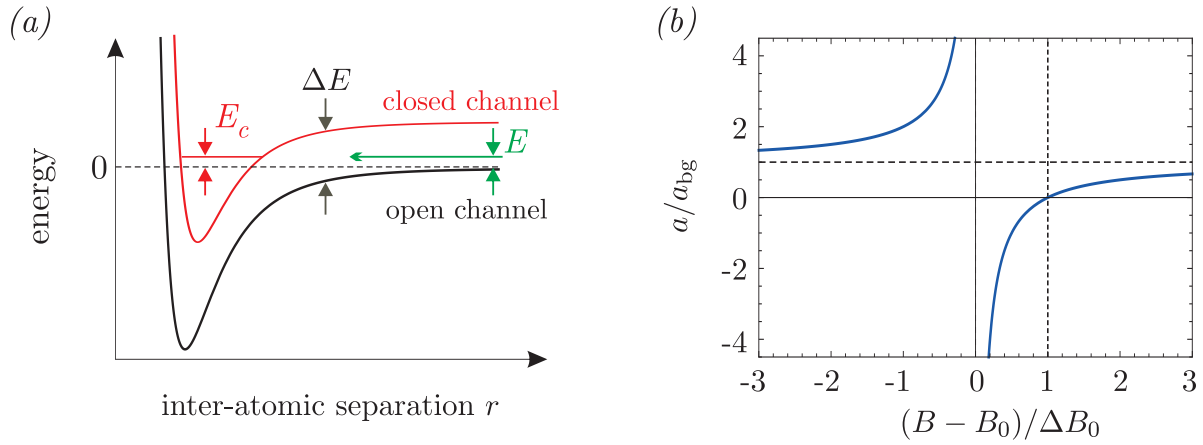

Fig. 3.3, Feshbach resonance, principle and tuning of the scattering length: *(a)* A Feshbach resonance occurs, when the energy E_c of a bound-state in the closed channel is tuned in resonance with the kinetic energy E of the scattering particles. The energy difference ΔE between the closed channel (red line) and the open channel (black line) can be tuned e.g. by an external magnetic field of variable strength B. *(b)* Scattering length a (blue line) as a function of the magnetic field strength B close to a FR. The FR is located at $B = B_0$ and has a width ΔB_0. The vertical dashed line indicates that we obtain $a = 0$ at $B = B_0 + \Delta B_0$. The horizontal dashed line indicates the asymptotic value $a = a_{\mathrm{bg}}$ far away from the center of the FR.

We label the different channels by the total spin $S = s_1 + s_2$ of the two colliding atoms and its projection onto the quantization axis $M_S = m_1 + m_2$, with $s_{1,2}$ and $m_{1,2}$ the quantum numbers of the single particles. Furthermore, the quantum numbers (l, m_l) indicate the relative angular momentum of the nuclear motion in the two-particle system. In the chromium BEC, we prepare all atoms in the energetically lowest state[43] $|s = 3, m_s = -3\rangle$, as described in section 3.1.2. Therefore, the open (s-wave) channel is labelled by the state $|S = 6, M_S = -6, l = 0, m_l = 0\rangle$. While in alkali systems there are usually only few channels coupled by the isotropic exchange interactions, the situation is different in chromium: the dipole-dipole interaction couples the open channel to several other channels, that fulfill a certain set of selection rules[44] [95, 127, 162].

[43] Note, that in chromium $|s, m_s\rangle = |J, m_J\rangle$, as the ground-state $^7S_3$ has zero electronic orbital angular momentum. Here, we choose the $|s, m_s\rangle$ representation to be consistent with Refs. [95, 127, 162].

[44] The selection rules for first order coupling via DDI are: $\Delta S = 0, \pm 2$; $\Delta l = 0, \pm 2$; and $\Delta m_l = 0, \pm 1, \pm 2$ (see appendix A.1.1). There is no coupling from $l = 0$ to $l = 0$. Due to the axial symmetry of the DDI potential, the projection of the angular momentum is conserved, i.e. $\Delta M_S + \Delta m_l = 0$. Even more channels are coupled (weakly) by the DDI at the second order.

Let us consider more closely the tuning of the scattering length in the vicinity of a Feshbach resonance (see Fig. 3.3). If the spin projections of the two coupled states are not the same, i.e. $\Delta M_S \neq 0$, also their associated magnetic moments show a difference $\Delta\mu_m \neq 0$. Then, the relative potential energy ΔE between the open and the closed channel depends on the strength B of an external magnetic field, with $\Delta E = \Delta\mu_m B$. We can therefore tune the energy E_c of the coupled state and modify the scattering length, as explained before. In the limit of small kinetic energies ($E \to 0$) the scattering length is given by [12, 163],

$$a(B) = a_{\mathrm{bg}} \left(1 - \frac{\Delta B_0}{B - B_0}\right), \tag{3.1}$$

with a_{bg} the so-called *background scattering length*, ΔB_0 the width and B_0 the center of the Feshbach resonance. The width ΔB_0 may be either positive or negative and depends on the value $\Delta\mu_m$ and the coupling strength between the two channels [163].

Atom losses close to Feshbach resonances

Usually close to Feshbach resonances, a strong increase in atom losses in the BEC is observed [55]. Two main loss mechanisms have been identified: on the one side, during very fast magnetic field ramps over the FR, *weakly bound molecules* are created [164]. Even a stable *molecular* BEC may be formed in this way, if the remaining atomic BEC is quickly removed from the system [165]. On the other side, *deeply bound molecules* may form by a decay from the resonantly coupled state [166]. In such process, while two atoms form a temporary bound-state in the closed channel, they collide with a third atom. Thus, the two atoms are transferred into a deeply bound-state and the released binding energy makes that all the three particles leave the trap. Both loss mechanisms have an influence on our experiment: The creation of deeply bound molecules limits the lifetime of our BEC close to the Feshbach resonance [74]. Furthermore, atom losses can occur through the formation of weakly bound molecules when we cross several (narrow) Feshbach resonances in the switch-on procedure of the strong magnetic field. We therefore ramp up the field *before* producing the BEC to keep the density of the atomic cloud and hence the production of the molecules at a low level.

Feshbach resonances in chromium

In chromium, 14 Feshbach resonances have been experimentally observed by atom loss spectroscopy, in the range $B = 0 - 600\,\mathrm{G}$ [95]. Three first-order and 8 second-order resonances belong to the incoming s-wave channel $|S = 6, M_S = -6, l = 0, m_l = 0\rangle$. Two resonances belong to a d-wave entrance channel, with one of them studied experimentally in more detail in Ref. [167]. One resonance is still unassigned. The broadest resonance, observed at $B_0 = 589.1\,\mathrm{G}$, has a theoretical width of $\Delta B_0 = 1.7\,\mathrm{G}$. It belongs to the incoming s-wave channel and a closed channel with quantum numbers $|S = 6, M_S = -5, l = 2, m_l = -1\rangle$. It is this Feshbach resonance that we use to tune the scattering length away from the background value $a_{\mathrm{bg}} = (102.5 \pm 0.4)\, a_0$ [144]. While Eq. (3.1) provides a simple relation $a(B)$, the precise control of the scattering length is still a challenging task in the experiment, as we will describe in the next section.

3.2.2 Experimental Realization of the Feshbach System

The required magnetic field strength $B \sim 600\,\mathrm{G}$ to reach the Feshbach resonance is conveniently produced in our setup by using the offset coils from the magnetic trap [74]. They are water-cooled, such that the heat is efficiently removed when operating the coils at the required current $I \sim 400\,\mathrm{A}$. With their relative distance of 75 mm and their radius of about 60 mm, the offset coils are close to Helmholtz configuration, producing an almost homogeneous magnetic field at the position of the atomic cloud. It was found, however, that the remaining field curvature (introducing trapping in radial direction and anti-trapping in z-direction) was still strong enough to prevent efficient evaporative cooling from the ODT. Thus, a BEC could not be obtained close to the FR. We therefore compensate the magnetic field curvature with a current of around 15 A running through the pinch coils[45] of the magnetic trap, in opposite direction with respect to the offset current [168, Ch.4.3]. After optimizing the curvature compensation current to the maximum BEC atom number, the remaining trapping frequencies, induced by the magnetic field, are $\nu_z < 10\,\mathrm{Hz}$ in the axial direction and $|\nu_{\mathrm{rad}}| < 5\,\mathrm{Hz}$ in the radial direction [168].

Current noise and active current stabilization

In order to observe strong dipolar effects ($\epsilon_{\mathrm{dd}} \geq 1$) in our chromium condensate, we have to tune the scattering length close to the zero value with an accuracy $\delta a \ll a_{\mathrm{dd}} \simeq 15\,a_0$. The goal to keep the scattering length in an interval $a = (0 \pm 1)\,a_0$, thus allows only a maximum peak-to-peak noise in the magnetic field[46] $(\delta B/B_0)_{\mathrm{pp}} \simeq 6 \cdot 10^{-5}$. Since the magnetic field strength is directly proportional to the current in the Feshbach coils, the problem is transferred to providing a current with a relative stability $(\delta I/I)_{\mathrm{pp}} \leq 6 \cdot 10^{-5}$ at an absolute value $I \sim 400\,\mathrm{A}$.

Among several power supplies tested, there was only one[47] showing sufficiently low peak-to-peak noise $(\delta I/I)_{\mathrm{pp}} = 5 \cdot 10^{-5}$ and an rms noise $(\delta I/I)_{\mathrm{rms}} = 1 \cdot 10^{-5}$ [74, App.B]. As the current is limited to 240 A in the devices, we use two power supplies in a master-slave configuration. We measure the current by a high-precision transducer[48] and perform active current stabilization by a low noise home-built proportional-integral (PI) controller acting on the resistance of a MOSFET[49]. The stabilization lowers the rms noise to $(\delta I/I)_{\mathrm{rms}} = 7 \cdot 10^{-6}$.

[45] The pinch coils are the central pair of coils in the magnetic trap setup, shown in red in Fig. 3.1.

[46] Close to its zero value, the scattering length varies with the magnetic field as $\{\mathrm{d}a/\mathrm{d}B\}|_{a=0} = a_{\mathrm{bg}}/\Delta B_0 \simeq 60\,a_0/\mathrm{G}$. Then, the absolute value of the peak-to-peak noise in magnetic field is evaluated by $(\delta B)_{\mathrm{pp}} = (2\,\delta a)/\{\mathrm{d}a/\mathrm{d}B\}|_{a=0} = 2\,a_0 \cdot 1\mathrm{G}/(60 a_0) \simeq 0.033\,\mathrm{G}$. With $B_0 = 589\,\mathrm{G}$ we finally obtain $(\delta B/B_0)_{\mathrm{pp}} \simeq 6 \cdot 10^{-5}$.

[47] Agilent, 6682

[48] Danfysik: 'Ultrastab 860 R'.

[49] We use two MOSFETs (metal-oxide-semiconductor field-effect transistor) in parallel configuration, model: 'Dynex:DIM400BSS12-A000'. In future, the use of a single MOSFET (e.g. 'Dynex:DIM1200DM12-E000') may be advantageous.

Eddy currents
The current in the Feshbach coils is dynamically computer-controlled by changing the set-point of the PI-controller [74, Ch.4.2.2]. If, however, we change the desired current value faster than the inverse bandwidth of the servo-loop ($\sim 1\,\mathrm{kHz}$), oscillations of the Feshbach current occur as we show in detail in appendix A.8. There, we also show that such oscillations are suppressed when using s-shaped current ramps. With this technique, we obtain well controlled ramps of the current on time scales around 1 ms. In addition, we find a delay of the magnetic field at the position of the atoms with respect to the current in the Feshbach coils (see also appendix A.8). Most likely this delay is produced by eddy currents in the copper gaskets of the vacuum chamber. We can describe the real magnetic field $B(t)$ by the differential equation [36] $\tau\dot{B}(t) + B(t) = B_{\mathrm{prog}}(t)$, where $B_{\mathrm{prog}}(t)$ is the programmed magnetic field value that would be present in absence of any delays. We have measured the delay time[50] $\tau = 0.25\,\mathrm{ms}$ (see also appendix A.8) which becomes relevant when performing very fast ramps in the scattering length, as shown in section 6.3.

3.2.3 Calibration of the Scattering Length

We have seen that we can provide a current in the Feshbach coils at a very low noise level. For an accurate tuning of the scattering length, however, we furthermore have to precisely determine the magnetic magnetic field close to the Feshbach resonance. Due to the small width of the FR, we are sensitive to any small shift in the external magnetic field, and we thus perform a *calibration of the scattering length* for each dataset that we produce. The basic idea of the calibration procedure is to transform the interaction energy of the trapped condensate into kinetic energy by releasing the BEC from the trap. We then deduce the scattering length from the extension of the BEC after a sufficiently long time-of-flight (TOF).

Principle of the calibration
In the limit of dominant contact interactions, the stationary Gross-Pitaevskii equation (2.15a) can be solved exactly in the TF-approximation. In this case, the interaction energy per particle E_{int}/N is directly proportional to the chemical potential μ, with $\mu \propto (Na)^{2/5}$ [89]. After suddenly releasing the BEC from the trap, the full interaction energy is transferred to kinetic energy. The resulting asymptotic expansion velocity v of the condensate is then given by $v \propto (Na)^{1/5}$. Hence, the radius of the BEC after sufficiently long time-of-flight (TOF) is $R = v \cdot t_{\mathrm{tof}} \propto (Na)^{1/5}\, t_{\mathrm{tof}}$, with t_{tof} the expansion time.
In presence of dipolar interactions, the expansion dynamics of the condensate is crucially modified [31, 32, 169]. However, the time-dependent condensate radii are still given ex-

[50] Note that the parameter $\tau = 0.25\,\mathrm{ms}$ is about a factor of two smaller than previously measured with the 'old' version of the PI controller [74, Ch.4.3].

actly within the TF approximation[51] [169]. We are thus able to numerically calculate the values R_y^5/N and R_z^5/N after TOF as a function of the scattering length, where R_y (R_z) is the Thomas-Fermi-radius of the BEC in the y-direction (z-direction). The result of such calculations are shown in Fig. 3.4*(a)*, for typical experimental parameters. For $a \gtrsim 40\,a_0$ both values scale linearly with the scattering length, comparable to the case of a non-dipolar BEC. In the regime $a < 40\,a_0$, however, the linear scaling is only observed in the y-direction, i.e. transverse to the alignment of the dipoles. Using a cigar-shaped trap ($\omega_x, \omega_y > \omega_z$), the value R_y^5/N tends to zero when[52] $a \approx a_{\mathrm{dd}} \simeq 15\,a_0$. Thus, the scaling of R_y^5/N with the scattering length is well described by the empirical formula

$$\frac{R_y^5}{N} = \sigma\,(a - a_{\mathrm{offset}})\,, \tag{3.2a}$$

leading to

$$a = \sigma^{-1}\,\frac{R_y^5}{N} + a_{\mathrm{offset}}\,, \tag{3.2b}$$

where the parameters σ and a_{offset} can be obtained from a linear fit to the calculated values of $\frac{R_y^5}{N}(a)$, as shown in Fig. 3.4*(b)*. In principle, we can measure R_y and N at different values of the magnetic field strength B close to the Feshbach resonance, and obtain the scattering length $a(B)$ via the relation (3.2b). In practice, it turns out that the uncertainties on the trapping frequencies, on the BEC radius and on the atom numbers are too large to perform an accurate calibration in such direct way. Nonetheless, we have performed measurements of R_y^5/N in low magnetic field (far from the Feshbach resonance) where $a = a_{\mathrm{bg}}$ and find a deviation of only 6.2% to the value calculated in the TF approximation (see Fig. 3.4*(b)*).

Considering the form of Eq. (3.2b), we see that any systematic scaling uncertainty on R_y^5/N may be absorbed by replacing the calculated parameter σ by an effective value, $\sigma \to \sigma_{\mathrm{eff}}$. Since we know precisely the background value of the scattering length, $a_{\mathrm{bg}} = (102.5 \pm 0.4)\,a_0$ [144], we obtain σ_{eff} directly from the expansion measurements, with the detailed procedure given in appendix A.7. Thus, the only required input from the calculations is the parameter a_{offset}. With the trap frequencies $\omega_{(x,y,z)} = 2\pi \cdot (680, 624, 270)\,\mathrm{Hz}$, we obtain the value $a_{\mathrm{offset}} = (14 \pm 1)\,a_0$ from the calculations in the TF approximation. Since the parameter a_{offset} is a crucial input in the calibration of the scattering length, we compare the TF-calculations to full numerical simulations of the expansion of the dBEC[53], which yield the slightly different value $a_{\mathrm{offset}} = (9 \pm 1)\,a_0$ (see Fig. 3.4*(b)*). We are using this latter value of a_{offset} for the calibration of the scattering length, since the

[51] In Ref. [169] a sign problem occurs in the expansion formulae. The corrected formualae are given explicitely in Ref. [113, A.5.9].

[52] In calculations without dipolar interactions we find the zero crossing at $a = 0\,a_0$.

[53] The simulations are performed by K. Pawłowski from the theory group of K. Rzążewski in Warsaw, using the numerical methods described in Ref. [118].

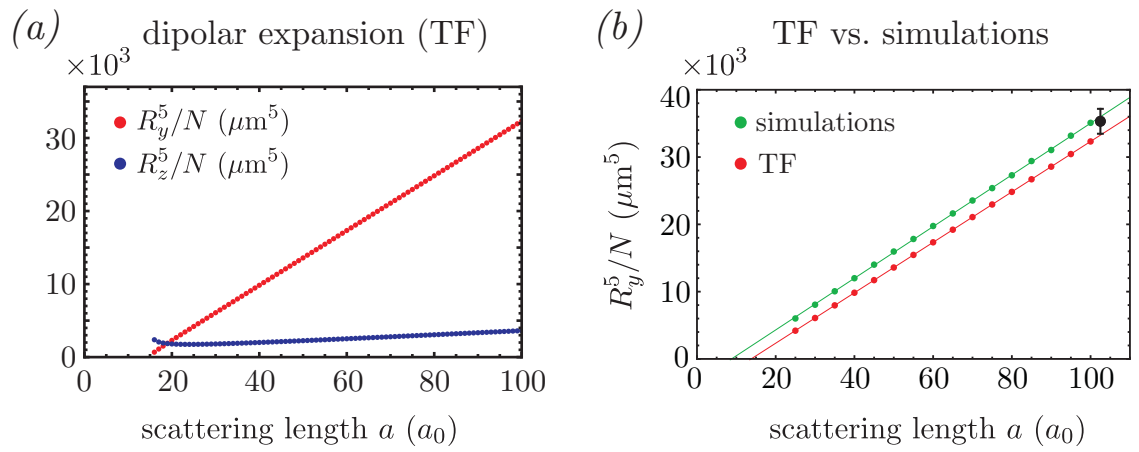

Fig. 3.4, Dipolar expansion: *(a)* Ratios R_y^5/N (red dots) and R_z^5/N (blue dots), calculated for different scattering lengths using the TF approximation (parameters: $\omega_{x,y,z} = 2\pi \cdot (680, 624, 270)\,\mathrm{Hz}$, $t_{\mathrm{tof}} = 7\,\mathrm{ms}$, $N = 20,000$). *(b)* Results of the calculations for R_y^5/N in the TF approximation (red dots) and using full numerical simulations (green dots). The lines are linear fits to the data from which we extract the value a_{offset} (see text). The experimental datapoint (black dot) is taken at $a = a_{\mathrm{bg}}$ in low magnetic field, where we obtain smaller uncertainties on R_y^5/N than in the measurements close to the FR.

simulations are expected to recover more closely the dynamics of the real dipolar BEC than the calculations within the TF approximation.

Measurements

In a typical calibration measurement, we create a BEC at $B \approx 626\,\mathrm{G}$ ($B \approx 578\,\mathrm{G}$) when measuring above (below) the FR. Then, we ramp the magnetic field to a value closer to the FR and hold the system for 4 ms at this value, for it to equilibrate. We then switch off the optical dipole trap and perform a 7 ms TOF before we take an absorption image of the cloud. Using a bimodal fit (accounting for the BEC and for the remaining thermal atoms), we extract the condensate radius R_y and the BEC atom number[54] N. In this way, we take at least four datapoints for each programmed current I_{FB} in the Feshbach coils to reduce the uncertainties on the values $R_y^5/N(I_{\mathrm{FB}})$.

Fitting procedure

The fitting of the data is performed in a two-step process (see appendix A.7 for details): We first fit the scaling parameter σ_{eff} and calculate the scattering length values $a_{\mathrm{exp}}(I_{\mathrm{FB}})$ via Eq. (3.2b) from the measured values $R_y^5/N(I_{\mathrm{FB}})$. In a second fitting procedure, the

[54] With the strong Feshbach field oriented along z, we cannot provide the maximum absorption cross section for the imaging light (propagating along x) [36]. We thus record a lower atom number in the absorption images than actually contained in the BEC. However, this effect is fully accounted for in our evaluation procedure, by introducing the effective scaling parameter σ_{eff}.

width and the center of the resonance is obtained by fitting the function

$$a(I_{\mathrm{FB}}) = a_{\mathrm{bg}} \cdot \left(1 - \frac{\Delta I_{\mathrm{FB}}}{I_{\mathrm{FB}} - I_{\mathrm{FB},0}}\right), \tag{3.3}$$

to the data, where the width and the center of the FR are expressed in terms of the Feshbach current. The goal of this two-step fitting procedure is to extract not only the fitting parameters ΔI_{FB} and $I_{\mathrm{FB},0}$ (and their uncertainties), but also the correlation between them. If we find e.g. an anti-correlation, the value of interest (in our case the scattering length) is better known than the single uncertainties on the fitting parameters would suggest. We discuss the determination of the uncertainty Δa on the scattering length in details in appendix A.7.

The results for the calibration of the scattering length are shown in Fig. 3.5. Using only the data *above* the FR ($B > B_0$) for the calibration, we obtain a small uncertainty Δa close to the datapoints, i.e. for $a \gtrsim 20\, a_0$. However, in the region $a < 0$ the uncertainty grows significantly. This indicates a rather large uncertainty on the fitting parameters ΔI_{FB} and $I_{\mathrm{FB},0}$, combined with a strong anti-correlation between them. If we also use the data for the magnetic field strengths *below* the resonance, the uncertainties on ΔI_{FB} and $I_{\mathrm{FB},0}$ typically decrease by a factor of around four, while the anti-correlation becomes smaller. As shown in Fig. 3.5*(b)*, we thus obtain a more precise calibration in the region $a < 0$, which is an interesting region for the experiments presented in this thesis.

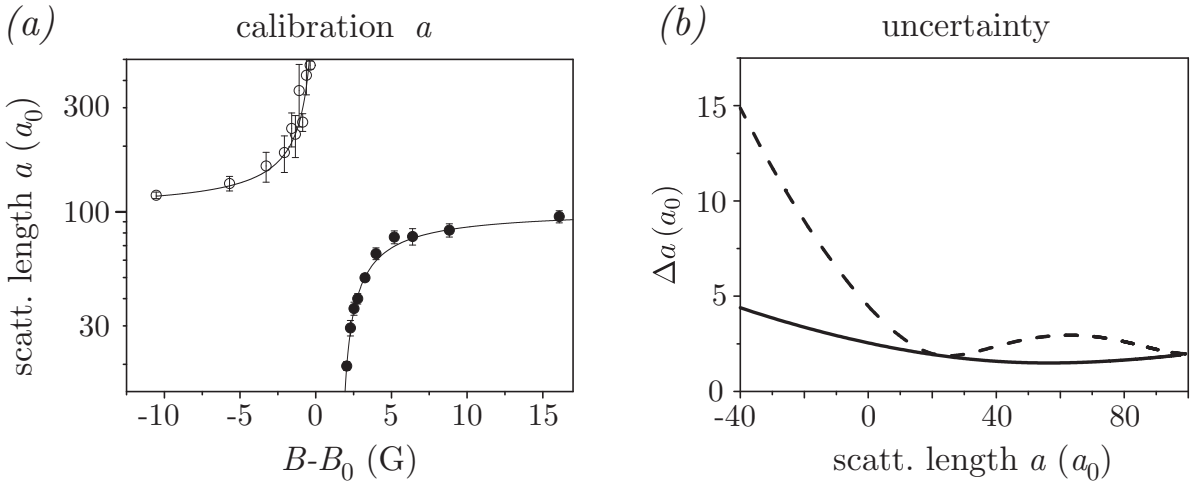

Fig. 3.5, Calibration of the scattering length: *(a)* Scattering length values computed from the measured values R_y^5/N above the Feshbach resonance (filled black dots) and below the FR (open black dots). The black line is a fit with the theoretically expected behaviour $a(B)$, given by Eq. (3.1). *(b)* Uncertainty Δa on the scattering length a. Using only the datapoints above the FR in the fitting procedure yields a large uncertainty Δa in the experimentally interesting region, i.e. when $a \lesssim 0$ (dashed line). When including datapoints below the FR (solid line), Δa decreases in this region, owing to reduced uncertainties on the fitting parameters.

The precise determination of the function $a(I_{\mathrm{FB}})$ is the main goal of the calibration procedure. However, to display the results in real physical parameters, we have to convert the Feshbach current into a magnetic field strength. Therefore, we have performed spectroscopy measurements on a thermal cloud for different values I_{FB}. For our settings of the PI controller[55], we obtain the scaling $\mathrm{d}B/\mathrm{d}I_{\mathrm{FB}} = (2.429 \pm 0.004)\,\mathrm{G}$, where the value $I_{\mathrm{FB}} = 0 - 20$ is given in arbitrary units used in the LABVIEW control program. Since the measured center of the Feshbach resonance $I_{\mathrm{FB},0}$ corresponds to the magnetic field value $B_0 = 589.1\,\mathrm{G}$ [95], the magnetic field is fully determined[56].

Width of the Feshbach resonance

To evaluate the width of the Feshbach resonance at $B_0 = 589.1\,\mathrm{G}$, we have collected the data of 14 calibrations of the scattering length. When calculating the mean value and the standard deviation of the single measured widths, we obtain the width $\Delta B_0 = (1.49 \pm 0.09)\,\mathrm{G}$ for the FR. This value is slightly lower than the theoretical prediction $\Delta B_{0,\mathrm{theo}} = 1.7\,\mathrm{G}$ [95].

[55] Analog output voltages of National Instruments cards: $U(I_{\mathrm{FB}} = 0) = 0\,\mathrm{V}$, $U(I_{\mathrm{FB}} = 20) = 10\,\mathrm{V}$. Converted voltages on PI controller: $\mathrm{DVsum}(I_{\mathrm{FB}} = 0) = 9.23\,\mathrm{V}$ and $\mathrm{DVsum}(I_{\mathrm{FB}} = 20) = 9.96\,\mathrm{V}$.

[56] The minimum field strength that we can reach is $B_{\mathrm{min}} = B(I_{\mathrm{FB}} = 0) = (577.9 \pm 0.2)\,\mathrm{G}$, while the maximum field strength is $B_{\mathrm{max}} = B(I_{\mathrm{FB}} = 20) = (626.0 \pm 0.2)\,\mathrm{G}$.

4 A BEC in a One-Dimensional Optical Lattice

In this chapter, the basic properties of a BEC trapped in a one-dimensional (1D) optical lattice potential are described, neglecting the dipolar interactions. We focus only on the topics that are relevant for this thesis. An overview over the broad physics of ultracold quantum gases in optical lattices can be found in Refs. [44, 170].
After introducing the basic formalism of one-dimensional lattice potentials, we investigate the case of a non-interacting BEC in a 1D lattice. Using this simplification (with respect to the interacting case), we derive a scheme for the experimental calibration of the lattice potential, based on the diffraction of a BEC from the lattice. Investigating furthermore the dynamics of a moving wavepacket in the system, we identify the transition from a regime of almost free propagation along the lattice direction to a regime with strongly suppressed motion. As a next step, we include the contact interactions in the system and derive the ground-state properties of a BEC in a 1D lattice. In very deep lattice potentials, the particle exchange between the lattice sites is suppressed on experimental time scales. The system then consists of an array of spatially separated condensates with their phases evolving independently in time. As a result, we observe "quantum carpet" structures, i.e. complex interference patterns after a time-of-flight, which we show at the end of the chapter.

4.1 The 1D Optical Lattice Potential

4.1.1 Characteristics of the Lattice Potential

The creation of an optical lattice potential, and of optical dipole traps in general, relies on the interaction between an atom and the electromagnetic field of a trapping laser. To be more precise, the oscillating electric field of the laser induces an electric dipole moment $\boldsymbol{d}$ in the atom, which then interacts with the light field. In this way, an optical trapping potential $V_{\mathrm{ODT}}(\boldsymbol{r})$ is created, with [43]

$$V_{\mathrm{ODT}}(\boldsymbol{r}) = -\boldsymbol{d} \cdot \boldsymbol{E}(\boldsymbol{r}) \propto \alpha(\omega_L) \, |\boldsymbol{E}(\boldsymbol{r})|^2 \,, \tag{4.1}$$

where $\alpha(\omega_L)$ is the polarizability of the atom, ω_L the laser frequency, and $I(\boldsymbol{r}) \propto |\boldsymbol{E}(\boldsymbol{r})|^2$ is the intensity of the laser light field, with $\boldsymbol{E}(\boldsymbol{r})$ the electric field amplitude at the position $\boldsymbol{r}$. The frequency of the laser is usually tuned far away from the atomic transitions to avoid heating effects by spontaneous emission from the excited states, thus obtaining an almost fully conservative trapping potential. In our experiments, we are using a far "red-detuned" laser, i.e. the laser frequency ω_L is much smaller than any resonance frequency in the atomic spectrum. In this way, an *attractive* trapping potential $V_{\mathrm{ODT}}(\boldsymbol{r})$ is created with its minima located in the high intensity regions of the laser beam.

Here and in the following, we consider laser beams with a Gaussian-shaped radial

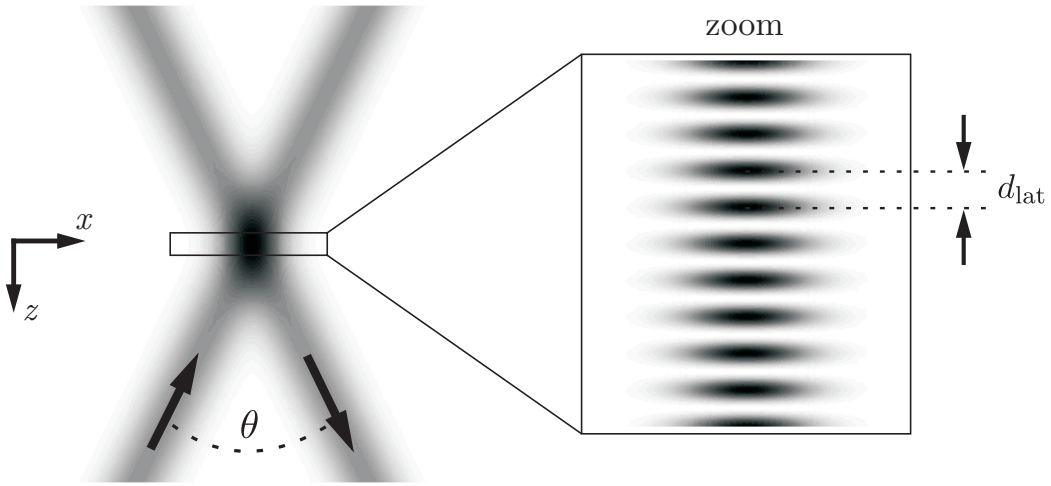

Fig. 4.1, Interference of two coherent laser beams: Two crossing laser beams (propagation direction given by the arrows) produce a regular 1D array of intensity maxima (darker shading means higher intensity). The spacing d_{lat} between the intensity maxima is defined by the wavelength of the laser and the inclusion angle θ between the laser beams (see text).

intensity profile[57]. Using a focussed laser beam or two *incoherent* laser beams in a crossed configuration, we can form a single container for an atomic cloud. In contrast, when overlapping two *coherent* laser beams, we observe a periodic array of intensity maxima, as shown in Fig. 4.1. Close to the crossing point of the two lasers, we obtain a *1D optical lattice potential* $V_{\mathrm{lat}}(z)$ of the form

$$V_{\mathrm{lat}}(z) = U_{\mathrm{lat}} \cdot \sin^2\left(\frac{\pi z}{d_{\mathrm{lat}}}\right), \tag{4.2}$$

with U_{lat} the *lattice depth* and d_{lat} the *lattice spacing* which specifies the distance between the intensity maxima. For the moment, we neglect any trapping perpendicular to the lattice direction z, which will be included in section 4.3. The lattice spacing is directly given by $d_{\mathrm{lat}} = \lambda/(2\cos[\theta/2])$, where λ is the wavelength of the laser and θ is the angle between the laser beams (see Fig. 4.1). From the lattice depth and the spacing d_{lat}, we derive the characteristic lattice parameters which are commonly used for the description

[57]The intensity profile of a Gaussian laser beam that propagates along z is given by $I(\boldsymbol{r}) = I_0\,(w_0/w(z))^2 \exp\left[-2\rho^2/(w(z))^2\right]$, with I_0 the intensity at the position ($\rho = 0, z = 0$); the beam radius $w(z)$ is given by $w(z) = w_0\sqrt{1+(z/z_R)^2}$, with w_0 the waist of the laser beam and z_R the Rayleigh length.

of ultra-cold gases in optical lattices:

$$k_{\mathrm{lat}} = \frac{\pi}{d_{\mathrm{lat}}} \qquad \text{the lattice wave number,} \tag{4.3a}$$

$$E_{\mathrm{R}} = \frac{\hbar^2 k_{\mathrm{lat}}^2}{2m} = \frac{\hbar^2 \pi^2}{2m d_{\mathrm{lat}}^2} \qquad \text{the recoil energy, and} \tag{4.3b}$$

$$s = \frac{U_{\mathrm{lat}}}{E_{\mathrm{R}}} \qquad \text{the dimensionless lattice depth.} \tag{4.3c}$$

4.1.2 Experimental Realization of the 1D Lattice

The optical lattice along the z-direction is produced by an ytterbium fiber laser[58] with a maximum output power $P = 20\,\mathrm{W}$, operating at a wavelength $\lambda = 1064\,\mathrm{nm}$. In contrast to the ODT laser, the lattice laser has a single output frequency at a narrow linewidth $\Delta\nu \simeq 70\,\mathrm{kHz}$. The long coherence length $L = c/\Delta\nu \sim 4\,\mathrm{km}$ allows for the creation of a standing-wave intensity pattern by interfering a single laser beam with itself in an "almost back-reflected" geometry, as illustrated in Fig. 4.2. The angle θ between the first and the back-reflected beam in our setup[59] is $\theta = 9.4^\circ \pm 1.3^\circ$, resulting in a lattice spacing $d_{\mathrm{lat}} = (533.8 \pm 0.5)\,\mathrm{nm}$. We have chosen the waists of the two lattice laser beams $w_{\mathrm{lat},1} = w_{\mathrm{lat},2} \simeq 72\,\mu\mathrm{m}$ to be larger than the waist of the ODT1 laser beam ($w_{\mathrm{ODT1}} = 30\,\mu\mathrm{m}$). Therefore, the radial confinement of the lattice is typically much smaller than the confinement by the underlying ODT. This confinement has to be taken into account, however, when applying deep lattice potentials as we show in section 5.3.1.
We tune the power of the lattice laser beam via an AOM[60] that uses a sheer-mode acoustic wave. Such device shows a reduced beam movement during intensity ramps when compared to standard AOMs, and thus ensures a stable operation of the lattice potential in the experiment.

4.2 The Non-Interacting BEC in a 1D Lattice

In this part of the chapter, we neglect all inter-atomic interactions to derive some basic properties of a BEC in a 1D lattice. The resulting formalism is closely related to the description of the quasi-free electron gas inside a crystal, found in many solid state physics textbooks [171–173]. We furthermore find an analogy to light diffraction from a phase grating when discussing the diffraction of a BEC from the optical lattice, a technique that we use to calibrate the depth of the optical lattice potential.

[58] IPG: 'YLR-20-1064-LP-SF´.

[59] Measuring the angle between the symmetry axis of the lattice and the z-axis of the vacuum chamber, we found only a small tilt of $1.9^\circ \pm 1.3^\circ$ [122, Ch.4.3]. This tilt is not expected to have any significant impact on our experiments.

[60] AA Opto-Electronic:MTS80, rise-time: $T = 1\,\mu\mathrm{s}$ for our beam diameter $d = 1\,\mathrm{mm}$

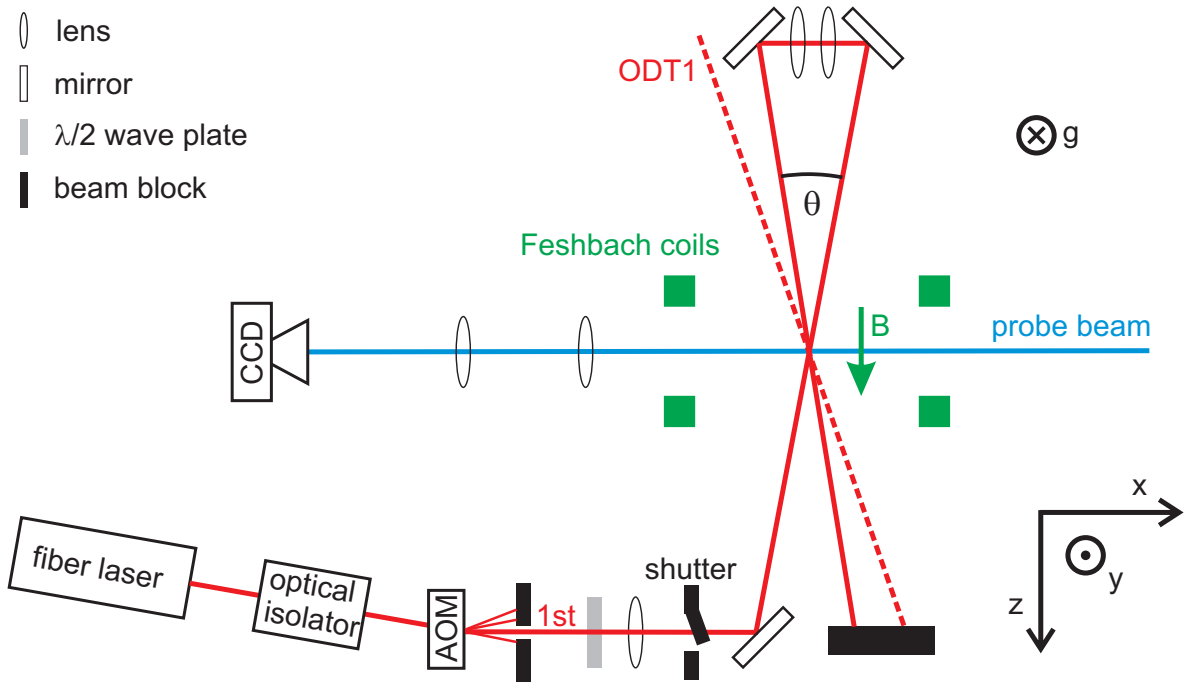

Fig. 4.2, Schematic drawing of the optical lattice setup (top view): The lattice laser beam (solid red line) is intensity controlled by an AOM and may be blocked by a shutter in front of the chamber. It is focussed to the center of the vacuum chamber (crossing point of solid and dashed red lines), then collimated and back-reflected with an angle $\theta = 9.4° \pm 1.3°$ with respect to the first beam. The symmetry axis of the lattice is well aligned with the external magnetic field $\boldsymbol{B}$ along z, which is created by the Feshbach coils (green). The tilt of the ODT1 laser beam (dashed red line) versus the z-axis is $8.0° \pm 1.5°$, and is exaggerated in the schematic drawing for a better illustration. Absorption images are recorded by the CCD camera, with the probe beam aligned in the x-direction, perpendicular to the lattice axis. Figure taken from [122].

4.2.1 Solution of the Schrödinger Equation by Mathieu Functions

In absence of interactions, a Bose-Einstein condensate in a 1D lattice is described by the Schrödinger equation

$$E\psi(z) = -\frac{\hbar^2}{2m}\frac{\partial^2}{\partial z^2}\psi(z) + U_{\mathrm{lat}}\cos^2\left(k_{\mathrm{lat}}z\right), \tag{4.4}$$

where we have applied a phase shift to the lattice potential given by Eq. (4.2), while keeping its form. Using simple algebra rules[61], and the substitution $\tilde{z} \overset{\mathrm{def}}{=} k_{\mathrm{lat}}z$, we can write Eq. (4.4) in the form of a Mathieu differential equation [174]

$$\frac{\partial^2}{\partial \tilde{z}^2}\psi(\tilde{z}) + \left[A - 2Q\cos(2\tilde{z})\right]\psi(\tilde{z}) = 0, \tag{4.5}$$

[61] We are using the trigonometric rule $\cos^2(z) = \left[1 + \cos(2z)\right]/2$ and divide by $E_{\mathrm{R}} = \hbar^2 k_{\mathrm{lat}}^2/(2m)$.

with the parameter $A \stackrel{\text{def}}{=} E/E_\text{R} - U_\text{lat}/(2E_\text{R})$ and the lattice parameter $Q \stackrel{\text{def}}{=} U_\text{lat}/(4E_\text{R}) = s/4$. The solutions of Eq. (4.5) are the so-called *Mathieu functions* $M(A, Q, \tilde{z})$, which can be computed numerically for known parameters A and Q. Recalling the periodicity of the lattice potential and according to Bloch's theorem, any eigenfunction of the system may be written in the form [170] $\psi(z) = \mathrm{e}^{iqz}u(z)$. Here, the function $u(z)$ is periodic in z with a period d_lat, and q is the quasi-momentum of the wavepacket. For the moment, we consider negligible center of mass motion ($q = 0$) such that any eigenfunction $\psi(z)$ of the system exhibits the characteristic lattice periodicity.
As a consequence of Floquet's theorem, any Mathieu function can be written in the form $M(A, Q, \tilde{z}) = \mathrm{e}^{ir\tilde{z}}f(A, Q, \tilde{z})$, with $f(A, Q, \tilde{z})$ being a 2π-periodic function in $\tilde{z}$. While in general complex and non-periodic, the Mathieu functions become real and periodic[62] for integer values of r, as requested by Bloch's theorem. Then, for a given Q, the parameter $A = A_r$ can only take a finite number of values and is called the *characteristic parameter*, with r being the *characteristic Mathieu exponent*. Note that, at given Q and r, there exists only one value A_r solving the Mathieu equation: for even values of r the Mathieu functions are symmetric, while they are anti-symmetric if r is odd.

4.2.2 Calibration of the Lattice Depth by BEC Diffraction

Since the lattice spacing d_lat is given via the laser wavelength and the geometry of the experimental setup (see section 4.1.1), the lattice depth U_lat is the only parameter that we need to determine from the experiment to have a full characterization of our system[63]. Among the existing methods [170], we choose the BEC diffraction method for a daily calibration of the lattice depth as it provides a precise result, is applicable for deep lattices, and consumes only little measurement time.

The underlying principle of this calibration scheme is closely related to the diffraction of laser light from a phase grating (see e.g. [175, Ch.12.6]). The difference is mainly the inverted role of matter and light: We first prepare a coherent matter wave (BEC) in its trap. Then, we suddenly turn on the periodic lattice potential and after a variable evolution time t_pulse we switch off all optical trapping potentials to observe the diffracted BEC in the "far field", i.e. after a sufficiently long time-of-flight[64].
At the time $t = 0$, i.e. directly before switching on the lattice potential, we can assume the wave function of the BEC $\psi(z)$ to be constant over the extent of two lattice sites. When we suddenly turn on the lattice, the system does not adiabatically evolve from the

[62] The periodic Mathieu functions are normalized via the relation $\int_{-\pi}^{\pi} M(A_r, Q, \tilde{z})\, M^*(A_r, Q, \tilde{z})\mathrm{d}\tilde{z} = \pi$.

[63] In our system, we do not control the absolute position of the lattice sites, i.e. there is no active phase stabilization of the lattice laser. This does not play a role in most of our experiments, as the lattice spacing is typically much smaller than the overall size of the BEC. We will comment on the influence of the random lattice phase shift when it is relevant for the measurements.

[64] Not only the role of matter and light are exchanged, but also the role of space and time: while in optics the components are located at different positions in space, we apply the elements (lattice potential, imaging) at different instants in time.

initial (flat) state to the ground state, described by the Mathieu function with lowest eigenenergy E. We rather project the initial state $\psi(\tilde{z}, t=0)$ into the basis of Mathieu functions, such that we can write

$$\begin{aligned}\psi(\tilde{z}, t=0) &= \sum_{r=0}^{r_{\max}} |M(A_r, Q, \tilde{z})\rangle \langle M(A_r, Q, \tilde{z}) \,|\, \psi(\tilde{z}, t=0)\rangle \\ &= \sum_{r=0}^{r_{\max}} c_r \frac{1}{\sqrt{\pi}} M(A_r, Q, \tilde{z}) \end{aligned} \tag{4.6}$$

with the coefficients c_r given by[65]

$$c_r \stackrel{\text{def}}{=} \langle M(A_r, Q, \tilde{z}) \,|\, \psi(\tilde{z}, t=0)\rangle = \int_{-\pi}^{\pi} \frac{1}{\sqrt{\pi}} M(A_r, Q, \tilde{z}) \frac{1}{\sqrt{2\pi}} \,\mathrm{d}\tilde{z}. \tag{4.7a}$$

As the Mathieu functions with odd r are anti-symmetric, the related coefficients c_r vanish due to the symmetry in the integration. We therefore replace $r \stackrel{\text{def}}{=} 2j$ and, exploiting the even symmetry of the remaining Mathieu functions, we obtain

$$c_{2j} = \frac{\sqrt{2}}{\pi} \int_0^{\pi} M(A_{2j}, Q, \tilde{z}) \,\mathrm{d}\tilde{z}. \tag{4.7b}$$

The time evolution of the eigenstates of the lattice system is determined by their eigenenergy $E = (A_{2j} + 2Q)\, E_{\mathrm{R}}$ (see section 4.2.1), and thus the wave function of the BEC at the time $t = t_{\text{pulse}}$ is given by

$$\begin{aligned}\psi(\tilde{z}, t_{\text{pulse}}) &= \sum_{j=0}^{j_{\max}} c_{2j} \frac{1}{\sqrt{\pi}} M(A_{2j}, Q, \tilde{z})\, \mathrm{e}^{-\frac{i}{\hbar}(A_{2j}+2Q)E_{\mathrm{R}} t_{\text{pulse}}} \\ &= \mathrm{e}^{-\frac{i}{\hbar}2QE_{\mathrm{R}} t_{\text{pulse}}} \sum_{j=0}^{j_{\max}} c_{2j} \frac{1}{\sqrt{\pi}} M(A_{2j}, Q, \tilde{z})\, \mathrm{e}^{-iA_{2j}\omega_{\mathrm{R}} t_{\text{pulse}}} \end{aligned} \tag{4.8}$$

where we have introduced the recoil frequency $\omega_{\mathrm{R}} = E_{\mathrm{R}}/\hbar$. We finally obtain the diffraction pattern in the far field (after TOF) by applying a Fourier transform to the in-trap wave function $\psi(\tilde{z}, t_{\text{pulse}})$. Dealing with periodic eigenstates in coordinate space, only states with discrete dimensionless momenta $\tilde{k} = 2n$ are populated, with n being an integer number. The relative populations of these states is given by

$$P_n(Q, t_{\text{pulse}}) = \left| \int_0^{2\pi} \frac{1}{2\pi} \psi(\tilde{z}, t_{\text{pulse}})\, \mathrm{e}^{-2in\tilde{z}} \,\mathrm{d}\tilde{z} \right|^2, \tag{4.9}$$

[65] We choose the normalization $\psi(\tilde{z}, t=0) = 1/\sqrt{2\pi}$, such that $\int_{-\pi}^{\pi} |\psi(\tilde{z})|^2 \mathrm{d}\tilde{z} = 1$. This choice requires to multiply the Mathieu functions by $1/\sqrt{\pi}$ in Eq. (4.7a).

and depends only on the time t_{pulse} and the lattice depth U_{lat} via the lattice parameter $Q = U_{\mathrm{lat}}/(4E_{\mathrm{R}})$. The normalization of the relative populations P_n is given by $\sum_{-n_{\mathrm{max}}}^{n_{\mathrm{max}}} P_n(Q, t_{\mathrm{pulse}}) = 1$, where n_{max} is the highest populated diffraction order.

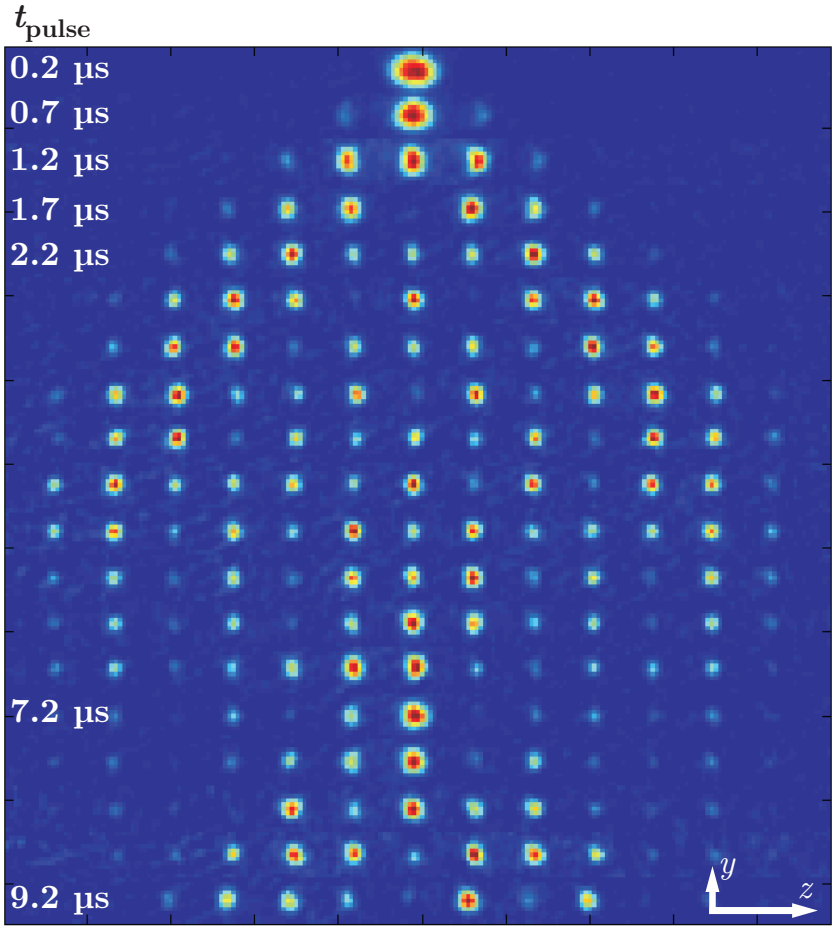

Fig. 4.3, Diffraction of a BEC from a light grating: Each line in the picture corresponds to a single absorption image, taken after a 6 ms TOF. The pulse time t_{pulse} is increased from 0.2 µs to 9.2 µs in steps of 0.5 µs. The field of view of a single absorption image is 67µm × 1.2mm in the y- and the z-direction, respectively.

In Fig. 4.3, we show the recorded absorption images, taken for a variable time t_{pulse} after a 6 ms TOF. In the first image, at the time $t_{\mathrm{pulse}} = 0.2\,\mu\mathrm{s}$, almost all the atoms are found in the zeroth order momentum component, resembling an unperturbed BEC. When increasing t_{pulse}, we observe that higher order momenta are populated, until the maximum order $n_{\mathrm{max}} = 6$ becomes visible at $t_{\mathrm{pulse}} \sim 3.2\,\mu\mathrm{s}$. The populations P_n then undergo oscillations, until at $t_{\mathrm{pulse}} \sim 7.2\,\mu\mathrm{s}$ the zeroth order exhibits a (non-perfect) revival, the populations in all the higher diffraction orders becoming small. In the final pictures (after $t_{\mathrm{pulse}} \sim 6.2\,\mu\mathrm{s}$), we observe a slight asymmetry in the populations $\pm n$, which is not in agreement with theory. This indicates a small misalignment of the lattice laser beams.

We compare the measurements with the calculations by the following procedure. We integrate the single absorption images along the y-direction and fit an 1D Gaussian function to every diffraction order in a semi-automatic procedure [122, Ch.A.2.2]. In this way, we extract the relative populations $P_n(t_{\mathrm{pulse}})$ in the discrete momentum peaks. Then, for each momentum component n we compare the measured dynamics of $P_n(t_{\mathrm{pulse}})$ with the calculated populations[66] $P_n(Q, t_{\mathrm{pulse}})$ for different lattice parameters $Q = U_{\mathrm{lat}}/(4E_{\mathrm{R}})$. By using the least-square method, we finally obtain the lattice depth U_{lat}. In Fig. 4.4,

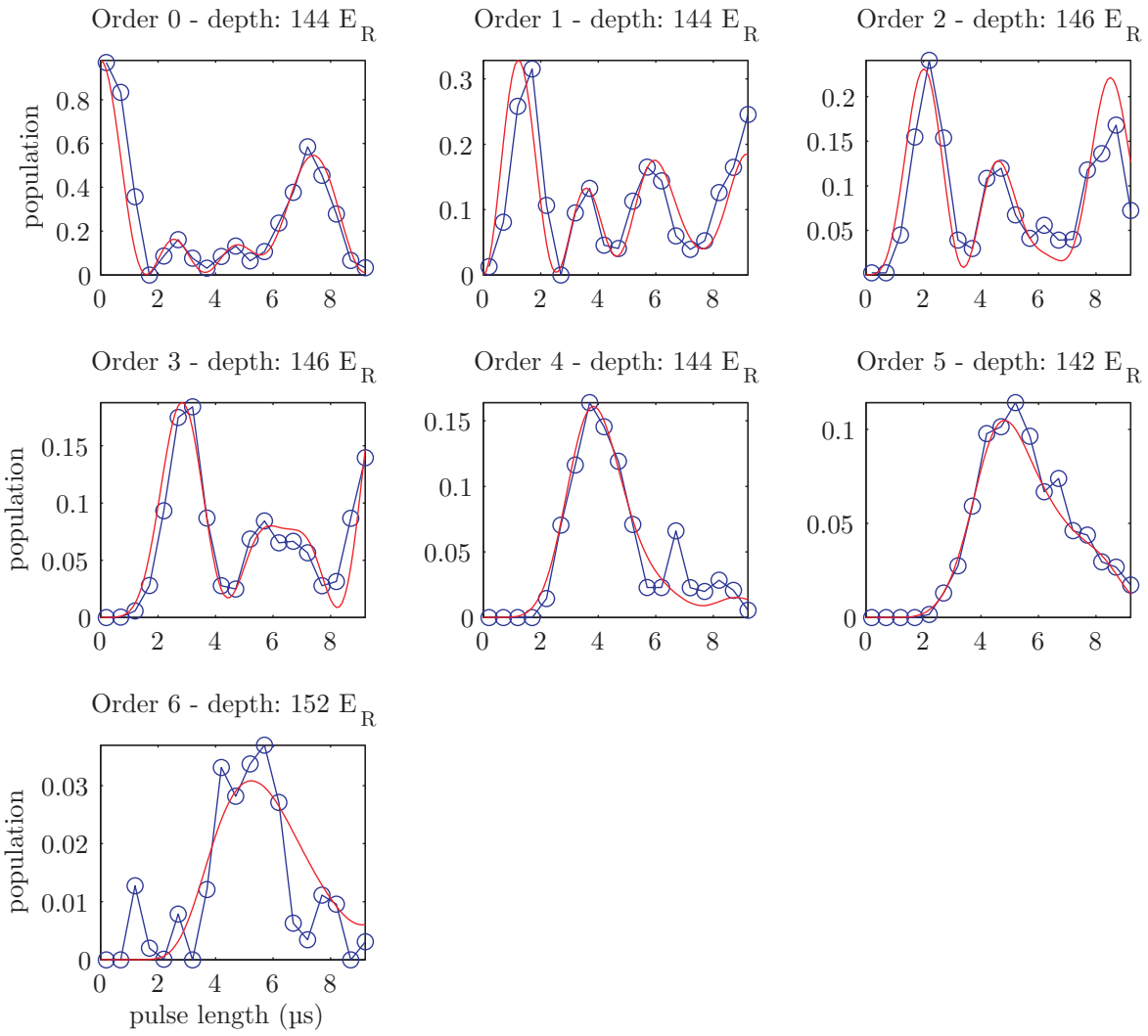

Fig. 4.4, Calibration of the lattice depth: For each diffraction order n, we compare the experimentally measured populations $P_n(t_{\mathrm{pulse}})$ (open blue circles) with the calculations via Eq. (4.9) (solid red lines). For each dataset, we extract the lattice depth U_{lat} by using the least-square method with the results given on top of each figure.

[66] In the calculation of the wave function, given by Eq. (4.8), for different lattice parameters we use the value $j_{\max} = n_{\max} + 1$, with $n_{\max}$ being the highest observed diffraction order.

we show the results of the evaluation of the absorption images from Fig. 4.3. We obtain independent fitting results of the lattice depth for each diffraction order. All of them match within a small intervall around the mean value $U_{\mathrm{lat}} = (144 \pm 2)\, E_{\mathrm{R}}$ (disregarding the weakly populated 6^{th} order).
From the calibration of the lattice depth, taken at the maximal laser power P_{lat}, we directly obtain the lattice depths at smaller laser powers by the linear scaling relation $U_{\mathrm{lat}} \propto P_{\mathrm{lat}}$. We checked the linearity of the scaling by recording diffraction patterns at different laser powers and found indeed good agreement [122, Ch.4.4.2.2].

4.2.3 Dynamics in Shallow and Deep Lattices

Let us now discuss the dynamics, i.e. the movement of a wavepacket in the periodic potential landscape. As we do not accelerate the condensate in the lattice, we are mainly interested in the dynamics of a wavepacket close to the zero quasi-momentum, $q \approx 0$, simplifying the discussion below. A thorough analysis of the dynamics of BECs in optical lattices is given in Ref. [170].

Originally investigated in the context of electrons moving inside a solid body with crystalline structure [171, 172], travelling wavepackets in periodic potentials are well understood in physics. The description of the momentum dependent energies $E(q)$ in terms of energy bands [173] has recently been experimentally demonstrated to be also valid for superfluids in optical lattices [176]. The full solution of the Schrödinger equation (4.4), including the movement of the wavepackets (i.e. $q \neq 0$), may be performed numerically. However, for our purposes, it is sufficient to consider two limiting cases:

1. *shallow lattices:* In the case of small lattice depths $U_{\mathrm{lat}} \approx 1\, E_{\mathrm{R}}$, the band structure of the lowest energy band is approximately given by [171],

$$\frac{E(\tilde{q})}{E_{\mathrm{R}}} = \tilde{q}^2 - \sqrt{4\tilde{q}^2 + \frac{s^2}{16}}, \tag{4.10}$$

   where $\tilde{q} = q/k_{\mathrm{lat}} - 1$. Expanding the expression (4.10) into a power series around $q = 0$ (using $s = U_{\mathrm{lat}}/E_{\mathrm{R}} = 1$), we obtain $E(q)/E_{\mathrm{R}} \approx \text{const.} - 0.015\, q/k_{\mathrm{lat}} + 0.98\, (q/k_{\mathrm{lat}})^2 + \mathcal{O}(q^3)$. Hence, at low momenta, the wavepackets moving in such shallow lattice potential show mainly quadratic dispersion, resulting in an almost free movement along the lattice potential[67]. As the lattice potential is only a weak perturbation to the system, the wavepackets are well described by delocalized Bloch waves extending over the full size of the condensate.

[67] At the edge of the Brillouin-zone, i.e. $q = k_{\mathrm{lat}}$, the dispersion curve flattens out, and the particles are reflected by the lattice when accelerated towards this momentum value. This regime is not relevant in our experiments, as we do not move or accelerate the BEC in the lattice.

2. *deeper lattices:* At increasing lattice depths, the movement of the wavepackets becomes gradually inhibited by the strong confinement at the positions of the individual lattice sites. In this case, the delocalized Bloch waves are not well suited for an intuitive description of the system anymore. In contrast, the so-called *Wannier functions* provide an orthogonal set of wave functions that are localized on the individual lattice sites[68]. The Wannier function $w_1(z - z_j)$, describing a wavepacket localized at $z = z_j$ in the lowest energy band, is constructed via a superposition of the Bloch functions [170]:

$$w_1(z - z_j) = \frac{1}{d_{\mathrm{lat}}} \int \mathrm{d}q \, \mathrm{e}^{-iz_j q} \, \phi_{1,q}(z), \tag{4.11}$$

where $\phi_{1,q}(z) = \mathrm{e}^{iqz} \sum_m c_m^1 \, \mathrm{e}^{imz2\pi/d_{\mathrm{lat}}}$ with m being integer numbers[69] and the coefficients c_m^1 define the weight of the different plane wave states.

Using the localized wave functions, given by Eq. (4.11), we can understand the movement of the wavepackets in terms of particles tunneling from one lattice site to the next one. The corresponding tunneling matrix element J, which measures the inter-site kinetic energy in the system, is then calculated by [177]

$$J = \int \mathrm{d}z \, w(z - z_j) \left(-\frac{\hbar^2}{2m} \frac{\partial^2}{\partial z^2} + V_{\mathrm{lat}}(z) \right) w(z - z_{j+1}). \tag{4.12}$$

In the approximation $s \gg 1$, the energy in the lowest band may be calculated analytically by solving the 1D Mathieu equation (4.5), with the resulting energy spectrum [178]

$$\frac{E(q)}{E_{\mathrm{R}}} = \sqrt{s} - 2\frac{J}{E_{\mathrm{R}}} \cos\left(q d_{\mathrm{lat}}\right) \tag{4.13a}$$

$$\text{with} \qquad J = \frac{4}{\sqrt{\pi}} s^{3/4} \mathrm{e}^{-2\sqrt{s}} \, E_{\mathrm{R}}. \tag{4.13b}$$

We see from Eq. (4.13a) that the tunneling matrix element J is directly related to the bandwidth of the lowest energy band via $J = (\max(E) - \min(E))/4$. Furthermore, using Eq. (4.13b), we may estimate the relevance of the tunneling in the system: when the tunneling time h/J is large on experimental time scales[70] (1-10 ms), the particle exchange between the lattice sites becomes negligible. While there is no clear threshold, we may neglect the tunneling in our experiments for lattice depths $U_{\mathrm{lat}} \gtrsim 15 \, E_{\mathrm{R}}$. In this regime of *very deep lattices*, the calculated tunneling time is larger than 40 ms.

[68] Note that the Wannier functions are not eigenfunctions of the lattice system.
[69] For usual lattice parameters it is sufficient to sum over $m_{\max} \sim 5$ plane wave states [177].
[70] The experimental time scale are estimated by the inverse trapping frequencies which typically range from 100 Hz to 1000 Hz.

For lattice depths $U_{\rm lat} \sim 10\, E_{\rm R}$, there is still particle exchange between the lattice sites. However, the lattice is sufficiently deep that the localized wave functions show almost no overlap from one site to the next. This greatly simplifies the description of an interacting condensate in a 1D optical lattice, which is the topic of the next section.

4.3 The Interacting BEC in a 1D Optical Lattice

Having discussed the non-interacting condensate in the perfectly periodic lattice potential, we now come closer to the real experimental conditions: we include an underlying harmonic trapping potential and also the inter-atomic contact interactions. We here consider the case of sufficiently deep lattices, where the BEC is split into a linear chain of spatially separated atomic samples. Assuming a harmonic trapping of all these "sub-condensates", we then apply the so-called tight-binding approximation. This allows us to derive some basic ground-state properties of the system, including the analytical expression for the atom number distribution over the lattice sites.

4.3.1 Tight Binding Approximation

In the experiment, we confine the BEC in an harmonic trapping potential $V_{\rm harm}(\boldsymbol{r})$, created by the ODT, which is overlapped with the 1D lattice potential $V_{\rm lat}(z)$, given by Eq. (4.2). Here, we restrict for simplicity the harmonic potential to be cylindrically symmetric along the lattice direction z. The full external trapping potential then writes

$$\begin{aligned} V_{\rm ext}(\boldsymbol{r}) &= V_{\rm harm}(\boldsymbol{r}) + V_{\rm lat}(z) \\ &= \frac{m}{2}\left[\omega_\rho^2\left(x^2+y^2\right) + \omega_z^2 z^2\right] + U_{\rm lat}\,\sin^2\left(\frac{\pi z}{d_{\rm lat}}\right), \end{aligned} \tag{4.14}$$

with ω_ρ and ω_z the radial and axial trapping frequencies of the ODT, respectively. When the lattice potential is deep enough, the initially single condensate is split into several sub-condensates that are localized at the discrete positions $z_j = j\, d_{\rm lat}$ with integer numbers j. In this case, we may apply the so-called *tight-binding approximation* (TBA). Here, we consider the "generalized" TBA [179], where the spatial parts of the on-site wave functions[71] $\Phi_j(\boldsymbol{r}, N_j)$ can depend on the local populations N_j of the lattice sites. The ground-state wave function of the whole lattice system may then be written in the form

$$\Psi(\boldsymbol{r}, t) \stackrel{\rm def}{=} \sum_j \psi_j(t)\, \Phi_j(\boldsymbol{r}, N_j), \tag{4.15a}$$

$$\text{with} \qquad \psi_j(t) \stackrel{\rm def}{=} \sqrt{N_j}\, \mathrm{e}^{-i\varphi_j(t)}, \tag{4.15b}$$

[71] The on-site wave functions $\Phi_j(\boldsymbol{r}, N_j)$ are normalized to unity, $\int \mathrm{d}^3 r\, |\Phi_j|^2 = 1$.

where the $\varphi_j(t)$ are the phases of the separated on-site condensates. As long as there is tunneling in the system, all the phases of the sub-condensates are the same and are determined through the chemical potential μ, with $\varphi_j(t) = \varphi(t) = \mu\, t/\hbar$.

In the TBA, the sinusoidal lattice potential at the position $z = z_j$ may be approximated by the leading term of a Taylor series, and thus takes the harmonic form

$$V_{\mathrm{lat}}(z - z_j) = U_{\mathrm{lat}} \cdot \sin^2\left(k_{\mathrm{lat}}(z - z_j)\right) \approx \frac{m}{2}\,\omega_{\mathrm{lat}}^2 (z - z_j)^2, \tag{4.16a}$$

$$\text{where} \qquad \omega_{\mathrm{lat}} = \sqrt{\frac{2U_{\mathrm{lat}}k_{\mathrm{lat}}^2}{m}} = 2\sqrt{s}\,\frac{E_{\mathrm{R}}}{\hbar} \tag{4.16b}$$

is the *on-site trapping frequency* in the lattice direction z. Hence, we obtain a linear array of harmonically trapped BECs, with each of them described by the Gross-Pitaevskii equation given by Eq. (2.15a). Note that, for simplicity, we neglect the dipolar interactions for the following description of the ground-state properties of the interacting condensate in the lattice.

4.3.2 Ground-State of a BEC in a 1D Lattice

Let us consider an interacting BEC in a sufficiently deep lattice, such that the on-site trapping frequency ω_{lat} is much larger than the radial trapping frequency ω_ρ in the system. If, in addition, the interaction energy per particle is much lower than $\hbar\omega_{\mathrm{lat}}$, the on-site condensates may only occupy the lowest energy level of the harmonic oscillator potential in the lattice direction [180]. In other words, this direction is frozen with respect to excitations and the system aquires a two-dimensional character. However, we stress that for typical parameters in our experiment, the 2D character does not apply for the interactions: the scattering of the particles is still a three dimensional process, well described by the s-wave scattering length a. In this *quasi two-dimensional regime*, the system is an array of pancake-like condensates, where the on-site wave functions $\Phi_j(\boldsymbol{r}, N_j)$ factorize as a Gaussian ϕ_{G} along z and a Thomas-Fermi profile $\phi_{\mathrm{TF}}^{(j)}$ in the radial directions[72] [179],

$$\Phi_j(\boldsymbol{r}, N_j) = \phi_{\mathrm{G}}(z - z_j)\,\phi_{\mathrm{TF}}^{(j)}(x, y, N_j). \tag{4.17}$$

With this ansatz for the wave functions of the on-site condensates, we insert the full wave function $\Psi(\boldsymbol{r})$ from Eq. (4.15a) into the stationary Gross-Pitaevskii equation, given by Eq. (2.15a). We recall that we do not take into account the dipolar interactions. By integrating over the spatial degrees of freedom, we obtain a set of j non-linear equations [179, 181]

$$\mu\psi_j = \varepsilon_j\psi_j + \mu_j\psi_j, \tag{4.18}$$

[72] The explicit form of the Gaussian is given by $\phi_{\mathrm{G}}(z) = (a_{\mathrm{lat}}\sqrt{\pi})^{-1/2}\exp\left[-z^2/(2a_{\mathrm{lat}}^2)\right]$, with $a_{\mathrm{lat}} \stackrel{\mathrm{def}}{=} \sqrt{\hbar/(m\omega_{\mathrm{lat}})}$. The TF profile in the radial directions has the form $(\phi_{\mathrm{TF}}^{(j)})^2 = n_{j,2D}/N_j \cdot \max\{[1 - (x^2 + y^2)/(R_\perp^{(j)})^2], 0\}$, with $n_{j,2D}$ the central 2D density and $R_\perp^{(j)}$ the radius of the BEC.

where we have neglected any contributions from the tunneling. The *global chemical potential* μ is thus expressed as the sum of the *on-site potential energy* $\varepsilon_j \stackrel{\text{def}}{=} m\omega_z^2(d_{\text{lat}}j)^2/2 \stackrel{\text{def}}{=} \Omega j^2$ arising from the underlying harmonic trapping in the z-direction, and the *local chemical potential* μ_j, as illustrated in Fig. 4.5. Note that Eq. (4.18) is valid only if the tunneling is not fully suppressed: then, the atoms distribute such among the lattice sites that, in the combined potential of ODT and lattice, the global chemical potential is constant across the full system. From the calculations performed explicitly in appendix A.3, we obtain

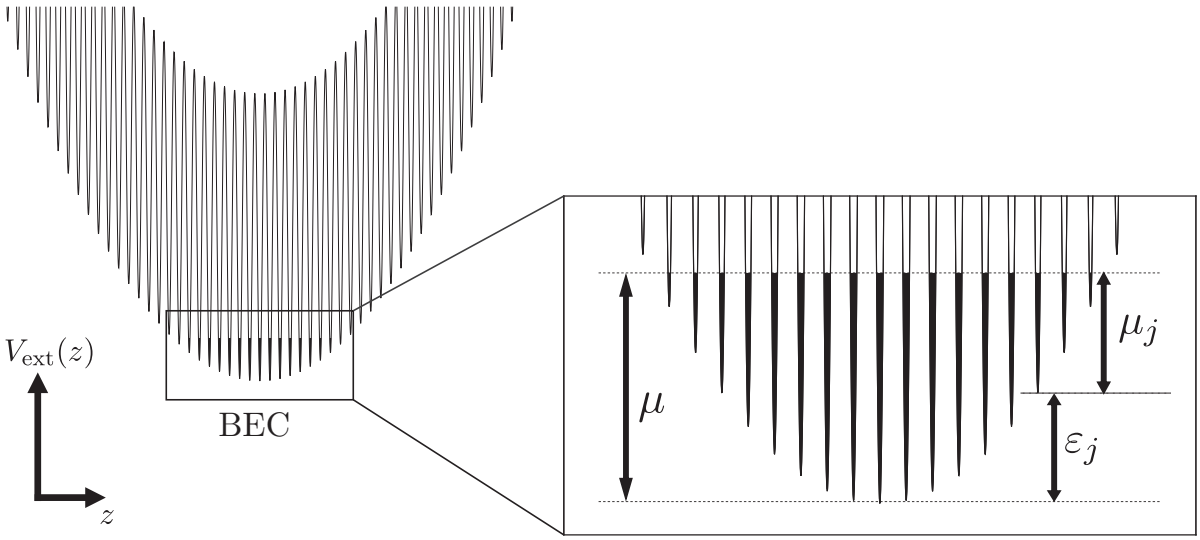

Fig. 4.5, BEC in the combined potential V_{ext} of ODT and lattice: *Left:* For the tight-binding approximation to be valid, we consider a trapping potential with the modulation U_{lat} of the lattice much larger than the chemical potential μ of the condensate. *Right:* Zoom into the region $V_{\text{ext}} \approx \mu$. The global chemical potential μ is the sum of the on-site potential energy ε_j and the local chemical potential μ_j.

the local chemical potential

$$\mu_j = U_1 \cdot N_j^{1/2}, \qquad \text{with} \quad U_1 \stackrel{\text{def}}{=} \sqrt{\frac{m\tilde{g}\,\omega_\rho^2}{\pi}}, \tag{4.19}$$

where we use $\tilde{g} \stackrel{\text{def}}{=} g/(\sqrt{2\pi}a_{\text{lat}})$, with g the contact coupling strength defined in Eq. (2.4b) and $a_{\text{lat}} \stackrel{\text{def}}{=} \sqrt{\hbar/(m\omega_{\text{lat}})}$ the harmonic oscillator length in the lattice direction. The radial TF radius $R_\perp^{(j)}$ of the j-th on-site condensate is then given by $R_\perp^{(j)} = \sqrt{2\mu_j/(m\omega_\rho^2)}$.

The most interesting quantity regarding our experiments is the atom number distribution N_j in the lattice. Inserting the local chemical potential from Eq. (4.19), into Eq. (4.18), we obtain

$$N_j = N_0 \cdot \max\left\{\left(1 - \frac{j^2}{j_{\text{inv}}^2}\right)^2, 0\right\}, \tag{4.20}$$

where $N_0 \stackrel{\text{def}}{=} (\mu/U_1)^2$ is the atom number in the central lattice site and the "inversion point" $j_{\text{inv}} \stackrel{\text{def}}{=} \sqrt{\mu/\Omega}$ yields the number of populated lattice sites: $N_{\text{lat}} = 2j_{\text{inv}} + 1$. With the total number of atoms defined by $N = \sum_j N_j$, we finally obtain the global chemical potential $\mu = \left(15N\,U_1^2\sqrt{\Omega}/16\right)^{2/5}$ (see appendix A.3 for details). The populations N_j of the lattice sites are therefore defined by the following (known) parameters: the total number of atoms N, the scattering length a, the lattice depth U_{lat}, and the trap frequencies ω_ρ and ω_z.

4.3.3 Phase Evolution of Decoupled BECs

So far, we have considered sufficiently large tunneling in the lattice such that we could define a constant global chemical potential μ. Let us now consider the case of *very deep lattices* where the particle exchange between the different lattice sites is suppressed. In such a system of decoupled condensates, any imbalance in the chemical potential from one lattice site to the next persists and eventually leads to an independent time evolution of the phases of the separated condensates.
In the context of bosonic quantum gases in optical lattices, there are two major influences on the relative phases of separated condensates that are discussed in the literature [182–187]:

(i) random relative phase evolution: In the presence of tunneling, the on-site populations N_j fluctuate around their equilibrium values (given by Eq. (4.20)), obeying a Poissonian number distribution. By increasing the lattice depth above a certain threshold, we suppress the tunneling and thus fix the populations at some (unknown) values. As a consequence, a random phase difference establishes between the on-site BECs which increases linearly in time. The dephasing time[73] $t_{\text{deph}} = \sqrt{2}\,h/U_1$ (with U_1 given by Eq. (4.19)) denotes the time when two on-site condensates close to the center of the system show a relative phase uncertainty $\Delta\varphi_j(t_{\text{deph}}) = 2\pi$. Calculating the dephasing time for the parameters[74] $\{U_{\text{lat}} = 20\,E_{\text{R}}, a = 25\,a_0, \omega_\rho = 2\pi \cdot 100\,\text{Hz}, \omega_z = 2\pi \cdot 300\,\text{Hz}$, and $N = 20,000\}$, we obtain $t_{\text{deph}} \simeq 87\,\text{ms}$. This time scale is rather long compared to the time for which we usually hold the BEC in the lattice. Therefore, the random phase evolution of the on-site condensates plays only a minor role in our experiments and will be neglected in the following.

(ii) deterministic relative phase evolution: When the tunneling is suppressed, the chemical potential cannot equilibrate among the lattice sites anymore. While the global chemical potential μ is now ill-defined, we introduce a *position dependent chemical potential* $\tilde{\mu}(z = j\,d_{\text{lat}}) = \epsilon_j + \mu_j$. Thus, when changing any external

[73] The relative phase difference between two neighbouring BECs is given by [183, 184] $[\Delta\varphi_j(t)]^2 = 1/(2N_j)\,(\mu_j t/\hbar)^2$, where we have neglected terms that arise from quantum fluctuations [182]. Inserting the local chemical potential $\mu_j = U_1\sqrt{N_j}$, and solving for the time t_{deph} such that $\Delta\varphi_j(t_{\text{deph}}) = 2\pi$, we obtain the expression given in the text.

[74] We have chosen this set of parameters, as they correspond to the experimental parameters of the measurements that we will present in section 4.4.2.

parameter $(a, U_{\mathrm{lat}}, \omega_{\rho,z})$, we also change the local values of $\widetilde{\mu}$ such that it differs from one lattice site to another. As we can calculate both ϵ_j and μ_j (see section 4.3.2), we obtain analytical expressions for the phases $\varphi_j(t) = \widetilde{\mu}(j\, d_{\mathrm{lat}})\, t/\hbar$ of the independent condensates in the lattice. The resulting deterministic evolution of the relative phases can be probed for example by the time-of-flight (TOF) technique, when the dephased matter waves interfere after switching off the trapping potential[75].

In conclusion of this section, we have determined the ground-state properties of a contact interacting BEC in a 1D lattice potential. The results obtained here for e.g. the populations of the lattice sites provide a good estimate for the case of a dipolar BEC at a weak relative dipole strength, i.e. for $\epsilon_{\mathrm{dd}} \ll 1$. Since the time-of-flight technique is a fundamental tool in our experiments to probe the ground-state of the BEC in the lattice, we next investigate the expansion of a condensate from a 1D lattice potential.

4.4 Expansion of a BEC from the Lattice

Due to the limited imaging resolution of around 6 µm in our experiment, we cannot resolve the in-trap density distribution of the BEC in the lattice. Therefore, we use the TOF technique to expand the atomic cloud before taking an absorption image. Since the spatially separated on-site condensates overlap during the expansion, the TOF technique is essentially an interference measurement in lattice experiments. It thus becomes a valuable tool to probe the relative phases between the on-site condensates.
We first discuss the expansion of a coherent array of BECs, i.e. with all the on-site condensates in phase with each other. Then, we examine the expansion from a lattice of increasing lattice depths. By comparing experimental data with simulations, we are able to identify the lattice depth above which we can neglect the tunneling of atoms between the lattice sites on experimental time scales.

4.4.1 Expansion of a Coherent Array of Condensates

We consider the case of a BEC in a lattice of intermediate depth, where tunneling is present and the chemical potential μ is constant over all the lattice sites. The system is then a coherent array of condensates, with the expansion first investigated in Ref. [180]. To describe the expansion process by analytical expressions we neglect all inter-atomic interactions. This is typically a valid assumption since the density of the cloud rapidly decreases after release from the trap and interactions do not play a role anymore.

[75] Experiments with a well controlled dephasing of independent BECs have been carried out in Refs. [186, 187]. There, the TOF technique has been extended to the so-called band-mapping technique, allowing for instance for the observation of the Talbot-effect with matter waves.

Again, we may use the analogy with the diffraction of laser light on a grating. In contrast with our previous considerations in section 4.2.2, the optical lattice introduces here a density modulation in the BEC rather than a periodic phase modulation. Therefore, the observed spatial pattern after TOF is determined by the Fourier transform of the in-trap wave function, corresponding to the optical analogon of the Fraunhofer diffraction [175, Ch.4]. Let us consider the simple case of a lattice with an equal filling of the N_{lat} lattice sites. The Fourier transform $\Phi(p_z)$ of the spatial wave function in the z-direction then writes [180]

$$\begin{aligned}\Phi(p_z) &= \phi_0(p_z) \sum_{j=-j_{\mathrm{inv}}}^{j_{\mathrm{inv}}} \mathrm{e}^{ip_z j d_{\mathrm{lat}}/\hbar} \\ &= \phi_0(p_z)\, \frac{\sin\left[N_{\mathrm{lat}} p_z d_{\mathrm{lat}}/(2\hbar)\right]}{\sin\left[p_z d_{\mathrm{lat}}/(2\hbar)\right]},\end{aligned} \tag{4.21}$$

where p_z is the momentum in the z-direction and $\phi_0(p_z)$ is the Fourier transform of the *on-site* wave functions. The momentum distribution $n_0(p_z) = |\phi_0(p_z)|^2$ of the on-site condensates determines the envelope of the full diffraction pattern $n(p_z) = |\Phi(p_z)|^2$. The second term in Eq. (4.21) is well known from the light diffraction on a multi-slit grating: it describes peaks in the momentum distribution at the discrete momentum values $p_{z,\eta} = \eta\, 2\pi\hbar/d_{\mathrm{lat}}$, with η being a positive or negative integer. We can therefore deduce the dynamics of the BEC after switching off the trapping potentials at $t = 0$: part of the cloud does not move in the z-direction, corresponding to the zeroth order momentum component. In contrast, higher momentum components move out very fast, their center of mass position being given by

$$z_\eta(t) = \frac{p_{z,\eta}}{m}\, t = \eta\, \frac{2\pi\hbar}{d_{\mathrm{lat}} m}\, t. \tag{4.22}$$

The relative population P_η of the diffraction orders is given by the envelope function of the momentum distribution $n_0(p_z) = |\phi_0(p_z)|^2$, as described above. In principle, one has therefore to calculate numerically the Fourier transform of the on-site Wannier wave functions, given by Eq. (4.11). An analytical solution, however, has been derived in Ref. [188] by approximating the Wannier functions by Gaussians. The width of the Gaussian σ was then determined by variational calculations, using the sinusoidal lattice potential given by Eq. (4.2). The resulting population $P_{\pm 1}$ of the first diffraction order can then be calculated by numerically solving the equation [188]

$$s = \frac{16}{(\ln P_{\pm 1})^2}\, (P_{\pm 1})^{-1/4}, \tag{4.23}$$

with s the dimensionless lattice depth. Following Ref. [188], we choose the populations P_η to be normalized to the population of the zero momentum component (this means that $P_0 = 1$ and in particular $\sum_\eta P_\eta \neq 1$).

In very deep lattices, the width of the Gaussian on-site wave functions is directly given by the harmonic oscillator length a_{lat}. In this case, the expression for relative population of the different momentum components is well approximated by [188] $P_\eta(s) \approx \exp\left[-4\eta^2/\sqrt{s}\right]$. For example, for $s = 20$ we obtain a relative population of the first order momentum peaks of $P_{\pm1}(20) \approx 0.4$ and only a weak population of the second order component $P_{\pm2}(20) \approx 0.03$.
The knowledge of the occupation numbers of the different diffraction orders will become important when we investigate the expansion dynamics of a dipolar condensate in chapter 6. Furthermore, Eq. (4.23) provides a calibration of the lattice depth, independent from the method described in section 4.2.2, by measuring the populations of the different momentum components after time-of-flight (see Ref. [122, Ch.4.4.1] for technical details).

4.4.2 Interference Measurements from Shallow and Deep Lattices

We have performed measurements on the expansion of a BEC from the 1D lattice, studying the cross-over from the shallow to the deep lattice regime. In the measurement sequence, we prepare a BEC ($N \sim 20,000$) in the ODT at a scattering length $a = 25\,a_0$. Then, we ramp up linearly the lattice depth U_{lat} at a rate of $10/3\,E_{\mathrm{R}}\mathrm{ms}^{-1}$, before switching off all trapping potentials and performing an 8 ms TOF. We repeat this sequence for different ramping times t, i.e. for different lattice depths U_{lat} just before the TOF, as illustrated in Fig. 4.6*(a)*.

In Fig. 4.6*(b)*, we show the absorption images that are recorded in the experiment. At small lattice depths $U_{\mathrm{lat}} \lesssim 3\,E_{\mathrm{R}}$, we observe only a single peak in the BEC density after TOF, i.e. vanishing populations $P_{\pm1}$ of the first order momentum components. Then, for increasing lattice depths, the first order momentum components become populated as we would expect from the expansion of a coherent array of condensates, discussed in section 4.4.1. In the regime $25\,E_{\mathrm{R}} < U_{\mathrm{lat}} < 39\,E_{\mathrm{R}}$, a temporary broadening of the three peaks is visible, while the general shape of the interference patterns is unchanged. At even larger lattice depths $U_{\mathrm{lat}} \geq 39\,E_{\mathrm{R}}$ the interference patterns exhibit a rich dynamics: the three momentum peaks split into several sub-peaks. The sub-peaks of maximum optical density move away from the center before coming back at the longest applied loading time $t = 16.38$ ms.

Simulations
We compare our measurements to simulations that follow closely the experimental sequence. According to the theoretical results of this chapter, the properties of the system depend crucially on the tunneling between the lattice sites. In a simple approach, we assume that tunneling is present only up to a certain lattice depth U_{fix}. At larger lattice depths, we model the system by completely decoupled on-site condensates. The parameters in the simulations are chosen close to the experimental ones: $\{N = 20,000, a = 25\,a_0, \omega_\rho = 2\pi\,100\,\mathrm{Hz}, \omega_z = 2\pi\,300\,\mathrm{Hz}\}$.

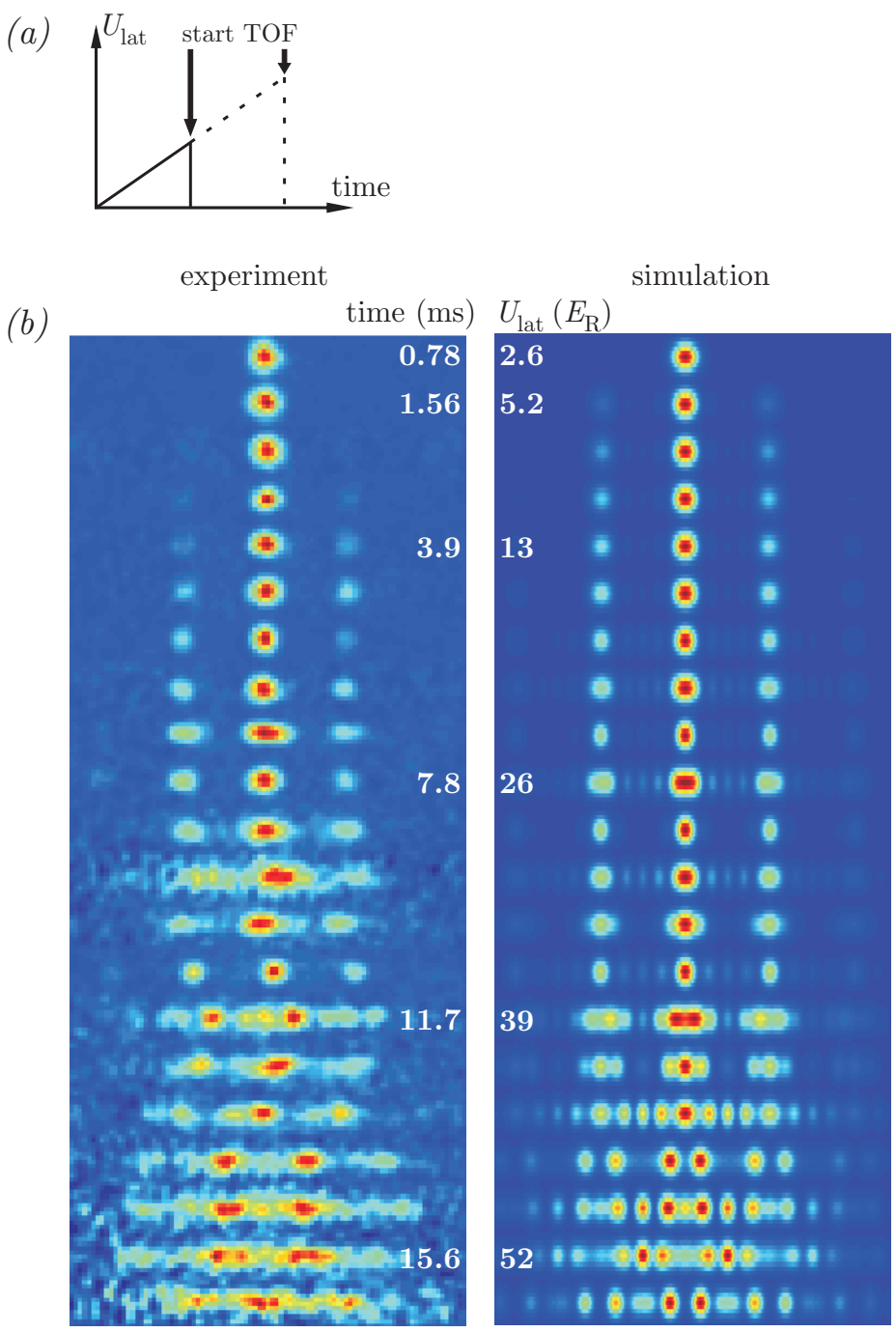

Fig. 4.6, Expansion of a BEC from a 1D lattice with increasing lattice depth: *(a)* Experimental sequence: we ramp up linearly the lattice depth at a rate of $10/3\,E_{\mathrm{R}}\,\mathrm{ms}^{-1}$ before switching off all trapping potentials to perform an 8 ms TOF (solid line). To probe the system at deeper lattices, we repeat the measurement using a longer loading time (dashed line). *(b)* Absorption pictures from the experiment and the density distribution obtained from the simulations. Fixing the on-site populations at $U_{\mathrm{fix}} = 13\,E_{\mathrm{R}}$, the simulations can reproduce the main features observed in the experiment.

In the regime $0 < U_{\mathrm{lat}} < U_{\mathrm{fix}}$, we calculate the equilibrium atom number distribution in the lattice, given by Eq. (4.20), for the different lattice depths used in the experiment. We then perform the TOF simulations, independently expanding the on-site condensates as explained in Ref. [89, Ch.13]. In this procedure, we approximate the on-site wave functions by 1D Gaussians of width $\sigma = a_{\mathrm{lat}}$ and with equal phases $\varphi_j = 0$.
When reaching the lattice depth U_{fix}, we model the suppression of the tunneling by fixing the on-site populations N_j such that $N_j(U_{\mathrm{lat}} > U_{\mathrm{fix}}) = N_j(U_{\mathrm{fix}})$. We now perform real-time simulations of the evolution of the independent phases $\varphi_j(t)$ of the separated on-site condensates: we split the linear lattice ramp into small time intervals $\Delta t \ll (\mu_0/\hbar)^{-1}$, with μ_0 the local chemical potential on the central lattice site. Then, we let the phases $\varphi_j(t)$ evolve linearly in time with $\varphi_j(t + \Delta t) = \varphi_j(t) + \widetilde{\mu}(z = jd_{\mathrm{lat}})\,\Delta t/\hbar$, where $\widetilde{\mu}(z = jd_{\mathrm{lat}})$ is the position-dependent chemical potential introduced in section 4.3.2. Finally, we simulate the TOF procedure at regular time intervals of the loading time, as explained above.
The results of the simulations are shown in Fig. 4.6*(b)*, next to the experimental data. Choosing the threshold $U_{\mathrm{fix}} = 13\,E_{\mathrm{R}}$ for the suppression of the tunneling, we can reproduce the main features observed in the experiment. We observe initially the discrete momentum peaks that we expect from the interference of a coherent array of condensates. Interestingly, the on-site condensates show a significant dephasing (indicated by the multi-peak structure after TOF) only at a lattice depth $U_{\mathrm{lat}} \sim 39\,E_{\mathrm{R}}$, much larger than the value U_{fix}. This is an effect of both, the weak dependence $\widetilde{\mu} \propto U_{\mathrm{lat}}^{1/8}$ of the chemical potential on the lattice depth and the timing of the experiment, i.e. the ramping speed of the lattice potential.

We see that we can model the measured phase dynamics of the dipolar ^{52}Cr condensate in the lattice by considering only contact interactions and a deterministic phase evolution between the on-site condensates. Indeed, it was shown in Ref. [51] that, in a 1D optical lattice, the effect of the *on-site* dipolar interactions on the phases of the condensates can be accounted for by introducing an effective s-wave scattering length. This effective scattering length replaces the true scattering length a, but the basic description of the system remains the same. The effect of the *inter-site* dipolar interactions on the phase dynamics of the system is typically small, as investigated also in Ref. [51].

Understanding the in-trap phase dynamics and the resulting density patterns after the TOF is required to interpret correctly the absorption images collected in our experiments. In particular, the dephasing of the on-site condensates in the deep lattice regime has consequences for our measurements: we have to adapt our evaluation routine of the absorption images to cope with the multi-peak patterns, as we explain in detail in section 5.3.1. Furthermore, our investigations of the collapse dynamics of a dipolar BEC in chapter 6 greatly rely on the discussion of the expansion of a BEC from the lattice.
In this chapter, we could explain all experimental observations even without taking into account the dipolar interactions. The situation is different, however, when entering the strongly dipolar regime for sufficiently low s-wave scattering lengths. Then, the dipolar

interactions crucially change the properties of the system, as we show in the next chapter presenting our measurements on the stability of a dipolar BEC in the 1D optical lattice.

5 Stability of a Dipolar BEC in a 1D Optical Lattice

In this chapter, we address the question about the stability of a dipolar condensate in the one-dimensional lattice potential. Due to the anisotropy of the dipole-dipole interaction, a single dBEC was found to be more stable in an oblate trap (pancake-shaped) than in a prolate (cigar-shaped) trapping potential [35]. In the multi-site configuration of the 1D lattice, however, we can encounter both a highly oblate on-site trapping geometry and a globally prolate shape of the underlying harmonic trapping potential. Therefore, the stability of a dipolar BEC in a 1D lattice is *a priori* unclear, motivating our experimental investigations with the results published in Ref. [75].

The chapter is structured as follows: we start by reviewing the basic instability mechanisms in homogeneous dipolar condensates. Then, we consider a single trapped dipolar condensate and briefly discuss the results of the stability measurements performed earlier in our group in this configuration [35]. We then turn our attention to the central part of this chapter: the stability of the dBEC in the lattice. After describing our measurement procedure, we show the stability diagram of the dBEC in the 1D optical lattice which is the major result. We finally discuss how inter-site interactions shift the stability threshold in very deep lattices, a particular effect of the long-range dipolar interactions.

5.1 Excitations in a Dipolar BEC

To investigate the destabilizing role of excitations in dipolar BECs, we consider the instructive case of a system with constant density. We therefore neglect trapping in all spatial directions (3D homogeneous case) or we consider trapping along one direction only (2D homogeneous case). Introducing the excitations as small density perturbations, we analyse their energy spectrum and search for unstable modes. The results obtained in these idealized systems will serve as a useful background when we will discuss the more complicated case of a trapped dipolar BEC.

5.1.1 Phonons in a 3D Homogeneous Dipolar BEC

We consider a 3D homogeneous dipolar condensate with a constant density n_0, independent of the spatial coordinates. Excitations are then introduced by adding small density modulations δn, which we assume to be plane waves with a well defined frequency ω and a quasi-momentum $\boldsymbol{q}$. Inserting the ansatz $n = n_0 + \delta n$ for the density into the hydrodynamic equations of a dipolar condensate [111] and keeping only terms linear in δn, one obtains the excitation energy spectrum $E(q)$ of a homogeneous dipolar BEC [14, Ch.5.1],

$$E(q) = \hbar\omega(q) = \sqrt{\left(\frac{\hbar^2 q^2}{2m}\right)^2 + \frac{\hbar^2 q^2}{2m}\, 2n_0 \left[g + g_{\mathrm{dd}}\, (3\cos^2\alpha - 1)\right]}, \tag{5.1}$$

where α denotes the angle between the quasi-momentum of the excitations and the polarization direction of the dipoles (the contact coupling strength g is defined in Eq. (2.4b) and the dipolar coupling strength g_{dd} is given by Eq. (2.9b)). Let us look at the limiting cases of the excitation spectrum: in the limit of large momenta, we recover the quadratic dispersion of a free particle $E_{\mathrm{free}}(q) = \hbar^2 q^2/(2m)$. In contrast, at low momenta, the excitations show a linear dispersion, comparable to sound waves, with a speed of sound $v_s = \omega/q$ determined by the density and the strength of the inter-atomic interactions[76]. Note that the dipoles create an anisotropic sound velocity $v_s(\alpha)$, i.e. the speed of sound depends on the propagation direction of the excitations. In a quasi-particle description, we can identify these low-momentum excitations as phonons, in close analogy to the theoretical description of excitations in solid state systems[77].

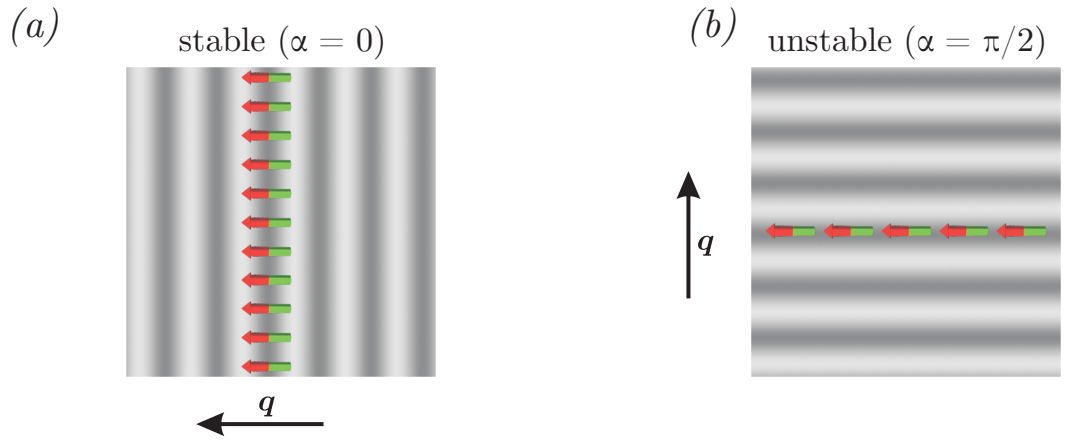

Fig. 5.1, Phonons in homogeneous dBECs: *(a)* Density waves (phonons) travelling parallel to the polarization direction of the dipoles ($\alpha = 0$). Lines of increased density (dark shaded areas) are generated with the dipoles sitting side-by-side. *(b)* For $\alpha = \pi/2$, the density maxima correspond to dipoles sitting in a head-to-tail configuration. The stability of the two configurations is discussed in the text.

In the limit of vanishing dipolar interactions ($g_{\mathrm{dd}} \ll g$), the excitation spectrum given in Eq. (5.1) reduces to the well-known Bogoliubov spectrum of purely contact interacting BECs [190]. In this case, the phonon dispersion does not depend on the direction of motion of the excitations. For dominant dipolar interactions (DI) ($g_{\mathrm{dd}} \gg g$), however, the dipolar excitation spectrum clearly reveals the anisotropy of the DI: Phonons travelling parallel to the orientation of the dipoles ($\alpha = 0$) yield real and positive excitation frequencies, i.e. a stable configuration of the system. In contrast, phonons moving in the perpendicular direction ($\alpha = \pi/2$) lead to imaginary excitation frequencies, indicating an unstable configuration of the dBEC. We illustrate this so-called *phonon instability* in Fig. 5.1. In

[76] In absence of dipolar interactions, the transition between linear and quadratic dispersion occurs at the quasi-momentum $q \sim \xi^{-1}$, where $\xi \stackrel{\mathrm{def}}{=} \hbar/\sqrt{2mn_0 g}$ is the so-called healing length of the condensate.

[77] The dipolar excitation spectrum, given in Eq. (5.1), may also be obtained by using quantum field theory which emphasizes the particle character of the excitations [113, 189].

the case $\alpha = 0$, the sound waves create lines of maximum density, with the dipoles sitting side-by-side as shown in Fig. 5.1*(a)*. In such configuration, the dipoles interact repulsively, leading to an increase in energy and hence a stable configuration of the system. This is different in the case $\alpha = \pi/2$. Here, the lines of maximum density are aligned *with* the dipoles, which attract each other in the head-to-tail configuration shown in Fig. 5.1*(b)*. The condensate can lower its energy by increasing the population of this unstable mode, which finally leads to the collapse of the whole system.

The required dipole strength for the phonon instability to occur in a 3D homogeneous dBEC is given by $\epsilon_{\mathrm{dd}} = g_{\mathrm{dd}}/g > 1$, as we can directly see from Eq. (5.1). Translating this value into a critical scattering length a_{crit} via Eq. (2.9c), this unstable situation corresponds to scattering lengths below $a_{\mathrm{crit}} = a_{\mathrm{dd}}$.

5.1.2 Rotons in a 2D Homogeneous Dipolar BEC

We now slightly change the system from the previous section and introduce a harmonic trapping potential in the polarization direction z of the dipoles. Thus, we create a 2D homogeneous sample with the dipoles mainly sitting in a side-by-side configuration. Assuming a Gaussian shape of the BEC along the confined direction, the excitation spectrum in the 2D homogeneous system takes the form (see appendix A.6)

$$E(q_\perp) = \sqrt{\left(\frac{\hbar^2 q_\perp^2}{2m}\right)^2 + \frac{\hbar^2 q_\perp^2}{2m}\, 2n_0 \left[g + 2g_{\mathrm{dd}}\, H_{2D}\left(\frac{q_\perp l_z}{\sqrt{2}}\right)\right]}, \tag{5.2}$$

where $q_\perp$ is the absolute value of the quasi-momentum perpendicular to the confined direction and l_z is the width of the Gaussian along z. The contribution of the dipolar interactions to the excitation spectrum is proportional to the function $H_{2D}(\chi) = 1 - \frac{3}{2}\sqrt{\pi}|\chi| \exp[\chi^2]\,\mathrm{erfc}[\chi]$, with $\mathrm{erfc}[\chi]$ the complementary error function. We see that the excitation spectra in the 3D and in the 2D homogeneous systems show a similar structure. However, they present one important difference: the effective dipolar contribution in the 2D case depends on the absolute value of the quasi momentum through the function $H_{2D}\left(q_\perp l_z/\sqrt{2}\right)$, shown in Fig. 5.2*(a)*, while it is independent of $|\boldsymbol{q}|$ in three dimensions.

Due to the competition between the monotonically decreasing function $H_{2D}\left(q_\perp l_z/\sqrt{2}\right)$ and the free-particle dispersion $E_{\mathrm{free}}(q_\perp) = \hbar^2 q_\perp^2/(2m)$, the excitation spectrum of a 2D homogeneous dipolar gas can exhibit a local minimum, as shown in Fig. 5.2*(b)*. Following Landau [17], the quasi-particles related to the excitations close to the local minimum are called *rotons*. This particular excitation spectrum in a dBEC is therefore often referred to as the *roton-maxon excitation spectrum* [15]. Note that the rotons in superfluid helium, discussed by Landau, may be illustrated by the rotation of a ring of atoms [18]. This picture, however, does not hold in the dipolar 2D homogeneous system, even though the excitation spectra show a similar form.
To investigate the dipolar system more closely, let us consider the excitations again as

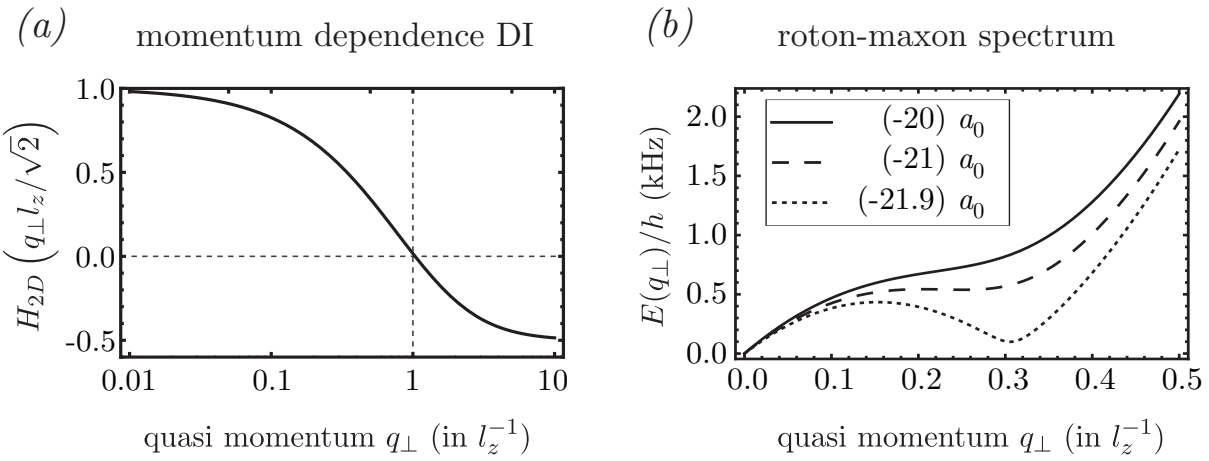

Fig. 5.2, Excitations in a 2D homogeneous dipolar BEC: *(a)* The function $H_{2D}\left(q_\perp l_z/\sqrt{2}\right)$, characterizing the momentum dependent dipolar interactions (DI): below $q_\perp \sim l_z^{-1}$, the DI is effectively repulsive, while above this momentum value the attraction dominates. *(b)* Excitation spectrum of the dipolar 2D homogeneous system for three different scattering lengths, specified in the inset. The spectra are calculated for chromium (mass / dipole strength) using the parameters $\{\omega_z = 2\pi \cdot 30\,\mathrm{kHz}, n_0 = 10^{15}\mathrm{cm}^{-3}\}$.

wavepackets. Their size in the z-direction is given by the width l_z of the condensate, which depends mainly on the external confinement. In the radial directions, the extension of the wavepackets is given by their wavelength, which is inversely proportional to the quasi-momentum $q_\perp$. At small momenta $q_\perp \ll l_z^{-1}$, the wavepackets are therefore highly anisotropic, with the dipoles mainly aligned side-by-side. As the dipoles effectively repel each other in this configuration, they stabilize the system giving a positive contribution to the excitation spectrum. In the extreme case $q_\perp l_z \to 0$, the dipoles can stabilize the sample even for negative scattering lengths as long as $g \gtrsim -2g_{\mathrm{dd}}$ (see Eq. (5.2)). For increasing momenta $q_\perp$, the radial size of the wavepackets decreases. When their overall shape is spherically symmetric, i.e. for $q_\perp \approx l_z^{-1}$, the dipolar contribution to the excitation energy vanishes. This behaviour is directly related to the vanishing dipolar interaction energy in a spherically symmetric BEC, shown in section 2.4.3. Eventually, in the limit of large momenta ($q_\perp \gg l_z^{-1}$), the effective dipolar interaction becomes attractive since the density wavepackets are cigar-shaped, with the dipoles aligned mainly in the head-to-tail configuration. The momentum dependence of the excitation spectrum, given by Eq. (5.2), is therefore induced by the anisotropy of the long-range dipolar interactions[78].

Roton instability

To discuss the phenomenon of the roton and the related instability, we first consider very

[78] A roton-type excitation spectrum is also predicted for BECs with isotropic non-local interactions [191, 192]. Here, the momentum of the rotons is related to the characteristic range of the interactions.

strong trapping in the z-direction. The system is then well inside the quasi-2D regime (see section 4.3.2), with its transverse size l_z given by the harmonic oscillator length. It is shown in Ref. [16] that in such geometry the dipoles do not reach sufficiently strong attraction to produce a roton minimum in the excitation spectrum of a purely dipolar system. However, including attractive contact interactions, the excitation spectrum may show the roton-maxon form in a small interval of negative scattering lengths, as illustrated in Fig. 5.2*(b)*. At even more negative scattering lengths, excitation frequencies close to the *characteristic roton momentum* q_{rot} become imaginary which indicates a *roton instability*. Since $q_{\mathrm{rot}} < l_z^{-1}$ in the quasi-2D regime, the effective dipolar interactions for this momentum value are repulsive[79], as discussed before. Thus, we deduce that the roton instability is driven by the attractive contact interactions in the quasi-2D regime.
The roton instability is qualitatively different, when considering only moderate trapping along z such that we obtain a chemical potential $\mu \sim \hbar\omega_z$. Then, the system is just at the threshold between the quasi-2D regime and the 3D regime. The width of the condensate l_z can now be found for example by variational calculations (see section 5.2). On the quasi-2D side, a purely dipolar system will always be stable, as explained above. In contrast, when crossing the threshold to the 3D regime, the effective DI can become attractive and may drive the system into the roton instability at a momentum $q_{\mathrm{rot}} > l_z^{-1}$. This mechanism even holds in presence of weak repulsive contact interactions, with the s-wave scattering length in the range $0 < a < a_{\mathrm{dd}}$.

The results obtained in the 2D homogeneous system are also relevant for trapped dipolar condensates. For example, in a numerical study [193], a roton-like dispersion of the excitations was found in an oblate dipolar BEC. Interestingly, a stable trapped condensate with a static density modulation can exist, the distance between the density maxima being related to the characteristic roton momentum q_{rot} [20, 21]. When driving a stable dBEC into the roton instability, the system is expected to decay into a multi-peak structure [37], in close analogy with the Rosensweig instability of surface waves in classical ferrofluid systems [66], illustrated in Fig. 5.3.

5.2 Stability of a Single Trapped dBEC

We now discuss the stability of a single trapped dipolar BEC. In this system, we develop an intuitive picture for the role of the dipolar interactions which can be either destabilizing or stabilizing, depending on the geometry of the external trapping potential. The discussion and the following calculation of the stability threshold of the single dBEC serves as a basis to understand the more complex case of the dBEC in the 1D optical lattice potential, which we investigate in section 5.3.

[79] The value $H_{2D}\left(q_{\mathrm{rot}} l_z/\sqrt{2}\right)$ is positive for values $q_{\mathrm{rot}} l_z < 1$, leading to a positive contribution of the dipoles to the excitation energy $E(q_{\mathrm{rot}})$.

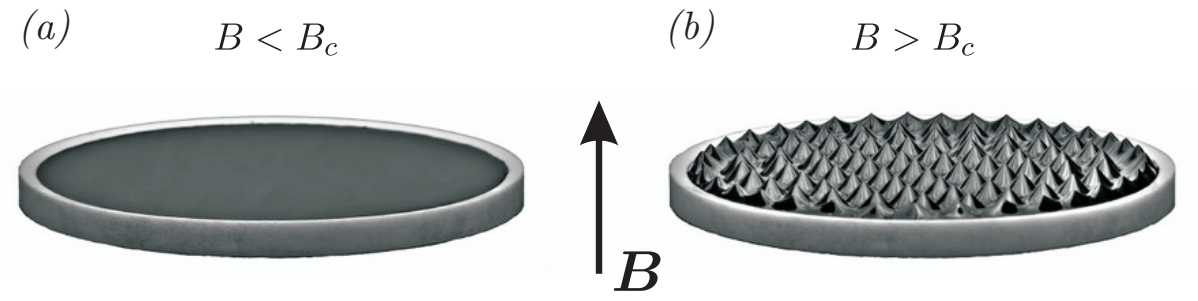

Fig. 5.3, Rosensweig instability in a classical ferrofluid: *(a)* A fluid consisting of ferromagnetic particles (ferrofluid) in a Petri dish develops a flat surface in earth's gravitational field. No change is observed, when raising a homogeneous external magnetic field $\boldsymbol{B}$, oriented perpendicular to the surface, to a strength smaller than the critical value B_c. *(b)* At the threshold $B = B_c$, the flat surface becomes unstable and develops a regular pattern of surface spikes, typically in a hexagonal order [66]. Images taken from [194].

Let us consider a dipolar atomic cloud in a harmonic trap with a cylindrical symmetry along the polarization direction of the dipoles, as illustrated in Fig. 5.4. If the cloud is elongated in the polarization direction (i.e. in a prolate trap), the dipoles are mainly attracting each other. The energy contribution of the dipolar interaction to the total energy of the system is negative in this configuration. Hence, the DI has a *destabilizing character* and a stable condensate can only be obtained at sufficiently strong repulsive contact interactions. In contrast, in an oblate cloud, the dipoles sit mainly side-by side. The resulting repulsive DI leads to a *dipolar stabilization* of the atomic sample. Now, the system can even be stable for attractive contact interactions. This simple geometrical argumentation is recovered by calculations and provides an intuitive picture of the system.

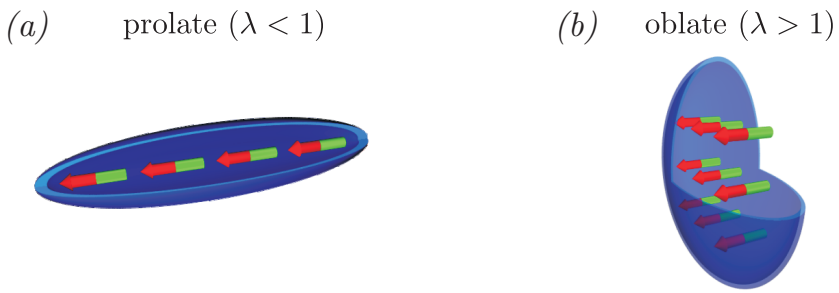

Fig. 5.4, A dBEC in different trapping geometries: *(a)* In a prolate trap with trap ratio $\lambda < 1$, the dipoles sit mainly in the attractive head-to-tail configuration. *(b)* An oblate trap ($\lambda > 1$) provides a more stable configuration of the dBEC, with the dipoles sitting mainly side-by-side.

Measurements

The geometry dependent stability of a single trapped dipolar BEC has been experimentally investigated in our group [35]. In the experiment, a cylindrically symmetric trap is used, with the symmetry axis oriented along the polarization direction z of the dipoles. The trap geometry is then conveniently described by the *trap ratio* $\lambda = \omega_z/\omega_\rho$, with ω_z and ω_ρ the trap frequency in the z-direction and in the radial directions, respectively. Figure 5.5*(a)* shows the measured stability diagram: the stable and the unstable regions for the dBEC are separated by the critical scattering length $a_{\rm crit}$, measured as a function of the trap ratio λ. We see that the stability of the dipolar BEC crucially depends on the trap ratio, since the external trapping potential mainly defines the shape of the condensate. Using a prolate trap ($\lambda < 1$), the condensate is experimentally found to be unstable at a positive critical scattering length $a_{\rm crit} = (15 \pm 3)\, a_0 \simeq a_{\rm dd}$. Then, for increasing trap ratios, the critical scattering length decreases. For the most oblate trap geometry in the experiment, with $\lambda = 10$, a *purely dipolar BEC* with $a_{\rm crit} \simeq 0$ is obtained. The measurements basically reproduce the expected results from our simple geometrical picture. However, the expected regime of the dipolar stabilization has not been reached.

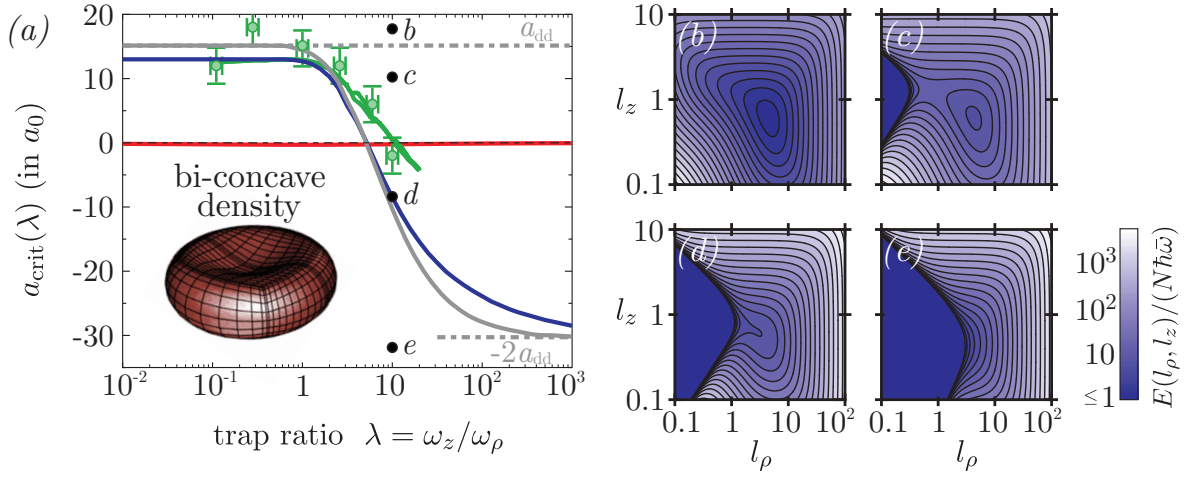

Fig. 5.5, Stability diagram of a single trapped dipolar BEC: *(a)* Experimental values (green dots) for the critical scattering length $a_{\rm crit}$ as a function of the trap ratio λ. The blue line shows the results for $a_{\rm crit}(\lambda)$ obtained from variational calculations for a mean trap frequency $\bar{\omega} = 2\pi \cdot 700\,\text{Hz}$ and $N = 20,000$ atoms. The grey line is obtained in the limit $N \to \infty$ and the red line marks the stability threshold for a purely contact interacting BEC using the same parameters. Full numerical simulations of the GPE [37] (green line) reveal a bi-concave BEC-density close to $a_{\rm crit}$ for oblate traps. *(b)-(e)* Energy landscape $E(l_\rho, l_z)$ in the variational calculations. Lines of equal energy are plotted for $\lambda = 10$ and $a = (18, 10, -8.5, -32)\, a_0$ as indicated by the black dots in *(a)*. The widths (l_ρ, l_z) are given in units of the mean harmonic oscillator length $\bar{a}_{\rm ho} = \sqrt{\hbar/(m\bar{\omega})}$. Figure taken from [113].

Calculation of the critical scattering length

The stability threshold of the dipolar condensate can be computed for a given set of trap parameters. The general procedure is to solve the Gross-Pitaevskii equation (2.15a), searching for the critical scattering length below which there exists no physical solution anymore. In the limit of infinite atom number, the GPE can be solved exactly in the Thomas-Fermi (TF) approximation [110] (see section 2.4.3). Alternatively, in the more realistic case of a finite atom number, the critical scattering length can be obtained by searching a minimum in the energy of the system through variational calculations. Close to the stability threshold the atomic cloud is well described by a Gaussian wave function[80]. The Gross-Pitaevskii energy functional, given by Eq. (2.17), then only depends on the widths (l_ρ, l_z) of the cloud in the radial and in the axial directions (see appendix A.4). The resulting energy landscape $E(l_\rho, l_z)$ is shown in the Figs. 5.5*(b)-(e)* for a dBEC in a trap with $\lambda = 10$ for different scattering lengths. A stable condensate, indicated by a global minimum at positive energy, is found for scattering lengths above $a_{\rm dd}$ (see Fig. 5.5*(b)*). For $a \lesssim a_{\rm dd}$, the global energy minimum transforms into a local minimum, presenting a *meta-stable state* for the BEC[81]. Crossing the critical scattering length, the local energy minimum vanishes and the system is expected to be unstable. Note that in the limit of infinite atom number, the variational calculations recover the result $a_{\rm crit}(\lambda)$ obtained in the TF approximation [113, Ch.4.2].

The stability diagram, obtained by the variational calculations, can be divided into two parts: at positive critical scattering lengths, i.e. for trap ratios $\lambda < \lambda_0 \approx 5.2$, we identify the destabilizing character of the DI as discussed above. At larger trap ratios, we expect a dipolar stabilization of the gas, where the most negative critical scattering length $a_{\rm crit,min} = -2a_{\rm dd} \simeq -30\,a_0$ is obtained in the extreme limit of infinite atom number and for a trap ratio $\lambda \to \infty$. This is in strong contrast with the behaviour of a purely contact interacting BEC for which the stability threshold shows almost no dependency on the trap geometry. Here the calculations yield $|a_{\rm crit}| < 0.4\,a_0$ in the full range of trap ratios.

Instability mechanisms in the trapped dBEC

To investigate the mechanisms of the instability, we recall the discussion about the excitations in homogeneous systems from section 5.1. There, the long-wavelength excitations were associated with phonons as they show a linear dispersion. Considering a trapped condensate, the global size of the BEC (given by the width of the Gaussian in the variational calculations) corresponds to the longest possible wavelength of an excitation in the system. Therefore, the Gaussian variational calculations can only predict the stability threshold associated with the phonon instability. Looking at the stability diagram in Fig. 5.5*(a)*,

[80] The choice of the Gaussian shape of the wave function is based on the solution of the GPE for negligible and weak interactions, see section 2.4.1.

[81] The BEC is said to be meta-stable, since it could decay into unstable configurations that are separated by a barrier in the energy landscape. Practically, the condensate will be stable on experimental time scales, if no excitations are created e.g. by fast ramps of the scattering length or sudden changes in the trapping potential.

the variational calculations match the measured critical scattering length in the regime of prolate traps ($\lambda < 1$). Thus, the instability mechanism in this regime is identified with the phonon instability. At larger trap ratios, however, the variational calculations predict a more stable situation than it is observed in the experiment. Only the results of a full numerical solution of the GPE [37] closely recover the observed stability threshold, as shown also in Fig. 5.5*(a)*. In such type of calculations no assumption is made on the shape of the wave function. It is suggested in Ref. [37] that the difference in the critical scattering length, obtained from numerical and variational calculations, indicates an instability via roton-like modes. Indeed, the numerical simulations show a decay of the condensate into a three-peak structure after reducing the scattering length below the critical value at a trap ratio $\lambda = 8$ for instance. Furthermore, the numerical calculations yield a bi-concave density distribution for the condensate close to the stability threshold (see Fig. 5.5*(a)*). Such deformation of the atomic cloud corresponds to the structured ground-states already mentioned in section 5.1.2.

So far, no clear sign of the roton instability has been experimentally observed in a dipolar BEC. In addition, the exploration of the regime with a strong dipolar stabilization was hindered by the technical difficulty to further increase the trap ratio of the single trap[82]. This limitation can be overcome by using the experimental setup of the 1D optical lattice: here, large (on-site) trap ratios $\lambda > 100$ can be created in the limit of very deep lattices. In such highly oblate trapping geometry we would expect the system to be stable down to very negative critical scattering lengths, where a roton minimum is expected to occur in the excitation spectrum. However, the attractive interactions between dipoles that are located on *different* lattice sites may destabilize the condensate. The stability of the dipolar BEC in the lattice is therefore an open question which we have addressed experimentally, with the results presented in the next section.

5.3 Stability Diagram of a ^{52}Cr - BEC in a 1D Lattice

We now present our measurements of the stability of a ^{52}Cr BEC in a 1D optical lattice. We first give a detailed description of the measurement procedure and the data evaluation. Then, we present the stability diagram of the dipolar BEC in the 1D lattice, which displays the critical scattering length as a function of the lattice depth. We will see that our results are in good agreement with the stability threshold obtained from numerical calculations, performed in the group of Luis Santos in Hannover.

[82] Note the logarithmic scale of the horizontal axis (trap ratio λ) in the stability diagram shown in Fig. 5.5*(a)*. To considerably lower the critical scattering length, the trap ratio must be increased much above $\lambda = 10$, which was difficult in the experimental setup of Ref. [35].

5.3.1 Measurement procedure

Before describing the details of the experimental procedure, let us consider the principle of the stability measurement. We first have to find an observable that is suited to identify the critical scattering length. From the discussion of the stability of a single trapped condensate, we know that above the stability threshold a stable BEC exists, with its radii determined e.g. by variational calculations. When reaching the critical scattering length, the condensate will suddenly shrink and collapse [36], following the largest gradient in the energy landscape presented in Fig. 5.5*(d)*. With the contraction of the condensate comes a dramatic increase in density, which in turn leads to strongly enhanced losses of atoms [195]. Hence, the idea of the measurement is the following: we load the BEC into the lattice in the stable regime and then approach the critical scattering length while measuring the number of atoms in the BEC. If the ramp in scattering length is sufficiently slow, the system remains in the stable state until we reach the critical scattering length that is identified by a sudden drop in the BEC atom number [35].

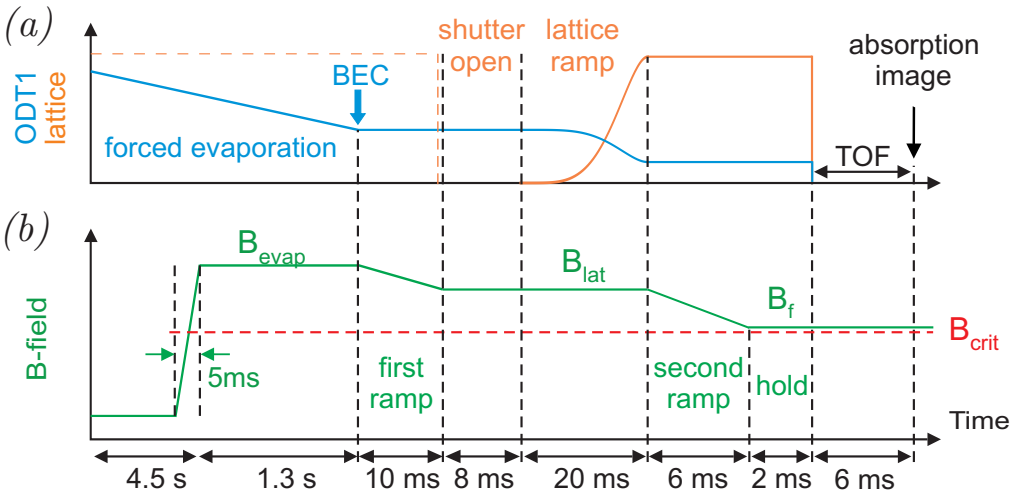

Fig. 5.6, Experimental sequence for stability measurements in the 1D lattice: *(a)* Time evolution of the power of the lattice laser beam (orange) and the horizontal beam of the optical dipole trap ("ODT1", blue). *(b)* Evolution of the magnetic field strength (green) defining the scattering length via the Feshbach resonance. The red dashed line illustrates the stability threshold, given by $a_{\mathrm{crit}} = a(B_{\mathrm{crit}})$.

To perform the stability measurements as described above, we have chosen the experimental sequence shown in Fig. 5.6. We show the time evolution of the most relevant parameters: the power in the lattice laser beam (defining the lattice depth), the power in the horizontal beam of the optical dipole trap ("ODT1", producing a confinement in the radial direction of the lattice), and the magnetic field strength which defines the scattering length close to the Feshbach resonance.
Once we have created a thermal cloud of atoms in the crossed ODT, we perform forced

evaporation by continuously lowering the power of the ODT laser beams[83]. Before reaching degeneracy, we switch on the strong magnetic field to a strength $B_{\mathrm{evap}} = 602\,\mathrm{G}$, well above the Feshbach resonance (FR) located at $B_0 = 589.1\,\mathrm{G}$. At the scattering length $a(B_{\mathrm{evap}}) = 90\,a_0$, we finish the evaporation and create the BEC in a trap with frequencies $\omega_{x,y,z} = 2\pi \cdot (440 \pm 14, 330 \pm 10, 290 \pm 10)\,\mathrm{Hz}$.
We then linearly decrease the magnetic field to $B = B_{\mathrm{lat}}$, to approach the FR with $a(B_{\mathrm{lat}}) = 60\,a_0$. As a next step, we load the BEC into the lattice by increasing the power of the lattice laser[84] in an s-shaped ramp to a variable value which defines the lattice depth U_{lat}. While doing so, the lattice introduces an additional transverse (radial) confinement. In order to keep the radial (x, y) trap frequencies constant during the ramp (and to avoid excitations in the BEC), we decrease the power in the ODT1 laser beam in an inverted s-shaped ramp[85].
In a second linear ramp of the magnetic field strength to the final value B_f, we then bring the system close to the stability threshold, defined by the critical scattering length $a_{\mathrm{crit}} = a(B_{\mathrm{crit}})$. We hold the condensate in this configuration for $t_{\mathrm{hold}} = 2\,\mathrm{ms}$, such that the system can equilibrate. After this holding time, we switch off all trapping potentials to perform a 6 ms time-of-flight and finally take an absorption image of the expanded cloud.

Loading of the BEC into the lattice

To probe the stability of the condensate in the lattice, we have to prepare the system in its ground-state, i.e. in the lowest energy band of the lattice. This implies that any excitation to higher bands has to be avoided during the loading of the lattice potential. We thus obtain a criterion for the speed of the lattice ramp [170]. In general, the adiabaticity criterion is given by [196] $\mathrm{d}U/\mathrm{d}t \ll (\Delta E)^2/\hbar$ with ΔE the spacing between the first and the second excited band and with $U(t)$ the time-dependent lattice depth during the ramp. At the center of the Brillouin zone, i.e. at quasi-momentum $q = 0$, the energy gap $\Delta E = 4\,E_{\mathrm{R}}$ is independent of the lattice depth, such that the adiabaticity criterion for the lattice ramp in our experimental sequence is given by

$$\frac{\mathrm{d}U}{\mathrm{d}t} \ll \frac{16\,E_{\mathrm{R}}^2}{\hbar}. \tag{5.3}$$

For our parameters (, the lattice must be ramped up much slower than $0.3\,E_{\mathrm{R}}/\mu\mathrm{s}$ to fulfill the criterion given by Eq. (5.3). Experimentally, we ramp up the lattice using an *s-shaped*

[83] During the sequence, we not only lower the power of the horizontal ODT beam, but we also decrease the light level of the vertical beam ("ODT2"). After reaching the BEC, the power in ODT2 is not changed anymore until it is switched off to perform the time-of-flight.

[84] The lattice laser beam is switched on during the production process of the BEC to heat the optical components in the beam path. During this time the beam is blocked by a shutter in front of the vacuum chamber. With this technique, we minimize the movement of the focus of the laser beam during the lattice ramp that is induced by thermal effects in the lenses.

[85] For our trap frequencies, and for the given parameters of the lattice laser beams (waists $w_{\mathrm{lat},1} = w_{\mathrm{lat},2} = 72\,\mu\mathrm{m}$), we can provide constant radial trap frequencies up to a lattice depth of around $200\,E_{\mathrm{R}}$. This is sufficient for all our experiments.

ramp of the form

$$U(\tilde{t}) = U_{\mathrm{lat}} \left[(k+1)\, \tilde{t}^{\,k} + k\, \tilde{t}^{\,k+1} \right], \tag{5.4}$$

with $\tilde{t} = t/T_{\mathrm{ramp}}$ the time in units of the ramp duration $T_{\mathrm{ramp}} = 20\,\mathrm{ms}$ and $k = 11$ the ramping parameter. The ramp, shown in Fig. 5.3*(a)*, is globally slow enough to ensure adiabaticity. In addition it is made slow at its beginning and at its end[86] to avoid any sloshing of the condensate in the trap. To experimentally test the adiabaticity of our loading proce-

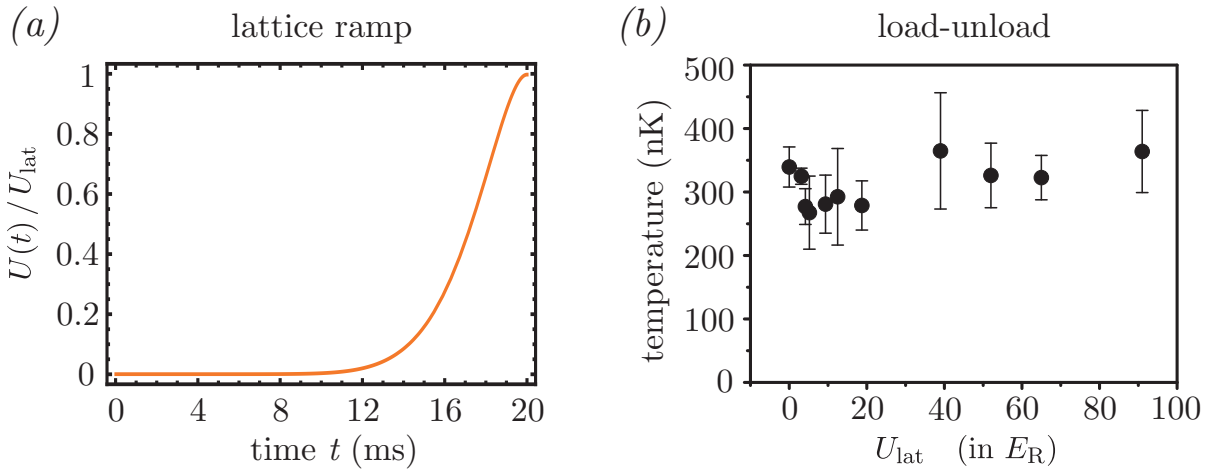

Fig. 5.7, Ramping of the lattice potential: *(a)* S-shaped lattice ramp, given by Eq. (5.4) with ramping time $T_{\mathrm{ramp}} = 20\,\mathrm{ms}$ and $k = 11$, as used in the stability measurements. *(b)* Temperature of the thermal cloud of a partly condensed system, after loading and unloading the condensate in a lattice of different depths U_{lat}. No measurable heating is observed, even for very deep lattices $U_{\mathrm{lat}} \sim 90\, E_{\mathrm{R}}$.

dure, we create a partly condensed system, such that we can measure the temperature of the remaining thermal cloud from its size after TOF [42]. We then load the condensate into the lattice and immediately unload it, using the same ramp inverted. Investigating lattice depths up to $90\, E_{\mathrm{R}}$ we cannot observe a significant heating of the sample, as we show in Fig. 5.7*(b)*. This indicates that we load the dBEC adiabatically into the lattice potential.

Evaluation of absorption images

After each experimental sequence we take an absorption image, i.e. we illuminate the atomic cloud with a resonant laser beam and record its shadow on a CCD camera [42]. With the imaging laser beam propagating along the x-direction, the recorded pattern is given by the three-dimensional density distribution integrated along the line-of-sight[87]. In

[86] The ramp of the lattice is slow at the beginning and at the end, since the derivative $\mathrm{d}U(\tilde{t})/\mathrm{d}\tilde{t}$ vanishes for both values $\tilde{t} = 0$ and $\tilde{t} = 1$ (see Eq. (5.4)).

[87] As the strong (Feshbach) magnetic field is aligned perpendicular to the imaging beam, we cannot provide the required σ^--polarization of the laser light to obtain the maximum absorption cross-section. We therefore use a superposition of σ^+ and σ^- polarized light and account for the reduced absorption as described in Ref. [168, Ch.4.4.2].

the images, taken after the expansion from the lattice, we observe the interference pattern of the condensate and, in addition, a thermal cloud in the background (see Fig. 5.8*(a)*). To extract the atom number in the condensate, we first integrate the recorded 2D

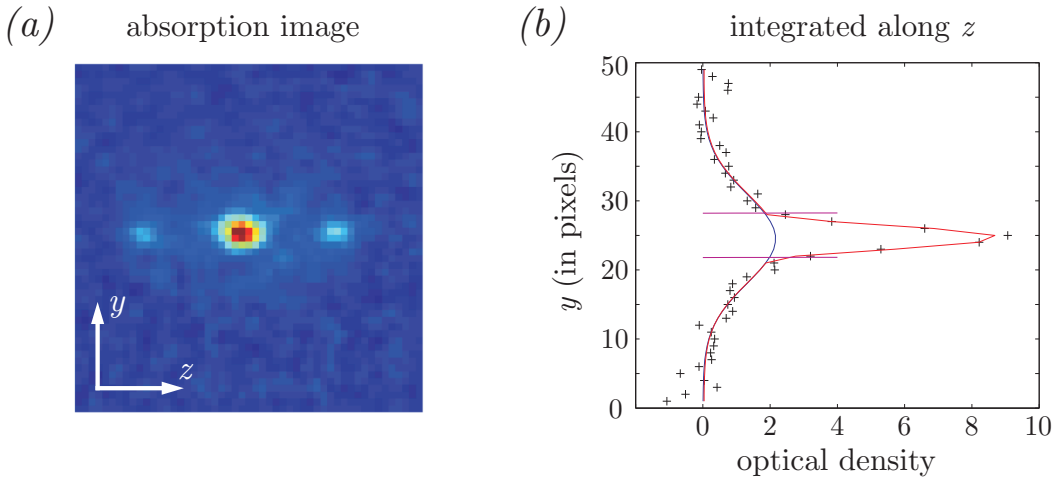

Fig. 5.8, Data acquisition and evaluation: *(a)* 2D density distribution of the atomic cloud after time-of-flight, recorded by absorption imaging (lattice depth $U_{\mathrm{lat}} = 10\,E_{\mathrm{R}}$, final scattering length $a = 20\,a_0$). The field of view is $(50 \times 50)\,\mathrm{pixels}^2 = (307 \times 307)\,\mu\mathrm{m}^2$. Red (blue) colors indicate high (low) density. *(b)* Density profile in the y-direction (black crosses) obtained by integrating the 2D density distribution along z. We extract the BEC atom number from a bi-modal fit (red line). Before performing the full fit, we fit the thermal cloud (blue line) to the wings of the density profile, i.e. we disregard the region between the magenta horizontal bars.

density distribution along the z-direction. Then, we perform a one-dimensional bi-modal fit, accounting for the presence of the condensate and the thermal cloud as shown in Fig. 5.8*(b)*. The 1D fitting function for the BEC is obtained by integrating the 3D density of a single condensate (see Eq. (2.22)) over the x- and y-direction with the result [197]

$$n_{\mathrm{BEC},1D}(y,t) = \frac{15\,N_{\mathrm{BEC}}}{16\,R_y(t)}\,\max\left[1 - \frac{y^2}{R_y^2(t)}, 0\right]^2 . \tag{5.5}$$

where N_{BEC} is the atom number in the condensate and $R_y(t)$ is the radius of the BEC after an expansion of time t. The thermal cloud has the following Gaussian shape,

$$n_{\mathrm{th},1D}(y,t) = \frac{N_{\mathrm{th}}}{\sqrt{2\pi}\,l_y(t,T)}\,\exp\left[-\frac{y^2}{2l_y^2(t,T)}\right], \tag{5.6}$$

with N_{th} the number of thermal atoms and $l_y(t,T)$ the width of the thermal cloud, determined by the expansion time t and the temperature T of the sample. We briefly explain the fitting procedure in Fig. 5.8 while more technical details are given in Ref. [122, Ch. A.2.]. By using the 1D fitting method, we obtain a reliable evaluation of the BEC

atom number N_{BEC} even when we load the condensate into very deep lattices: here, the absorption images show complicated multi-peak patterns in the z-direction, as shown in section 4.4.2. This effect arises due to the dephasing of the on-site condensates and their subsequent interference during the TOF.

5.3.2 Stability Diagram in the 1D Lattice

We perform the stability measurements, as described in the previous section, for different lattice depths in the range from $U_{\mathrm{lat}} = 0\,E_{\mathrm{R}}$ to $63\,E_{\mathrm{R}}$, loading typically around 15 sites of the lattice potential[88]. For each lattice depth, we measure the number of atoms in the condensate as a function of the scattering length at which we finally hold the system. We show two of such datasets in Fig. 5.9, one for a dBEC loaded into a lattice of depth $U_{\mathrm{lat}} = (6.2 \pm 0.6)\,E_{\mathrm{R}}$ and the other with the condensate in a very deep lattice with $U_{\mathrm{lat}} = (37 \pm 4)\,E_{\mathrm{R}}$. When reducing the final scattering length, we observe that the BEC atom number decreases slowly until it abruptly falls down to zero. We identify this drop with fact that the stability threshold has been reached. While for $U_{\mathrm{lat}} = 6.2\,E_{\mathrm{R}}$ the condensate becomes unstable at positive scattering lengths, we observe a stable dBEC even at negative scattering lengths in the case of the very deep lattice. Thus, the data shown in Fig. 5.9 already indicates a dipolar stabilization in the deep lattice regime.

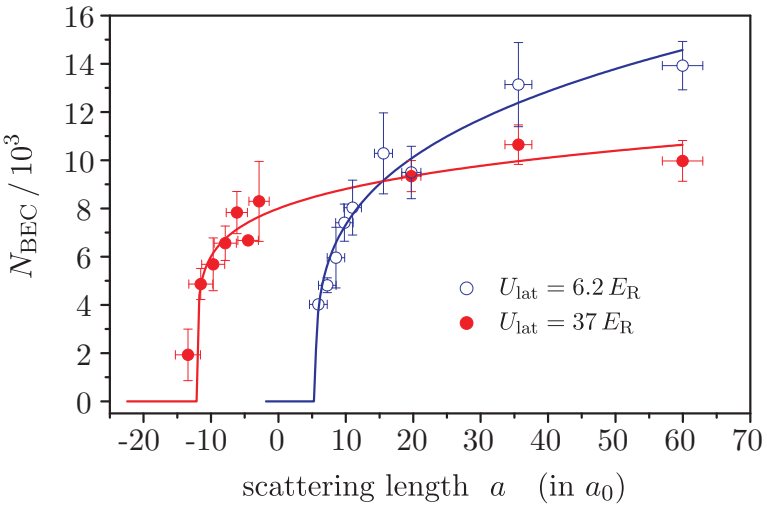

Fig. 5.9, Stability measurements: Atom numbers in the BEC N_{BEC} as a function of the final scattering length a for $U_{\mathrm{lat}} = (6.2 \pm 0.6)\,E_{\mathrm{R}}$ (open blue dots) and $U_{\mathrm{lat}} = (37 \pm 4)\,E_{\mathrm{R}}$ (filled red dots). The lines correspond to a fit of the experimental data by an empirically chosen function, from which is extracted the critical scattering length (see text for details).

[88] The exact atom number distribution, i.e. the number of populated lattice sites N_{lat}, depends in general on the lattice depth, as given by Eq. (4.20). The value given here corresponds to a lattice depth $U_{\mathrm{lat}} = 15\,E_{\mathrm{R}}$.

To extract the critical scattering length a_{crit} from the measurements, we perform a fit with the empirically chosen function

$$N_{\mathrm{BEC}}(a) = \max\left[N_0\,(a - a_{\mathrm{crit}})^{\beta}\,, 0\right], \tag{5.7}$$

where N_0, a_{crit} and the exponent β are the fitting parameters [35]. The function $N_{\mathrm{BEC}}(a)$ accounts for the observed decrease of the BEC atom number when approaching the critical scattering length. Note, however, that there is no physical background of the chosen functional form.

By evaluating datasets taken for different lattice depths, we obtain the *stability diagram* of the dipolar BEC in the 1D optical lattice, shown in Fig. 5.10. It displays the measured critical scattering length a_{crit} as a function of the lattice depth U_{lat}. We measure $a_{\mathrm{crit}} = (12 \pm 2)\,a_0$ when the dBEC is only confined by the ODT, i.e. for $U_{\mathrm{lat}} = 0$. For increasing lattice depths, we observe a decrease of the critical scattering length, passing from positive to negative values for $U_{\mathrm{lat}} \sim 10\,E_{\mathrm{R}}$. Finally, in the case of very deep lattices, the system proves to be stable down to $a_{\mathrm{crit}} = (-17 \pm 3)\,a_0$.

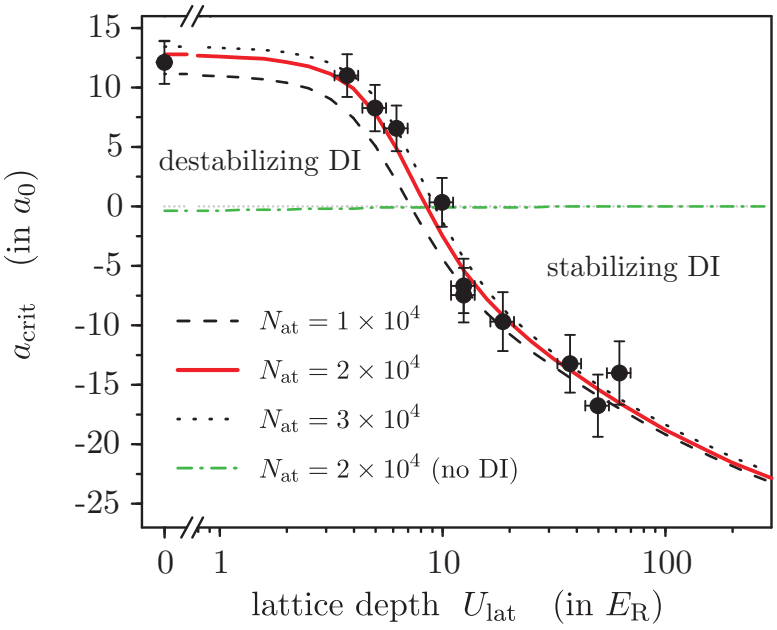

Fig. 5.10, Stability diagram of the dBEC in the 1D optical lattice: Measured critical scattering length a_{crit} (black dots) as a function of the lattice depth U_{lat}. Red and black lines are the results from numerical calculations for different BEC atom numbers with chromium parameters. The green line shows the stability threshold with the dipolar interactions (DI) neglected, but same parameters otherwise. Positive critical scattering lengths are associated with destabilizing dipolar interactions, while negative values of a_{crit} indicate stabilizing DI.

In the following we discuss the mechanisms that define the stability of the dBEC in the 1D lattice. To do so we divide the stability diagram into three regimes:

(i) For shallow lattices with $U_{\text{lat}} \lesssim 3\,E_{\text{R}}$, the lattice has no significant effect on the stability of the system. Hence, the relevant trap aspect ratios are given by the trap frequencies of the underlying harmonic trap, $\lambda_x \overset{\text{def}}{=} \omega_z/\omega_x \simeq 0.66$ and $\lambda_y \overset{\text{def}}{=} \omega_z/\omega_y \simeq 0.88$, which are both smaller than unity. Therefore, from our considerations of the single trapped dBEC in section 5.2, we would expect the system to become unstable close to the value $a = a_{\text{dd}} \simeq 15\,a_0$ [35]. Measuring $a_{\text{crit}}(U_{\text{lat}} = 0) = (12 \pm 2)\,a_0$ and $a_{\text{crit}}(U_{\text{lat}} = 3.7E_{\text{R}}) = (11 \pm 2)\,a_0$, we almost recover the expected stability threshold.

(ii) Then, the region $3\,E_{\text{R}} \leq U_{\text{lat}} \leq 15\,E_{\text{R}}$ represents the transition from shallow to deep lattices. In this regime, the stability of the system is determined by the non-trivial interplay between the contact and the dipolar interactions, and the tunneling between the lattice sites. For large tunneling rates, it is the overall prolate shape of the condensate which mainly defines the stability threshold. This results in a positive critical scattering length, as explained above. In deeper lattices, however, it is mainly the very oblate on-site geometry which is relevant for the stability of the system: when the tunneling is suppressed on experimental time scales (for $U_{\text{lat}} \sim 15\,E_{\text{R}}$), we observe a negative critical scattering length as we would expect for a single oblate dBEC.

(iii) For very deep lattices ($U_{\text{lat}} > 15\,E_{\text{R}}$) the critical scattering length decreases further to very negative values. This can be explained by the increasing mean on-site trap ratio $\bar{\lambda}_{\text{on-site}} \overset{\text{def}}{=} \omega_{\text{lat}}/\sqrt{\omega_x\omega_y}$: for a lattice depth $U_{\text{lat}} = 15\,E_{\text{R}}$ we obtain $\bar{\lambda}_{\text{on-site}} \sim 70$, while the largest lattice depth $U_{\text{lat}} = 63\,E_{\text{R}}$ yields $\bar{\lambda}_{\text{on-site}} \sim 140$. We will come back in details on this regime in section 5.4. There, we study the inter-site effects due to the long-range dipolar interactions, which have a considerable influence on the stability of the system.

Comparison with numerical calculations

Our experimental results are in excellent agreement with numerical mean-field calculations, taking into account the combined trapping potential created by the ODT and the lattice. On the one side, this confirms that our experimental results correspond to the stability threshold of a dBEC in the ground-state of the lattice potential. On the other side, it also shows that numerical mean-field calculations can predict the stability threshold of a dBEC in such a complex trapping geometry.

In the calculations, the critical scattering length is obtained by integrating the time-dependent Gross-Pitaevskii equation (given by Eq. (2.14)) in imaginary time on a three-dimensional numerical grid, and looking for a stable ground-state. The calculations reveal

a weak dependence of the stability threshold on the BEC atom number[89], as shown in Fig. 5.10. For lattice depths $U_{\mathrm{lat}} > 15E_{\mathrm{R}}$ the variation of a_{crit} with the BEC atom number is very small and well below our experimental uncertainties. Dealing with very deep lattices we note that, in absence of tunneling, the system cannot evolve into its global ground-state: when loading the dBEC in lattices with $U_{\mathrm{lat}} \gtrsim 15\,E_{\mathrm{R}}$, the atom number distribution does not follow the equilibrium distribution derived in section 4.3.2. However, real-time simulations of the experimental sequence show that the small deviation from the "true" ground-state of the system has almost no influence on the stability threshold.

The calculations offer furthermore the possibility to compare the stability of the chromium BEC to a purely contact interacting BEC with chromium parameters otherwise. We are thus able to test whether it is the dipolar interactions that stabilize the BEC in the deep lattice regime or if the quantum pressure stabilizes the system as it was shown for samples of small atom numbers [3, 198]. For our trapping parameters, the calculated stability threshold of a BEC without dipolar interactions varies only in a very small interval $|a_{\mathrm{crit}}| < 0.4\,a_0$ in the full range of lattice depths. Thus, we deduce that our dBEC is mainly stabilized by the dipolar interactions, with a negligible influence of the quantum pressure. In other words, we have shown for the first time that a BEC with attractive contact interactions can be stabilized in an interaction-dominated regime. One further asset in our system is the interaction between the lattice sites: even when the tunneling is suppressed on experimental time scales, the spatially separated samples can interact via the long-range dipolar interactions. We therefore investigate next the role played by the dipolar *inter-site interactions* which, indeed, are non-negligible in our system.

5.4 Effects of Inter-site Interactions on the Stability of a dBEC

We now study the influence of the dipolar inter-site interactions on the stability of the lattice system. We therefore look closely to the regime of very deep lattices. Only here we can make a separation between the on-site interactions and the inter-site interactions, as the tunneling is negligible on experimental time scales. We first analyse by which amount the dipolar inter-site interactions shift the stability threshold. For this task we use both numerical and variational calculations and compare their results to the experimentally measured critical scattering length. Finally, we discuss in more detail the inter-site coupling in the context of the elementary roton-type excitations.

[89] Note, that we distinguish between the atom number N_{at} used in the calculations, and the BEC atom number N_{BEC} measured after time-of-flight in the experiment. The value N_{at} should be compared to the experimental atom number prior to the holding time at the final scattering length, which is about $20,000$ for $U_{\mathrm{lat}} \lesssim 10\,E_{\mathrm{R}}$ and about $15,000$ in deeper lattices.

5.4.1 Analysis of Inter-site Effects in the Lattice

In our experiment, both on-site and inter-site interactions are always present and cannot be "switched off" selectively to test their relative influence on the stability of the system. However, the effect of the inter-site interactions can be revealed by the numerical calculations (described in the previous section) by introducing a truncated dipolar interaction potential $V_{\rm dd}^{\rm box}(\boldsymbol{r}) = V_{\rm dd}(\boldsymbol{r})\,[\Theta((\boldsymbol{r}\cdot\hat{\boldsymbol{z}}) + d_{\rm lat}/2) - \Theta((\boldsymbol{r}\cdot\hat{\boldsymbol{z}}) - d_{\rm lat}/2)]$, where $\Theta(\xi)$ is the Heaviside function. Such cutoff of the dipolar interactions in the lattice direction z effectively amounts to removing the inter-site interactions, still taking into account the full short-range and the long-range on-site interactions.
In Fig. 5.11, we compare the measured stability threshold to the calculations with $V_{\rm dd}^{\rm box}(\boldsymbol{r})$ and with the full dipolar potential $V_{\rm dd}(\boldsymbol{r})$. The calculations with the full dipolar potential agree well the experimental data. In contrast, the calculations with the inter-site interactions removed predict a substantially lower stability threshold: for the lattice depth $U_{\rm lat} \simeq 20\,E_{\rm R}$, the difference compared to the datapoints is $\Delta a_{\rm crit} \simeq 8\,a_0$, which is about three times our experimental uncertainty. Hence, we identify a *destabilizing character* of the dipolar inter-site interactions. Note that in both cases (with and without inter-site interactions) the stability threshold in the calculations approaches the fundamental limit $-2a_{\rm dd} \simeq -30\,a_0$ for very large lattice depths. In this regime, the spatially separated condensates behave like infinitely extended discs that do not interact, as we have shown in section 2.5.1.

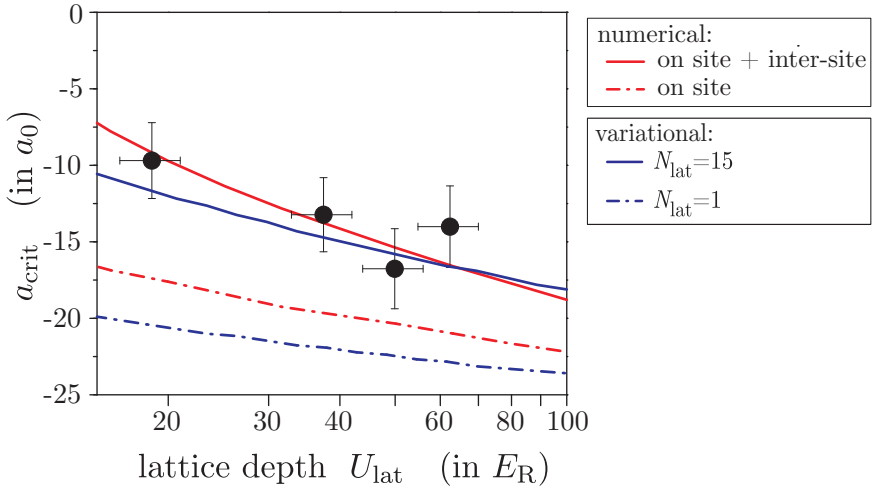

Fig. 5.11, Destabilization of the dBEC by inter-site interactions: Zoom into the stability diagram in the deep lattice regime $U_{\rm lat} > 15\,E_{\rm R}$. Black dots show the experimental values for the critical scattering length. Red lines show the results of numerical calculations with the inter-site interactions included (solid red line) or excluded (dashed-dotted red line). Similar results are obtained by variational calculations with $N_j = 2000$ atoms per lattice site. Here, the inter-site interactions are included in a calculation with $N_{\rm lat} = 15$ lattice sites (solid blue line) and excluded by using $N_{\rm lat} = 1$ (dashed-dotted blue line).

In a second approach, we analyse the inter-site effects by performing variational calculations with a Gaussian ansatz for the on-site wave functions. For an efficient calculation, all these wave functions are assumed to be the same and radially symmetric. We define the on-site trap geometry by the radial trap frequency $\omega_\rho = \sqrt{\omega_x \omega_y} = 2\pi \cdot 380\,\mathrm{Hz}$ and the axial trap frequency given by the dimensionless lattice depth s via $\omega_{\mathrm{lat}} = 2\sqrt{s}\, E_{\mathrm{R}}/\hbar$. To find the stability threshold, we minimize the total energy of the system, which is composed by the total on-site energy[90] and the total inter-site energy, given by Eq. (2.35). We calculate the stability threshold *including* the inter-site interactions, by considering a system of $N_{\mathrm{lat}} = 15$ lattice sites with a constant filling of $N_i = 2000$ atoms per site. Despite the simplified model, we closely recover the measured critical scattering length, as shown in Fig. 5.11. Similarly to the numerical results, a calculation with the inter-site interactions removed, i.e. using $N_{\mathrm{lat}} = 1$, predicts a more stable system.

Note that the Gaussian variational calculations can only predict the phonon instability threshold of the system, referring to the discussion in section 5.2. The good agreement of the calculations with the experimental results indicates that, indeed, the system becomes unstable by the long-wavelength phonon-like modes. However, due to the highly oblate on-site trapping geometry, we would expect that the system undergoes a roton instability instead (see section 5.1.2). This contradiction can be resolved by considering the inter-site coupling of the elementary excitations, that we discuss in the next section.

5.4.2 Inter-site Coupling of Excitations

We have seen that the dipolar inter-site interactions in our 1D lattice configuration play a significant role for the stability of the system. Now we show that this effect is closely connected with an inter-site coupling of the elementary excitations that we have introduced in section 5.1. Therefore, we discuss the influence of the inter-site coupling on the excitation spectrum of a multi-site system with 2D homogeneous dipolar samples [26, 27]. Then, we apply the results to the case of a trapped dipolar BEC in a 1D optical lattice [28, 29].

Let us first consider the simple case of two layers of a 2D homogeneous gas with the dipoles aligned out of the plane, as before. The excitations of the system are again described by local density perturbations. If a local density maximum spontaneously forms on one of the sites, the dipoles on the other site will also form a maximum at the same spot, due to the attraction of the dipoles. By such dipolar coupling mechanism, the excitation is shared between the two lattice sites.

In a multi-site system, the excitations might even extend over several lattice sites. Calculating the excitation spectrum of a system of N_{lat} coupled 2D homogenous samples yields a band-like spectrum with a set of N_{lat} excitation modes [26, 27]. In Fig. 5.12*(a)*, we

[90] To obtain total on-site energy, we calculate the energy of a single dipolar BEC trapped on one site of the lattice potential (see appendix A.4) and multiply by the number of populated lattice sites N_{lat}.

show the energy spectrum of the collective excitations for $N_{\mathrm{lat}} = 15$ dipolar condensates, using parameters close to the experimental ones. The lowest lying mode of the band-

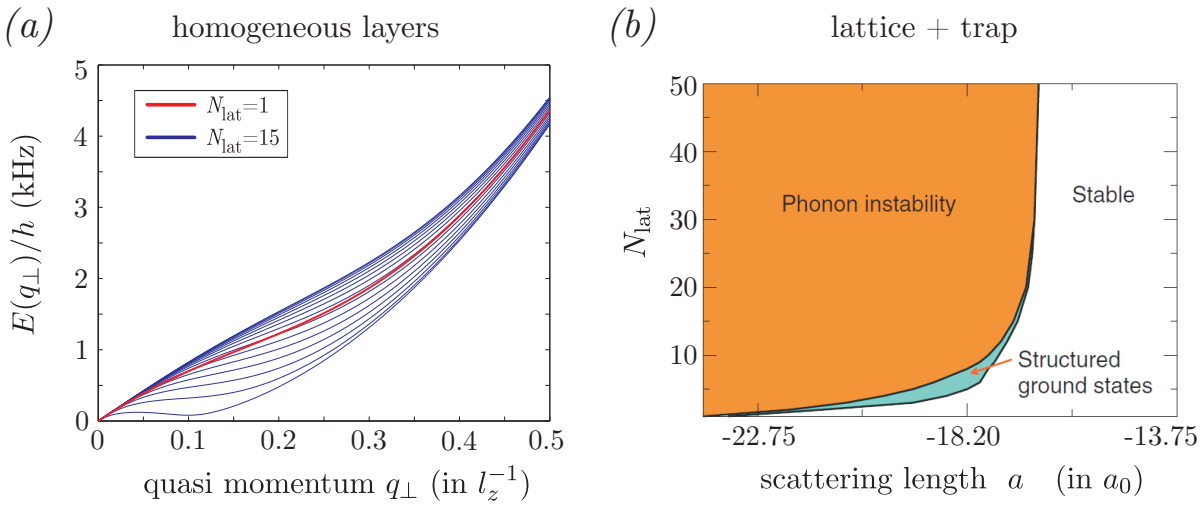

Fig. 5.12, Inter-site coupling in homogeneous and trapped dBECs: *(a)* Band-like excitation spectrum in a system of $N_{\mathrm{lat}} = 15$ coupled 2D homogeneous chromium BECs (blue lines). The red line shows a single site spectrum with same parameters: trap frequency $\omega_{\mathrm{lat}} = 2\pi \cdot 42\,\mathrm{kHz}$, scattering length $a = -17\,a_0$, density $n = 10^{15}\mathrm{cm}^{-3}$, lattice spacing $d_{\mathrm{lat}} = 534\,\mathrm{nm}$. *(b)* Phonon instability threshold and regions with structured ground-states (obtained by numerical calculations), depending on the number of lattice sites N_{lat} and the scattering length a, taken from Ref. [28]. The calculations are performed with a Gaussian distribution of the atom numbers on the different lattice sites, with $N_0 = 3300$ atoms in the central site. Parameters: $\omega_{\mathrm{lat}} = 2\pi \cdot 48\,\mathrm{kHz}$, radial trap frequency $\omega_\rho = 2\pi \cdot 143\,\mathrm{Hz}$, $d_{\mathrm{lat}} = 560\,\mathrm{nm}$, and chromium parameters for mass and dipole strength.

like excitation spectrum is significantly softened, i.e. it is showing lower energies $E(q_\perp)$ compared to the spectrum of a single populated site. As a consequence, the lattice system is prone to develop a roton instability already at higher scattering lengths than a single-site system. In addition, we observe that the quasi-momentum q_{rot}, corresponding to the local minimum in the excitation spectrum, is found at smaller momentum values than in the single-site configuration. This means that the more lattice sites are populated, the longer is the wavelength of the excitations involved in the roton instability. Essentially, it is the *global* extension of the system in the lattice direction, which defines the wavelength of the most unstable roton mode.

Numerical calculations allow to translate the effect of the roton softening to a trapped multi-site system: for instance a bi-concave structure is expected to emerge in the on-site wave function of a dBEC in a 1D lattice, while a single-site system does not show such modulation for the same parameters [29]. Furthermore, it was found that such structured

states emerge mainly, if only few lattice sites[91] are populated [28], as shown in Fig. 5.12*(b)*. Loading many lattice sites, the roton instability may not be distinguished anymore from the long-wavelength phonon instability, as the characteristic roton wavelength exceeds the radial size of the system. This argument applies to our stability measurements presented in section 5.3, since we load around 15 lattice sites. The inter-site coupling of the excitations thus explains why the Gaussian variational calculations are able to reproduce the measured critical scattering length in the regime of very deep lattices.

Conclusion

In this chapter, we have presented the results of our experimental investigation of the stability of a dipolar Bose-Einstein condensate in a one-dimensional optical lattice. In contrast to the case of purely contact interacting systems, an optical lattice changes drastically the stability properties of a dipolar BEC. In particular in deep lattices, we have shown that a condensate can be stabilized even for negative s-wave scattering lengths by the repulsive *on-site* dipolar interactions. In this regime, we have furthermore identified a significant destabilization of the system by the dipolar *inter-site* interactions.
The determination of the stability threshold is fundamental for any further investigations of lattice gases with strong dipolar interactions. It sets the basis, for example, for our studies of the *instability dynamics* of a dBEC in the lattice, presented in the next chapter.

[91] The number of filled lattice sites that leads to a visible modulation of the ground-state, depends crucially on the lattice spacing d_{lat}. The calculations of Ref. [28] are performed with parameters close to our experimental ones, using $d_{\mathrm{lat}} = 560\,\mathrm{nm}$.

6 Collapse of a Dipolar BEC in a 1D Optical Lattice

The subject of this chapter is the collapse dynamics of the dBEC in the 1D optical lattice, i.e. its time evolution in the unstable regime after the stability threshold is crossed rapidly. Usually in such studies, the system is driven into instability by a change in the scattering length [9, 10, 36, 53]. Here, we use a new technique: we induce the collapse of an initially stable dBEC in the lattice by only reducing the lattice depth below the stability threshold, while keeping the interaction strength constant. Generally speaking, the collapse is induced by a deconfinement of the system. Choosing the lattice depth *above* the stability threshold, one would not expect any instability to occur. However, even in this case, a collapsed cloud is observed in the absorption images taken after time-of-flight. Since the system is stable in-trap, we identify a novel collapse scenario: a TOF-triggered collapse which we discuss in details in this chapter.
In the beginning of the chapter, we discuss briefly the collapse dynamics of a single dBEC, previously studied in our group [36, 53, 113]. Then, we present the measurements of the collapse dynamics of a dBEC in a 1D optical lattice of moderate lattice depth. The measurements are supported by real-time simulations of the collapse dynamics, again contributed by the group of Luis Santos, in a close collaboration with our experiment. Our results, both experimental and theoretical, are published in Ref. [76]. Finally, motivated by the search for a roton-type of collapse, we propose a method to perform collapse measurements in the regime of very deep lattices.

6.1 Interaction-Induced Collapse of a Single dBEC

In this first part of the chapter, we aim for a basic description of the collapse dynamics of a dBEC. Before discussing the case of a dipolar gas, let us first consider the collapse of a BEC with dominant contact interactions, as studied in samples of ^{85}Rb [10]. Such system is stable for repulsive inter-atomic interactions, while no stable configuration exists for dominant attraction between the atoms. Thus, the collapse of the system can be induced by switching the scattering length from a positive to a negative value and its subsequent collapse dynamics is described by a three-step process [199]:

(i) The condensate shrinks globally due to the attractive inter-particle interactions.

(ii) The collapse of the BEC occurs, which is a fast and irreversible process: very narrow density peaks form at the center of the condensate, leading to substantial atom losses via inelastic collisions.

(iii) The sample explodes by emitting atom bursts from the central region. Since the outer regions of the condensate are not involved in the collapse process, there typically exists a remnant BEC after the explosion.

Due to the isotropic nature of the contact interactions, there is no preferential direction for the atom bursts that are emitted from a purely contact interacting BEC after the collapse[92]. In contrast, the collapse dynamics of a dipolar BEC, even when confined in a spherically symmetric trap, shows highly anisotropic features, as we explain now by reviewing the experimental results obtained in our group [36].

In the collapse measurements in Ref. [36], a BEC of chromium atoms is prepared in an essentially round trap[93] with the scattering length controlled by an external magnetic field close to a Feshbach resonance. The sequence to induce the collapse (see Fig. 6.1*(a)*) is the following: starting in a stable configuration, the scattering length is rapidly reduced from an initial value $a_i = 30\,a_0$ to a final value $a_f = 5\,a_0$, thus crossing the stability threshold at $a_{\rm crit} = (15 \pm 3)\,a_0$ [35] (see section 5.2). Note that the "real" scattering length $a(t)$ has a delay with respect to the programmed value due to eddy currents in the metallic vacuum chamber, as explained in more detail in section 3.2.2. After the ramp, the dBEC is held in the trap for a variable time $t_{\rm hold}$ before the trap is switched off and an absorption image is taken after an 8 ms TOF.

The upper row of Fig. 6.1*(b)* shows the measured time evolution of the *remnant BEC*[94] for different holding times. The images are obtained by averaging typically five absorption pictures after removing the broad isotropic thermal cloud. We see that during the collapse dynamics a highly anisotropic feature develops: such feature is remarkably clear at $t_{\rm hold} = 0.5\,$ms where the density pattern exhibits an angular structure that reflects the *d*-wave symmetry of the dipole-dipole interaction potential. On the contrary, at $t_{\rm hold} = 0\,$ms, the system has not collapsed yet, but takes a very elongated shape along the external magnetic field. Indeed, in this case, the condensate is released from the trap before the scattering length $a(t)$ has reached the stability threshold.
Integrating over the optical density in the experimental images shown in Fig. 6.1*(b)* yields the BEC atom number $N_{\rm BEC}$ that is shown in Fig. 6.1*(c)* as a function of $t_{\rm hold}$. The initial BEC atom number is about $16,000$. One observes a fast decrease until $t_{\rm hold} \simeq 0.5\,$ms and an almost constant value $N_{\rm BEC} \simeq 6000$ at longer holding times. Even though the BEC atom number is measured *after* the TOF, its variation with the holding time gives a good estimate of the time scale of the collapse dynamics, as we will discuss in more detail in section 6.2. Hence, the time scale of the collapse dynamics in the single trap is around 0.5 ms that we will compare later to our measurements of the collapse in the lattice.

In addition to the measurements, the collapse of the single dBEC has been investigated theoretically by numerical real-time simulations[95] based on the time-dependent Gross-

[92]The directed "jets" that have been observed in Ref. [10] are actually created by the interference of matter-waves from two point-like sources of atom bursts in the elongated trap [199].

[93]With the trap frequencies $(\omega_x, \omega_y, \omega_z) = 2\pi \cdot (660, 400, 530)\,$Hz, the trap is not exactly spherically symmetric due to the crossed configuration of the ODT.

[94]To be consistent with the nomenclature in Ref. [36], we define the remnant BEC as the part of the atomic cloud obtained after removing the thermal cloud from the absorption images.

[95]The numerical simulations are performed in the group of M. Ueda in Tokyo.

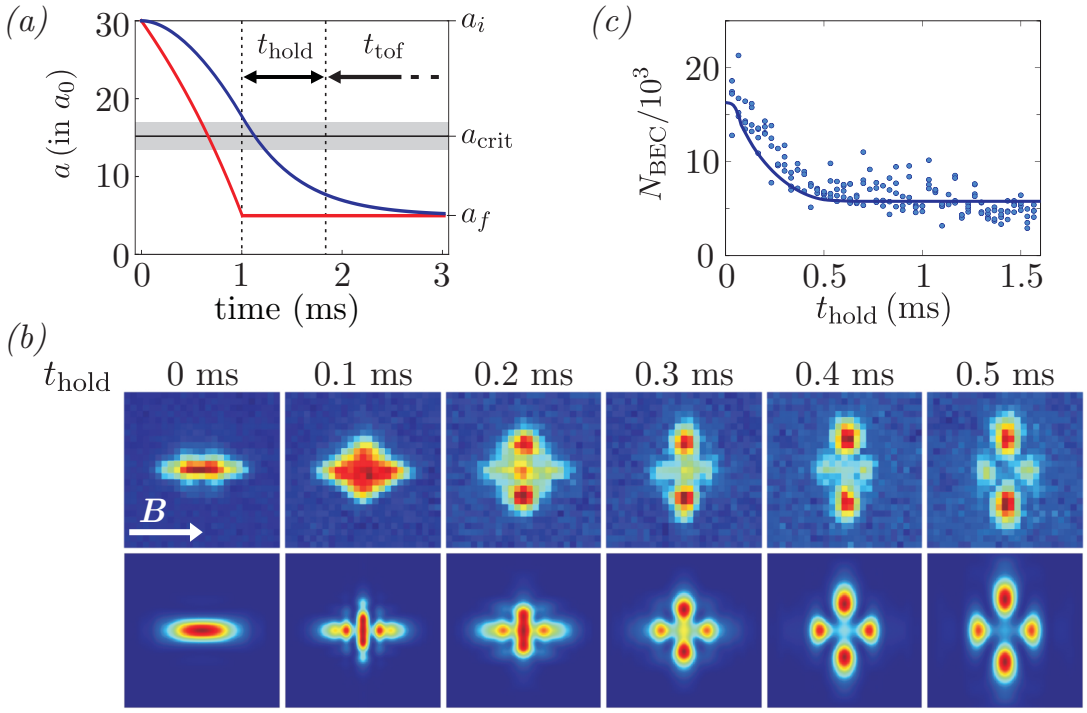

Fig. 6.1, Collapse dynamics of a dBEC in a single round trap: *(a)* Experimental sequence to induce the collapse. Both the programmed ramp (red line) of the scattering length $a(t)$ and the real ramp taking into account the eddy currents (blue line) are shown. The stability threshold is $a_{\rm crit} = (15 \pm 3)a_0$ [35], the uncertainty being illustrated by the grey zone. *(b)* Time evolution of the remnant BEC for different values of $t_{\rm hold}$: the upper row corresponds to experimental images taken after TOF and the lower row shows the results of numerical simulations. *(c)* Evolution of the atom number in the remnant BEC after TOF as a function of $t_{\rm hold}$, extracted from the measurements (dots) and from the simulations (line). All figures are taken from Ref. [36].

Pitaevskii equation. A crucial point in the simulations is to include the three-body atom losses that occur during the collapse dynamics. Else, the condensate only contracts to a single point of the numerical grid and no collapse dynamics can be observed. With the empirically chosen three-body loss rate[96] $L_3 = 2 \cdot 10^{-40}\mathrm{m}^6/\mathrm{s}$, the simulations reproduce both the d-wave density pattern after TOF (see the lower row in Fig. 6.1*(b)*) and the measured evolution of the atom number $N_{\rm BEC}(t_{\rm hold})$ shown in Fig. 6.1*(c)*.
The simulations allow furthermore to reconstruct the in-trap time evolution of the dBEC after the stability threshold has been passed: First, the dBEC contracts radially, forming a very thin cigar along the direction of the external magnetic field. Then, strong atom losses occur at the center of the cloud, such that the centripetal force of the dipoles weakens and the BEC finally explodes in the radial directions (x, y) due to the surplus of the quantum pressure. Since the atoms at both ends of the cigar are not involved in the

[96]The three-body loss rate L_3 enters the Gross-Pitaevskii equation, as we show in section 6.2.3.

collapse process, they remain at their positions during the explosion of the cloud. This leads to the characteristic d-wave density pattern that is preserved during the TOF.
We see that the simulations reveal the real-time collapse dynamics of the dBEC, which is not accessible in the experiment. Due to the limited imaging resolution, the system can only be probed after an expansion, i.e. after a TOF. As our investigation of the collapse of the dBEC in the 1D lattice is also supported by such type of simulations, we will describe them in more detail in section 6.2.3.

6.2 Deconfinement-Induced Collapse in the 1D Lattice

We now present our studies of the collapse of a dBEC in the 1D optical lattice. First we describe our new technique to induce the collapse of the dBEC through a change in the lattice depth, i.e. by changing the external confinement of the system. We then present the results of the collapse measurements, including a quantitative analysis of the time scale of the collapse dynamics. In addition, we show a novel collapse scenario, where the collapse of an initially stable dBEC is triggered by the time-of-flight procedure (necessary to image the atoms) itself. Our experimental results are supported by numerical simulations, which also allow for a real-time study of the TOF-triggered collapse.

6.2.1 Experimental Sequence

The experimental sequence to study the collapse of a dBEC in a 1D optical lattice consists basically of two parts: First, we prepare the chromium BEC in a stable lattice configuration at a scattering length below the value a_{dd}. Then, we induce the collapse by lowering the lattice depth, thus crossing the stability threshold that we have mapped before.
The preparation of the condensate in the lattice potential is similar to the procedure described in section 5.3.1: We produce a BEC in the crossed ODT with the harmonic trap frequencies $(\omega_x, \omega_y, \omega_z) = 2\pi \cdot (540 \pm 20, 270 \pm 15, 470 \pm 15)\,\mathrm{Hz}$, at a scattering length $a = 98\,a_0$. We then reduce the scattering length within 6 ms to $a = 40\,a_0$, where we load the BEC into the 1D optical lattice potential at a depth $U_{\mathrm{init}} = 12.6\,E_{\mathrm{R}}$. For the loading process, we use the s-shaped ramp given by Eq. (5.4) with a ramp duration $T_{\mathrm{ramp}} = 4\,\mathrm{ms}$ and a ramping parameter $k = 4$, such that we fulfill very well the adiabaticity criterion given by Eq. (5.3). The scattering length is further lowered[97] to $a = (2 \pm 2)\,a_0$ within 4 ms, where we wait for 1 ms for the eddy currents to settle. At this stage of the sequence, the condensate is stable and contains typically 15,000 atoms. This configuration corresponds to the starting point of our collapse measurements.
To perform the collapse measurements, we reduce the lattice depth linearly from the initial depth U_{init} to a variable depth U within 100 µs. The value of U is chosen arbitrarily

[97] The parameters of the s-shaped ramp for the Feshbach magnetic field are the same as for the lattice ramp: $T_{\mathrm{ramp}} = 4\,\mathrm{ms}$ and $k = 4$. Note that the two ramps have a slightly different form, with the one of the Feshbach field given by Eq. (A.33) in appendix A.8.

above or below the stability threshold, as shown in Fig. 6.2*(a)*. We then hold the system in this final configuration for a variable time t_{hold}, before we switch off all the trapping lasers and perform an 8 ms TOF (see Fig. 6.2*(b)* for an illustration of the sequence). Our

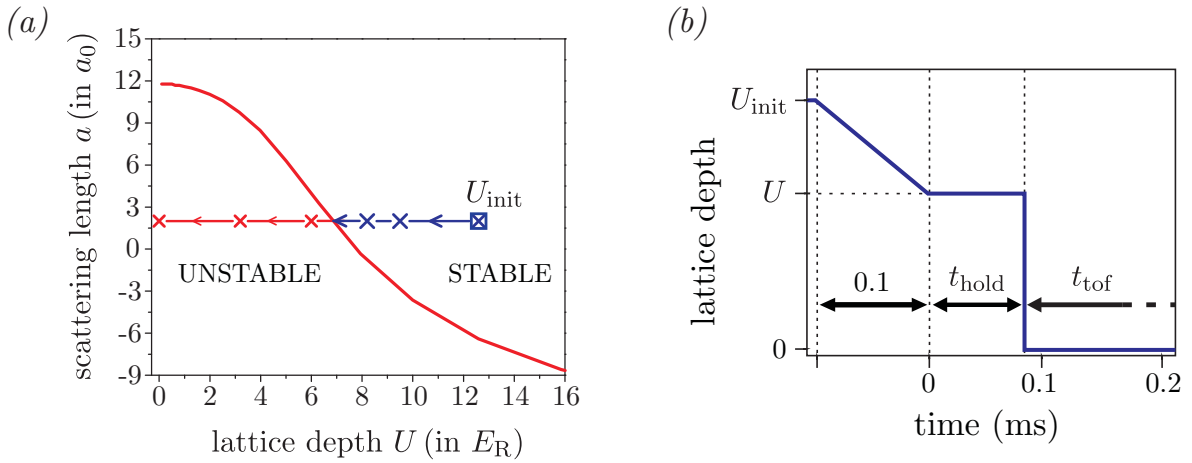

Fig. 6.2, Experimental sequence of confinement-induced collapse: *(a)* The system is prepared in a stable configuration at a lattice depth $U_{\mathrm{init}} = 12.6\, E_{\mathrm{R}}$ and a scattering length $a = (2 \pm 2)\, a_0$ (blue square). Then, the lattice depth is reduced to the final depth U with the values $U = (12.6, 9.5, 8.2, 6.3, 3.2, 0)\, E_{\mathrm{R}}$ (blue and red crosses). Thus U is chosen above and below the stability threshold (red line), which is calculated numerically for our parameters. *(b)* Timing of the experiment. After the linear lattice ramp of duration 100 µs, we hold the system for a variable time t_{hold} and then perform an 8 ms TOF. Note that the time origin is chosen at the end of the lattice ramp to be consistent with the studies presented in section 6.2.3.

imaging procedure is here different than for the stability measurements: we switch off the Feshbach magnetic field (oriented along z) after 4 ms of TOF and apply a low magnetic field ($B \sim 10$ G) along the imaging direction x. This field is kept on during the remaining TOF and the imaging procedure. We can thus make use of the maximum absorption cross-section for the imaging, increasing the signal-to-noise ratio in the absorption images [36]. We have checked explicitly that the switching of the magnetic fields does not change the shape of the condensate after TOF[98]. More technical details for the switch-off procedure of the Feshbach magnetic field can be found in Ref. [113, Ch.5.2.1].

With the new technique to induce the collapse by changing the external confinement, we can, in principle, drive the system into the unstable regime on the microseconds scale. The technical limit of the lattice ramping time is on the order of 1 µs only and is given by the rise time of the acousto-optical modulator. We choose, however, our ramping time of 100 µs such that we cannot not observe any excitations of the BEC when operating in the

[98] Following the procedure described in Ref. [36], we have performed d-wave collapse measurements using a single trapped dBEC, with and without switching off the Feshbach magnetic field during the TOF. We checked that we obtain the same d-wave structure of the collapsed cloud in both the cases.

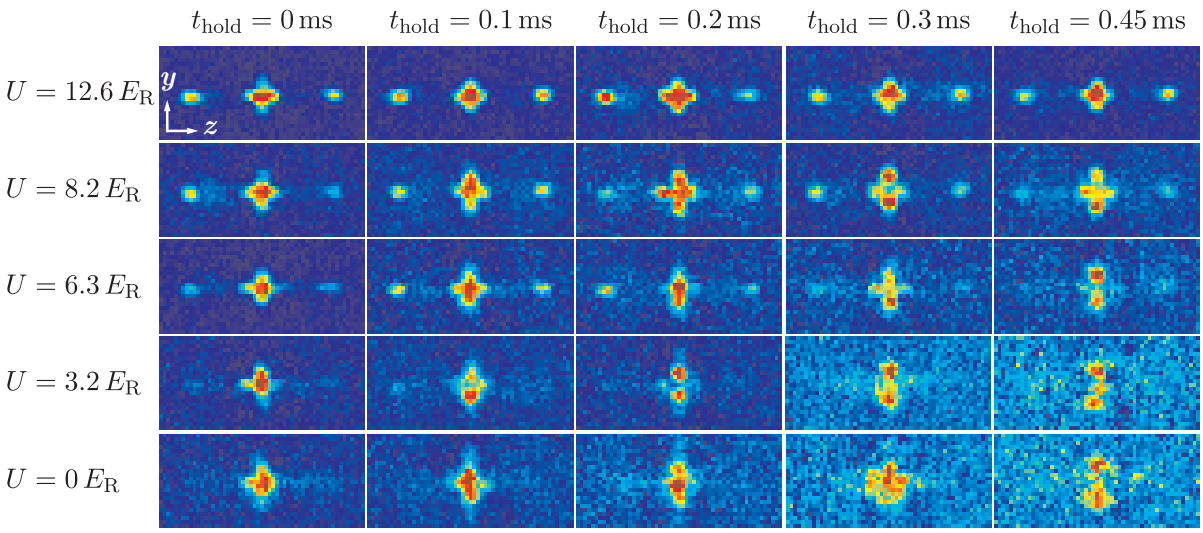

Fig. 6.3, Collapse dynamics of a dBEC in a 1D lattice: Evolution of the system for increasing holding time t_{hold} and different final lattice depth U, following the experimental sequence described in section 6.2.1. Each image is an average of five absorption pictures with the thermal cloud removed and the color scale is adjusted individually for better visibility (field of view: $190 \times 337\,\mu\mathrm{m}^2$).

stable regime with $a > a_{\mathrm{dd}}$. The ramping time is still considerably shorter than in the case of the interaction-induced collapse, where the ramp duration is typically restricted to around 1 ms [36]. Hence, this technique provides a new and powerful tool to investigate the dynamics of dipolar BECs close to the stability threshold.

6.2.2 Collapse of a Coherent Array of dBECs

Following the procedure described above, we measure the time evolution of the system for a varying holding time t_{hold} and for different final lattice depths $U \leq U_{\mathrm{init}} = 12.6\,E_{\mathrm{R}}$. Our results are shown in Fig. 6.3. Each image of the density distribution is obtained by averaging five absorption pictures, taken under exactly the same experimental conditions. Before the averaging process, we fit the broad isotropic thermal cloud, present on each picture, by a Gaussian and subtract it from the absorption images. Therefore, the images in Fig. 6.3 show only the interference patterns of the remaining coherent atoms.

We first consider the two smallest lattice depths $U = 0$ and $U = 3.2\,E_{\mathrm{R}}$, well below the stability threshold located at around $7\,E_{\mathrm{R}}$. We observe a decay of the number of coherent atoms when increasing the in-trap holding time, which is indicated by the increasing background noise in the images. From this observation we infer that the dBEC is collapsing *in-trap*, i.e. while still confined by the external trapping potential. In addition, we observe that the collapsed clouds show mainly structures in the y-direction, transversal to the external B-field and the lattice direction.

In contrast, if the final lattice depth is chosen above the stability threshold, i.e. in the cases $U = 12.6\,E_\mathrm{R}$ and $U = 8.2\,E_\mathrm{R}$, there is no visible decay of the atom numbers. Here, the TOF images basically show the usual interference pattern of a coherent array of condensates (see section 4.4.2): we observe the central zero-momentum component and the two side peaks corresponding to the lattice recoil momenta $\pm 2\hbar k_\mathrm{lat}$ (with $k_\mathrm{lat} = \pi/d_\mathrm{lat}$). However, the central density peak shows a deviation with respect to the usual shape obtained in non-dipolar BECs: it develops a *d*-wave shape that is similar to the one observed in a single collapsed dBEC [36], shown in section 6.1. Due to our limited imaging resolution, the characteristic cloverleaf shape of the central peak becomes more clear if we expand the condensate for longer times t_tof, as shown in Fig. 6.4. For both the stable in-trap configurations, considered here, we do not expect any in-trap evolution of the system. Therefore, the observed *d*-wave collapse of the zero-momentum component must be triggered by the time-of-flight (TOF-triggered collapse). Such collapse behaviour is fundamentally different from the interaction-induced collapse shown in Ref. [36]. There, the collapse happened partly during the TOF because the ramp in the scattering length has not converged yet to its final value due to the eddy currents.
Finally, in the case $U = 6.3\,E_\mathrm{R}$, which is just below the stability threshold, we observe a slow decay of the atom number with increasing t_hold, but also a *d*-wave density pattern of the central cloud. The observed dynamics of the system hence shows features of both an in-trap collapse, as well as a TOF-triggered collapse. Using numerical real-time simulations, we will investigate the complex dynamics of the system in details in section 6.2.3. Before that, however, we study the time scale of the collapse dynamics by performing a quantitative analysis of the absorption images taken in the collapse measurements.

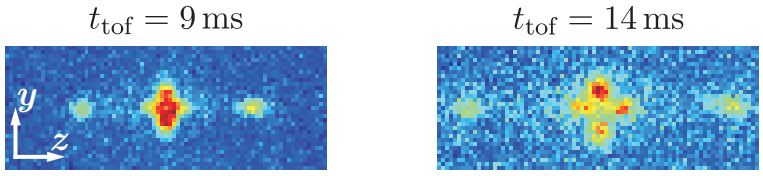

Fig. 6.4, *d*-wave collapse of the zero-momentum component: The images show the remaining coherent atoms of a BEC that is released from a lattice of depth $8\,E_\mathrm{R}$, for the two different expansion times $t_\mathrm{tof} = 9\,\mathrm{ms}$ and $t_\mathrm{tof} = 14\,\mathrm{ms}$. Due to the limited resolution of our imaging system, the *d*-wave shape of the central density peak is more visible at long expansion times (field of view: $190 \times 497\,\mu\mathrm{m}^2$).

By integrating the optical density in the images shown in Fig. 6.3, we obtain the number of remaining coherent atoms for each lattice depth as a function of t_hold. For further processing, we calculate the *remnant fraction*, defined as the number of coherent atoms normalized by the total number of atoms, i.e. including the thermal cloud. Normalizing the data in such way removes partly the shot-to-shot fluctuations that occur due to the variation of the total atom number in the experiment. We then extract an *atom loss rate*

for short holding times $t_{\mathrm{hold}} \leq 0.6\,\mathrm{ms}$ from an exponential fit[99] to the remnant fraction, as shown in Fig. 6.5*(a)*. We note that the choice of the exponential fitting function is not related to any physical model, but describes well the data in the considered time interval and thus enables to quantify the time scale of the collapse dynamics. The resulting loss

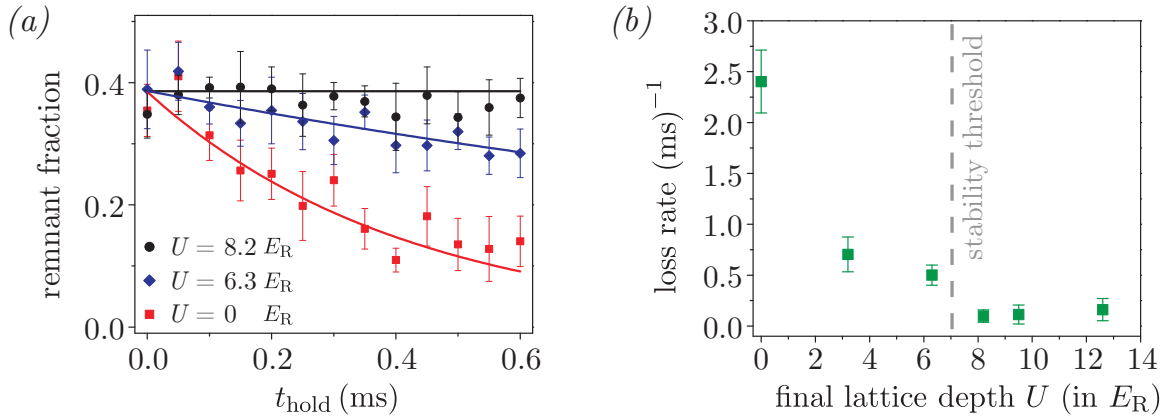

Fig. 6.5, Loss rate in collapse dynamics: *(a)* Evolution of the remnant fraction (see text for definition) for different final lattice depths U, from which the loss rate is extracted by fitting an exponential function (solid lines). *(b)* Loss rate extracted from the different datasets, versus final lattice depth U. The vertical dashed line marks the stability threshold obtained from numerical calculations.

rate, shown in Fig. 6.5*(b)*, is crucially depending on whether the final lattice depth U is chosen above or below the stability threshold. For values of U above the stability threshold (located at around $7\,E_{\mathrm{R}}$) the loss rate is smaller than $0.25\,\mathrm{ms}^{-1}$. This indicates that there is basically no in-trap evolution of the system, as expected. When crossing the calculated stability threshold, the loss rate suddenly increases. If we completely ramp down the lattice potential, the loss rate increases further to about $2.5\,\mathrm{ms}^{-1}$. The remnant fraction thus reduces by around 60% when holding the atoms for 0.4 ms in the trap. Therefore, in the case $U = 0\,E_{\mathrm{R}}$, our measurements agree well with the observed atom number decay in a single dBEC [36] (see section 6.1). Measuring a smaller loss rate at larger lattice depths (but below the stability threshold), we infer that the presence of a lattice slows down the collapse dynamics of the system.

While the loss rate measurements provide an estimate for the time scale of the collapse dynamics, they cannot clearly distinguish whether the atom losses occur in-trap or during the TOF. In contrast, numerical simulations can reveal the real-time dynamics of the collapsing system. Therefore, they are a valuable tool to investigate the collapse dynamics of a dipolar BEC, as we show in the following section 6.2.3.

[99] We fit the measured remnant fraction by a function $F(t) = F_0 \exp[-Lt]$, with F_0 and the loss rate L being the fitting parameters.

6.2.3 Numerical Simulations of the Collapse Dynamics

In a collaboration with the theory group in Hannover, we have examined more closely the collapse dynamics of the dipolar condensate in the lattice by means of numerical simulations. The simulations are based on the time-dependent Gross-Pitaevskii equation (given by Eq. (6.1)),

$$i\hbar\frac{\partial}{\partial t}\psi(\boldsymbol{r},t) = \Big[-\frac{\hbar^2}{2m}\boldsymbol{\nabla}^2 + V_{\mathrm{ext}}(\boldsymbol{r}) - i\hbar\frac{L_3}{2}\,N^2\,|\psi(\boldsymbol{r},t)|^4 + N\,\frac{4\pi\hbar^2 a}{m}\,|\psi(\boldsymbol{r},t)|^2 + N\int \mathrm{d}^3r'\,V'_{\mathrm{dd}}(\boldsymbol{r}-\boldsymbol{r}')\,|\psi(\boldsymbol{r}',t)|^2\Big]\psi(\boldsymbol{r},t), \tag{6.1}$$

where the non-unitary term proportional to L_3 describes three-body atom losses due to inelastic collisions. N is the initial number of atoms in the condensate and $V_{\mathrm{ext}}(\boldsymbol{r})$ is the combined trapping potential of ODT and lattice with $V_{\mathrm{ext}}(\boldsymbol{r}) = U\sin^2(\pi z/d_{\mathrm{lat}}) + m\sum_{i=x,y,z}\omega_i^2 r_i^2/2$. The contact interactions are included via the s-wave scattering length a and the dipole-dipole interaction potential $V'_{\mathrm{dd}}(\boldsymbol{r}-\boldsymbol{r}')$ is given by Eq. (2.6).
As a first step, the ground-state of the condensate is calculated for a scattering length $a = 2\,a_0$ and a lattice depth $U = U_{\mathrm{init}} = 12.6\,E_{\mathrm{R}}$. This task is performed by integrating the GPE in imaginary time, with the loss parameter L_3 set to zero. Then, the simulations are performed by a real-time evolution of Eq. (6.1), following our experimental sequence and choosing[100] $L_3 = 2\cdot 10^{-40}\mathrm{m}^6/\mathrm{s}$. In analogy to the experimental imaging procedure, the time-evolution of the system, shown in Fig. 6.6*(a)*, is illustrated by integrating the atomic density along the x-direction. After sufficiently long expansion of the dBEC in the TOF, the dilute cloud undergoes a ballistic expansion, since interactions do not play a role anymore. Calculating the momentum distribution of the system in this regime (see Fig. 6.6*(b)*) yields the spatial density distribution of the atomic cloud in the far field of the TOF, corresponding to the absorption images taken in the experiment. Finally, the time evolution of the number N of coherent atoms is extracted from the simulations, with the results presented in Fig. 6.6*(c)*. We note that the time origin in the simulations, $t = 0$, is set at the end of the lattice ramp. Furthermore, a fixed holding time $t_{\mathrm{hold}} = 0.6\,\mathrm{ms}$ is chosen, before starting the TOF.

Collapse dynamics
We split the discussion of the collapse dynamics, shown in Fig. 6.6, into three parts: First, we discuss the deconfinement-induced collapse of a single dBEC ($U = 0\,E_{\mathrm{R}}$). Then, we consider the stable in-trap configurations ($U = 8.2\,E_{\mathrm{R}}$ and $U = 12.6\,E_{\mathrm{R}}$) and finally we address the unstable situations at the lattice depths $U = 3.2\,E_{\mathrm{R}}$ and $U = 6.3\,E_{\mathrm{R}}$.

(i) By choosing the final lattice depth $U = 0\,E_{\mathrm{R}}$, we obtain an unstable in-trap configuration of the system. At the end of the lattice ramp, the periodic density

[100] The loss rate L_3 is chosen equal to the value that is used in the simulations of the d-wave collapse of a single dBEC [36] (see section 6.1).

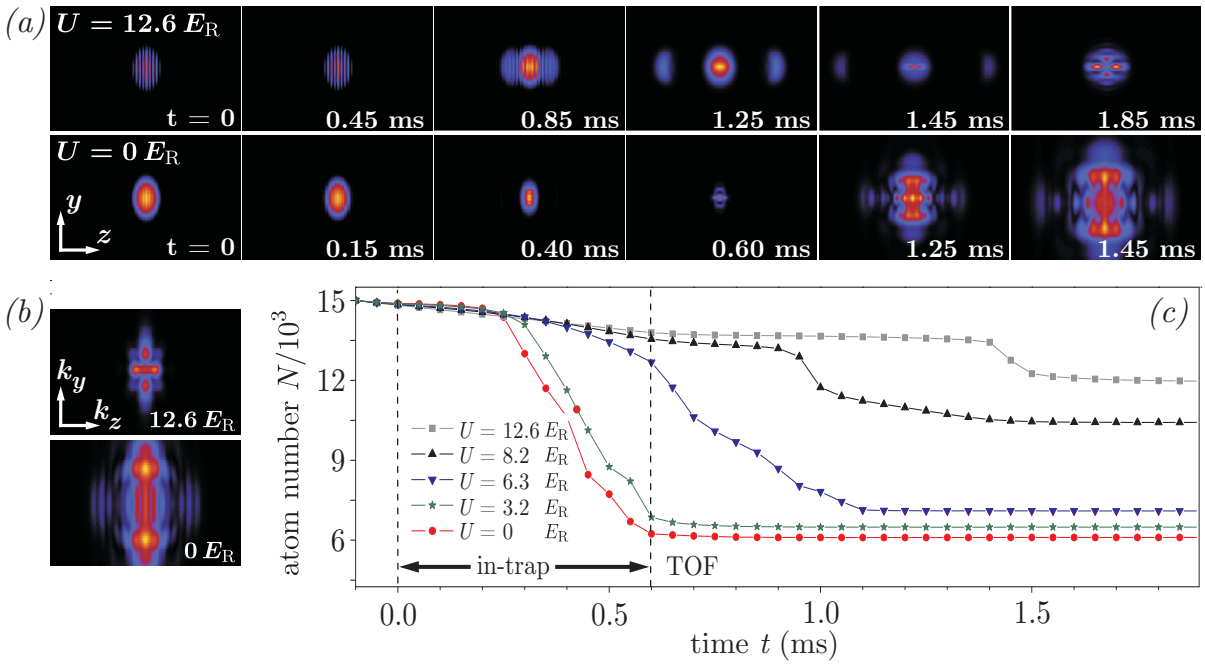

Fig. 6.6, Real-time simulations of the collapsing dBEC: *(a)* Time evolution of the system for a final lattice depth $U = 12.6\,E_\mathrm{R}$ (first row) and $U = 0\,E_\mathrm{R}$ (second row). Note that the snapshots in the two sequences are taken at different times t, with the time origin set at the end of the lattice ramp. At the time $t = 0.6\,\mathrm{ms}$ the TOF is started, i.e. the trapping potentials are suddenly switched off. *(b)* Momentum distribution of the system in the ballistic regime, corresponding to the spatial density distribution in the far field of the TOF (for $U = 12.6\,E_\mathrm{R}$, only the zero-momentum component is shown). *(c)* Evolution of the atom numbers N for different final lattice depths U (specified in the figure).

modulation vanishes due to the absence of the lattice potential, as shown in the second row of the images in Fig. 6.6*(a)*. The condensate then shrinks and shows strong atom losses while it is still trapped in the harmonic potential. The decay of the BEC atom number slows down at around $t = 0.5\,\mathrm{ms}$ and after the release from the trap (at $t = 0.6\,\mathrm{ms}$) we do not observe any atom losses anymore. The simulations therefore confirm our hypothesis that, for $U = 0\,E_\mathrm{R}$, the collapse is initiated in the trap. In addition, the simulations show a loss of about 60% of the atoms within the first 0.5 ms of the in-trap holding time, which is close to our experimental results. During the TOF, the cloud explodes mainly radially. Its shape in the far field of the TOF (see Fig. 6.6*(b)*) is similar to the one observed in the experiment for the longest applied holding time.

(ii) Considering the stable in-trap configurations $U = 12.6\,E_\mathrm{R}$ and $U = 8.2\,E_\mathrm{R}$, the evolution of the atom number, shown in Fig. 6.6*(c)*, clearly supports the hypothesis of the TOF-triggered collapse: while there are almost no in-trap atom losses, we observe a sudden drop in the atom number only some time after switching off the trapping potentials. For $U = 12.6\,E_\mathrm{R}$ the drop occurs at $t \simeq 1.45\,\mathrm{ms}$, where we also

observe the collapse of the zero-momentum component in the images in Fig. 6.6*(a)* (upper row). The collapsed cloud then develops the d-wave pattern that is also recorded after TOF in the experiment. We explain this novel collapse scenario in more detail in the text below.

(iii) Holding the dBEC at a non-zero lattice depth below the stability threshold, we observe that the decay of the atom number is delayed with respect to the case $U = 0\,E_{\mathrm{R}}$. In particular for $U = 6.3\,E_{\mathrm{R}}$, which is just below the stability threshold, the collapse is initiated in-trap, but the strong atom losses stop only during the TOF. Note that the system would collapse completely in-trap if we would choose a longer holding time in the simulations. In contrast, for a shorter holding time $t_{\mathrm{hold}} \lesssim 0.3\,\mathrm{ms}$, the collapse occurs mainly during the TOF. Comparable to the stable configurations, the zero-momentum component then collapses in TOF and develops the d-wave shape that we observe experimentally.

TOF-triggered collapse of a dBEC

The TOF-triggered collapse that we observe after releasing the dBEC from a stable lattice configuration can be seen as a special case of the deconfinement-induced collapse − it occurs after switching off all the trapping potentials. This novel collapse scenario may be explained by a two-step process: during the initial phase of the TOF, the different momentum components of the wave function separate very quickly, thus forming individual wavepackets. The spatially separated atomic clouds then evolve independently and may either expand indefinitely or collapse, depending on their shape and population.

In the initial phase of the expansion, until a time $t \sim \hbar/E_{\mathrm{R}}$, the dynamics of the system is well described by the expansion of a coherent array of non-interacting condensates (see section 4.4.1). This relies on the fact that the lattice recoil energy E_{R} is much larger than any other energy scale in the system. The different momentum components of the BEC thus move away from each other, with the relative velocities given by multiples of $\hbar k_{\mathrm{lat}}/m$ (with $k_{\mathrm{lat}} = \pi/d_{\mathrm{lat}}$ the lattice recoil momentum). As we can see in the images of Fig. 6.6*(a)*, the different wavepackets are almost spatially separated at around 0.25 ms after the release from the trap (i.e. at $t = 0.85\,\mathrm{ms}$). After such short expansion time, their shape is still given by the envelope of the initially trapped condensate. According to our considerations in section 4.4.1, only the zero-momentum component and the $\pm 2\hbar k_{\mathrm{lat}}$ components are significantly populated at a lattice depth $U = 12\,E_{\mathrm{R}}$: the central wavepacket contains around 60% of all coherent atoms, while only 20% of the atoms occupy each of the two outer wavepackets.

With the given shape and populations, the stability of the individual wavepackets can be examined by variational calculations with a Gaussian ansatz for the wave functions (see section 5.2). The calculations show that only in the zero-momentum component the dipolar interactions are sufficiently strong to destabilize the atomic cloud. In the side-peaks, however, the density is too low to induce the collapse, matching with our experimental observation.

We emphasize that the *inter-site coherence* in the lattice plays a crucial role for the TOF-triggered collapse to occur. Considering the expansion of an *incoherent* array of condensates, their interference pattern will not show well-separated density peaks. The density distribution is instead given by a very broad Gaussian-shaped atomic cloud, since the rapidly expanding on-site wave functions are adding incoherently. As a result, the density in the system drops very fast after the release from the trap and the interactions do not induce a collapse of the atomic cloud.
In addition to the inter-site coherence, the *anisotropy* of the dipole-dipole interaction is required to observe the TOF-triggered collapse. In the trap, the system is stable due to the highly oblate shape of the on-site condensates, thus stabilized by the repulsive part of the DDI. During the TOF, however, the shape of the wavepackets (corresponding to the different momentum components) becomes relevant. Here, the attractive part of the DDI becomes dominant and drives the system into the instability.

Concluding the collapse measurements for moderate lattice depths, we have shown that we can induce the collapse of a dipolar BEC by changing only the depth of an optical lattice potential at a constant interaction strength. The time scale of the in-trap collapse depends on the final lattice depth, the collapse dynamics being slowed down at increasing lattice depths. We have also shown that a coherent array of dipolar BECs, which is stable in-trap, can undergo a collapse upon release from the trapping potential (TOF-triggered collapse). Such collapse behaviour arises due to the combined effect of the inter-site coherence and the anisotropy of the dipole-dipole interaction. We note that the TOF-triggered collapse is specific to dipolar lattice gases: neither a single dipolar BEC, nor a contact interacting gas with attractive interactions will become unstable during the TOF if it was stable in-trap.
Finally, we mention that our observations in the chromium BEC can be generalized to other dipolar systems, when expressing the scattering length a in units of the dipole length a_{dd}. The deconfinement-induced collapse, and its extreme case the TOF-triggered collapse, then occur in the strongly dipolar regime with $a < a_{\mathrm{dd}}$.

6.3 Collapse in Deep Lattices - Techniques for Roton Measurements

Based on our studies of the stability and the collapse of a dipolar BEC in the 1D optical lattice, we now propose an experimental sequence to investigate the collapse dynamics in the regime of very deep lattices ($U_{\mathrm{lat}} \gtrsim 20\, E_{\mathrm{R}}$). This regime is particularly interesting, as the quasi-two-dimensional on-site condensates may collapse into multi-peak structures via roton-like modes, as discussed in section 5.1.2. So far, such type of collapse has not been observed in a dipolar gas. In our experimental approach, we follow the idea presented in Ref. [37]. The numerical simulations in this work show a roton-type collapse of a single

oblate dBEC, if the system forms a structured ground-state before it is driven into the unstable regime. We therefore aim to cross the narrow parameter range[101] where the structured ground-states are predicted to appear [28], while the system is still trapped in the lattice. The principle of this measurement is straight forward, its actual realization, however, features some challenges that we discuss now.

Dephasing of on-site condensates

In the very deep lattice regime, the tunneling between the lattice sites is suppressed on experimental time scales. By changing any parameter of the system, such as the lattice depth or the scattering length, the individual on-site condensates will dephase in time, as discussed in section 4.3.3. The resulting complex interference patterns after TOF (see section 4.4.2) then lead to a very low signal-to-noise ratio in our absorption images. In this case, the identification of any radial structures in the density distribution is very difficult. We therefore keep the dephasing at a low level by optimizing our experimental sequence to the shortest possible holding time in the deep lattice, with the details given below.

Collapse in TOF

Following the proposed measurement scheme, the collapse must be initiated *inside* the highly oblate trapping geometry provided by the deep lattice to observe the desired roton features. However, a collapse can also be triggered *after* the release of the dBEC from the lattice potential, as shown in section 6.2.3. The latter scenario should be avoided not to confuse the two different types of collapses in the measurements. A possible solution to suppress a collapse arising in TOF is the following: to perform the TOF, at first only the underlying harmonic confinement of the ODT is suddenly removed. The on-site condensates then expand shortly in the radial directions inside the 2D geometry of the lattice sites[102]. Then, after a short delay Δt, the lattice confinement is switched off for the remaining TOF. We have tested this sequence by releasing a dBEC from a stable configuration ($U = (8 \pm 1)\, E_\mathrm{R}$, $a = (4 \pm 3)\, a_0$), where a TOF-triggered collapse is expected to occur. Figure 6.7 shows that, for zero delay in the lattice switch-off, we indeed observe a collapse of the system. In contrast, for delay times $\Delta t \geq 0.2\,\mathrm{ms}$, the TOF-triggered collapse is suppressed, resulting in the usual interference patterns of a coherent array of condensates.

Measurement sequence

The experimental sequence that we propose for the collapse measurements is the following: At first, a stable dipolar condensate is prepared in a lattice of moderate depth $U_\mathrm{init} \sim 10\, E_\mathrm{R}$ at an initial scattering length $a_i > a_\mathrm{dd}$. Then, *both* the scattering length and the lattice depth are ramped at the same time to reach the unstable region in the very deep lattice

[101] Loading around 3-7 lattice sites may provide the largest range of parameters, where structured ground-states are expected to form [28] (see also section 5.4.2).

[102] The radial confinement created by the lattice does probably not affect the radial expansion of the on-site BECs for short expansion times after switching off the ODT. This should be checked, however, by numerical simulations.

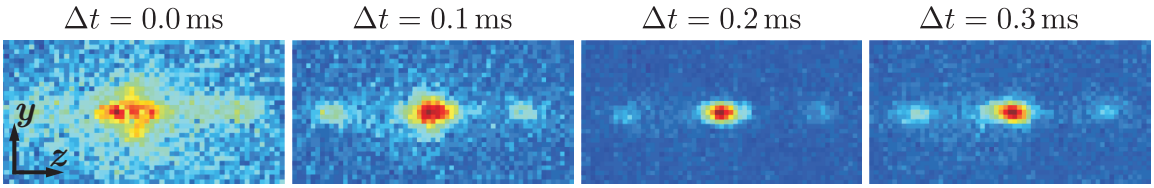

Fig. 6.7, Delayed lattice switch-off: Atomic density distribution after TOF, for different delay times Δt between ODT and lattice switch-off. The parameters in the sequence are $a = (4 \pm 3)\, a_0$, $U_{\mathrm{init}} = (13 \pm 1)\, E_{\mathrm{R}}$, $U = (8 \pm 1)\, E_{\mathrm{R}}$, $t_{\mathrm{hold}} = 0.4\,\mathrm{ms}$ and $t_{\mathrm{tof}} = 9\,\mathrm{ms}$. Each image is an average of four absorption images with the thermal cloud removed (field of view: $190 \times 374\,\mu\mathrm{m}^2$).

regime. The minimum ramping time of around 1 ms is defined by the control of the Feshbach magnetic field, and is limited e.g. by eddy currents in the metallic vacuum chamber (see appendix A.8).

We illustrate such sequence in Fig. 6.8 with parameters that we used in an experiment. The dBEC is prepared in a lattice of depth $U_{\mathrm{init}} = (8 \pm 1)\, E_{\mathrm{R}}$ at a scattering length $a_i = (40 \pm 2)\, a_0$. The trap frequencies of the underlying harmonic trap are similar to the ones used in the collapse measurements presented in section 6.2.1. Within 1 ms, we then ramp up the lattice depth linearly to $U = (50 \pm 5)\, E_{\mathrm{R}}$ and at the same time we decrease the scattering length in an s-shaped ramp[103] to $a_f = (-19 \pm 4)\, a_0$. Note that we take into account the eddy currents when calculating the time-dependent scattering length

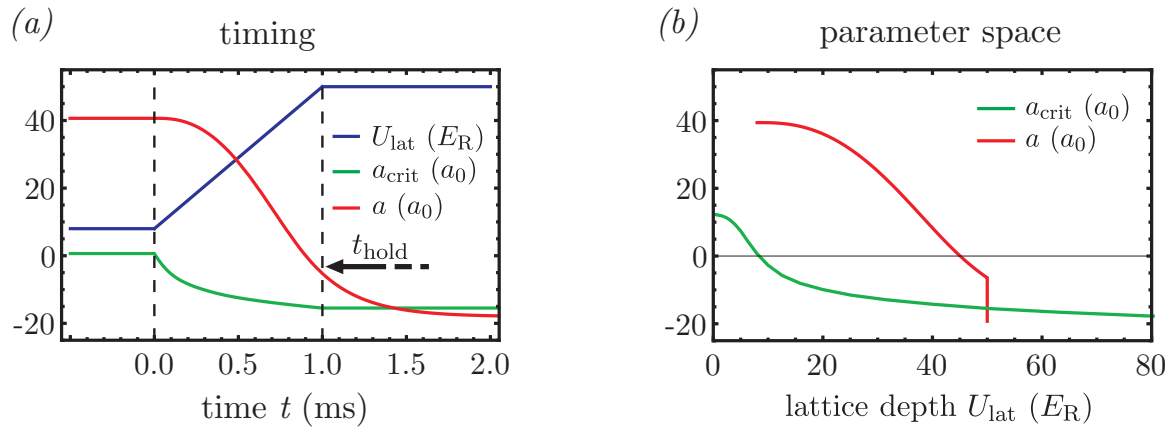

Fig. 6.8, Collapse in very deep lattices - Sequence: *(a)* Timing of the experiment. The lattice depth U_{lat} (blue line) and the scattering length a (red line, eddy currents included) are ramped simultaneously, before holding the system for a variable time t_{hold}. The green line shows the critical scattering length $a_{\mathrm{crit}}(U_{\mathrm{lat}})$ calculated for $N = 15,000$ atoms. *(b)* Sequence in parameter space. The value of a (red line) is shown as a function of the lattice depth U_{lat}. The green line again indicates the stability threshold $a_{\mathrm{crit}}(U_{\mathrm{lat}})$.

[103] The ramp of the scattering length is performed by ramping the Feshbach magnetic field in an s-shaped form, as given by Eq. (A.33) in appendix A.8. We use the parameters $T_{\mathrm{ramp}} = 1\,\mathrm{ms}$ and $k = 3$.

$a(t)$, shown in Fig. 6.8*(a)*. We therefore cross the stability threshold, given by the critical scattering length a_{crit}, only *after* the end of the programmed ramp. Then, we hold the condensate for a variable time t_{hold} in the trap, before we switch off the ODT. After a delay $\Delta t = 0.2\,\mathrm{ms}$, we also switch off the lattice potential to perform a 15 ms TOF, and finally take an absorption image.
Our sequence is a modification of the "standard" interaction-induced collapse, as we can see from the trajectory in parameter space shown in Fig. 6.8*(b)*. While tuning only the scattering length a would result in a vertical trajectory $a(U_{\mathrm{lat}})$, here we obtain a diagonal line by tuning both parameters a and U_{lat} at the same time. A short vertical movement in parameter space still occurs, since the ramp of the scattering length is delayed with respect to the lattice ramp due to the eddy currents.

Preliminary observations

Figure 6.9 shows two single absorption images of the dBEC, taken for the holding times $t_{\mathrm{hold}} = 0.16\,\mathrm{ms}$ and $t_{\mathrm{hold}} = 0.2\,\mathrm{ms}$, with the thermal cloud removed. We observe four density peaks (instead of three as in the case of moderate lattice depths), which indicates that there is some dephasing between the on-site condensates when ramping a and U_{lat}. Let us first consider the image taken at $t_{\mathrm{hold}} = 0.16\,\mathrm{ms}$. The two central density peaks show a "double structure" in the y-direction. We thus assume that there was a collapse of the system. Even the weakly populated outer peaks show a similiar structure which is, however, hard to distinguish from the background noise. The appearance of structures in *all* the density peaks is in contrast with the case of the TOF-triggered collapse. There, only the peaks with the largest population are expected to become unstable after the release from the lattice. The observed structures could therefore indicate that the collapse has been induced in-trap, as desired for the roton measurements[104]. According to the sequence shown in Fig. 6.8*(a)*, we would expect that after an in-trap holding time $t_{\mathrm{hold}} = 0.16\,\mathrm{ms}$ the stability threshold has *not* been passed yet. However, the collapse might be still induced in the trap, considering that the lattice is switched off 0.2 ms after the ODT and taking into account our uncertainty on the scattering length ($\Delta a \simeq 4\,a_0$).

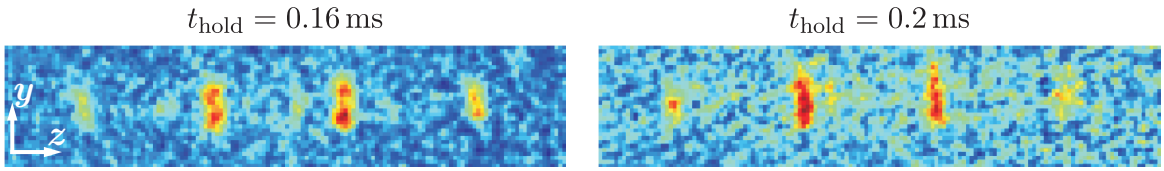

Fig. 6.9, Collapse in very deep lattices - Images: Single absorption images (with the thermal cloud removed) taken for different times t_{hold} after finishing the collapse ramp. The field of view is $190 \times 883\,\mu\mathrm{m}^2$.

[104]The assumption that the collapse is initiated in-trap has to be carefully checked by simulations. It is possible that, due to the attractive contact interactions ($a = -19\,a_0$), even the weakly populated density peaks may become unstable during the TOF.

In the image taken for $t_{\mathrm{hold}} = 0.2\,\mathrm{ms}$, we observe an even stronger expansion of the two central density peaks in the y-direction, while the two outer peaks are hardly visible. There is no clear structure in the atomic clouds anymore, the observation of small density modulations might, however, be hindered by the background noise in the absorption images[105] or by the limited resolution of our imaging system. If we hold the system longer than 0.2 ms in the trap, we observe a mostly exploded cloud without any visible structures. It may be that the strong expansion of the collapsed system in the y-direction is related to a roton-type collapse. If the on-site condensates collapse into a radial multi-peak structure, we would indeed expect the formation of a complicated interference pattern, created by multiple atom bursts [37]. While the exact collapse dynamics is difficult to predict, numerical simulations may again show the real-time evolution of the system.

The different techniques presented in this section open a way to experimentally investigate roton features of a dBEC in a deep 1D optical lattice. We have seen that such study is at the technical limit of our experimental apparatus, concerning the control of the interactions and the imaging resolution. Therefore, a substantial technical improvement will be required to further explore the interesting physics of strongly dipolar quasi-two-dimensional BECs.

[105] An averaging of the absorption images to reduce the background noise is more difficult than before: the atomic interference patterns are typically shifted in the z-direction from shot to shot. This is due to the fact that we do not actively stabilize the phase of the lattice laser.

7 Summary and Outlook

Summary

The main subject of this thesis was the study of the static and dynamic properties of a dipolar chromium Bose-Einstein condensate (BEC) in a one-dimensional optical lattice potential. The stability of the system was investigated by measuring the critical s-wave scattering length, i.e. the threshold between the stable and the unstable regime, as a function of the lattice potential depth. Furthermore, I presented studies on the dynamics of a dipolar BEC (dBEC) undergoing an instability either inside the trap or after the release from a stable lattice configuration.

To perform the measurements, we have modified an existing experimental setup to load the harmonically trapped ^{52}Cr BEC into a one-dimensional (1D) optical lattice. The atomic dipoles were polarized in the direction of the lattice by an external magnetic field that was also used to tune the s-wave scattering length in the vicinity of a Feshbach resonance. A major task was to precisely calibrate the two tunable parameters: the lattice potential depth U_{lat} and the s-wave scattering length a. Measuring the BEC atom number while reducing the scattering length, we determined the stability threshold of the ^{52}Cr BEC for different lattice depths. For shallow lattices, the dBEC was found unstable for positive critical s-wave scattering lengths a_{crit}, indicating a destabilizing character of the dipolar interactions. Here, the prolate shape of the underlying harmonic trapping potential led to an effective attraction between the dipoles. In contrast, in the regime of very deep lattices, a stable system was observed even for negative scattering lengths down to $a_{\mathrm{crit}} = (-17 \pm 3)\, a_0$ (with a_0 the Bohr radius). In this case, the system is a stack of spatially separated quasi-two-dimensional dBECs, located on the lattice sites. Due to the highly oblate shape of the on-site trapping potentials, the dipoles are mainly aligned in the repulsive side-by-side configuration thus stabilizing the system. Finally, in the full range from shallow to very deep lattices, the measured stability threshold was found to agree very well with the results from numerical mean-field calculations, performed in the group of Luis Santos in Hannover. In the limit of very deep lattices, we have furthermore performed variational calculations, assuming a Gaussian shape for the wave functions of the on-site dBECs. Both calculations confirmed the stabilization of the system by the on-site dipolar repulsion, but also revealed a significant destabilization by the attractive dipolar inter-site interactions.

The measured stability diagram, showing the function $a_{\mathrm{crit}}(U_{\mathrm{lat}})$, has set the basis for our investigation of the instability dynamics of the dipolar lattice gas. We thus prepared a stable dipolar system in a lattice of moderate depth. Here, the tunneling of atoms between the lattice sites ensured the coherence among the highly oblate sub-condensates. We then drove the system from the stable to the unstable regime by only reducing the lattice depth, i.e. by a change of the external confinement, while keeping the two-body

interaction strength fixed. Using this new technique, we found that the in-trap collapse dynamics of an unstable dBEC is slowed down for increasing lattice depths U_{lat}. Choosing U_{lat} above the stability threshold, the system showed almost no in-trap time evolution. However, after the release from the stable lattice configuration, we observed that the dBEC collapsed in the time-of-flight (TOF) as confirmed by real-time simulations. This novel collapse scenario relies on the anisotropy of the dipole-dipole interaction and the inter-site coherence of the dBEC in the lattice.

The studies presented in this thesis are relevant for any future experiments on strongly dBECs in lattices. In particular, the realization of a stack of stable quasi-two-dimensional dipolar BECs with attractive contact interactions may motivate further experimental investigations, as such system is promising to show novel dipolar phenomena related to the roton-maxon excitation spectrum. For example, structured ground-states or a roton-type collapse via multiple density peaks might occur. In this extreme parameter region, however, experimental studies face several challenges: a dephasing between the sub-condensates or a collapse in TOF might hinder the desired observations. In a set of test measurements, we have addressed these challenges experimentally and proposed solutions to reveal interesting roton features of a dBEC in a deep one-dimensional optical lattice.

Outlook

In our experiments we have reached a high level of control over the interactions in the ^{52}Cr BEC and over its external confinement. The goal to observe self-organized density structures and other novel quantum phases, however, requires to go beyond the technical capabilities of the current experimental system. In parallel to the work presented in this thesis, we have therefore planned and partly installed a new experimental setup. It is now being completed and will be described in following PhD theses. In the new setup, we will transport[106] the dipolar quantum gas from the (basically unchanged) metallic vacuum chamber to a specially designed glass cell. The latter offers a large optical access to image the atoms through a high-resolution microscope objective, allowing to resolve structures on a length scale of around 1 µm. We thus enhance our current imaging resolution by approximately a factor of six. The microscope objective will furthermore be used to tightly focus a laser beam, realizing an optical dipole trap on micrometer size. By moving the position of the trapping beam faster than the atoms can follow[107], we can create time-averaged trapping potentials of almost arbitrary shape in the focal plane [39].

Our new system may enable the in-trap observation of *self-organized structures* of dBECs in different trapping geometries. Quasi-two-dimensional systems can be studied,

[106] We will transport the atoms in a single-beam optical dipole trap over a distance of around 40 cm by moving the focussing lens with a high-precision air-bearing translation stage, as performed in Ref. [200].

[107] To dynamically vary the position of the laser in the focal plane, we will actively control the angle of the laser beam before the microscope objective, using two electro-optical deflectors.

as well as e.g. dipolar condensates in toroidal traps (created by "painting" a circle with the laser beam of the dipole trap). The latter case has been subject to a theoretical study, showing that the dBEC may form a *self-induced Josephson-junction* [201]: with the dipoles aligned in the plane of the trap, the anisotropic dipole-dipole interaction (DDI) breaks the rotational symmetry of the system and the atoms may accumulate at two opposite sites of the ring-trap. Coherent tunneling phenomena, such as Josephson oscillations and quantum self-trapping can then take place depending on the initial population imbalance on the two sites.
Interesting systems to visibly demonstrate the long-range character of the DDI are *dBECs in multi-well potentials*. By toggling the trapping laser beam very fast from one position to the next, such potential is created with a tunable distance and alignment between the wells. Depending on the (tunable) ratio between the on-site and the inter-site interactions, various ground-state phases are expected to occur [116, 202]: in a system of three potential wells in a linear arrangement, all the atoms may be found for instance in the two outer wells. Such state relies on repulsive dipolar inter-site interactions and cannot form when only short-range interactions are present. A detailed theoretical investigation of dipolar BECs in multi-well potentials has been performed by David Peter in the scope of his diploma thesis in our group [118, 120]. It was found that, in a triple-well potential, a state with an almost empty central well can indeed be obtained for realistic experimental parameters, close to the stability threshold of the system.

The parameter range to observe the interesting dipolar effects is typically very narrow. It is enlarged, however, for larger dipole strengths of the magnetic atoms. In addition to the technical improvements, we therefore decided to replace our "working horse" chromium by the most magnetic element dysprosium (Dy), with a magnetic dipole moment μ_m of 10 Bohr magneton (compare Cr: $\mu_\mathrm{m} = 6\,\mu_\mathrm{B}$). The ^{164}Dy BEC, realized by the group of B. Lev in 2011, has shown strong dipolar effects even without reducing the s-wave scattering length a [40]. Indeed, the relative dipole strength $\epsilon_\mathrm{dd} \propto \mu_\mathrm{m}^2\, m/a$ (with m the atomic mass) is expected to be around eight times larger than in chromium[108]. In addition, the fermionic isotope ^{161}Dy has recently been cooled below the Fermi temperature by the Lev group [41], opening the route to study quantum degenerate *dipolar Fermi gases* and *dipolar Bose-Fermi mixtures*.

Already above the threshold to quantum degeneracy, both bosonic and fermionic dysprosium isotopes are expected to show interesting *scattering properties*. Reason is the anisotropic scattering potential which relies on the strong DDI, but also on the non-zero electronic orbital angular momentum (with a quantum number $L = 6$) in the ground-state. Spin changing collisions are thus enhanced when compared to other atomic species [203, 204], allowing e.g. for studies of spinor physics at very low external magnetic fields. Furthermore, partial waves higher than the usual s-wave contribute to the elastic scattering processes, even at ultra-low temperatures [41]. Following the methods presented

[108] The scaling of the relative dipole strengths between chromium and dysprosium is not exactly known, as the s-wave scattering length of ^{164}Dy is still undetermined.

in Ref. [205], our new setup may be suited to directly image the various partial waves at selectable collision energies: making use of the tunable trapping potentials, two ultracold thermal clouds[109] can be accelerated towards each other to collide at a well controlled relative velocity. The elastically scattered atoms, imaged after time-of-flight, are expected to form density patterns of particular symmetries that directly reflect the symmetries of the partial waves involved in the scattering process.
Regarding the experiments with dysprosium BECs, the *s*-wave scattering lengths of the bosonic isotopes ^{162}Dy and ^{164}Dy in the zero-temperature limit are yet undetermined. Here, due to the anisotropic two-body interaction potentials, many Feshbach resonances are expected to occur for magnetic field strengths up to 200 Gauss [206]. Measuring the positions and the widths of these resonances will give further insight into the scattering properties of dysprosium and set the basis to control the contact interactions in the system.

[109] For bosons, the temperature of the clouds should be chosen just above condensation temperature. Finite temperature effects are thus minimized and interference effects (as observed for BECs) can be avoided.

A appendix

A.1 Scattering Properties of Bosonic Dipolar Gases

In this section, we discuss the basic elastic and inelastic scattering properties of cold and ultra-cold bosonic dipolar gases, mainly summarizing the theoretical results from Refs. [57, 58, 101, 108, 109, 207–210]. The studies presented here are motivated by the question whether or not dipolar scattering effects are relevant in ultra-cold chromium samples. We furthermore comment on the relevance of dipolar scattering in several other atomic and molecular species, where ultra-cold samples exist.

A.1.1 Elastic Dipolar Scattering

In this part, we consider the elastic scattering properties of two bosonic dipolar particles. After describing the coupling of different partial waves by the dipole-dipole interaction, we discuss the energy-dependent elastic scattering cross-section. Finally, we compare the characteristic dipolar parameters of different existing dipolar systems.
Let us consider a system of two polarized dipolar particles (with the polarization direction z) at a relative distance r. The dipoles interact only via the dipole-dipole interaction potential $V'_{\rm dd}(r,\vartheta) = d^2\,(1-3\cos^2\vartheta)/r^3$ with d the (electric or magnetic) dipole strength and ϑ defining the relative alignment of the dipoles (see section 2.2.2). The equation of relative motion of the two particles can be written in a dimensionless form [58],

$$\left[-\frac{1}{2}\nabla^2 + \frac{1}{r^3}(1-3\left(\hat{r}\,\cdot\,\hat{z}\right)^2)\right]\,\psi(\boldsymbol{r}) = E_{\rm rel}\psi(\boldsymbol{r}), \tag{A.1}$$

if all distances and energies are measured in *dipole units*, i.e. in units of the dipole length D and the dipole energy E_D:

$$D \stackrel{\rm def}{=} \frac{m_{\rm red}d^2}{\hbar^2}, \quad \text{and} \quad E_D \stackrel{\rm def}{=} \frac{d^2}{D^3} = \frac{\hbar^6}{m_{\rm red}^3 d^4}, \tag{A.2}$$

where $m_{\rm red} = m/2$ is the reduced mass of the two-particle system. In absence of the dipolar interactions, the spherical harmonics $Y_{lm}(\hat{r})$ solve the eigenvalue problem of the angular part of equation (A.1) [96]. However, the situation is different in presence of the dipolar interactions: the dipole-dipole interaction (DDI) potential couples states of

different angular momenta, with the strength given by the *potential matrix elements* $V_{ll'}^{(m)}$,

$$\begin{aligned} V_{ll'}^{(m)} &\stackrel{\text{def}}{=} \langle lm|\, 1-3(\hat{r}\,\cdot\,\hat{z})^2\,|l'm\rangle \\ &= \left[1-\frac{3}{2l+1}\left(\frac{(l-m)(l+m)}{2l-1}+\frac{(l-m+1)(l+m+1)}{2l+3}\right)\right]\delta_{l,l'} \\ &\quad -\frac{3}{2l+3}\sqrt{\frac{((l+1)^2-m^2)((l+2)^2-m^2)}{(2l+1)(2l+5)}}\,\delta_{l,l'-2} \\ &\quad -\frac{3}{2l-1}\sqrt{\frac{((l-1)^2-m^2)(l^2-m^2)}{(2l-3)(2l+1)}}\,\delta_{l,l'+2} \end{aligned} \tag{A.3}$$

with $|lm\rangle = Y_{lm}(\hat{r})$ and $\delta_{\alpha,\alpha'}$ the Kronecker delta. We see that, due to its d-wave symmetry, the DDI potential couples states with a difference in relative angular momenta[110] $\Delta l = |l-l'| = 2$ and $\Delta l = 0$ (for $l = l' \neq 0$). Hence, the spherical harmonics do not represent eigenstates of the system at small distances r, where the coupling by the dipole-dipole interaction is strong. During the scattering process, the eigenstate of the system contains contributions from several spherical harmonics, with a weight depending on the distance between the dipolar particles r. Therefore, a *coupled-channel* calculation is required to calculate the elastic scattering properties of a dipolar gas. While in principle an infinite number of channels has to be considered in such calculations, the results for the elastic scattering cross-section have shown to converge by using a finite set of channels in the so-called adiabatic representation of the scattering states [58]. In Fig. A.1, we show the results from Ref. [58] for the elastic scattering cross-section σ (averaged over the full solid angle) as a function of the relative kinetic energy E. We see that, for energies $E \gg E_D$, the strongest contribution to the elastic scattering cross-section is given by $\sigma_{lm,l'm} = \sigma_{21,21}$ which belongs to an incoming and outgoing d-wave channel with quantum numbers $(l,m) = (l',m) = (2,1)$. Then for a decreasing energy E, the s-wave scattering cross-section $\sigma_{00,00}$ grows until it becomes the dominant term in the low energy limit $E \ll E_D$.

This result in the low energy regime seems counter-intuitive, since the dipole-dipole interaction does not directly couple an ingoing and an outgoing s-wave channel due to the vanishing potential matrix element for $l = l' = 0$. However, it has been shown that a second order coupling via the d-wave channel introduces an effective scattering potential [57, 207]

$$V_{00}(r) \approx -\frac{\left|V_{02}^{(0)}/r^3\right|^2}{l(l+1)/(2r^2)} \stackrel{\text{def}}{=} -\frac{C_4}{r^4}, \tag{A.4}$$

[110] Due to the cylindrical symmetry of the dipole-dipole interaction potential, the projection of the angular momentum m is conserved in the scattering process [58]. In general, it is the total value $m + M_S$ which is conserved, with M_S the spin projection of the two-body system. Here, we assume that M_S does not change during the collision, which can be ensured in the experiment by trapping the atoms in the energetically lowest Zeeman sublevel.

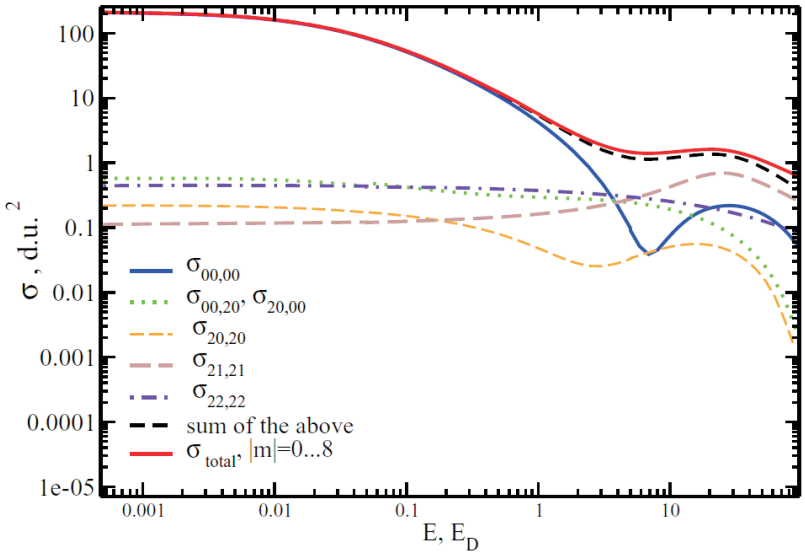

Fig. A.1, Elastic dipolar scattering: Total elastic scattering cross section σ_{total} (red line) in dipole units (d.u.) in dependence of the energy E in units of the dipolar energy E_D [58]. Furthermore, the contributions $\sigma_{lm,l'm}$ of the most important scattering processes are shown, with the quantum numbers (l, m) denoting the incoming and (l', m) the outgoing channel. Figure taken from [58].

with the potential matrix element $V_{02}^{(0)}$ given by Eq. (A.3). In dipole units and using $l = 2$, the resulting coefficient is $C_4 = (4/3)\sqrt{5}$. We may estimate a finite interaction range $r_{4,0}$ of this potential using Heisenberg's uncertainty relation [57] (see section 2.2.1):

$$r_{4,0} = \sqrt{\frac{2d\,C_4}{\hbar^2}} \approx 1.09\,D. \tag{A.5}$$

We compare the dipolar parameters of different atomic and one molecular species in Tab. A.1, choosing only systems where ultra-cold samples have been realized. We see that, for typical temperatures $T \leq 100\,\mu\text{K}$ of cold thermal samples, only dysprosium and the polar molecules are expected to show significant scattering via higher partial waves ($l > 0$), as they fulfill the condition $E_D/k_B < 100\,\mu\text{K}$.
Furthermore, if the interaction range $r_{4,0} \approx 1.09\,D$ is comparable to the typical interaction range $r_0 \approx 100\,a_0$ of the short-range interactions, the dipolar induced s-wave scattering becomes important for ultra-low temperatures. Refering to Tab. A.1, we see that e.g. for dysprosium we obtain $r_{0,4} \sim 218\,a_0$. We therefore expect a significant contribution of the dipolar interactions to the elastic s-wave scattering properties in this system. For chromium the scattering is probably dominated by the short-range interactions, as we obtain $r_{0,4} \sim 25\,a_0 \ll r_0$.

species	dipole moment	D	E_D/k_B
^{87}Rb	$1\,\mu_\mathrm{B}$	$0.6\,a_0$	16 K
^{52}Cr	$6\,\mu_\mathrm{B}$	$23\,a_0$	13 mK
^{164}Dy	$10\,\mu_\mathrm{B}$	$200\,a_0$	53 µK
K-Rb	~ 0.5 Debye	$60,000\,a_0$	1 nK

Tab. A.1, Dipole length D and dipole energy E_D for different dipolar systems: Except from chromium, the table displays the parameters for rubidium (Rb) which is widely used in ultra-cold atoms experiments, dysprosium (Dy) as it exhibits the largest magnetic dipole moment of all condensed atomic species and of a potassium-rubidium molecule (K-Rb). In the case of the molecule, we specify the electric dipole moment measured in a sample of fermionic ^{40}K^{87}Rb molecules in the singlet ground-state [59].

A.1.2 Inelastic Dipolar Scattering

The inelastic scattering properties of a dipolar gas, i.e. the recombination of three dipoles to a weakly bound dimer and a single dipole, have been theoretically investigated in Ref. [210]. It was found that a universal description of the three-body scattering process is possible, if both, the dipole length D and the s-wave scattering length a are much larger than the interaction range $r_0 \sim 100\,a_0$ of the short-range interactions (see section 2.2.1). Under this assumption, the three-body recombination rate K_3 in a dipolar BEC takes the following form[111] [210],

$$K_3 \simeq \frac{32\sqrt{3}\pi^2\hbar}{m}\left[a^4 + 0.44\,a^2D^2\right] + \frac{2\,\cdot\,495\hbar}{3!\,m}\,D^4, \tag{A.6}$$

with m the mass of a single particle. If the scattering length is much larger than the dipole length, i.e. $a/D \gg 1$, the recombination rate approaches the well known result $K_3 \propto a^4$ for short-range interacting bosons in the universal regime $a \gg r_0$ [211]. In the dipolar case, however, one obtains additional terms proportional to the dipole length D which are explained by the creation of atom-dimer states with non-zero angular momentum. In particular, when $a/D \ll 1$, the rate K_3 is entirely determined by the dipole length, with $K_3 \propto D^4$.

In systems of polar molecules, the dipole strength can be tuned by an external electric field. Furthermore, the s-wave scattering length can be varied by the same field, close to a so-called *shape-resonance* [101, 108], in analogy to the Feshbach resonance technique discussed in section 3.2.1. Thus, the universal regime $(D, a) \gg r_0$ can be reached in molecular systems, enabling future experimental studies of inelastic dipolar scattering processes.

[111] We have divided the result obtained in Ref. [210] by the Bose-enhancement factor 3!, as we consider a BEC instead of a thermal cloud.

The situation is different in atomic systems with permanent magnetic dipoles where the dipole length D is fixed: here, the dipolar inelastic scattering is only relevant if the condition $D \gg r_0$ is fulfilled for the given atomic parameters. Since this is not the case for chromium (see Tab. A.1), dipolar contributions to the inelastic scattering properties of a ^{52}Cr BEC are expected to be small. They may be substantial, however, in ultracold dysprosium samples. Due to the unknown short-range scattering properties, experimental studies are required to further investigate the influence of the inelastic collisions in this system.

A.2 GPE in Thomas-Fermi Approximation with Contact Interactions

This section describes the ground-state properties of a BEC with dominant contact interactions, discussed in section 2.4.2. In the TF approximation, and neglecting the dipolar interactions, the stationary Gross-Pitaevskii equation, given by Eq. (2.15a), writes

$$\mu\psi(\boldsymbol{r}) \stackrel{\text{TF}}{=} \left[V_{\text{ext}}(\boldsymbol{r}) + g\, n(\boldsymbol{r})\right] \psi(\boldsymbol{r}), \tag{A.7}$$

with μ the chemical potential, g the contact coupling strength and with the harmonic potential given by $V_{\text{ext}}(\boldsymbol{r}) = m/2\,(\omega_x^2 x^2 + \omega_y^2 y^2 + \omega_z^2 z^2)$. Hence, the density distribution $n(\boldsymbol{r}) = N\ |\psi(\boldsymbol{r})|^2$ of the BEC in each direction has the shape of an inverted parabola:

$$n(\boldsymbol{r}) = \frac{\mu - V_{\text{ext}}(\boldsymbol{r})}{g} = n_0 \ \cdot\ \max\left\{\left(1 - \frac{x^2}{R_x^2} - \frac{y^2}{R_y^2} - \frac{z^2}{R_z^2}\right), 0\right\}, \tag{A.8}$$

where $n_0 \stackrel{\text{def}}{=} n(0) = 15N/(8\pi R_x R_y R_z)$ is the central density of the condensate, with (R_x, R_y, R_z) its Thomas-Fermi radii in the respective directions. The boundary $n(\boldsymbol{R}) = 0$ of the BEC is determined by the condition $V_{\text{ext}}(\boldsymbol{R}) = \mu$, with $\boldsymbol{R} = (R_x, R_y, R_z)$. Therefore, the TF radii are given by $R_i^2 = 2\mu/(m\omega_i^2)$ with $i = x, y, z$. The chemical potential is then obtained via the normalization condition $\int \mathrm{d}r^3 n(\boldsymbol{r}) = N$, with the result [89]

$$\mu = \frac{15^{2/5}}{2} \left(\frac{Na}{\bar{a}_{\text{ho}}}\right)^{2/5} \hbar\bar{\omega}, \tag{A.9}$$

where $\bar{\omega} = (\omega_x\omega_y\omega_z)^{1/3}$ is the mean trapping frequency and $\bar{a}_{\text{ho}} = \sqrt{\hbar/(m\bar{\omega})}$ the mean harmonic oscillator length. With this result, we obtain the mean condensate radius $\bar{R} = (R_x R_y R_z)^{1/3}$ in the form that we have used in section 2.4.2:

$$\bar{R} = 15^{1/5}\, \bar{a}_{\text{ho}} \left(\frac{Na}{\bar{a}_{\text{ho}}}\right)^{1/5} \approx 1.72\, \bar{a}_{\text{ho}} \left(\frac{Na}{\bar{a}_{\text{ho}}}\right)^{1/5}. \tag{A.10}$$

A.3 Calculations on the Ground State in a 1D Optical Lattice

In this part, we show the explicit calculations of the ground-state properties of a contact interacting BEC in a 1D lattice, discussed in section 4.3. We obtain analytical results for e.g. the local chemical potential μ_j and the atom number distribution N_j on the lattice sites.

Let us first consider the properties of a (sub-)condensate located on the j-th lattice site. We assume the tight-binding approximation to be valid with the harmonically trapped on-site condensates well inside the quasi-2D regime [179]. The spatial part of the on-site wave functions can then be written in the form $\Phi_j(\boldsymbol{r}, N_j) = \phi_{\mathrm{G}}(z - z_j)\, \phi_{\mathrm{TF}}^{(j)}(x, y, N_j)$, assuming a Gaussian shape[112] in the z-direction and a Thomas-Fermi profile in the radial directions. Inserting this ansatz for the wave function into the stationary GPE (2.15a) and integrating over the z-direction, we obtain

$$\left[-\frac{\hbar^2}{2m}\nabla_\perp^2 + \mathcal{V}(\boldsymbol{r}_\perp) + \tilde{g}N_j \left|\phi_{\mathrm{TF}}^{(j)}\right|^2\right] \phi_{\mathrm{TF}}^{(j)} = \mu_j \phi_{\mathrm{TF}}^{(j)}, \tag{A.11}$$

with μ_j the local chemical potential, $\tilde{g} \stackrel{\mathrm{def}}{=} g/(\sqrt{2\pi}a_{\mathrm{lat}})$ the 2D coupling strength[113], $\boldsymbol{r}_\perp = (x, y)$ the radial coordinates, and $\mathcal{V}(\boldsymbol{r}_\perp) = m\omega_\rho^2 {\boldsymbol{r}_\perp}^2/2$ the harmonic trapping potential in the radial directions. For simplicity, we have assumed a cylindrically symmetric harmonic trapping potential, with ω_ρ the radial trap frequency. In the TF-approximation, we neglect the kinetic term in Eq. (A.11), and thus obtain the radial wave function $\phi_{\mathrm{TF}}^{(j)}(\boldsymbol{r}_\perp)$ via

$$\left|\phi_{\mathrm{TF}}^{(j)}(\boldsymbol{r}_\perp)\right|^2 = \frac{\mu_j - \mathcal{V}(\boldsymbol{r}_\perp)}{\tilde{g}N_j} = \frac{\mu_j}{\tilde{g}N_j} \cdot \max\left\{\left(1 - \frac{{\boldsymbol{r}_\perp}^2}{\left(R_\perp^{(j)}\right)^2}\right), 0\right\}, \tag{A.12}$$

where $R_\perp^{(j)} = \sqrt{2\mu_j/(m\omega_\rho^2)}$ is the TF radius of the condensate on the j-th lattice site. From the normalization condition $\int \mathrm{d}^2R \left|\phi_{\mathrm{TF}}^{(j)}\right|^2 = 1$, we obtain the local chemical potential

$$\mu_j = \sqrt{\frac{m\tilde{g}\,\omega_\rho^2}{\pi}}\, N_j^{1/2} \stackrel{\mathrm{def}}{=} U_1 \cdot N_j^{1/2}, \tag{A.13}$$

$$\text{with} \quad U_1 \stackrel{\mathrm{def}}{=} \sqrt{\frac{m\tilde{g}\,\omega_\rho^2}{\pi}}.$$

[112] The Gaussian wave function is given by $\phi_{\mathrm{G}}(z) = (a_{\mathrm{lat}}\sqrt{\pi})^{-1/2} \exp\left[-z^2/(2a_{\mathrm{lat}}^2)\right]$, with $a_{\mathrm{lat}} \stackrel{\mathrm{def}}{=} \sqrt{\hbar/(m\omega_{\mathrm{lat}})}$ the harmonic oscillator length in the lattice direction.

[113] The 2D coupling strength is obtained by integrating out the z-direction in the interaction *energy* term, $g \int \mathrm{d}z\, \mathrm{d}^2R\, |\phi_{\mathrm{G}}(z)\phi_{\mathrm{TF}}(\boldsymbol{r}_\perp)|^4 = \tilde{g} \int \mathrm{d}^2R |\phi_{\mathrm{TF}}(\boldsymbol{r}_\perp)|^4$.

U_1 is a constant that depends neither on the number of atoms nor on the site index and is determined by the dimensionality of the system[114]. We now consider the *global* properties of the lattice system. As shown in section 4.3.2, we can write the global chemical potential μ as the sum of the local chemical potential μ_j and the local potential energy $\varepsilon_j \overset{\text{def}}{=} m\omega_z^2(d_{\text{lat}}j)^2/2 \overset{\text{def}}{=} \Omega j^2$ that arises from the harmonic trapping in the lattice direction z. With the local chemical potential given by Eq. (A.13), we thus obtain an expression for the atom number N_j on the j-th lattice site,

$$N_j = \max\left\{\left(\frac{\mu - \Omega\, j^2}{U_1}\right)^2, 0\right\} \overset{\text{def}}{=} N_0 \cdot \max\left\{\left(1 - \frac{j^2}{j_{\text{inv}}^2}\right)^2, 0\right\}, \tag{A.14}$$

where $N_0 \overset{\text{def}}{=} (\mu/U_1)^2$ is the atom number in the central lattice site and $j_{\text{inv}} \overset{\text{def}}{=} \sqrt{\mu/\Omega}$ is the inversion point above which the lattice sites are not occupied anymore. The global chemical potential μ is then calculated using the condition[115] $\sum_j N_j = N$. We first replace the lattice site index by $j \to z_j/d_{\text{lat}}$, where the z_j are the (discrete) positions of the lattice sites in the z-direction and d_{lat} is the spacing between the sites. We then express N_j via Eq. (A.14) and use continuous variables, i.e. we replace $z_j \to z$. By integrating over the z-direction, we finally obtain the global chemical potential μ:

$$\mu = \left(\frac{15}{16} N\, U_1^2 \sqrt{\Omega}\right)^{2/5}, \tag{A.15}$$

which agrees with the results given in Refs. [179, 180]. We can thus express the ground-state properties of a BEC in a 1D lattice in terms of the trap parameters (harmonic trap and lattice), the contact coupling strength and the total atom number in the system.

A.4 Variational Calculations with a Gaussian-Shaped Dipolar BEC

Here, we describe the principle of the Gaussian variational calculations, an efficient numerical method to calculate the critical scattering length of a trapped dipolar BEC. For simplicity, we assume a cylindrically symmetric harmonic trap, with the symmetry axis aligned with the polarization direction z of the dipoles. The according trap frequencies are given by ω_ρ and ω_z in the radial and in the axial direction, respectively. Close to the stability threshold, the interactions are typically sufficiently weak such that the shape of the dBEC is well described by a Gaussian (see section 2.4.1). We therefore write the wave

[114] In general, the relation is given by $\mu_j = U_\alpha |\psi_j|^\alpha$, where $\alpha = 4/(2 + D)$ is determined by the dimensionality D of the system [179]. Therefore, we obtain $\alpha = 1$ in the quasi-2D system.

[115] The condition $\sum_j N_j = N$ ensures that the sum of the local atom numbers N_j equals the total number of atoms N in the system.

function of the BEC in the form

$$\psi_{\mathrm{G}}(\rho, z) \stackrel{\mathrm{def}}{=} \frac{1}{\pi^{3/4}\, l_\rho^2 l_z}\, \exp\!\left[-\frac{\rho^2}{2\, l_\rho^2} - \frac{z^2}{2\, l_z^2}\right], \tag{A.16}$$

where l_ρ (l_z) is the radial (axial) width of the condensate. With this ansatz, we can calculate the energy per particle via Eq. (2.17). This yields the following terms for the kinetic energy E_{kin}, the potential energy E_{pot}, the contact interaction energy E_{contact} and the dipolar interaction energy E_{dip}:

$$\begin{aligned}
\frac{E_{\mathrm{kin}}}{N\,\hbar\bar{\omega}} &= \frac{a_{\mathrm{ho}}^2}{4}\left(\frac{2}{l_\rho^2} + \frac{1}{l_z^2}\right) \\
\frac{E_{\mathrm{pot}}}{N\,\hbar\bar{\omega}} &= \frac{2l_\rho^2 + \lambda^2 l_z^2}{4\, a_{\mathrm{ho}}^2 \lambda^{2/3}} \\
\frac{E_{\mathrm{contact}}}{N\,\hbar\bar{\omega}} &= \frac{N}{\sqrt{2\pi}}\left(\frac{a_{\mathrm{ho}}}{l_\rho}\right)^2 \frac{a}{l_z} \\
\frac{E_{\mathrm{dip}}}{N\,\hbar\bar{\omega}} &= -\frac{N}{\sqrt{2\pi}}\left(\frac{a_{\mathrm{ho}}}{l_\rho}\right)^2 \frac{a_{\mathrm{dd}} f_{\mathrm{dip}}(\kappa)}{l_z},
\end{aligned} \tag{A.17}$$

with N the BEC atom number, $\bar{\omega} = (\omega_\rho^2 \omega_z)^{1/3}$ the mean trapping frequency, $a_{\mathrm{ho}} = \sqrt{\hbar/(m\bar{\omega})}$ the mean harmonic oscillator length, $\lambda = \omega_z/\omega_\rho$ the trap aspect ratio, $\kappa = l_\rho/l_z$ the cloud aspect ratio, and $f_{\mathrm{dip}}(\kappa)$ the dipolar anisotropic function given by Eq. (2.23b). For a given set of parameters $\{N, \omega_\rho, \omega_z, a\}$, the equilibrium values of the widths l_ρ and l_z, and thus the ground-state wave function, may be found by searching the global minimum of the total energy (given by the sum of the energy terms written above) in a variational calculation. Depending on the starting conditions in the calculations, also meta-stable states (i.e. local energy minima) can be found in such procedure, as we show in section 5.2. If no local or global energy minimum exists for positive values l_ρ, l_z, the condensate is unstable for this set of parameters.

A.5 Dipolar Interaction Energy between Two Gaussian-Shaped Clouds

In this part, we derive the interaction energy between two Gaussian-shaped dipolar BECs. The result of these calculations is used to obtain the total inter-site interaction energy in a linear array of dipolar BECs in section 2.5.3. Furthermore, by variational calculations, it allows to calculate the stability threshold of a dBEC confined in a 1D optical lattice, with the result shown in section 5.4.1. The derivation of the dipolar inter-site energy, that is shown here, has been performed by David Peter in the scope of his diploma thesis in our group [118, Ch. 2.2].

The wave functions of the two dipolar condensates, each confined by a cylindrically

symmetric trap along the polarization direction z, are approximated by the Gaussian forms

$$\Psi_1(\rho, z) = \frac{1}{\pi^{3/4}\sigma_\rho\sqrt{\sigma_z}} \exp\left(-\frac{\rho^2}{2\sigma_\rho^2} - \frac{z^2}{2\sigma_z^2}\right), \tag{A.18a}$$

$$\text{and} \quad \Psi_2(\rho, z) = \frac{1}{\pi^{3/4}\sigma_\rho\sqrt{\sigma_z}} \exp\left(-\frac{\rho^2}{2\sigma_\rho^2} - \frac{(z-l)^2}{2\sigma_z^2}\right), \tag{A.18b}$$

where σ_ρ (σ_z) is the radial (axial) size of the condensates and l the distance between them. The corresponding atomic densities are defined via $n_j(\boldsymbol{r}) = N\,|\Psi_j(\boldsymbol{r})|^2$ with $j = 1, 2$. The spacing between the clouds is assumed to be much larger than the axial size, i.e. $l \gg \sigma_z$, such that the overlap of the wave functions is small. Introducing the total wave function $\Psi(\boldsymbol{r}) = \Psi_1(\boldsymbol{r}) + \Psi_2(\boldsymbol{r})$ and using the dipolar term from the Gross-Pitaevskii energy functional (2.17), the total dipolar energy in the system is given by

$$\begin{aligned} E_{\text{dip}} &= \frac{N^2}{2} \int \mathrm{d}^3 r \int \mathrm{d}^3 r' \, |\Psi(\boldsymbol{r})|^2 \, V'_{\text{dd}}(\boldsymbol{r}, \boldsymbol{r}') \, |\Psi(\boldsymbol{r}')|^2 \\ &\simeq 2\, E_{\text{on,dip}} + E_{\text{inter}}, \end{aligned} \tag{A.19a}$$

where we have used the approximation $\Psi_1(\boldsymbol{r})\Psi_2(\boldsymbol{r}) \simeq 0$ and the definitions for the dipolar *on-site energy* (note the indices for the local densities n_j)

$$\begin{aligned} E_{\text{on,dip}} &\stackrel{\text{def}}{=} \frac{1}{2} \int \mathrm{d}^3 r \int \mathrm{d}^3 r' n_1(\boldsymbol{r}) V'_{\text{dd}}(\boldsymbol{r}, \boldsymbol{r}') n_1(\boldsymbol{r}') \\ &= \frac{1}{2} \int \mathrm{d}^3 r \int \mathrm{d}^3 r' n_2(\boldsymbol{r}) V'_{\text{dd}}(\boldsymbol{r}, \boldsymbol{r}') n_2(\boldsymbol{r}'), \end{aligned} \tag{A.19b}$$

and the *inter-site energy*

$$E_{\text{inter}} \stackrel{\text{def}}{=} \int \mathrm{d}^3 r \int \mathrm{d}^3 r' n_1(\boldsymbol{r}) V'_{\text{dd}}(\boldsymbol{r}, \boldsymbol{r}') n_2(\boldsymbol{r}'). \tag{A.19c}$$

We have chosen the definition of the dipolar inter-site energy such that it is defined globally, i.e. we count it only once for the full system. In contrast, the dipolar on-site energy agrees with the definition for a single cloud. We therefore have to add up the contributions from both the condensates to obtain the total dipolar on-site energy in the system.

To evaluate of the dipolar inter-site energy, we write it in terms of the Fourier transforms, using the convolution theorem twice:

$$E_{\text{inter}} = (2\pi)^{3/2} \int \mathrm{d}^3 k \, \mathcal{F}\{n_1\}\mathcal{F}\{V'_{\text{dd}}\}\mathcal{F}\{n_2\}. \tag{A.20}$$

The choice of the Gaussian form for the density distributions $n_j(\boldsymbol{r})$ allows for a simple expression of their Fourier transforms

$$\mathcal{F}\{n_j\} = \frac{N}{(2\pi)^{3/2}} \exp\left(-\frac{1}{4}k_\rho^2\sigma_\rho^2 - \frac{1}{4}k_z^2\sigma_z^2 - il\delta_{j2}k_z\right), \tag{A.21}$$

where $k_\rho^2 = k_x^2 + k_y^2$, $\delta_{12} = 0$ and $\delta_{22} = 1$. We see that the relative distance l between the two clouds in coordinate space has transformed into a phase shift in Fourier space. Using the Fourier transform of the dipolar potential [113, Ch. A.5.2] $\mathcal{F}\{V'_{\mathrm{dd}}\} = -g_{\mathrm{dd}}\,(1 - 3k_z^2/k^2)$, we obtain the following expression for the inter-site interaction energy:

$$E_{\mathrm{inter}} = -\frac{g_{\mathrm{dd}}N^2}{(2\pi)^3}\int \mathrm{d}^3k \left(1 - 3\frac{k_z^2}{k^2}\right) \exp\left(-\frac{1}{2}k_\rho^2\sigma_\rho^2 - \frac{1}{2}k_z^2\sigma_z^2 - ilk_z\right). \tag{A.22}$$

For the next step, we exchange the integration variable $\boldsymbol{k}$ by the dimensionless variable $\boldsymbol{q} = \sigma_\rho\boldsymbol{k}$. We furthermore define the cloud aspect ratio $\kappa = \sigma_\rho/\sigma_z$ and the dimensionless distance $L = l/\sigma_\rho$ between the clouds, such that

$$E_{\mathrm{inter}} = -\frac{g_{\mathrm{dd}}N^2}{(2\pi)^3\sigma_\rho^3}\int \mathrm{d}^3q \left(1 - 3\frac{q_z^2}{q^2}\right) \exp\left(-\frac{1}{2}q_\rho^2 - \frac{1}{2}q_z^2\kappa^{-2} - iLq_z\right). \tag{A.23}$$

To perform the integration, we use the spherical coordinates (q, θ, φ): the integration over the angle φ simply yields a factor 2π as the system is cylindrically symmetric. With the substitution $u \stackrel{\mathrm{def}}{=} \cos\theta$, we obtain

$$E_{\mathrm{inter}} = -\frac{2\pi\,\cdot\, g_{\mathrm{dd}}N^2}{(2\pi)^3\sigma_\rho^3}\int_0^\infty \mathrm{d}q \int_{-1}^{1} \mathrm{d}u\, q^2\left(1 - 3u^2\right) \exp\left(-\frac{1}{2}q^2\left((1-u^2) + \kappa^{-2}u^2\right) - iqLu\right). \tag{A.24}$$

The final analytical step is the integration over q, leading to the result

$$E_{\mathrm{inter}} = -\frac{g_{\mathrm{dd}}N^2}{(2\pi)^{3/2}\sigma_\rho^3}\int_0^1 \mathrm{d}u\, \frac{(1-3u^2)(1-u^2(\eta+L^2))}{(1-\eta u^2)^{5/2}} \exp\left(-\frac{L^2u^2}{2(1-\eta u^2)}\right). \tag{A.25}$$

For simplified notation, we have used $\eta \stackrel{\mathrm{def}}{=} 1 - \kappa^{-2}$ and furthermore, we have changed the integration limits, exploiting the even symmetry in the variable u. The last remaining integration over u has to be performed numerically. Therefore, Eq. (A.25) is the final analytical result for the dipolar interaction energy of two Gaussian-shaped clouds, in agreement with Ref. [51].

A.6 Excitation Spectrum of a 2D Homogeneous Dipolar BEC

Here, we show a brief derivation of the excitation spectrum in a 2D homogeneous dipolar gas, discussed in section 5.1.2. A more detailed treatment can be found in Refs. [16, 26, 27]. We start from the excitation spectrum in the 3D homogeneous system, given by Eq. (5.1),

$$E(q) = \hbar\omega(q) = \sqrt{\left(\frac{\hbar^2 q^2}{2m}\right)^2 + \frac{\hbar^2 q^2}{2m}\, 2n_0\,[g + g_{\rm dd}\,(3\cos^2\alpha - 1)]}, \tag{A.26}$$

where n_0 is the (constant) atomic density, $q = |\boldsymbol{q}|$ is the quasi-momentum of the excitations and α the angle between their propagation direction and the polarization direction z of the dipoles. We see that in Eq. (A.26), the contact and the dipolar interactions are represented by the Fourier transform of the two-body interaction potential (see Eq. (2.8)) given by $\widetilde{V}_{\rm int} = g + g_{\rm dd}(3\cos^2\alpha - 1)$.
In a 2D homogeneous condensate, we may approximate the shape of the wave function in the z-direction by a Gaussian $\phi_{\rm G}(z) = (l_z\sqrt{\pi})^{-1/2}\exp[-z^2/(2l_z^2)]$, with l_z the width of the sample. The atomic density along z is then given by $n(z) = |\phi_{\rm G}(z)|^2 = (l_z\sqrt{\pi})^{-1}\,\exp[-z^2/l_z^2]$ with its Fourier transform $\widetilde{n}(q_z) = (2\pi)^{-1/2}\,\exp[-q_z^2 l_z^2/4]$. With this ansatz for the wave function, we obtain the effective 2D interaction potential in Fourier space $\widetilde{V}_{\rm int}^{(2D)}(q_\perp)$ via [16]

$$\begin{aligned}
\widetilde{V}_{\rm int}^{(2D)}(q_\perp) &\stackrel{\rm def}{=} \int_{-\infty}^{\infty} \widetilde{n}(q_z)\,\widetilde{V}_{\rm int}\,\widetilde{n}(-q_z)\,{\rm d}q_z \\
&= \frac{1}{2\pi}\int_{-\infty}^{\infty} {\rm e}^{-q_z^2 l_z^2/2}\left[g + g_{\rm dd}\left(\frac{3q_z^2}{q_\perp^2 + q_z^2} - 1\right)\right]{\rm d}q_z \\
&= \frac{1}{\sqrt{2\pi}l_z}\left[g + 2g_{\rm dd}\,H_{2D}\left(\frac{q_\perp l_z}{\sqrt{2}}\right)\right],
\end{aligned} \tag{A.27}$$

where we have used $\cos^2\alpha = q_z^2/q^2 = q_z^2/(q_\perp^2 + q_z^2)$ with $q_\perp$ (q_z) the radial (axial) component of the quasi-momentum. The function $H_{2D}(\chi)$ that we obtain from the integration is given by $H_{2D}(\chi) = 1 - \frac{3}{2}\sqrt{\pi}|\chi|\exp[\chi^2]\,{\rm erfc}[\chi]$, with ${\rm erfc}[\chi]$ the complementary error function. We furthermore introduce the two-dimensional homogeneous density $n_{2D} = \sqrt{2\pi}\,l_z\,n_0$. Finally, by replacing in Eq. (A.26) the expressions $q \to q_\perp$, $n_0 \to n_{2D}$ and $\widetilde{V}_{\rm int} \to \widetilde{V}_{\rm int}^{(2D)}(q_\perp)$, we obtain the excitation spectrum of a 2D homogeneous dBEC,

$$\begin{aligned}
E(q_\perp) &= \sqrt{\left(\frac{\hbar^2 q_\perp^2}{2m}\right)^2 + \frac{\hbar^2 q_\perp^2}{2m}\,2\,n_{2D}\,\widetilde{V}_{\rm int}^{(2D)}(q_\perp)} \\
&= \sqrt{\left(\frac{\hbar^2 q_\perp^2}{2m}\right)^2 + \frac{\hbar^2 q_\perp^2}{2m}\,2n_0\,\left[g + 2g_{\rm dd}\,H_{2D}\left(\frac{q_\perp l_z}{\sqrt{2}}\right)\right]}.
\end{aligned} \tag{A.28}$$

A.7 Fitting Procedure in Calibration of the Scattering Length

In this part, we describe the fitting procedure used in the calibration of the scattering length (see section 3.2.3). The calibration procedure relies on the linear scaling relation between the scattering length a and the quantity R_y^5/N, where R_y is the condensate radius in the y-direction after time-of-flight (TOF) and N the BEC atom number. In section 3.2.3, we write this scaling relation in the form

$$R_y^5/N = \sigma_{\text{eff}}(a - a_{\text{offset}}), \tag{A.29}$$

with the effective scaling parameter σ_{eff} and the offset $a_{\text{offset}} = (9 \pm 1)\, a_0$ that we obtain from numerical simulations[116]. In the measurements, we record the condensate radius R_y and the atom number N for different values of the current I_{FB} in the Feshbach coils. This current produces the magnetic field close to the Feshbach resonance (FR), that we use to tune the scattering length a. We take at least four datapoints per value I_{FB} and compute the mean value $\overline{\frac{R_y^5}{N}}(I_{\text{FB}})$.

As a first step in the fitting procedure, we extract the scaling parameter σ_{eff} by fitting Eq. (A.29) to the mean data $\overline{\frac{R_y^5}{N}}(I_{\text{FB}})$ in a logarithmic fit:

$$\log\left\{\overline{\frac{R_y^5}{N}}(I_{\text{FB}})\right\} \overset{\text{fit}}{=} \log\left\{\sigma_{\text{eff}}\left[a_{\text{bg}}\left(1 - \frac{\Delta I_{\text{FB}}}{I_{\text{FB}} - I_{\text{FB},0}}\right) - a_{\text{offset}}\right]\right\}. \tag{A.30}$$

Here, we have replaced $a \to a_{\text{bg}}\left(1 - \frac{\Delta I_{\text{FB}}}{I_{\text{FB}} - I_{\text{FB},0}}\right)$, with $a_{\text{bg}} = (102.5 \pm 0.4)\, a_0$ the background scattering length [144] and with the additional fitting parameters ΔI_{FB} and $I_{\text{FB},0}$ that characterize the width and the center of the resonance in terms of the Feshbach current[117]. We are using a logarithmic fit as otherwise the data on the lower side of the FR ($I_{\text{FB}} < I_{\text{FB},0}$), where R_y^5/N takes very large values, would be strongly over-weighted with respect to the data on the upper side of the FR, where R_y^5/N tends to zero.

From this fit, in principle, we already obtain all the relevant information (width and position of the FR) for the calibration of the scattering length. However, as we are furthermore interested in the uncertainty of the scattering length, we need to know the correlation between the fitting parameters ΔI_{FB} and $I_{\text{FB},0}$. Hence, we perform a second fit of the form

$$\log\left\{a_{\text{exp}}(I_{\text{FB}})\right\} \overset{\text{fit}}{=} \log\left\{a_{\text{bg}}\left(1 - \frac{\Delta I_{\text{FB}}}{I_{\text{FB}} - I_{\text{FB},0}}\right)\right\}, \tag{A.31}$$

where we have inserted the scattering length a_{exp}, which we obtain from the measured values $R_y^5/N(I_{\text{FB}})$ using the relation (3.2b): $a_{\text{exp}} = \sigma_{\text{eff}}^{-1}\, \frac{R_y^5}{N} + a_{\text{offset}}$. The MATLAB fitting

[116] The scaling parameter a_{offset} depends in general on the trap frequencies used in the calibration measurement. Here, we use $\omega_{(x,y,z)} = 2\pi \cdot (680, 624, 270)\,\text{Hz}$, as specified in section 3.2.3.

[117] In principle it is possible to obtain σ_{eff} by using only datapoints far away from the Feshbach resonance, where $a \simeq a_{\text{bg}}$. However, it has proven more robust and precise to perform the fit with the full dataset and the formula given by Eq. (A.30).

routine 'leasqr.m' directly provides the correlation between the two fitting parameters. Replacing for clarity the variables $x \stackrel{\text{def}}{=} \Delta I_{\text{FB}}$ and $y \stackrel{\text{def}}{=} I_{\text{FB},0}$, with their fitting uncertainties Δx and Δy and their correlation s_{xy}, we can compute the uncertainty of the scattering length [212]

$$(\Delta a)^2 = (\partial a/\partial x)^2 \cdot (\Delta x)^2 + (\partial a/\partial y)^2 \cdot (\Delta y)^2 + 2 \cdot (\partial a/\partial x)\Delta x\,(\partial a/\partial y)\Delta y \cdot s_{xy}. \tag{A.32}$$

Depending on the magnitude and the sign of the correlation s_{xy}, we can, in general, identify three different cases:

i) $s_{xy} = 0$: There is no correlation between the two variables. This means, the uncertainties on x and y are summed in quadrature, just as for any uncorrelated parameters.

ii) $s_{xy} = 1$: The parameters are fully correlated, meaning that $\Delta a = (\partial a/\partial x) \cdot \Delta x + (\partial a/\partial y) \cdot \Delta y$. Therefore, we are just adding linearly the single uncertainties.

iii) $s_{xy} = -1$: The parameters are fully anti-correlated, which means that the uncertainties on the single parameters (partly) compensate each other. The value of interest (in our case the scattering length a) is then better known than the uncertainties on each parameter suggest.

In our case, due to the non-trivial function $a(I_{\text{FB}}, I_{\text{FB},0}, \Delta I_{\text{FB}}) = a_{\text{bg}}\left(1 - \frac{\Delta I_{\text{FB}}}{I_{\text{FB}} - I_{\text{FB},0}}\right)$, the sign of the correlation does not immediately tell if the uncertainty on a is increasing or decreasing. Going through the calculations, we find indeed that a negative correlation means smaller uncertainties in the experimentally interesting region *above* the FR.

The full uncertainty on the scattering length that we specify in section 3.2.3 does not only include the uncertainties on ΔI_{FB} and $I_{\text{FB},0}$ given by Eq. (A.32). We also include the uncertainties on the background scattering length [144] $\Delta a = \frac{\partial a}{\partial a_{\text{bg}}} \cdot 0.4\,a_0$ and on the offset value $\Delta a_{\text{offset}} = 1\,a_0$ (see section 3.2.3). Both of these uncertainties are added in quadrature to the terms given in Eq. (A.32) as they are uncorrelated with the errors of the fitting procedure.

A.8 Magnetic Field Ramps at the Feshbach Resonance

Close to the magnetic Feshbach resonance at $B_0 = 589.1\,\text{G}$, we aim for a high level of control over the magnetic field strength, as the scattering length is directly related to it. As explained in section 3.2.2, we tune the current in the Feshbach coils by adding a variable voltage to the set-point of a proportional-integral controller (PI) (see also Ref. [74, Ch.4.2.2]).
Performing slow magnetic field ramps (ramping time $T_{\text{ramp}} \gg 1\,\text{ms}$), the magnetic field at the position of the atoms will directly follow the value programmed at the computer. For fast ramps ($T_{\text{ramp}} \sim 1\,\text{ms}$), however, we have observed strong deviations between

the programmed field value and its actual value measured by Zeeman spectroscopy. We have identified two reasons for the deviations: *(i)* due to the limited bandwidth of the active current stabilization, the PI controller may introduce delays and oscillations in the Feshbach current when its set-point is suddenly changed and *(ii)* eddy currents in the metallic vacuum chamber yield an additional delay of the real magnetic field with respect to the programmed value. We have experimentally addressed both issues, with the results shown in Fig. A.2.

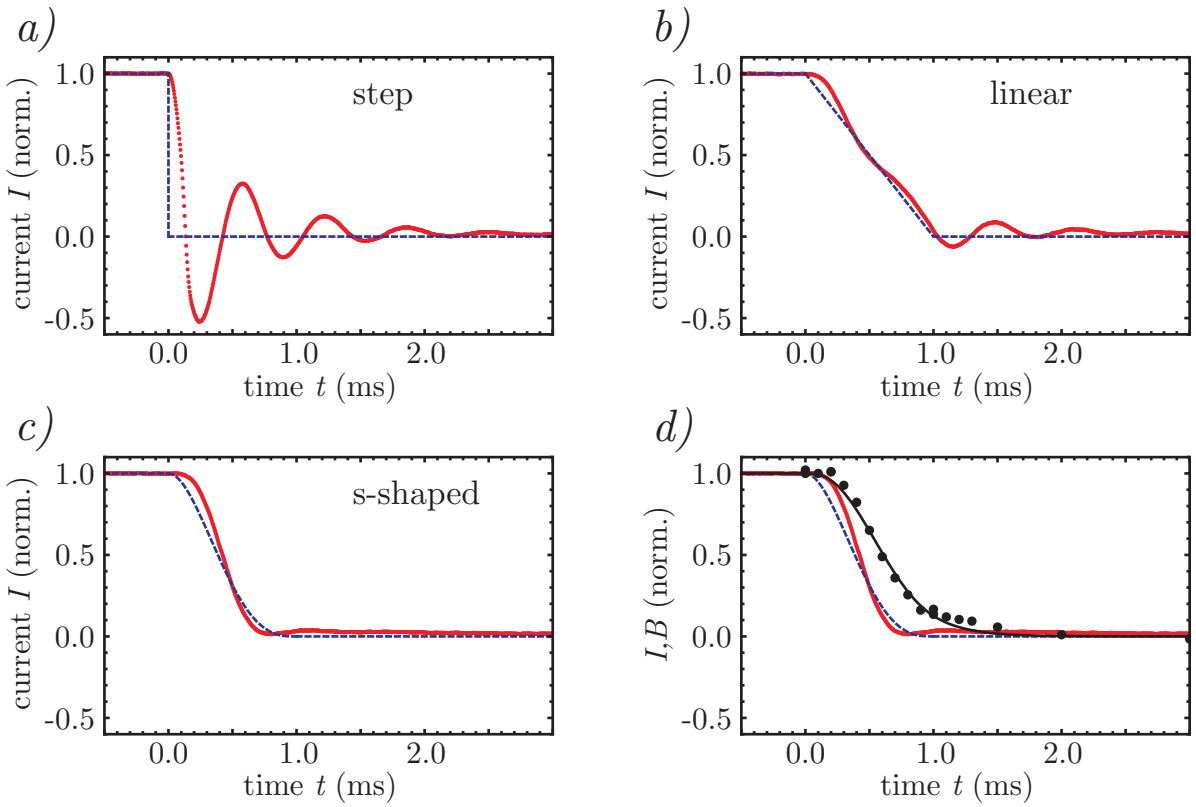

Fig. A.2, Measured Feshbach current and magnetic field at cloud position: Current running through the Feshbach coils (red dots), measured by a transducer, and programmed value of the current (dashed blue line), both in normalized units. *(a)* We observe strong oscillations in the measured current after a sudden change in the programmed value. *(b)* The oscillations are reduced when using a linear ramp and *(c)* are almost suppressed when using the s-shaped ramp given by Eq. (A.33). *(d)* The black dots show the measured field strength B at the position of the atoms, also in normalized units. The measured field exhibits a delay with respect to both the programmed value and the measured current in the coils. The data is well described by the numerical solution $B(t)$ of the differential equation (A.34) with the parameter $\tau = 0.25\,\mathrm{ms}$ (black line).

Optimized magnetic field ramps

We measure the current in the Feshbach coils by a transducer, when the programmed field B_{prog} is changed from $B_i = 626\,\mathrm{G}$ to $B_f = 602\,\mathrm{G}$ by *(a)* a jump, *(b)* a linear ramp or *(c)* an s-shaped ramp. When programming a sudden jump for the field B_{prog}, we observe

strong oscillations of the Feshbach current which are damping out after around 2 ms. These oscillations are reduced when using a linear ramp (with a ramping time of 1 ms), and almost vanish when using an s-shaped ramp of the form

$$B_{\mathrm{prog}}(\widetilde{t}) = B_f - (B_f - B_i) \cdot \left[(k+1) \cdot (1-\widetilde{t})^k - k \cdot (1-\widetilde{t})^{k+1}\right], \tag{A.33}$$

where $\widetilde{t} = t/T_{\mathrm{ramp}}$ is the time normalized by the ramping time T_{ramp} and $k \geq 2$ is the ramping parameter that characterizes the "steepness" of the s-shaped curve. The particular form of the ramp given by Eq. (A.33) ensures a smooth behaviour of the programmed field, as both the derivatives of B_{prog} at the beginning ($\widetilde{t} = 0$) and at the end ($\widetilde{t} = 1$) of the ramp vanish. For the measurements presented here, we have used the parameters $T_{\mathrm{ramp}} = 1\,\mathrm{ms}$ and $k = 3$.

Eddy currents

As mentioned before, eddy currents in the metallic vacuum chamber lead to a delay of the real magnetic field $B(t)$ at the position of the atoms with respect to the programmed field $B_{\mathrm{prog}}(t)$. The field $B(t)$ is well described by the differential equation [36]

$$\tau \dot{B}(t) + B(t) = B_{\mathrm{prog}}(t) \tag{A.34}$$

and we can measure its value at different times of the s-shaped ramp by performing Zeeman spectroscopy[118]. As expected for the s-shaped ramp, we see no oscillations in the measured magnetic field and the behaviour of $B(t)$ is well described by the numerical solution of Eq. (A.34) with the parameter $\tau = 0.25\,\mathrm{ms}$. At the time $t = 1\,\mathrm{ms}$, i.e. at the end of the programmed ramp, the real magnetic field has accomplished around 90 % of the ramp. We can therefore experimentally realize well controlled ramps of the Feshbach magnetic field on time scales around 1 ms.

[118] Each value of the magnetic field shown in Fig. A.2 is the result of a spectroscopy measurement: We vary the detuning of the probe laser in the absorption imaging and extract the resonance frequency from a Lorentzian fit to the recorded atom numbers. From the known Zeeman shift of the magnetic sublevels, we can eventually calculate the magnetic field at the position of the atoms.

References*

[1] M. H. Anderson, J. R. Ensher, M. R. Matthews, C. E. Wieman, and E. A. Cornell: "*Observation of Bose-Einstein Condensation in a Dilute Atomic Vapor.*" Science **269**, 198–201 (1995)

[2] K. Davis, M. Mewes, M. Andrews, N. Druten, D. Durfee, D. Kurn, and W. Ketterle: "*Bose-Einstein Condensation in a Gas of Sodium Atoms.*" Physical Review Letters **75**, 3969–3973 (1995)

[3] C. Bradley, C. Sackett, J. Tollett, and R. Hulet: "*Evidence of Bose-Einstein Condensation in an Atomic Gas with Attractive Interactions.*" Physical Review Letters **75**, 1687–1690 (1995) note: See erratum Ref. [4].

[4] C. Bradley, C. Sackett, J. Tollett, and R. Hulet: "*Evidence of Bose-Einstein Condensation in an Atomic Gas with Attractive Interactions [Phys. Rev. Lett. 75, 1687 (1995)].*" Physical Review Letters **79**, 1170 (1997)

[5] W. S. Bakr, A. Peng, M. E. Tai, R. Ma, J. Simon, J. I. Gillen, S. Fölling, L. Pollet, and M. Greiner: "*Probing the Superfluid-to-Mott Insulator Transition at the Single-Atom Level.*" Science **329**, 547–550 (2010)

[6] J. F. Sherson, C. Weitenberg, M. Endres, M. Cheneau, I. Bloch, and S. Kuhr: "*Single-atom-resolved fluorescence imaging of an atomic Mott insulator.*" Nature **467**, 68–72 (2010)

[7] C. Raman, M. Köhl, R. Onofrio, D. Durfee, C. Kuklewicz, Z. Hadzibabic, and W. Ketterle: "*Evidence for a Critical Velocity in a Bose-Einstein Condensed Gas.*" Physical Review Letters **83**, 2502–2505 (1999)

[8] L. P. Pitaevskii, and S. Stringari: "*Bose-Einstein condensation.*" (Clarendon Press, Oxford and New York, 2003)

[9] J. Roberts, N. Claussen, S. Cornish, E. Donley, E. Cornell, and C. Wieman: "*Controlled Collapse of a Bose-Einstein Condensate.*" Physical Review Letters **86**, 4211–4214 (2001)

[10] E. A. Donley, N. R. Claussen, S. L. Cornish, J. L. Roberts, E. A. Cornell, and C. E. Wieman: "*Dynamics of collapsing and exploding Bose-Einstein condensates.*" Nature **412**, 295–299 (2001)

[11] W. Ketterle, S. Inouye, M. R. Andrews, J. Stenger, H.-J. Miesner, and D. M. Stamper-Kurn: "*Observation of Feshbach resonances in a Bose–Einstein condensate.*" Nature **392**, 151–154 (1998)

[12] C. Chin, P. Julienne, and E. Tiesinga: "*Feshbach resonances in ultracold gases.*" Reviews of Modern Physics **82**, 1225–1286 (2010)

*Most references are linked to the internet (pdf-version): The authors' names to the digital object identifier (doi) and the journal name to the URL-adress.

[13] M. Baranov: "*Theoretical progress in many-body physics with ultracold dipolar gases.*" Physics Reports **464**, 71–111 (2008)

[14] T. Lahaye, C. Menotti, L. Santos, M. Lewenstein, and T. Pfau: "*The physics of dipolar bosonic quantum gases.*" Reports on Progress in Physics **72**, 126401 (2009)

[15] L. Santos, G. V. Shlyapnikov, and M. Lewenstein: "*Roton-Maxon Spectrum and Stability of Trapped Dipolar Bose-Einstein Condensates.*" Phys. Rev. Lett **90**, 250403 (2003)

[16] U. Fischer: "*Stability of quasi-two-dimensional Bose-Einstein condensates with dominant dipole-dipole interactions.*" Physical Review A **73**, 031602 (2006)

[17] L. Landau: "*Theory of the Superfluidity of Helium II.*" Physical Review **60**, 356–358 (1941)

[18] R. Feynman: "*Atomic Theory of the Two-Fluid Model of Liquid Helium.*" Physical Review **94**, 262–277 (1954)

[19] D. Henshaw, and A. Woods: "*Modes of Atomic Motions in Liquid Helium by Inelastic Scattering of Neutrons.*" Physical Review **121**, 1266–1274 (1961)

[20] O. Dutta, and P. Meystre: "*Ground-state structure and stability of dipolar condensates in anisotropic traps.*" Physical Review A **75**, 053604 (2007)

[21] S. Ronen, D. Bortolotti, and J. Bohn: "*Radial and Angular Rotons in Trapped Dipolar Gases.*" Physical Review Letters **98**, 030406 (2007)

[22] K. Góral, L. Santos, and M. Lewenstein: "*Quantum Phases of Dipolar Bosons in Optical Lattices.*" Physical Review Letters **88**, 170406 (2002)

[23] A. Bühler, and H. P. Büchler: "*Supersolid phase in atomic gases with magnetic dipole interaction.*" Physical Review A **84**, 023607 (2011)

[24] Z. Hadzibabic, S. Stock, B. Battelier, V. Bretin, and J. Dalibard: "*Interference of an Array of Independent Bose-Einstein Condensates.*" Physical Review Letters **93**, 180403 (2004)

[25] Z. Hadzibabic, P. Krüger, M. Cheneau, B. Battelier, and J. Dalibard: "*Berezinskii–Kosterlitz–Thouless crossover in a trapped atomic gas.*" Nature **441**, 1118–1121 (2006)

[26] D.-W. Wang, and E. Demler: "*Collective excitations and instabilities in multi-layer stacks of dipolar condensates.*" arXiv:cond-mat/0812.1838 (2008)

[27] M. Klawunn, and L. Santos: "*Hybrid multisite excitations in dipolar condensates in optical lattices.*" Physical Review A **80**, 013611 (2009)

[28] P. Köberle, and G. Wunner: "*Phonon instability and self-organized structures in multilayer stacks of confined dipolar Bose-Einstein condensates in optical lattices.*" Physical Review A **80**, 063601 (2009)

[29] R. Wilson, and J. Bohn: "*Emergent structure in a dipolar Bose gas in a one-dimensional lattice.*" Physical Review A **83**, 023623 (2011)

[30] A. Griesmaier, J. Werner, S. Hensler, J. Stuhler, and T. Pfau: "*Bose-Einstein Condensation of Chromium.*" Physical Review Letters **94**, 160401 (2005)

[31] A. Griesmaier, J. Stuhler, T. Koch, M. Fattori, T. Pfau, and S. Giovanazzi: "*Comparing Contact and Dipolar Interactions in a Bose-Einstein Condensate.*" Physical Review Letters **97**, 250402 (2006)

[32] T. Lahaye, T. Koch, B. Fröhlich, M. Fattori, J. Metz, A. Griesmaier, S. Giovanazzi, and T. Pfau: "*Strong dipolar effects in a quantum ferrofluid.*" Nature **448**, 672–675 (2007)

[33] R. G. Hulet, J. M. Gerton, D. Strekalov, and I. Prodan: "*Direct observation of growth and collapse of a Bose-Einstein condensate with attractive interactions.*" Nature **408**, 692–695 (2000)

[34] A. Gammal, T. Frederico, and L. Tomio: "*Critical number of atoms for attractive Bose-Einstein condensates with cylindrically symmetrical traps.*" Physical Review A **64**, 055602 (2001)

[35] T. Koch, T. Lahaye, J. Metz, B. Fröhlich, A. Griesmaier, and T. Pfau: "*Stabilization of a purely dipolar quantum gas against collapse.*" Nature Physics **4**, 218–222 (2008)

[36] T. Lahaye, J. Metz, B. Fröhlich, T. Koch, M. Meister, A. Griesmaier, T. Pfau, H. Saito, Y. Kawaguchi, and M. Ueda: "*d-Wave Collapse and Explosion of a Dipolar Bose-Einstein Condensate.*" Physical Review Letters **101**, 080401 (2008)

[37] R. Wilson, S. Ronen, and J. Bohn: "*Angular collapse of dipolar Bose-Einstein condensates.*" Physical Review A **80**, 023614 (2009)

[38] J. L. Bohn, R. M. Wilson, and S. Ronen: "*How does a dipolar Bose-Einstein condensate collapse?*" Laser Physics **19**, 547–549 (2009)

[39] K. Henderson, C. Ryu, C. MacCormick, and M. G. Boshier: "*Experimental demonstration of painting arbitrary and dynamic potentials for Bose–Einstein condensates.*" New Journal of Physics **11**, 043030 (2009)

[40] M. Lu, N. Burdick, S. Youn, and B. Lev: "*Strongly Dipolar Bose-Einstein Condensate of Dysprosium.*" Physical Review Letters **107**, 190401 (2011)

[41] M. Lu, N. Burdick, and B. Lev: "*Quantum Degenerate Dipolar Fermi Gas.*" Physical Review Letters **108**, 215301 (2012)

[42] W. Ketterle, D. S. Durfee, and D. M. Stamper-Kurn: "Making, probing and understanding Bose-Einstein condensates." in: *Proceedings of the International School of Physics Enrico Fermi, Course CXL: Bose-Einstein condensation in atomic gases.* (IOS Press, Amsterdam, 1999)

[43] R. Grimm, M. Weidemüller, and Y. B. Ovchinnikov: "Optical Dipole Traps for Neutral Atoms." in: *Advances In Atomic, Molecular, and Optical Physics*. (Academic Press, United States, 2000)

[44] I. Bloch: "*Ultracold quantum gases in optical lattices.*" Nature Physics **1**, 23–30 (2005)

[45] M. Lewenstein, A. Sanpera, V. Ahufinger, B. Damski, A. Sen, and U. Sen: "*Ultracold atomic gases in optical lattices: mimicking condensed matter physics and beyond.*" Advances in Physics **56**, 243–379 (2007)

[46] M. Greiner, O. Mandel, T. Esslinger, T. W. Hänsch, and I. Bloch: "*Quantum phase transition from a superfluid to a Mott insulator in a gas of ultracold atoms.*" Nature **415**, 39–44 (2002)

[47] E. Haller, M. Gustavsson, M. J. Mark, J. G. Danzl, R. Hart, G. Pupillo, and H.-C. Nägerl: "*Realization of an Excited, Strongly Correlated Quantum Gas Phase.*" Science **325**, 1224–1227 (2009)

[48] Q. Beaufils, R. Chicireanu, T. Zanon, B. Laburthe-Tolra, E. Maréchal, L. Vernac, J.-C. Keller, and O. Gorceix: "*All-optical production of chromium Bose-Einstein condensates.*" Physical Review A **77**, 061601 (2008)

[49] G. Bismut, B. Pasquiou, E. Maréchal, P. Pedri, L. Vernac, O. Gorceix, and B. Laburthe-Tolra: "*Collective Excitations of a Dipolar Bose-Einstein Condensate.*" Physical Review Letters **105**, 040404 (2010)

[50] G. Bismut, B. Laburthe-Tolra, E. Marechal, P. Pedri, O. Gorceix, and L. Vernac: "*Anisotropic excitation spectrum of a dipolar quantum Bose gas.*" arXiv:cond-mat/1205.6305 (2012)

[51] M. Fattori, G. Roati, B. Deissler, C. D'Errico, M. Zaccanti, M. Jona-Lasinio, L. Santos, M. Inguscio, and G. Modugno: "*Magnetic Dipolar Interaction in a Bose-Einstein Condensate Atomic Interferometer.*" Physical Review Letters **101**, 190405 (2008)

[52] S. E. Pollack, D. Dries, M. Junker, Y. P. Chen, T. A. Corcovilos, and R. G. Hulet: "*Extreme Tunability of Interactions in a 7-Li Bose-Einstein Condensate.*" Physical Review Letters **102**, 090402 (2009)

[53] J. Metz, T. Lahaye, B. Fröhlich, A. Griesmaier, T. Pfau, H. Saito, Y. Kawaguchi, and M. Ueda: "*Coherent collapses of dipolar Bose-Einstein condensates for different trap geometries.*" New Journal of Physics **11**, 055032 (2009)

[54] K. Aikawa, A. Frisch, M. Mark, S. Baier, A. Rietzler, R. Grimm, and F. Ferlaino: "*Bose-Einstein Condensation of Erbium.*" Physical Review Letters **108**, 210401 (2012)

[55] J. Stenger, S. Inouye, M. Andrews, H.-J. Miesner, D. Stamper-Kurn, and W. Ketterle: "*Strongly Enhanced Inelastic Collisions in a Bose-Einstein Condensate near Feshbach Resonances.*" Physical Review Letters **82**, 2422–2425 (1999)

[56] R. V. Krems, G. C. Groenenboom, and A. Dalgarno: "*Electronic Interaction Anisotropy between Atoms in Arbitrary Angular Momentum States.*" The Journal of Physical Chemistry A **108**, 8941–8948 (2004)

[57] J. L. Bohn, M. Cavagnero, and C. Ticknor: "*Quasi-universal dipolar scattering in cold and ultracold gases.*" New Journal of Physics **11**, 055039 (2009)

[58] V. Roudnev, and M. Cavagnero: "*Resonance phenomena in ultracold dipole-dipole scattering.*" Journal of Physics B: Atomic, Molecular and Optical Physics **42**, 044017 (2009)

[59] K.-K. Ni, S. Ospelkaus, M. H. G. d. Miranda, A. Pe'er, B. Neyenhuis, J. J. Zirbel, S. Kotochigova, P. S. Julienne, D. S. Jin, and J. Ye: "*A High Phase-Space-Density Gas of Polar Molecules.*" Science **322**, 231–235 (2008)

[60] K.-K. Ni, S. Ospelkaus, D. Wang, G. Quemener, B. Neyenhuis, M. H. G. d. Miranda, J. L. Bohn, J. Ye, and D. S. Jin: "*Dipolar collisions of polar molecules in the quantum regime.*" Nature **464**, 1324–1328 (2010)

[61] S. Ospelkaus, K.-K. Ni, D. Wang, M. H. G. d. Miranda, B. Neyenhuis, G. Quemener, P. S. Julienne, J. L. Bohn, D. S. Jin, and J. Ye: "*Quantum-State Controlled Chemical Reactions of Ultracold Potassium-Rubidium Molecules.*" Science **327**, 853–857 (2010)

[62] M. H. G. d. Miranda, A. Chotia, B. Neyenhuis, D. Wang, G. Quéméner, S. Ospelkaus, J. L. Bohn, J. Ye, and D. S. Jin: "*Controlling the quantum stereodynamics of ultracold bimolecular reactions.*" Nature Physics **7**, 502–507 (2011)

[63] C.-H. Wu, J. W. Park, P. Ahmadi, S. Will, and M. W. Zwierlein: "*Ultracold Fermionic Feshbach Molecules of 23Na-40K.*" arXiv:cond-mat/1206.5023 (2012)

[64] V. Bendkowsky, B. Butscher, J. Nipper, J. P. Shaffer, R. Löw, and T. Pfau: "*Observation of ultralong-range Rydberg molecules.*" Nature **458**, 1005–1008 (2009)

[65] W. Li, T. Pohl, J. M. Rost, S. T. Rittenhouse, H. R. Sadeghpour, J. Nipper, B. Butscher, J. B. Balewski, V. Bendkowsky, R. Löw, and T. Pfau: "*A Homonuclear Molecule with a Permanent Electric Dipole Moment.*" Science **334**, 1110–1114 (2011)

[66] M. D. Cowley, and R. E. Rosensweig: "*The interfacial stability of a ferromagnetic fluid.*" Journal of Fluid Mechanics **30**, 671 (1967)

[67] G. E. Astrakharchik, J. Boronat, I. L. Kurbakov, and Y. E. Lozovik: "*Quantum Phase Transition in a Two-Dimensional System of Dipoles.*" Physical Review Letters **98**, 060405 (2007)

[68] H. P. Büchler, E. Demler, M. Lukin, A. Micheli, N. Prokof'ev, G. Pupillo, and P. Zoller: "*Strongly Correlated 2D Quantum Phases with Cold Polar Molecules: Controlling the Shape of the Interaction Potential.*" Physical Review Letters **98**, 060404 (2007)

[69] P. Pedri, and L. Santos: "*Two-Dimensional Bright Solitons in Dipolar Bose-Einstein Condensates.*" Physical Review Letters **95**, 200404 (2005)

[70] I. Tikhonenkov, B. Malomed, and A. Vardi: "*Anisotropic Solitons in Dipolar Bose-Einstein Condensates.*" Physical Review Letters **100**, 090406 (2008)

[71] P. Köberle, D. Zajec, G. Wunner, and B. Malomed: "*Creating two-dimensional bright solitons in dipolar Bose-Einstein condensates.*" Physical Review A **85**, 023630 (2012)

[72] N. Cooper, E. Rezayi, and S. Simon: "*Vortex Lattices in Rotating Atomic Bose Gases with Dipolar Interactions.*" Physical Review Letters **95**, 200402 (2005)

[73] A. Griesmaier: "*Dipole-dipole interaction in a degenerate quantum gas: Bose-Einstein condensation of chromium atoms.*" (PhD thesis, Stuttgart, 2006)

[74] T. Koch: "*Enhancing the dipolar character of a Bose-Einstein condensate: From perturbative effects to a purely dipolar quantum gas.*" (PhD thesis, Stuttgart, 2008)

[75] S. Müller, J. Billy, E. Henn, H. Kadau, A. Griesmaier, M. Jona-Lasinio, L. Santos, and T. Pfau: "*Stability of a dipolar Bose-Einstein condensate in a one-dimensional lattice.*" Physical Review A **84**, 053601 (2011)

[76] J. Billy, E. A. L. Henn, S. Müller, T. Maier, H. Kadau, A. Griesmaier, M. Jona-Lasinio, L. Santos, and T. Pfau: "*Deconfinement-induced collapse of a coherent array of dipolar Bose-Einstein condensates.*" Physical Review A **86**, 051603 (2012)

[77] W. D. Phillips: "*Nobel Lecture: Laser cooling and trapping of neutral atoms.*" Reviews of Modern Physics **70**, 721–741 (1998)

[78] A. Einstein: "*Quantentheorie des einatomigen idealen Gases. Zweite Abhandlung.*" Sitzungsberichte der Preußischen Akademie der Wissenschaften 245–257 (1925)

[79] J. Klaers, J. Schmitt, F. Vewinger, and M. Weitz: "*Bose–Einstein condensation of photons in an optical microcavity.*" Nature **468**, 545–548 (2010)

[80] J. P. Eisenstein, and A. H. MacDonald: "*Bose–Einstein condensation of excitons in bilayer electron systems.*" Nature **432**, 691–694 (2004)

[81] R. Balili, V. Hartwell, D. Snoke, L. Pfeiffer, and K. West: "*Bose-Einstein Condensation of Microcavity Polaritons in a Trap.*" Science **316**, 1007–1010 (2007)

[82] J. Kasprzak, M. Richard, S. Kundermann, A. Baas, P. Jeambrun, J. M. J. Keeling, F. M. Marchetti, M. H. Szymańska, R. André, J. L. Staehli, V. Savona, P. B. Littlewood, B. Deveaud, and L. S. Dang: "*Bose–Einstein condensation of exciton polaritons.*" Nature **443**, 409–414 (2006)

[83] J. F. Allen, and A. D. Misener: "*Flow of Liquid Helium II.*" Nature **141**, 75 (1938)

[84] P. Kapitza: "*Viscosity of Liquid Helium below the lambda-Point.*" Nature **141**, 74 (1938)

[85] F. London: "*On the Bose-Einstein Condensation.*" Physical Review **54**, 947–954 (1938)

[86] L. D. Landau, E. M. Lifshitz, and L. E. Reichl: "*Statistical Physics, Part 1 (Third Edition).*" Physics Today **34**, 74 (1981)

[87] O. Penrose: "*CXXXVI. On the quantum mechanics of helium II.*" Philosophical Magazine Series 7 **42**, 1373–1377 (1951)

[88] O. Penrose, and L. Onsager: "*Bose-Einstein Condensation and Liquid Helium.*" Physical Review **104**, 576–584 (1956)

[89] C. J. Pethick, and H. Smith: "*Bose-Einstein Condensation in Dilute Gases.*" (Cambridge University Press, Cambridge, 2001)

[90] V. Bagnato, D. Pritchard, and D. Kleppner: "*Bose-Einstein condensation in an external potential.*" Physical Review A **35**, 4354–4358 (1987)

[91] F. Dalfovo, S. Giorgini, and S. Stringari: "*Theory of Bose-Einstein condensation in trapped gases.*" Reviews of Modern Physics **71**, 463–512 (1999)

[92] R. M. Ziff, G. E. Uhlenbeck, and M. Kac: "*The ideal Bose-Einstein gas, revisited.*" Physics Reports **32**, 169–248 (1977)

[93] J. Dalibard: "Collisional dynamics of ultra-cold atomic gases." in: *Proceedings of the International School of Physics Enrico Fermi, Course CXL: Bose-Einstein condensation in gases.* (IOS Press, Amsterdam, 1998)

[94] Y. Castin: "Bose-Einstein Condensates in Atomic Gases: Simple Theoretical Results." in: *Coherent atomic matter waves.* serie: Les Houches. ed.: R. Kaiser, C. Westbrook, and F. David. (Springer, Berlin / Heidelberg, 2001)

[95] J. Werner, A. Griesmaier, S. Hensler, J. Stuhler, T. Pfau, A. Simoni, and E. Tiesinga: "*Observation of Feshbach Resonances in an Ultracold Gas of 52Cr.*" Phys. Rev. Lett **94**, 183201 (2005)

[96] C. Cohen-Tannoudji: "*Quantum mechanics.*" (Wiley-Interscience, Weinheim, 1996)

[97] L. d. Broglie: "The Wave Nature of the Electron." in: *Nobel Lectures, Physics 1922–1941.* (Elsevier, Amsterdam, 1965)

[98] W. Krauth: "*Quantum Monte Carlo Calculations for a Large Number of Bosons in a Harmonic Trap.*" Physical Review Letters **77**, 3695–3699 (1996)

[99] G. Astrakharchik, and Y. Lozovik: "*Super-Tonks-Girardeau regime in trapped one-dimensional dipolar gases.*" Physical Review A **77**, 013404 (2008)

[100] V. Hnizdo: "*Generalized second-order partial derivatives of 1/r.*" Eur. Journal of Physics **32**, 287–297 (2011)

[101] D. Bortolotti, S. Ronen, J. Bohn, and D. Blume: "*Scattering Length Instability in Dipolar Bose-Einstein Condensates.*" Physical Review Letters **97**, 160402 (2006)

[102] S. Ronen, D. Bortolotti, D. Blume, and J. Bohn: "*Dipolar Bose-Einstein condensates with dipole-dependent scattering length.*" Physical Review A **74**, 033611 (2006)

[103] M. Marinescu, and L. You: "*Controlling Atom-Atom Interaction at Ultralow Temperatures by dc Electric Fields.*" Physical Review Letters **81**, 4596–4599 (1998)

[104] I. Bloch, and W. Zwerger: "*Many-body physics with ultracold gases.*" Reviews of Modern Physics **80**, 885–964 (2008)

[105] E. Lieb, R. Seiringer, and J. Yngvason: "*Bosons in a trap: A rigorous derivation of the Gross-Pitaevskii energy functional.*" Physical Review A **61**, 043602 (2000)

[106] H. R. Sadeghpour, J. L. Bohn, M. J. Cavagnero, B. D. Esry, I. I. Fabrikant, J. H. Macek, and A. R. P. Rau: "*Collisions near threshold in atomic and molecular physics.*" Journal of Physics B: Atomic, Molecular and Optical Physics **33**, R93–R140 (2000)

[107] D.-W. Wang: "*An effective many-body theory for strongly interacting polar molecules.*" New Journal of Physics **10**, 053005 (2008)

[108] S. Yi, and L. You: "*Trapped atomic condensates with anisotropic interactions.*" Physical Review A **61**, 041604 (2000)

[109] S. Yi, and L. You: "*Trapped condensates of atoms with dipole interactions.*" Physical Review A **63**, 053607 (2001)

[110] C. Eberlein, S. Giovanazzi, and D. O'Dell: "*Exact solution of the Thomas-Fermi equation for a trapped Bose-Einstein condensate with dipole-dipole interactions.*" Physical Review A **71**, 033618 (2005)

[111] D. O'Dell, S. Giovanazzi, and C. Eberlein: "*Exact Hydrodynamics of a Trapped Dipolar Bose-Einstein Condensate.*" Physical Review Letters **92**, 250401 (2004)

[112] S. Giovanazzi, A. Görlitz, and T. Pfau: "*Tuning the Dipolar Interaction in Quantum Gases.*" Physical Review Letters **89**, 130401 (2002)

[113] J. Metz: "*Collapse of dipolar Bose-Einstein condensates for different trap geometries.*" (PhD thesis, Stuttgart, 2010)

[114] N. Parker, and D. O'Dell: "*Thomas-Fermi versus one- and two-dimensional regimes of a trapped dipolar Bose-Einstein condensate.*" Physical Review A **78**, 041601 (2008)

[115] M. Zaman, and D. Blume: "*Aligned dipolar Bose-Einstein condensate in a double-well potential: From cigar shaped to pancake shaped.*" Physical Review A **80**, 053622 (2009)

[116] T. Lahaye, T. Pfau, and L. Santos: "*Mesoscopic Ensembles of Polar Bosons in Triple-Well Potentials.*" Physical Review Letters **104**, 170404 (2010)

[117] P. Köberle: "*Ground-state structures and dynamics of dipolar Bose-Einstein condensates in single and multi-layered traps.*" (PhD thesis, Stuttgart, 2011)

[118] D. Peter: "*Theoretical investigations of dipolar quantum gases in multi-well potentials.*" (Diploma thesis, Stuttgart, 2011)

[119] M. Rosenkranz, Y. Cai, and W. Bao: "*Effective dipole-dipole interactions in multi-layered dipolar Bose-Einstein condensates.*" arXiv:cond-mat/1201.6176 (2012)

[120] D. Peter, K. Pawlowski, T. Pfau, and K. Rzazewski: "*Mean-field description of dipolar bosons in triple-well potentials.*" arXiv:cond-mat/1201.2615v1 (2012)

[121] A. Pikovski, M. Klawunn, G. Shlyapnikov, and L. Santos: "*Interlayer Superfluidity in Bilayer Systems of Fermionic Polar Molecules.*" Physical Review Letters **105**, 215302 (2010)

[122] H. Kadau: "*A dipolar Bose-Einstein Condensate in a one-dimensional Optical Lattice.*" (Diploma thesis, Stuttgart, 2011)

[123] J. Stuhler: "*Kontinuierliches Laden einer Magnetfalle mit lasergekühlten Chromatomen.*" (PhD thesis, Konstanz, 2001)

[124] A. Griesmaier: "*Aufbau einer kombinierten magneto-optischen Falle für Chrom und Rubidium.*" (Diploma thesis, Stuttgart, 2002)

[125] P. Schmidt: "*Scattering properties of ultra-cold chromium atoms.*" (PhD thesis, Stuttgart, 2003)

[126] S. Hensler: "*Wechselwirkungen in ultrakalten dipolaren Gasen.*" (PhD thesis, Stuttgart, 2004)

[127] J. Werner: "*Observation of Feshbach resonances in an ultracold gas of 52Cr.*" (PhD thesis, Stuttgart, 2006)

[128] M.-O. Mewes, M. Andrews, N. Druten, D. Kurn, D. Durfee, and W. Ketterle: "*Bose-Einstein Condensation in a Tightly Confining dc Magnetic Trap.*" Physical Review Letters **77**, 416–419 (1996)

[129] C. Foot: "*Atomic physics.*" (Oxford University Press, Oxford, 2003)

[130] C. J. Dedman, J. Nes, T. M. Hanna, R. G. Dall, K. G. H. Baldwin, and A. G. Truscott: "*Optimum design and construction of a Zeeman slower for use with a magneto-optic trap.*" Review of Scientific Instruments **75**, 5136 (2004)

[131] J. Prodan, W. Phillips, and H. Metcalf: "*Laser Production of a Very Slow Monoenergetic Atomic Beam.*" Physical Review Letters **49**, 1149–1153 (1982)

[132] C. Townsend, N. Edwards, C. Cooper, K. Zetie, C. Foot, A. Steane, P. Szriftgiser, H. Perrin, and J. Dalibard: "*Phase-space density in the magneto-optical trap.*" Physical Review A **52**, 1423–1440 (1995)

[133] A. S. Arnold, and P. J. Manson: "*Atomic density and temperature distributions in magneto-optical traps.*" J. Opt. Soc. Am. B **17**, 497–506 (2000)

[134] C. Bradley, J. McClelland, W. Anderson, and R. Celotta: "*Magneto-optical trapping of chromium atoms.*" Physical Review A **61**, 053407 (2000)

[135] P. O. Schmidt, S. Hensler, J. Werner, T. Binhammer, A. Görlitz, and T. Pfau: "*Continuous loading of cold atoms into a Ioffe Pritchard magnetic trap.*" Journal of Optics B: Quantum and Semiclassical Optics **5**, S170–S177 (2003)

[136] J. Stuhler, P. Schmidt, S. Hensler, J. Werner, J. Mlynek, and T. Pfau: "*Continuous loading of a magnetic trap.*" Physical Review A **64**, 031405 (2001)

[137] P. O. Schmidt, S. Hensler, J. Werner, T. Binhammer, A. Görlitz, and T. Pfau: "*Doppler cooling of an optically dense cloud of magnetically trapped atoms.*" Journal of the Optical Society of America B **20**, 960 (2003)

[138] W. Ketterle, and D. E. Pritchard: "*Atom cooling by time-dependent potentials.*" Physical Review A **46**, 4051–4054 (1992)

[139] K. B. Davis, M.-O. Mewes, and W. Ketterle: "*An analytical model for evaporative cooling of atoms.*" Applied Physics B Laser and Optics **60**, 155–159 (1995)

[140] C. A. Sackett, C. C. Bradley, and R. G. Hulet: "*Optimization of evaporative cooling.*" Physical Review A **55**, 3797–3801 (1997)

[141] E. A. L. Henn, J. A. Seman, E. R. F. Ramos, A. H. Iavaronni, T. Amthor, and V. S. Bagnato: "*Evaporation in atomic traps: A simple approach.*" American Journal of Physics **75**, 907 (2007)

[142] D. Guéry-Odelin, J. Söding, P. Desbiolles, and J. Dalibard: "*Is Bose-Einstein condensation of atomic cesium possible?*" Europhysics Letters (EPL) **44**, 25–30 (1998)

[143] S. Hensler, J. Werner, A. Griesmaier, P. Schmidt, A. Görlitz, T. Pfau, S. Giovanazzi, and K. Rzazewski: "*Dipolar relaxation in an ultra-cold gas of magnetically trapped chromium atoms.*" Applied Physics B: Lasers and Optics **77**, 765–772 (2003)

[144] B. Pasquiou, G. Bismut, Q. Beaufils, A. Crubellier, E. Maréchal, P. Pedri, L. Vernac, O. Gorceix, and B. Laburthe-Tolra: "*Control of dipolar relaxation in external fields.*" Physical Review A **81**, 042716 (2010)

[145] J. D. Jackson: "*Classical electrodynamics.*" (Wiley, New York, 1975)

[146] D. Brink, and C. Sukumar: "*Majorana spin-flip transitions in a magnetic trap.*" Physical Review A **74**, 035401 (2006)

[147] M. Fattori, T. Koch, S. Goetz, A. Griesmaier, S. Hensler, J. Stuhler, and T. Pfau: "*Demagnetization cooling of a gas.*" Nature Physics **2**, 765–768 (2006)

[148] T. Hänsch, and B. Couillaud: "*Laser frequency stabilization by polarization spectroscopy of a reflecting reference cavity.*" Optics Communications **35**, 441–444 (1980)

[149] J. Werner: "*Kontinuierliches Laden einer Magnetfalle mit lasergekühlten Chromatomen.*" (Diploma thesis, Stuttgart, 2000)

[150] P. Rehme: "*Laden eines Wellenleiters mit lasergekühlten Chromatomen.*" (Diploma thesis, Stuttgart, 2006)

[151] C. Wieman, and T. Hänsch: "*Doppler-Free Laser Polarization Spectroscopy.*" Physical Review Letters **36**, 1170–1173 (1976)

[152] E. D. Black: "*An introduction to Pound–Drever–Hall laser frequency stabilization.*" American Journal of Physics **69**, 79 (2001)

[153] R. W. P. Drever, J. L. Hall, F. V. Kowalski, J. Hough, G. M. Ford, A. J. Munley, and H. Ward: "*Laser phase and frequency stabilization using an optical resonator.*" Applied Physics B Photophysics and Laser Chemistry **31**, 97–105 (1983)

[154] M. Schmitt: "*Laserstabilisierung mit einem hochstabilen Transferresonator.*" (Bachelor thesis, Stuttgart, 2010)

[155] B. Steinheil: "*Aufbau eines frequenzverdoppelten Diodenlasersystems zur Untersuchung ultrakalter Chrom-Atome.*" (Diploma thesis, Stuttgart, 2003)

[156] B. Fröhlich, T. Lahaye, B. Kaltenhäuser, H. Kübler, S. Müller, T. Koch, M. Fattori, and T. Pfau: "*Two-frequency acousto-optic modulator driver to improve the beam pointing stability during intensity ramps.*" Review of Scientific Instruments **78**, 043101 (2007)

[157] J. Stuhler, A. Griesmaier, T. Koch, M. Fattori, T. Pfau, S. Giovanazzi, P. Pedri, and L. Santos: "*Observation of Dipole-Dipole Interaction in a Degenerate Quantum Gas.*" Physical Review Letters **95**, 150406 (2005)

[158] V. Roudnev, and M. Cavagnero: "*Universal resonant ultracold molecular scattering.*" Physical Review A **79**, 014701 (2009)

[159] S. Giere, M. Kurrat, and U. Schumann: "HV dielectric strength of shielding electrodes in vacuum circuit-breakers." in: *20th International Symposium on Discharges and Electrical Insulation in Vacuum.* (Conference Publications, Tours (France), 2002)

[160] I. Mazets, and G. Kurizki: "*Modification of Scattering Lengths via Magnetic Dipole-Dipole Interactions.*" Physical Review Letters **98**, 140401 (2007)

[161] H. Feshbach: "*Unified Theory of Nuclear Reactions.*" Reviews of Modern Physics **36**, 1076–1078 (1964)

[162] J. Stuhler, A. Griesmaier, J. Werner, T. Koch, M. Fattori, and T. Pfau: "*Ultracold chromium atoms: from Feshbach resonances to a dipolar Bose-Einstein condensate.*" Journal of Modern Optics **54**, 647–660 (2007)

[163] E. Timmermans, P. Tommasini, M. Hussein, and A. Kerman: "*Feshbach resonances in atomic Bose–Einstein condensates.*" Physics Reports **315**, 199–230 (1999)

[164] F. A. Abeelen, and B. J. Verhaar: "*Time-Dependent Feshbach Resonance Scattering and Anomalous Decay of a Na Bose-Einstein Condensate.*" Physical Review Letters **83**, 1550–1553 (1999)

[165] K. Xu, T. Mukaiyama, J. R. Abo-Shaeer, J. K. Chin, D. E. Miller, and W. Ketterle: "*Formation of Quantum-Degenerate Sodium Molecules.*" Physical Review Letters **91**, 210402 (2003)

[166] V. Yurovsky, A. Ben-Reuven, P. Julienne, and C. Williams: "*Atom loss from Bose-Einstein condensates due to Feshbach resonance.*" Physical Review A **60**, R765–R768 (1999)

[167] Q. Beaufils, A. Crubellier, T. Zanon, B. Laburthe-Tolra, E. Maréchal, L. Vernac, and O. Gorceix: "*Feshbach resonance in d-wave collisions.*" Physical Review A **79**, 032706 (2009)

[168] B. Fröhlich: "*Strong Dipolar Effects in a Chromium Bose-Einstein Condensate.*" (Diploma thesis, Stuttgart, 2007)

[169] S. Giovanazzi, P. Pedri, L. Santos, A. Griesmaier, M. Fattori, T. Koch, J. Stuhler, and T. Pfau: "*Expansion dynamics of a dipolar Bose-Einstein condensate.*" Physical Review A **74**, 013621 (2006)

[170] O. Morsch, and M. Oberthaler: "*Dynamics of Bose-Einstein condensates in optical lattices.*" Reviews of Modern Physics **78**, 179–215 (2006)

[171] N. W. Ashcroft, N. D. Mermin, and J. Gress: "*Festkörperphysik.*" (Oldenbourg, München, 2001)

[172] C. Kittel: "*Einführung in die Festkörperphysik.*" (Oldenbourg, München, 2006)

[173] J. Slater: "*A Soluble Problem in Energy Bands.*" Physical Review **87**, 807–835 (1952)

[174] N. McLachlan: "*Theory and application of Mathieu functions.*" (Clarendon Press, Oxford, 1947)

[175] G. Brooker: "*Modern classical optics.*" (Oxford University Press, Oxford, 2003)

[176] P. T. Ernst, S. Götze, J. S. Krauser, K. Pyka, D.-S. Lühmann, D. Pfannkuche, and K. Sengstock: "*Probing superfluids in optical lattices by momentum-resolved Bragg spectroscopy.*" Nature Physics **6**, 56–61 (2009)

[177] M. Greiner: "*Ultracold quantum gases in three-dimensional optical lattice potentials.*" (PhD thesis, München, 2003)

[178] W. Zwerger: "*Mott-Hubbard transition of cold atoms in optical lattices.*" Journal of Optics B: Quantum and Semiclassical Optics **5**, S9–S16 (2003)

[179] A. Smerzi, and A. Trombettoni: "*Nonlinear tight-binding approximation for Bose-Einstein condensates in a lattice.*" Physical Review A **68**, 023613 (2003)

[180] P. Pedri, L. Pitaevskii, S. Stringari, C. Fort, S. Burger, F. S. Cataliotti, P. Maddaloni, F. Minardi, and M. Inguscio: "*Expansion of a Coherent Array of Bose-Einstein Condensates.*" Physical Review Letters **87**, 220401 (2001)

[181] A. Trombettoni, and A. Smerzi: "*Discrete Solitons and Breathers with Dilute Bose-Einstein Condensates.*" Physical Review Letters **86**, 2353–2356 (2001)

[182] M. Lewenstein, and L. You: "*Quantum Phase Diffusion of a Bose-Einstein Condensate.*" Physical Review Letters **77**, 3489–3493 (1996)

[183] Y. Castin, and J. Dalibard: "*Relative phase of two Bose-Einstein condensates.*" Physical Review A **55**, 4330–4337 (1997)

[184] J. Javanainen, and M. Wilkens: "*Phase and Phase Diffusion of a Split Bose-Einstein Condensate.*" Physical Review Letters **78**, 4675–4678 (1997)

[185] C. Orzel, A. K. Tuchman, M. L. Fenselau, M. Yasuda, and M. A. Kasevich: "*Squeezed states in a Bose-Einstein condensate.*" Science **291**, 2386–2389 (2001)

[186] M. Gustavsson, E. Haller, M. J. Mark, J. G. Danzl, R. Hart, A. J. Daley, and H.-C. Nägerl: "*Interference of interacting matter waves.*" New Journal of Physics **12**, 065029 (2010)

[187] M. J. Mark, E. Haller, J. G. Danzl, K. Lauber, M. Gustavsson, and H.-C. Nägerl: "*Demonstration of the temporal matter-wave Talbot effect for trapped matter waves.*" New Journal of Physics **13**, 085008 (2011)

[188] M. Cristiani, O. Morsch, J. Müller, D. Ciampini, and E. Arimondo: "*Experimental properties of Bose-Einstein condensates in one-dimensional optical lattices: Bloch oscillations, Landau-Zener tunneling, and mean-field effects.*" Physical Review A **65**, 063612 (2002)

[189] J.-M. Hou, T.-T. Zhao, and L.-J. Zhang: "*Excitations in a Dipolar Bose–Einstein Condensate.*" International Journal of Theoretical Physics **47**, 1211–1218 (2008)

[190] R. Ozeri, N. Katz, J. Steinhauer, and N. Davidson: "*Colloquium: Bulk Bogoliubov excitations in a Bose-Einstein condensate.*" Reviews of Modern Physics **77**, 187–205 (2005)

[191] N. Henkel, R. Nath, and T. Pohl: "*Three-Dimensional Roton Excitations and Supersolid Formation in Rydberg-Excited Bose-Einstein Condensates.*" Physical Review Letters **104**, 195302 (2010)

[192] A. P. Ivashin, and Y. M. Poluektov: "*Short-wave excitations in non-local Gross-Pitaevskii model.*" Central European Journal of Physics **9**, 857–864 (2011)

[193] R. M. Wilson, S. Ronen, and J. L. Bohn: "*Critical Superfluid Velocity in a Trapped Dipolar Gas.*" Physical Review Letters **104**, 094501 (2010)

[194] S. Bohlius: "*The Rosensweig instability in isotropic magnetic gels.*" (PhD Thesis, Bayreuth, 2008)

[195] E. Burt, R. Ghrist, C. Myatt, M. Holland, E. Cornell, and C. Wieman: "*Coherence, Correlations, and Collisions: What One Learns about Bose-Einstein Condensates from Their Decay.*" Physical Review Letters **79**, 337–340 (1997)

[196] J. H. Denschlag, J. E. Simsarian, H. Häffner, C. McKenzie, A. Browaeys, D. Cho, K. Helmerson, S. L. Rolston, and W. D. Phillips: "*A Bose-Einstein condensate in an optical lattice.*" Journal of Physics B: Atomic, Molecular and Optical Physics **35**, 3095–3110 (2002)

[197] J. Billy: "*Propagation quantique d'ondes de matière guidées: Laser à atomes et localisation d'Anderson.*" (PhD thesis, Paris, 2010)

[198] C. C. Bradley, C. A. Sackett, and R. G. Hulet: "*Bose-Einstein Condensation of Lithium: Observation of Limited Condensate Number.*" Physical Review Letters **78**, 985–989 (1997)

[199] M. Ueda, and H. Saito: "*A Consistent Picture of a Collapsing Bose–Einstein Condensate.*" Journal of the Physical Society of Japan **72**, 127–133 (2003)

[200] B. Kasch, H. Hattermann, D. Cano, T. E. Judd, S. Scheel, C. Zimmermann, R. Kleiner, D. Koelle, and J. Fortágh: "*Cold atoms near superconductors: atomic spin coherence beyond the Johnson noise limit.*" New Journal of Physics **12**, 065024 (2010)

[201] M. Abad, M. Guilleumas, R. Mayol, M. Pi, and D. M. Jezek: "*A dipolar self-induced bosonic Josephson junction.*" Europhysics Letters **94**, 10004 (2011)

[202] T. Lahaye, T. Pfau, and L. Santos: "*Erratum: Mesoscopic Ensembles of Polar Bosons in Triple-Well Potentials [Phys. Rev. Lett. 104, 170404 (2010)].*" Physical Review Letters **105**, 239904 (2010)

[203] M. Lu, S. H. Youn, and B. L. Lev: "*Trapping Ultracold Dysprosium: A Highly Magnetic Gas for Dipolar Physics.*" Physical Review Letters **104**, 063001 (2010)

[204] S. Kotochigova, and A. Petrov: "*Anisotropy in the interaction of ultracold dysprosium.*" Physical Chemistry Chemical Physics **13**, 19165 (2011)

[205] N. R. Thomas, N. Kjærgaard, P. S. Julienne, and A. C. Wilson: "*Imaging of s and d Partial-Wave Interference in Quantum Scattering of Identical Bosonic Atoms.*" Physical Review Letters **93**, 173201 (2004)

[206] A. Petrov, E. Tiesinga, and S. Kotochigova: "*Anisotropy induced Feshbach resonances in a quantum dipolar gas of magnetic atoms.*" arXiv:physics.atom-ph/1203.4172 (2012)

[207] A. Avdeenkov, and J. Bohn: "*Collisional dynamics of ultracold OH molecules in an electrostatic field.*" Physical Review A **66**, 052718 (2002)

[208] J. L. Bohn: "*Inelastic collisions of ultracold polar molecules.*" Physical Review A **63**, 052714 (2001)

[209] A. V. Gorshkov, P. Rabl, G. Pupillo, A. Micheli, P. Zoller, M. D. Lukin, and H. P. Büchler: "*Suppression of Inelastic Collisions Between Polar Molecules With a Repulsive Shield.*" Physical Review Letters **101**, 073201 (2008)

[210] C. Ticknor, and S. T. Rittenhouse: "*Three Body Recombination of Ultracold Dipoles to Weakly Bound Dimers.*" Physical Review Letters **105**, 013201 (2010)

[211] B. D. Esry, C. H. Greene, and J. P. Burke: "*Recombination of Three Atoms in the Ultracold Limit.*" Physical Review Letters **83**, 1751–1754 (1999)

[212] M. Drosg: "*Dealing with uncertainties: A guide to error analysis.*" (Springer, Berlin, 2007)

Danksagung

Abschließend möchte ich noch vielen lieben Leuten ganz herzlich danken, ohne die eine erfolgreiche Durchführung dieser Doktorarbeit unmöglich gewesen wäre.

Allen voran danke ich meiner Freundin Anna. Du hast mich die ganzen Jahre während der Doktorarbeit unterstützt, auch wenn es "mal" wieder später wurde bis ich zuhause war. Die physikfreie Zeit mit Dir war immer der perfekte Ausgleich zur intensiven Arbeit am Experiment. 1000 Dank für Alles!

Aus wissenschaftlicher Sicht habe ich die größte Unterstützung von Tilman Pfau erhalten. Tilman, Deine Fähigkeit junge Menschen für die Physik zu begeistern habe auch ich erfahren: schon als Hiwi durfte ich z.B. mit nach Düsseldorf auf die DPG-Tagung fahren. Über die Diplomarbeit bis schließlich zur Doktorarbeit habe ich immer Deine Motivation bewundert neue Wege zu gehen und die Eigenarten der (Quanten-) Welt zu entschlüsseln. Vielen Dank Dir dafür, dass ich in diese spannende Quantenwelt eintauchen durfte.
Ein Hauptgrund warum ich es so lange am Pi5 ausgehalten habe, ist eindeutig die gute Stimmung und der Zusammenhalt am gesamten Institut. Der Weg zum gemeinsamen Mittagessen erinnerte schon beinahe an Völkerwanderung und die vielen Events wie das Schlittenfahren am Solitude, die Institutssportspiele und die tollen (wenn auch etwas verregneten) Wanderausfahrten werden mir immer im Gedächtnis bleiben. Danke an alle Pi5-ler!
Ein spezielles Dankeschön geht an Karin Otter, Bea Olgun-Lichtenberg, Oliver Nagel und Nadine Prellwitz, die mich (und das ganze Pi5) in allen Organisationsfragen unterstützt haben. So konnten mich weder Inventarisierungen noch Zollformulare oder Reisekostenanträge vom Abschluss meiner Doktorarbeit abhalten. Ich möchte mich außerdem bei Frau Ohlendorf bedanken, die alles perfekt organisierte als ich ein Jahr in Hannover angestellt war.

Meine ersten experimentellen Techniken wurden mir während der Diplomarbeit am EIT-Experiment von Harald Kübler beigebracht. Kaum zu glauben wie Du die Organisation der gesamten Instituts-IT geschafft hast und Dir trotzdem Zeit für jede meiner Fragen genommen hast. Danke dafür!
Nach der Diplomarbeit durfte ich dann drei tolle Monate in Florenz verbringen und die Welt der ultrakalten Atome kennenlernen. Abgesehen von der Physik erinnere ich mich gerne ans Schweinshaxn-Essen im "Bovaro", an die Wanderung in den Appeninen und an den gemeinsamen Streik gegen die Kürzungen der staatlichen Forschungsgelder in Rom. Neben vielen anderen möchte ich mich besonders bei Matteo Zaccanti, Giacomo Roati, Ben Deissler, Mattia Jona-Lasinio, Marco Fattori und Giovanni Modugno für diese schöne Zeit bedanken.
Wieder zurück in Stuttgart bot mir Tilman die Möglichkeit, am Chrom-BEC-Experiment einzusteigen. Dort traf ich dann auf Ashok Mohapatra als Post-Doc und Jonas Metz als Doktorand, die mich in die Geheimnisse zur Erzeugung des Cr-BEC einweihten. Auch

wenn das Experiment in diesem ersten Jahr meiner Doktorarbeit nicht immer so wollte wie wir, haben wir nie den Mut verloren und viel Spaß zusammen gehabt. Jonas, bei Dir möchte ich mich ganz herzlich dafür bedanken, dass Du mir so viele Male anschaulich die Physik der dipolaren Quantengase erklärt hast (ich sag bloß "Finger-Finger-Interaction"). Beim gemeinsamen Kicken oder bei einem Bier konnten wir aber auch die Arbeit kurz vergessen und viel gemeinsam lachen.

Anfang 2010 zogen sich Ashok und Jonas dann vom Experiment zurück. Wie froh war ich, dass mit Juliette Billy und Emanuel Henn gleich zwei neue und erfahrene Post-Docs zu "Chromis" wurden. Gemeinsam brachten wir das Experiment wieder auf Vordermann: schon bald gab es die ersten Cr-BECs im optischen Gitter. Heiße Diskussionen, Höhen und Tiefen am Experiment haben uns in den gemeinsamen drei Jahren fest zusammengeschweißt. Juliette, ich möchte mich bei Dir für die vielen lustigen Momente (nicht vergessen: "Unterlegscheibe") und ganz besonders für das Korrekturlesen meiner Doktorarbeit bedanken. Emanuel, vielen Dank für die Ruhe die Du immer ausgestrahlt hast und auch für die brasilianischen Cashew-Nuts, dank derer wir so manche lange Labornacht überlebt haben.
Viel Leben in die "Bude" und wichtige Beiträge zum Experiment brachten auch unsere Diplomanden, Bachelors und Hiwis. Während meiner Doktorarbeit waren das: Yong Wan, Andreas Wünsch, Philipp Weinmann, David Peter, Matthias Schmitt und Holger Kadau. Vielen Dank Euch allen für Euer Engagement!
Zusammen mit Holger und Matthias komplettiert Thomas Maier das neue Doktoranden-Dreigestirn am Experiment. Das gute alte Cr-BEC-Setup ist zwar inzwischen beerdigt (R.I.P.), aber mit Euren Fähigkeiten bezwingt ihr auch Dysprosium. Viel Erfolg dabei!

Nachdem sich die ersten experimentellen Erfolge eingestellt hatten, wurde schon bald Kontakt zur Theoriegruppe von Luis Santos in Hannover aufgenommen. Es folgten viele spannende Diskussionen mit ihm und Mattia Jona-Lasinio, der inzwischen von Florenz nach Hannover gewechselt hatte. Mattias Simulationen konnte einige Geheimnisse lüften die im Experiment verborgen blieben und als Resultat entstanden aus unserer Kooperation zwei schöne Veröffentlichungen. Nicht nur die Diskussionen mit Euch haben mir immer Spaß gemacht, es herrschte bei unseren Treffen auch immer eine freundschaftliche Atmosphäre. Für Beides möchte ich mich bei Euch bedanken.
Eine weitere besondere "theoretische" Verbindung bestand zu unseren polnischen Freunden aus Warschau, Kazik Rzążewski und Krzysiek Pawłowski. Während Euren Aufenthalten in Stuttgart habt ihr Euch toll ins Institut und ins Cr1-Team integriert. Zusammen mit David Peter habt ihr Alles aus unserem "Calcmaster" herausgeholt und wichtige Simulationen für gegenwärtige und zukünftige Experimente durchgeführt. Unvergessen werden auch die gemeinsamen Institutssportspiele sein, bei denen wir alle beim 1000m-Lauf gegen Dich, Krzysiek, das Nachsehen hatten. Vielen Dank für die schöne Zeit und die wissenschaftliche Bereicherung unseres Experiments.
Auch bei den Theorie-Gruppen sind aller guten Dinge drei: ich möchte mich bei Prof. Wunner und Patrick Köberle bedanken, für die zahlreichen time-of-flight Simulationen die

im Laufe der Jahre mit ihren mächtigen Codes durchgeführt wurden. Des Öfteren sind wir vom Experiment einfach den Gang runter gegangen und haben an Patricks Tür geklopft. Daraus sind einige interessante Gespräche und zukunftsgerichtete Projekte entstanden.

Herr Wunner, Ihnen möchte ich außerdem für die Übernahme des Prüfungsvorsitzes meiner Doktorprüfung danken. Ihre angenehme Art und Ihre Expertenkenntnisse auf dem Gebiet der dipolaren Quantengase haben meine Wahl sehr einfach gemacht. Ich war sehr froh, dass wir einen Prüfungstermin zusammen mit Herrn Giessen finden konnten, dem ich herzlich für die Übernahme des Mitberichts zu meiner Arbeit danke.

Ganz zum Schluss geht ein riesiges Dankeschön an meine Eltern. Ihr habt mir während meiner ganzen Zeit an der Uni den Rücken gestärkt und ich wusste, dass ich mit jedem Problem zu Euch kommen konnte. Jedes Wochende zuhause war (und ist) mindestens genauso erholsam wie Urlaub und mobilisierte wieder alle Kräfte für die Arbeit.